

## Combined Author Index

- Aaronson, H.I. 1649-1658A  
2285-2297A  
2347-2351A  
2445-2470A  
2541-2547A
- Abinandanan, T.A. 1083-1090A  
3569-3573A  
Acsehrad, O. 3569-3573A  
Actis, F. 25-31A  
Adams, B.L. 3709-3718A  
Agarwal, H. 2599-2606A  
3443-3448A
- Aghaie-Khafri, M. 1363-1371A  
Agnew, S.R. 813-822A  
851-858A  
965-972A
- Ahmadi, G. 101-110B  
Ahn, J. 2933-2945A  
Aich, S. 3489-3498A  
Aidun, D.K. 101-110B  
Ajdelsztajn, L. 647-655A  
Akahori, T. 503-510A  
Akan, S. 1245-1254A  
Akdut, N. 1931-1938A  
Alcalá, J. 3187-3199A  
Aldinger, F. 2775-2779A  
Alhajeri, S. 3145-3153A  
Almer, J.D. 3839-3845A  
An, Y.G. 3121-3126A  
Ando, S. 823-829A  
831-836A  
1137-1144A
- Ankern, S. 465-476B  
Apelian, D. 231-239A  
Ardell, A.J. 921-927B  
Arita, M. 3535-3540A  
Armstrong, W.D. 613-623B  
Arnyowicz, D. 687-691A  
Anvanitidis, I. 589-594B  
Arzt, E. 1549-1557A  
Asaka, K. 495-501A  
Asta, M. 735-741A  
Asthana, R. 2119-2128A  
Atwood, R.C. 209-221B  
Au, D. 2053-2065A  
Aurelio, G. 1307-1317A  
Austin, C. 3127-3136A  
Babu, S.S. 1189-1200A  
Baburaj, E.G. 2729-2736A  
Bacon, D.J. 721-733A  
777-782A  
783-789A  
809-812A  
591-596A
- Bacroix, B. 1213-1219A  
Baek, W.-H. 1069-1074A  
Baggerly, R.G. 837-850A  
Bakshai, A. 3521-3526A  
Balogh, M.P. 567-574A  
Banerjee, R. 2129-2138A  
Banerjee, S. 1919-1929A  
Bao, H. 3201-3204A  
Barnett, M.R. 1893-1900A  
Baró, M.D. 1865-1868A  
Barsoum, M.W. 2775-2779A  
Bastian, F.L. 647-655A  
Basu, B. 3847-3859A  
Bate, P.S. 93-100A  
Batra, I.S. 3573-3576A  
Baxter, G.J. 3215-3225A  
3227-3234A  
3457-3464A
- Becker, R. 69-78B  
Beckermann, C. 731-740B  
741-755B  
932-937B
- Bedolla, E. 1201-1211A  
Bell, T. 3241-3248A  
Benhadad, S. 2005-2017A  
Bernier, A. 551-559B  
Beuth, J. 3127-3136A  
Beuth, J.L. 417-426A  
Bewlay, B.P. 3349-3356A  
Beyerlein, I.J. 3839-3845A  
Bhadeshia, H.K.D.H. 1075-1081A  
3339-3347A
- Bhattacharya, B. 3605-3618A  
Bhavani, S.H. 565-575B  
Biery, N. 3127-3136A  
Biery, N.E. 417-426A  
Bingert, J.F. 949-954A  
955-963A  
965-972A
- Biro, E. 2019-2030A  
Blaine, D. 2185-2194A  
Blum, W. 291-303A  
305-310A  
319-327A
- Bocanegra, E.H. 2581-2591A  
Bodin, A. 1589-1603A  
1883-1891A  
2593-2598A
- Boerma, D.O. 3075-3087A  
1201-1211A  
Boettinger, W.J. 1779-1794A  
Böhmer, H.J. 3187-3199A  
Bouchard, D. 403-411B  
Bourke, M.A.M. 757-763A  
Bousquet-Melou, P. 365-376B  
Bowman, W.G. 1883-1891A  
Bowen, P. 3045-3054A  
3719-3730A
- Boyce, B.L. 899-918A  
Bozzolo, G. 265-284B  
Brandon, D.G. 551-559B  
561-564B
- Braun, M.W. 2485-2494A  
Brehm, H. 363-371A  
Breutinger, F. 291-303A  
Brimacombe, J.K. 413-423B  
Bronsveld, P.M. 3075-3087A  
Brooks, J.A. 5-15A  
Brown, C.M. 1725-1735A  
Brown, D.W. 757-763A  
Buchheit, T.E. 539-554A  
Burkins, M.S. 937-947A  
Butts, D.A. 3205-3214A  
Cailletaud, G. 2825-2833A  
Campbell, J.P. 899-918A  
Campo, J. 1307-1317A  
Canadine, D. 3661-3672A  
Carlson, K.D. 731-740B  
741-755B
- Carpenter, R.W. 437-442A  
Celotto, S. 801-807A  
Chae, S.W. 973-980A  
Chakraborty, S. 605-612B  
Chan, K.S. 401-416A  
Chandran, K.S.R. 3489-3498A  
Chandrasekar, S. 1245-1254A  
Chang, B.H. 1275-1280A  
Chang, K.-M. 3465-3478A  
Chang, S.-Y. 2859-2867A  
Chang, W.-S. 757-764B  
Chao, C.-G. 31-40B  
637-646A
- Chao, C.-H. 2703-2711A  
Chaturvedi, M.C. 2005-2017A  
Chawla, N. 73-81A  
3861-3869A
- Chechenin, N.G. 2593-2598A  
3075-3087A  
3011-3017A  
3393-3402A  
707-711A
- Chen, H.Z. 1263-1273A  
Chen, J.H. 2623-2634A  
Chen, L.H. 1287-1292A  
Chen, Q. 897-900B  
Chen, Q.Z. 1319-1330A  
Chen, S.-W. 995-1002A  
Chen, S.P. 529-537A  
Chen, T. 1737-1742A  
Chen, W. 1429-1436A  
Chen, Y.L. 2713-2718A  
3777-3785A  
3787-3794A
- Chen, Y.M. 3117-3120A  
Cheng, H.F. 3565-3568A  
Cheong, Y.M. 919-925A  
Cheung, N. 2107-2118A  
Chezan, A.R. 3075-3087A
- Chhabra, P.N. 1245-1254A  
Chi, M.-Y. 661-668B  
Chi, R. 41-46B  
Chiba, Y. 2659-2665A  
Cho, Y.K. 713A  
Choi, J. 1487-1497A  
Choi, W.S. 973-980A  
Chong, S.H. 2425-2431A  
Chou, I. 1681-1687A  
Chow, C.K. 1103-1115A  
Christenson, T.R. 539-554A  
Christodoulou, N. 1103-1115A  
Chumlyakov, Y. 3661-3672A  
Chung, K. 647-655A  
Chung, K.H. 125-134A  
3795-3801A
- Chung, Y.-H. 665-673A  
Cisneros, M.M. 2139-2144A  
3273-3278A
- Cizek, P. 1331-1349A  
Claessens, S. 2573-2580A  
Claves, S.R. 693-713A  
Cockcroft, S. 2053-2065A  
Cockeram, B.V. 33-56A  
3403-3419A  
3685-3707A
- Cola, M. 1509-1520A  
Collins, P.C. 2129-2138A  
Conejo, A.N. 187-199B  
Cooper, K.P. 2789-2799A  
Corbin, S.F. 117-124A  
Cornish, L.A. 987-993A  
Cortie, M.B. 987-993A  
Cox, M.J. 437-442A  
Cramb, A.W. 129-136B  
Craus, C.B. 3075-3087A  
Cuello, G.J. 1307-1317A  
Czerwinski, F. 2963-2972A  
da Costa, C.E. 3541-3553A  
Daehn, G.S. 183-191A  
363-371A  
2649-2658A
- Damodaran, A.D. 391-400A  
Das, S. 3031-3044A  
Das, S.K. 3731-3740A  
David, S.A. 1189-1200A  
Davidson, D.L. 401-416A  
Davies, C.H.J. 1331-1349A  
Davies, H. 1853-1857A  
Dayananda, M.A. 3375-3392A  
De Cooman, B.C. 1091-1102A  
1659-1667A  
1931-1938A  
2573-2580A
- de Diego, N. 777-782A  
783-789A
- De Graef, M. 3127-3136A  
De Hosson, J.Th.M. 3075-3087A  
de la Rubia, T.D. 285-296B  
De Meyer, M. 1659-1667A  
Degnan, C.C. 2973-2983A  
Delph, T.J. 383-390A  
Demura, M. 2607-2613A  
Dewing, E.W. 140-142B  
901-908B  
909-913B
- Dey, G.K. 1437-1447A  
1919-1929A  
3573-3576A  
3329-3337A
- Di Nunzio, P.E. 3205-3214A  
Di Ruscio, M. 140-142B  
Diep, Q.B. 555-565A  
Dighe, M.D. 1229-1243A  
Ding, H. 3249-3253A  
Ding, W. 3045-3054A  
Ditze, A. 355-364B  
929-930B
- Divinski, S. 765-775A  
Dixit, S. 3031-3044A  
Doherty, R.D. 1859-1860A  
Domey, J.J. 101-110B  
Dong, H. 1201-1211A  
Dong, S.J. 1275-1280A  
2240-2244A
- Draper, S.L. 3871-3874A
- Du, H. 1963-1969A  
Dunand, D.C. 1669-1680A  
Dunn, M. 203A  
Duprez, L. 1931-1938A  
Dutta, P. 605-612B  
Dutta, R.S. 1437-1447A  
Dwarakadasa, E.S. 391-400A  
Dye, D. 2921-2931A  
Dymont, F. 797-800A  
Dyson, B.F. 2549-2557A  
Eagar, T.W. 2559-2567A  
Eberl, F. 2825-2833A  
Eisenlohr, P. 291-303A  
305-310A  
135-143A
- El-Eskandarany, M.S. 2145-2153A  
775-785B
- El-Kaddah, N. 2775-2779A  
El-Raghy, T. 3127-3136A  
Elliott, A. 3591-3595A  
Ellner, M. 2309-2316A  
Enos, D.G. 1151-1166A  
Escalante, J.I. 3273-3278A  
Evangelista, E. 373-381A  
Evans, J.W. 321-324B  
669-676B  
677-683B
- Everett, R.K. 3293-3295A  
Eylon, D. 3527-3534A  
Fan, L. 2240-2244A  
Fan, Z. 3511-3520A  
Fedoseyev, A. 3876-3881A  
Fehrenbacher, L. 675-679A  
Fernández, A.I. 3089-3098A  
Fernández, J.R. 791-796A  
Ferry, M. 1499-1507A  
3747-3754A
- Field, R.D. 965-972A  
Fine, M.E. 575-580A  
1531-1539A
- Fischer, T.E. 145-157A  
159-164A
- Flemings, M.C. 2737-2746A  
Fonda, R.W. 2495-2505A  
2507-2518A  
319-327A
- Forest, S. 2825-2833A  
385-392B
- Forsberg, S. 1669-1680A  
Fray, M. 3831-3838A  
Fras, E. 2129-2138A  
Fray, D.J. 685-693B  
Froes, F.H. 2729-2736A  
Fruehan, R.J. 335-344B  
Fu, H. 3249-3253A  
Fu, Y. 183-191A  
Fujita, N. 3339-3347A  
Fujita, T. 506-509B  
Fukunaga, K. 3137-3144A  
Fukuyama, H. 47-54B  
257-264B
- Fung, K.-Z. 2433-2443A  
Furuhara, T. 2327-2335A  
Furuya, Y. 3421-3431A
- Gajdardziska-Josifovska, M. 1541-1547A  
Gale, W.F. 3205-3214A  
Gangloff, R.P. 1991-2004A  
Gao, T. 3285-3292A  
Gao, Y.-K. 1775-1778A  
Garces, J.E. 265-284B  
Garcia, A. 2107-2118A  
Garcia, R. 932-937B  
Genç, A. 2729-2736A  
German, R.M. 2185-2194A  
Gheorghe, I. 2155-2162A  
Ghosh, A. 891-896B  
Ghosh, S. 1569-1572A  
Gibbs, R.K. 1019-1026A  
Gogia, A.K. 2763-2766A  
Goh, C.-S. 3433-3442A  
Gokhale, A.M. 555-565A  
2599-2606A  
3443-3448A  
2775-2779A  
3457-3464A
- Golczewski, J. 3457-3464A  
Goldberg, A. 3457-3464A

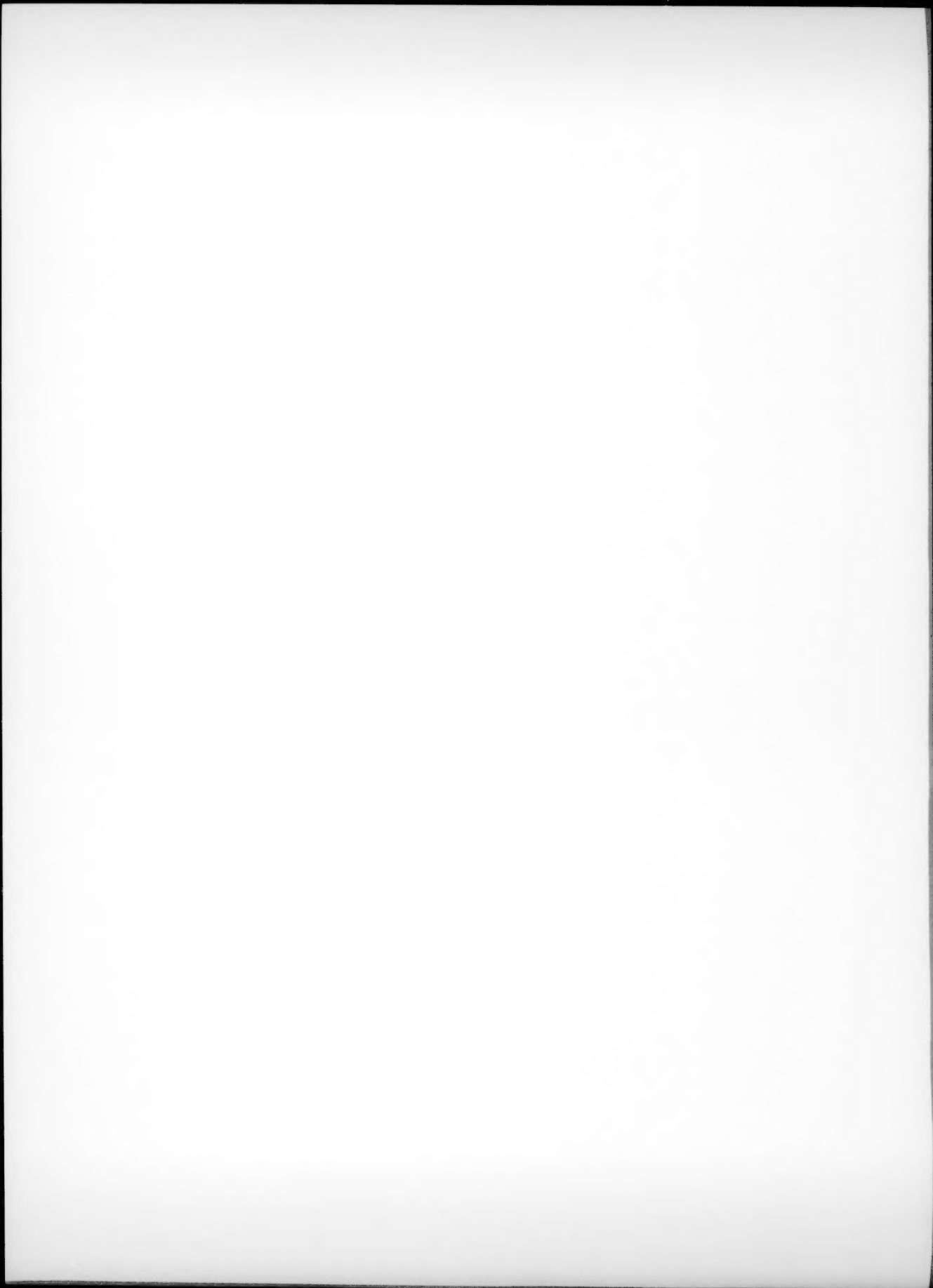
Gong, C.L.	3565-3568A	Hochanadel, P.	1509-1520A		2649-2658A	Kim, Y.-W.	2847-2857A
González, A.	25-31A	Hodgson, P.D.	1019-1026A	Jiang, L.	1287-1292A	Kim, Y.H.	3255-3272A
Gopalakrishnan, P.	1475-1485A		1331-1349A	Jiang, T.	813-816B	Kim, Y.S.	919-925A
Gorissen, R.	163-172B		1893-1900A	Jirincy, V.	669-676B		3155-3164A
	639B		2985-2993A		677-683B	Kimura, S.	427-436A
Gotoh, T.	823-829A	Holappa, L.	595-603B	Jo, S.-K.	703-709B	Kimura, Y.	3241-3248A
Goyeau, B.	365-376B	Holden, T.M.	749-755A	Jog, C.S.	1083-1090A	King, F.	1429-1436A
Graham, S.	2599-2606A	Holt, R.A.	749-755A	Johnsen, J.	3019-3024A	Kinoshta, H.	2073-2080A
	3443-3448A		859-865A	Johnson, W.C.	1901-1911A	Kirkaldy, J.S.	3357-3365A
Granada, D.G.	3619-3633A	Hong, J.H.	1565-1569A	Jonas, J.J.	2719-2727A	Kishida, K.	2607-2613A
Gray, G.T., III	581-589A	Hong, M.-H.	1069-1074A	Jones, A.R.	2713-2718A	Klarstrom, D.L.	1287-1292A
	955-963A	Hong, S.-G.	1689-1698A		3777-3785A	Klassen, R.J.	1103-1115A
Green, P.M.	1737-1742A	Hong, S.I.	3155-3164A		3787-3794A	Knowles, D.M.	1319-1330A
Gregori, A.	1009-1018A	Horita, Z.	2173-2184A	Jones, H.N., III	2789-2799A		3165-3172A
Gremaud, M.	2095-2106A	Horstemeyer, M.F.	555-565A	Jones, W.K., Jr.	321-324B	Kobayashi, T.	3741-3746A
Griffiths, M.	859-865A		2599-2606A	Jonsson, L.	173-185B	Koizumi, Y.	3741-3746A
Groza, J.	3019-3024A		3443-3448A	Jönsson, P.	173-185B	Kokawa, H.	625-635A
Grugel, R.N.	3876-3881A	Horton, J.A.	851-858A	Jordan, J.L.	1737-1742A	Komanduri, R.	2995-3010A
Gu, Y.F.	1281-1283A	Hosford, W.F.	1255-1261A	Joshi, V.	2763-2766A	Komatsu, S.-Y.	487-493A
Guan, X.S.	1292-1295A	Hossain, Md.K.	257-264B	Ju, J.-B.	2615-2622A	Kong, M.	3298-3300A
Guillemet, A.F.	1307-1317A	Hou, Z.-B.	2995-3010A	Juan, J.S.	2581-2591A	Konishi, J.	413-423B
Guo, D.	377-384B	Howe, J.M.	1561-1565A	Juarez, R.	2229-2235A	Koo, J.B.	3803-3815A
Guo, J.	3249-3253A		2391-2411A	Jung, S.-M.	930-932B	Kool, W.H.	1971-1980A
Guo, R.Q.	1541-1547A	Howes, B.	403-411B	Jung, S.-W.	1213-1219A	Korsunsky, A.M.	2921-2931A
Gupta, S.	315-319B	Hsiao, I.C.	1373-1384A	Kad, B.K.	937-947A	Koss, D.A.	3293-3295A
Gutkin, M.Yu.	1351-1362A	Hsu, C.-W.	31-40B	Kadaya, Y.	2549-2557A	Kotil, T.	3661-3672A
Ha, M.	1487-1497A	Hu, C.-T.	17-23A	Kafuku, H.	3235-3240A	Koutzaki, S.H.	1579-1588A
Haarberg, G.M.	577-587B	Hu, H.	897-900B	Kalinuma, R.	2817-2824A	Kozhakhmetov, S.	551-559B
	901-908B	Huang, H.S.	657-664A	Kalashnikov, I.S.	3569-3573A		561-564B
	909-913B	Huang, J.C.	1373-1384A	Kamat, S.V.	2763-2766A	Kratochvil, J.	319-327A
Hackenberg, R.E.	3619-3633A		1461-1473A	Kamp, N.	1125-1136A	Krauss, G.	1627-1637A
Haefner, D.R.	3839-3845A	Huang, P.	1117-1124A	Kampe, S.L.	2747-2753A	Krendelsberger, N.	3311-3319A
Haj-Ali, R.M.	1939-1947A	Huang, Z.	813-816B	Kang, S.-J.L.	1213-1219A	Krzanowski, J.E.	1579-1588A
Hall, B.J.	3279-3284A		1681-1687A	Kang, S.B.	1521-1530A	Kucharová, K.	883-889A
Hall, M.G.	2347-2351A	Hudson, N.	565-575B	Kang, T.	1487-1497A	Kudoh, M.	2073-2080A
Hamada, I.	1743-1754A	Hui, J.	3499-3510A	Kang, Y.-B.	915-920B	Kuhlmann-Wilsdorf, D.	2519-2539A
	2907-2919A	Hui, C.M.	1765-1773A	Kaptay, G.	1869-1873A	Kulkarni, S.K.	1437-1447A
Hamel, F.G.	403-411B	Hunt, D.W.	3165-3172A	Karlsson, B.	2869-2881A	Kulkarni, U.D.	3573-3576A
Hampikian, J.M.	1737-1742A	Hunter, A.	1499-1507A	Karthikeyan, S.	329-336A	Kumar, A.	1617-1626A
Han, F.S.	3565-3568A		3747-3754A	Kaschner, G.C.	757-763A	Kumar, K.C.H.	3847-3859A
Han, J.-H.	665-673A	Hurkmans, A.	3121-3126A		949-954A	Kumar, M.	2353-2371A
Han, Q.	2067-2072A	Hurley, P.J.	1019-1026A		955-963A	Kumar, P.	605-612B
Han, S.	2237-2240A		2985-2993A	Kashiwaya, Y.	129-136B	Kuribayashi, K.	2677-2683A
	3298-3300A	Hwang, B.	2933-2945A	Kashyap, B.P.	2763-2766A		2947-2953A
Han, X.	2835-2845A	Hwang, D.-Y.	2859-2867A	Kassner, M.E.	311-317A		2955-2961A
Han, X.J.	1221-1228A	Hwang, K.S.	657-664A		337-343A	Kuroda, D.	3137-3144A
Hanan, J.C.	3839-3845A	Hwang, S.K.	973-980A		3145-3153A	Kurz, W.	2337-2345A
Hansen, S.G.	577-587B	Hwang, S.M.	3255-3272A	Katgerman, L.	1971-1980A	Kwak, W.J.	3255-3272A
Hao, Y.L.	3137-3144A	Iglesias, M.M.	797-800A	Kattner, U.R.	1779-1794A	Kwon, D.	2615-2622A
Hara, T.	3241-3248A	Iguchi, M.	155-162B	Katarov, I.	1027-1040A	Kwon, H.	455-465A
Harada, H.	1281-1283A		695-702B	Kelly, G.L.	1019-1026A	Kwon, S.C.	919-925A
	3741-3746A	Ikeda, M.	487-493A		1893-1900A	Kwun, S.I.	973-980A
Hardin, R.A.	731-740B	Im, K.S.	919-925A	Kempen, A.T.W.	1041-1050A	Laha, K.	1617-1626A
	741-755B	Inoue, A.	135-143A	Kenzhaliev, E.	551-559B	Lahiri, A.K.	499-501B
Harding, R.A.	3719-3730A		2145-2153A		561-564B	Lam, Y.C.	477-488B
Hartwig, K.T.	965-972A	Inoue, T.	511-519A	Kerr, H.W.	2667-2676A	Lan, C.W.	3011-3017A
Haseeb, A.S.M.A.	921-927B	Iorio, L.E.	3349-3356A	Kestens, L.	1091-1102A	Langdon, T.G.	249-259A
Hasegawa, H.	427-436A	Iribarren, M.J.	797-800A	Khrishish, T.A.	285-296B		883-889A
Hashimoto, H.	3321-3328A	Irons, G.A.	377-384B	Ki, H.	1817-1830A		1865-1868A
Hayashi, M.	47-54B	Isaenkova, M.	867-874A		1831-1842A		2173-2184A
Hayashi, Y.	921-927B	Isaka, M.	3235-3240A	Kikuchi, M.	3339-3347A	Lannutti, J.J.	165-170A
Hayes, P.	827-838B	Isheim, D.	2317-2326A	Kim, B.-C.	1449-1459A		183-191A
Hayes, P.C.	839-849B	Ishida, K.	2817-2824A	Kim, B.-N.	3449-3455A	Larose, J.	3555-3564A
	817-825B	Iwasaki, K.	1292-1295A	Kim, B.-S.	711-716B	Larsen, M.	3349-3356A
	851-863B	Iwashita, C.	1681-1687A		717-721B	Larsen, R.J.	949-954A
	865-876B	Jack, T.R.	1429-1436A	Kim, C.	2237-2240A	Lassila, D.H.	3457-3464A
	877-890B	Jacobs, M.H.	1795-1804A		3298-3300A	LaVan, D.A.	539-554A
Hayes, R.W.	329-336A	Jahanshahi, S.	61-67B	Kim, D.I.	3155-3164A	Lavernia, E.J.	125-134A
Hayes, T.A.	337-343A	Jak, E.	817-825B	Kim, E.-P.	1213-1219A		145-157A
He, J.	145-157A		827-838B	Kim, H.W.	1521-1530A		159-164A
	159-164A		839-849B	Kim, J.-S.	1449-1459A		647-655A
He, L.M.	3578-3582A		851-863B	Kim, J.K.	1541-1547A		3795-3801A
He, Y.H.	1287-1292A		865-876B		3155-3164A	Lebensohn, R.A.	2635-2648A
He, Z.	681-685A		877-890B	Kim, J.S.	701-704A	LeBrun, J.-L.	591-596A
Headley, T.J.	5-15A	James, K.E.	2921-2931A	Kim, K.-B.	1449-1459A	Lebrun, J.L.	2825-2833A
Heenan, R.K.	1883-1891A	Janas, A.	3831-3838A	Kim, M.H.	973-980A	Ledbetter, H.	203A
Helfter, G.	137-140B	Jang, J.-I.	2615-2622A	Kim, M.J.	437-442A	Lee, B.-W.	2615-2622A
Heinz, B.	489-498B	Jang, W.	1755-1763A	Kim, N.J.	701-704A	Lee, B.J.	1565-1569A
Henry, M.F.	713A	Jata, K.V.	2847-2857A		3649-3659A	Lee, B.S.	1565-1569A
	3803-3815A	Jayakumar, T.	1617-1626A	Kim, S.	1399-1412A	Lee, C.S.	3173-3185A
Hermida, J.D.	235-241B	Jayaraman, P.	2649-2658A		1755-1763A	Lee, D.N.	1605-1616A
Herrera, R.	25-31A	Jensen, M.V.R.S.	2921-2931A		2237-2240A	Lee, H.-C.	1057-1067A
Herzig, C.	765-775A	Jentoftsen, T.E.	901-908B		3298-3300A	Lee, H.-G.	915-920B
Hickson, M.R.	1019-1026A		909-913B		3876-3881A		930-932B
Hillert, M.	2299-2308A	Jeong, S.	1487-1497A	Kim, S.-H.	703-709B	Lee, H.-Y.	1449-1459A
Hiraga, K.	3449-3455A	Jephcoat, A.P.	743-747A		1605-1616A	Lee, I.F.	3011-3017A
Hirano, T.	2607-2613A	Ji, J.-F.	637-646A	Kim, S.K.	701-704A	Lee, J.	125-134A
Hirth, J.P.	1649-1658A	Ji, S.	3511-3520A		1051-1056A		647-655A
	2541-2547A	Jia, J.	3249-3253A	Kim, S.S.	919-925A		1399-1412A
Ho, C.Y.	91-100B	Jian, Z.	2947-2953A	Kim, T.-H.	1449-1459A	Lee, J.-C.	665-673A
Ho, K.M.	813-822A	Jiang, C.	3597-3603A	Kim, W.-S.	2615-2622A	Lee, J.D.	3155-3164A
Ho, N.J.	1461-1473A	Jiang, G.	183-191A	Kim, W.J.	3155-3164A	Lee, J.H.	3255-3272A

Lee, K.B.	455-465A	M'Hamdi, M.	2081-2093A	Mohanty, P.S.	1817-1830A	Olijnyk, H.	743-747A
Lee, P.D.	209-221B	Ma, D.	223-233B		1831-1842A	Omori, T.	2817-2824A
	443-454A	Ma, J.	681-685A	Molinari, A.	613-624A	Ono, N.	2817-2824A
	1795-1804A	Ma, L.	3465-3478A	Molloseau, C.L.	335-344B	Ono-Nakazato, H.	393-401B
Lee, P.S.	1805-1815A	Maciejewski, J.	675-679A	Mondal, D.P.	3031-3044A	Osetsy, Y.N.	777-782A
Lee, S.	3709-3718A	Magnin, B.	1971-1980A	Monnet, G.	591-596A		783-789A
	1069-1074A	Mahajan, S.	2347-2351A	Montero-Ocampo, C.	2229-2235A	Ostrovski, O.	61-67B
	1213-1219A	Mahieu, J.	2573-2580A	Montheillet, F.	2719-2727A	Ou, S.	731-740B
	1487-1497A	Mahmudi, R.	1363-1371A	Monti, A.M.	791-796A		741-755B
	2933-2945A	Maier, H.J.	3661-3672A	Moon, H.	1487-1497A	Ovecoglu, L.	2729-2736A
	3173-3185A	Majder, D.	2053-2065A	Moon, S.M.	55-59B	Overfelt, R.A.	565-575B
	3649-3659A	Majka, T.F.	1627-1637A	Moore, K.T.	1561-1565A	Padula, S.A., II	1949-1962A
Lee, S.-B.	930-932B	Majla, J.	1509-1520A	Morales, R.	589-594B	Pahutová, M.	883-889A
Lee, S.H.	55-59B	Makhoul, M.	297-303B	Morales, R.D.	187-199B	Pai, B.C.	391-400A
Lee, W.-B.	1689-1698A		305-314B	Mori, H.	3055-3063A		2755-2761A
Lee, W.-S.	2801-2810A	Maki, J.	2573-2580A	Morisawa, S.	393-401B	Palaniappa, M.	1475-1485A
Lee, W.C.	3649-3659A	Maki, T.	2327-2335A	Morris, J.R.	813-822A	Pang, J.W.L.	749-755A
Lee, W.Y.	3578-3582A	Malinov, S.	1027-1040A	Mosca, H.O.	265-284B		3215-3225A
Lee, Y.	1399-1412A	Mancha, H.	2139-2144A	Moverare, J.J.	57-71A		3227-3234A
Lee, Y.-K.	1913-1917A		3273-3278A	Moylan, S.P.	1245-1254A	Paradkar, A.G.	2763-2766A
Lei, P.-X.	661-668B	Maniruzzaman, M.	297-303B	Muddle, B.C.	1331-1349A	Park, C.-G.	1689-1698A
Leith, S.D.	539-554A		305-314B		1649-1658A	Park, I.	3591-3595A
Lemanowicz, I.	163-172B		345-354B		2381-2389A	Park, J.H.	55-59B
	639B	Mankhand, T.R.	3465-3478A		2541-2547A		723-729B
Leo, P.H.	1901-1911A	Mannan, S.K.	932-937B		2985-2993A	Park, J.K.	425-436B
Lerch, B.A.	3871-3874A	Manzano, A.	2835-2845A	Muir, D.	137-140B		437-449B
Leu, C.-C.	17-23A	Mao, S.X.	675-679A	Mukai, K.	506-509B		1051-1056A
Levenfeld, B.	1843-1851A	Marks, L.D.	1949-1962A	Mukhopadhyay, A.K.	3635-3648A	Park, K.-T.	705-707A
Levey, F.C.	987-993A	Marras, S.I.	2747-2753A	Mukhopadhyay, P.	1919-1929A		2859-2867A
Lewandowski, J.J.	3555-3564A	Marte, J.S.	2081-2093A	Muliana, A.	1939-1947A	Park, S.-H.	1689-1698A
Li, D.	1991-2004A	Martin, C.L.	2747-2753A	Mun, S.-H.	1057-1067A	Park, T.Y.	3155-3164A
	3111-3115A	Martukanitz, R.P.	1189-1200A	Murakumo, T.	3741-3746A	Park, W.	3649-3659A
Li, D.Y.	1981-1989A	Maruyama, K.	875-882A	Murata, M.	47-54B	Parks, K.D.	1189-1200A
Li, J.-K.	1775-1778A	Marx, B.	2185-2194A	Mutale, C.-T.	355-364B	Pasianot, R.C.	791-796A
Li, L.	2031-2042A	Masaki, S., Jr.	3741-3746A		929-930B	Patankar, S.N.	2729-2736A
Li, M.	2677-2683A	Mason, T.A.	949-954A	Na, S.-J.	757-764B	Patel, S.J.	3465-3478A
Li, W.	165-170A		955-963A	Nabarro, F.R.N.	213-218A	Paton, N.E.	837-850A
	201-207B	Massalski, T.B.	2277-2283A		2473-2474A	Patrick, T.R.C.	79-89B
	3201-3204A	Masuda, M.	921-927B	Nadeau, J.-P.	403-411B	Paumelle, C.	403-411B
Li, W.-C.	2163-2172A	Mathiesen, R.H.	613-623B	Nagashio, K.	2677-2683A	Paunova, R.	633-638B
Li, X.	1057-1067A	Matlock, D.K.	1627-1637A		2947-2953A	Pawlik, R.J.	597-612A
	2835-2845A		3099-3110A	Nagata, K.	2955-2961A	Pedersen, A.S.	3755-3760A
	3019-3024A	Matsuoka, S.	3421-3431A		47-54B	Pehlke, R.D.	519-541B
	3367-3373A	Matsuura, K.	2073-2080A		257-264B		2251-2273A
Li, X.-D.	2205-2215A	Matz, J.E.	2559-2567A	Nagata, M.T.	3099-3110A	Peng, Z.F.	3065-3066A
	2217-2227A	Maudlin, P.J.	955-963A	Nagumo, M.	495-501A	Pequet, Ch.	2095-2106A
Li, X.Z.	675-679A	Maugis, P.	3357-3365A	Nainaparampil, J.J.	1579-1588A	Pereira, J.M.	581-589A
Li, Y.	651-660B	Mazumdar, D.	891-896B	Nakajima, K.	427-436A		3871-3874A
	3111-3115A		937-941B	Nakano, T.	521-528A	Pereira, L.C.	3569-3573A
Li, Z.	1117-1124A	Mazumder, J.	1817-1830A	Nakazawa, S.	1281-1283A	Perez-Prado, M.-T.	3145-3153A
Liang, C.	2163-2172A		1831-1842A	Nalla, R.K.	899-918A	Pérez-Prado, M.T.	279-290A
Liauw, P.K.	1287-1292A	Mazumder, P.	3763-3775A	Nam, J.	165-170A		311-317A
Lienert, U.	3839-3845A	McCabe, R.J.	575-580A	Nandy, T.K.	2763-2766A	Pérez-Sáez, R.B.	2581-2591A
Lima, M.	2337-2345A	McKenna, V.T.	1531-1539A	Natarajan, T.T.	775-785B	Perlovich, Y.	867-874A
Lin, C.-F.	2801-2810A	McLain, S.	146-147B	Nath, S.K.	3479-3488A	Pete, T.P.	2747-2753A
Lin, C.-K.	1715-1724A	McLean, M.	443-454A	Navruz, N.	204A	Peters, J.O.	899-918A
Lin, H.K.	1461-1473A		1795-1804A	Necker, C.T.	965-972A	Pettermann, H.E.	3187-3199A
Lin, S.-T.	2163-2172A		2549-2557A		2635-2648A	Pleifer, H.	163-172B
Lin, S.C.	2623-2634A		279-290A	Neculae, A.	365-376B		639B
Liu, G.	3249-3253A	McNelly, T.R.	2173-2184A	Neeraj, T.	891-898A	Piehler, H.R.	3709-3718A
Liu, J.	41-46B		345-362A	Nes, E.	305-310A	Pietrzyk, M.	1509-1520A
Liu, Y.	145-157A	McQueen, H.J.	2135-2144A	Ni, J.	3111-3115A	Pillai, R.M.	2755-2761A
	159-164A	Méndez, M.	3273-3278A	Nie, J.F.	1649-1658A	Pillai, U.T.S.	391-400A
	3576-3578A		2139-2144A		2381-2389A	Piotrowski, G.	3861-3869A
Liu, Z.-K.	2781-2787A	Mendoza, G.	3273-3278A		2541-2547A	Pishbin, H.	1363-1371A
	3597-3603A		1413-1427A	Niesen, L.	3075-3087A	Poirier, D.R.	3874-3876A
Liu, Z.G.	2195-2203A	Mercer, C.	2031-2042A	Niinomi, M.	477-486A	Polasik, S.J.	73-81A
Lobo, A.	1437-1447A	Messler, R.W., Jr.	3578-3582A		487-493A	Pollock, T.M.	3127-3136A
Locci, I.E.	597-612A	Meyer, J.D.	539-554A		503-510A	Pond, R.C.	801-807A
	1385-1397A	Michael, J.R.	1639-1648A		3137-3144A		809-812A
Long, M.	311-317A	Miettinen, J.	1351-1362A	Nilsson, J.-O.	1009-1018A		3787-3794A
López, B.	3089-3098A	Mikaelian, K.N.	413-423B	Nitsche, H.	1041-1050A	Porter, W.D.	2775-2779A
López, H.F.	2139-2144A	Miltzer, Y.	417-426A	Nó, M.L.	2581-2591A	Powell, B.R.	567-574A
	3273-3278A	Miller, U.	2713-2718A	Noe, R.D.	265-284B	Pownceby, M.I.	79-89B
	3831-3838A		3787-3794A	Noguchi, K.	2659-2665A	Prabhu, N.	1919-1929A
López, V.H.	932-937B	Milligan, W.W.	1949-1962A	Noh, J.-W.	1069-1074A	Pragani, R.	3521-3526A
Lorentsen, O.-A.	901-908B	Mills, M.J.	329-336A		1213-1219A	Prasad, A.J.K.	345-354B
	909-913B		891-898A	Nozue, A.	2659-2665A	Prasad, P.M.	345-354B
Lorentzen, T.	3535-3540A		1725-1735A	Nurislamova, G.V.	1865-1868A	Preuss, M.	3215-3225A
Lowekamp, J.B.	2043-2052A	Mills, W.J.	55-59B	O'Brien, J.M.	1255-1261A		3227-3234A
Lowke, J.J.	2703-2711A	Min, D.J.	723-729B	O'Neill, J.	675-679A		3019-3024A
Lu, H.-Y.	3055-3063A	Minoda, T.	2891-2898A	Oda, Y.	511-519A	Prinz, F.	3755-3760A
Lu, W.	3673-3683A	Miodownik, A.P.	3367-3373A	Odén, M.	57-71A	Pryds, N.H.	231-239A
Ludwig, A.	707-711A	Mishin, Y.	765-775A	Odenhal, H.-J.	163-172B	Przystupa, M.A.	1437-1447A
Lui, T.S.	1263-1273A	Mishra, K.G.	137-140B		639B	Purdy, G.R.	2347-2351A
	2623-2634A	Misolek, W.Z.	693-713A	Offerman, S.E.	1883-1891A	Putyera, K.	3578-3582A
Lundström, D.	2869-2881A	Mitteijer, E.J.	1041-1050A	Oh, J.	3649-3659A	Pyo, S.G.	3649-3659A
Luo, A.A.	567-574A	Miwa, K.	3025-3030A	Oh, J.C.	3173-3185A	Pyshmintsev, I.Yu.	1659-1667A
Luo, J.	3719-3730A	Mizoguchi, S.	427-436A	Oh, K.H.	1057-1067A	Qian, M.	1283-1287A
Luo, S.-J.	995-1002A	Mo, A.	2081-2093A	Oh, Y.-J.	1565-1569A		1860-1862A
Lynch, D.C.	142-146B	Mohamed, F.A.	261-278A	Oh-Ishi, K.	2173-2184A	Qiao, Y.	145-157A
				Oishi, K.	2327-2335A		159-164A

- Quintard, M. 365-376B  
 Raban, R. 3127-3136A  
 Rack, H.J. 2155-2162A  
 Radjai, A. 3025-3030A  
 Radmilovic, V. 2413-2423A  
 Raj, B. 1617-1626A  
 Raj, S.V. 597-612A  
 1385-1397A  
 Rajan, T.P.D. 2755-2761A  
 Ramakrishnan, S.S. 1475-1485A  
 Raman, R.K.S. 3296-3297A  
 Ramesh, A. 1137-1144A  
 Ramesh, K.T. 927-935A  
 Ramsoskar, K. 613-623B  
 Randle, V. 1853-1857A  
 Ranganath, V.R. 3731-3740A  
 Rangaswamy, P. 757-763A  
 Rao, K.B.S. 1617-1626A  
 Rao, P.S.P. 345-354B  
 Rapp, R.A. 315-319B  
 Rappaz, M. 2095-2106A  
 2685-2694A  
 2695-2701A  
 Ratchev, I.P. 651-660B  
 Rau, C. 613-623B  
 Ravi, M. 391-400A  
 Ray, K.K. 3731-3740A  
 Ray, R.K. 3605-3618A  
 Ray, S. 3479-3488A  
 Recarte, V. 2581-2591A  
 Recina, V. 2869-2881A  
 Reddy, R.G. 543-550B  
 Reddy, S.N.S. 2899-2906A  
 Reed, R.C. 2921-2931A  
 Rekveldt, M.Th. 1883-1891A  
 Ren, Y.Y. 3065-3066A  
 Reuter, M.A. 595-603B  
 Reynolds, W.T., Jr. 2391-2411A  
 Rhaipu, S. 83-32A  
 93-100A  
 Rhee, C.-H. 930-932B  
 Richards, N.L. 2005-2017A  
 Ricker, R.E. 2883-2889A  
 Ringer, S.P. 1649-1658A  
 Ritchie, R.O. 899-918A  
 Rivera-Díaz-del-Castillo, P.E.J. 1075-1081A  
 Ro, Y. 1281-1283A  
 Roberts, S.M. 2921-2931A  
 Robertson, D.P. 1541-1547A  
 Rodriguez Torres, C.E. 25-31A  
 Rodriguez, A.S. 2229-2235A  
 Rodriguez, H.H. 187-199B  
 Rodriguez, R. 125-134A  
 Rodriguez-Ibabe, J.M. 3089-3098A  
 Rogge, R.B. 757-763A  
 Roghani, G. 827-838B  
 839-849B  
 Rohatgi, P.K. 1541-1547A  
 Rollet, A.D. 3709-3718A  
 Rosén, E. 385-392B  
 Rosen, R.S. 337-343A  
 Roviglione, A.N. 235-241B  
 Roy, A. 669-676B  
 677-683B  
 Ruano, O.A. 219-229A  
 Rubal, M.P. 581-589A  
 Ryoo, H.S. 973-980A  
 Ryu, H.-B. 2811-2816A  
 Sabau, A.S. 243-255B  
 Sage, D. 859-865A  
 Saha, R. 3861-3869A  
 Sahai, Y. 315-319B  
 Sakai, Y. 3241-3248A  
 Salama, I. 2775-2779A  
 Salem, J.A. 597-612A  
 1385-1397A  
 Samarasekera, I.V. 5-29B  
 413-423B  
 425-436B  
 437-449B  
 Sánchez, F.H. 25-31A  
 Sankarasubramanian, R. 1083-1090A  
 Sato, H. 875-882A  
 Sato, Y.S. 625-635A  
 Saunders, N. 3367-3373A  
 Savage, M.F. 891-898A  
 Savray, R.A. 1659-1667A  
 Sawla, S. 3031-3044A  
 Saxena, A. 1939-1947A  
 Schaffer, G.B. 3279-3284A  
 Schlaefer, C. 2185-2194A  
 Schoenfeld, S.E. 937-947A  
 Schuh, C. 1669-1680A  
 Schuster, J.C. 3311-3319A  
 Schweitzer, G.K. 146-147B  
 355-364B  
 929-930B  
 Schwerdtfeger, K. 1151-1166A  
 Scully, J.R. 1167-1181A  
 1297A  
 1991-2004A  
 319-327A  
 1287-1292A  
 201-207B  
 499-501B  
 589-594B  
 Seetharaman, V. 3817-3830A  
 Sehitoglu, H. 3661-3672A  
 Seidman, D.N. 2317-2326A  
 Seifert, H.J. 2775-2779A  
 Semiatin, S.L. 2719-2727A  
 3527-3534A  
 3817-3830A  
 2685-2694A  
 Sémoroz, A. 2695-2701A  
 2237-2240A  
 665-673A  
 Serra, A. 809-812A  
 Sha, W. 1027-1040A  
 Shah, S. 1245-1254A  
 Shakeri, H.R. 1699-1713A  
 Shankar, P. 1475-1485A  
 Shankar, S. 465-476B  
 Shen, G. 2719-2727A  
 Shen, H.F. 69-78B  
 Shengjie, Y. 477-488B  
 Sherby, O.D. 219-229A  
 Shi, Y.W. 1275-1280A  
 2240-2244A  
 Shi, Z. 1003-1007A  
 2569-2572A  
 Shibata, K. 1292-1295A  
 Shiflet, G.J. 2495-2505A  
 2507-2518A  
 3619-3633A  
 Shimono, M. 511-519A  
 Shin, D.H. 705-707A  
 2859-2867A  
 1755-1763A  
 Shin, K. 506-509B  
 Shinozaki, N. 2973-2983A  
 Shipway, P.H. 1765-1773A  
 Shiue, R.K. 3565-3568A  
 Shui, J.P. 1659-1667A  
 Shveykin, V.P. 1949-1962A  
 Shyam, A. 201-207B  
 589-594B  
 Sietsma, J. 1589-1603A  
 1883-1891A  
 Silva, E.M. 3569-3573A  
 Simao, R.A. 3569-3573A  
 Simard, D. 403-411B  
 Sinclair, I. 1125-1136A  
 Singh, K.K. 891-896B  
 Singh, P. 137-140B  
 Singh, S.N. 345-354B  
 Siqueira, C.A. 2107-2118A  
 Sivaprasad, S. 3731-3740A  
 Sklenicka, V. 883-889A  
 Skrotzki, B. 489-498B  
 Smith, B.J. 1862-1865A  
 Smith, P.M. 146-147B  
 613-623B  
 Snigirev, A. 1413-1427A  
 Soboyejo, W.O. 2413-2423A  
 Soffa, W.A. 711-716B  
 Sohn, H.Y. 717-721B  
 3375-3392A  
 173-185B  
 Solheid, H. 1041-1050A  
 Sommer, F. 703-709B  
 Song, B. 723-729B  
 Song, H.S. 1263-1273A  
 Song, J.M. 2623-2634A  
 1963-1969A  
 155-162B  
 Song, S.G. 487-493A  
 Sowayama, N. 2811-2816A  
 Speer, J.G. 3099-3110A  
 373-381A  
 Spigarelli, S. 625-632B  
 Sridhar, S. 605-612B  
 Srinivasan, K. 1125-1136A  
 Starink, M.J. 937-947A  
 581-589A  
 140-142B  
 1939-1947A  
 2883-2889A  
 757-763A  
 613-624A  
 2685-2694A  
 2695-2701A  
 2433-2443A  
 1461-1473A  
 1559-1560A  
 3249-3253A  
 2607-2613A  
 665-673A  
 1963-1969A  
 1117-1124A  
 3285-3292A  
 3321-3328A  
 687-691A  
 3874-3876A  
 2817-2824A  
 503-510A  
 3137-3144A  
 875-882A  
 3235-3240A  
 883-889A  
 3839-3845A  
 279-290A  
 2173-2184A  
 3521-3526A  
 2073-2080A  
 Takai, K. 2659-2665A  
 477-488B  
 681-685A  
 Tan, W. 2667-2676A  
 1183-1188A  
 Tanaka, M. 2043-2052A  
 417-426A  
 1559-1560A  
 502-506B  
 3731-3740A  
 1183-1188A  
 2043-2052A  
 2173-2184A  
 1919-1929A  
 1229-1243A  
 3499-3510A  
 3763-3775A  
 1737-1742A  
 425-436B  
 437-449B  
 795-812B  
 1991-2004A  
 1351-1362A  
 901-908B  
 909-913B  
 41-46B  
 3499-3510A  
 529-537A  
 521-528A  
 695-702B  
 757-763A  
 859-865A  
 1103-1115A  
 2635-2648A  
 3235-3240A  
 823-829A  
 831-836A  
 3111-3115A  
 1843-1851A  
 3541-3553A  
 613-624A  
 61-67B  
 2729-2736A  
 1229-1243A  
 3499-3510A  
 3763-3775A  
 2195-2203A  
 3241-3248A  
 1103-1115A  
 577-587B  
 3479-3488A  
 707-711A  
 521-528A  
 Uememoto, M. 2195-2203A  
 591-596A  
 625-635A  
 1183-1188A  
 2043-2052A  
 3839-3845A  
 393-401B  
 Stefansson, N. 3527-3534A  
 Steif, R. 581-589A  
 Sterten, A. 140-142B  
 Steward, R. 1939-1947A  
 Stoudt, M.R. 2883-2889A  
 Stout, M.G. 757-763A  
 Straffellini, G. 613-624A  
 Strezov, L. 2685-2694A  
 2695-2701A  
 2433-2443A  
 Su, P. 1461-1473A  
 Su, X. 1559-1560A  
 Su, Y. 3249-3253A  
 Suga, Y. 2607-2613A  
 Suh, J.-Y. 665-673A  
 Sun, E.Y. 1963-1969A  
 Sun, J. 1117-1124A  
 Sun, Y.Q. 3285-3292A  
 Sun, Z.M. 3321-3328A  
 Sundin, S. 687-691A  
 Sung, P.K. 3874-3876A  
 Sutou, Y. 2817-2824A  
 Suzuki, A. 503-510A  
 3137-3144A  
 875-882A  
 Suzuki, M. 3235-3240A  
 Svoboda, M. 883-889A  
 Swift, G.A. 3839-3845A  
 Swisher, D.L. 279-290A  
 2173-2184A  
 3521-3526A  
 2073-2080A  
 Takai, K. 2659-2665A  
 477-488B  
 681-685A  
 Tan, W. 2667-2676A  
 1183-1188A  
 Tanaka, M. 2043-2052A  
 417-426A  
 1559-1560A  
 502-506B  
 3731-3740A  
 1183-1188A  
 2043-2052A  
 2173-2184A  
 1919-1929A  
 1229-1243A  
 3499-3510A  
 3763-3775A  
 1737-1742A  
 425-436B  
 437-449B  
 795-812B  
 1991-2004A  
 1351-1362A  
 901-908B  
 909-913B  
 41-46B  
 3499-3510A  
 529-537A  
 521-528A  
 695-702B  
 757-763A  
 859-865A  
 1103-1115A  
 2635-2648A  
 3235-3240A  
 823-829A  
 831-836A  
 3111-3115A  
 1843-1851A  
 3541-3553A  
 613-624A  
 61-67B  
 2729-2736A  
 1229-1243A  
 3499-3510A  
 3763-3775A  
 2195-2203A  
 3241-3248A  
 1103-1115A  
 577-587B  
 3479-3488A  
 707-711A  
 521-528A  
 Uememoto, M. 2195-2203A  
 591-596A  
 625-635A  
 1183-1188A  
 2043-2052A  
 3839-3845A  
 393-401B  
 Ustundag, E. 937-947A  
 Usui, T. 581-589A  
 140-142B  
 1939-1947A  
 2883-2889A  
 757-763A  
 613-624A  
 2685-2694A  
 2695-2701A  
 2433-2443A  
 1461-1473A  
 1559-1560A  
 3249-3253A  
 2607-2613A  
 665-673A  
 1963-1969A  
 1117-1124A  
 3285-3292A  
 3321-3328A  
 687-691A  
 3874-3876A  
 2817-2824A  
 503-510A  
 3137-3144A  
 875-882A  
 3235-3240A  
 883-889A  
 3839-3845A  
 279-290A  
 2173-2184A  
 3521-3526A  
 2073-2080A  
 Takai, K. 2659-2665A  
 477-488B  
 681-685A  
 Tan, W. 2667-2676A  
 1183-1188A  
 Tanaka, M. 2043-2052A  
 417-426A  
 1559-1560A  
 502-506B  
 3731-3740A  
 1183-1188A  
 2043-2052A  
 2173-2184A  
 1919-1929A  
 1229-1243A  
 3499-3510A  
 3763-3775A  
 1737-1742A  
 425-436B  
 437-449B  
 795-812B  
 1991-2004A  
 1351-1362A  
 901-908B  
 909-913B  
 41-46B  
 3499-3510A  
 529-537A  
 521-528A  
 695-702B  
 757-763A  
 859-865A  
 1103-1115A  
 2635-2648A  
 3235-3240A  
 823-829A  
 831-836A  
 3111-3115A  
 1843-1851A  
 3541-3553A  
 613-624A  
 61-67B  
 2729-2736A  
 1229-1243A  
 3499-3510A  
 3763-3775A  
 2195-2203A  
 3241-3248A  
 1103-1115A  
 577-587B  
 3479-3488A  
 707-711A  
 521-528A  
 Uememoto, M. 2195-2203A  
 591-596A  
 625-635A  
 1183-1188A  
 2043-2052A  
 3839-3845A  
 393-401B  
 Vaisburd, S. 551-559B  
 561-564B  
 2139-2144A  
 625-632B  
 1865-1868A  
 735-741A  
 3847-3859A  
 2475-2483A  
 2485-2494A  
 529-537A  
 1589-1603A  
 1883-1891A  
 1883-1891A  
 693-713A  
 1971-1980A  
 2593-2598A  
 1843-1851A  
 193-201A  
 2763-2766A  
 2353-2371A  
 2391-2411A  
 2445-2470A  
 2139-2144A  
 1561-1565A  
 311-317A  
 2353-2371A  
 3121-3126A  
 3541-3553A  
 1351-1362A  
 1659-1667A  
 285-296B  
 2433-2443A  
 329-336B  
 243-255B  
 2067-2072A  
 3847-3859A  
 721-733A  
 3847-3859A  
 17-23A  
 219-229A  
 183-191A  
 2649-2658A  
 3578-3582A  
 995-1002A  
 3393-3402A  
 1287-1292A  
 2775-2779A  
 467A  
 171-181A  
 3145-3153A  
 2353-2371A  
 3393-3402A  
 707-711A  
 201-207B  
 3201-3204A  
 625-632B  
 1699-1713A  
 661-668B  
 1549-1557A  
 1795-1804A  
 1057-1067A  
 1091-1102A  
 1145-1150A  
 2019-2030A  
 1221-1228A  
 111-119B  
 121-127B  
 3565-3568A  
 91-100B  
 765-773B  
 1681-1687A  
 613-623B  
 3311-3319A  
 765-773B  
 171-181A  
 1229-1243A  
 1385-1397A  
 3831-3838A  
 2413-2423A  
 2899-2906A  
 385-392B  
 1057-1067A  
 837-850A  
 73-81A  
 3861-3869A  
 1429-1436A  
 241-248A  
 265-284B  
 2425-2431A  
 2811-2816A  
 93-100A



Withers, P.J.	3215-3225A	Xu, S.	41-46B	Yoon, D.Y.	713A	Zhang, W.F.	3117-3120A
Wittig, J.E.	3227-3234A	Xu, X.	1795-1804A		3803-3815A	Zhang, X.Y.	3661-3672A
Woo, D.-H.	2373-2379A		1805-1815A	Yoon, U.S.	425-436B	Zhang, Y.	315-319B
Wright, S.I.	915-920B	Xu, Y.	2195-2203A		437-449B	Zhang, Z.F.	3321-3328A
Wroblewski, T.	949-954A	Xu, Z.	41-46B	Yoshida, H.	2891-2898A	Zhao, B.	865-876B
Wu, B.	2825-2833A	Yamabe-Mitarai, Y.	1281-1283A	Yoshinari, M.	511-519A		877-890B
Wu, J.-H.	543-550B	Yamauchi, K.	1743-1754A	Young, C.J.	3293-3295A	Zhilyaev, A.P.	1865-1868A
Wu, M.	1715-1724A		2907-2919A	Young, G.A., Jr.	1167-1181A	Zhou, J.	1413-1427A
Wu, N.-C.	3673-3683A	Yan, X.Y.	685-693B		1297A	Zhou, S.H.	2781-2787A
Wu, R.J.	171-181A	Yanar, C.	2413-2423A	Yu, S.C.M.	477-488B	Zhou, T.	3205-3214A
Wu, S.K.	3055-3063A	Yang, H.T.Y.	1245-1254A	Yu, Y.	1399-1412A	Zhou, Y.	1275-1280A
Wu, X.	1765-1773A	Yang, R.	3137-3144A	Yurko, J.A.	2737-2746A		2019-2030A
Wu, Y.	3499-3510A	Yang, S.	171-181A	Zabinski, J.	675-679A		2240-2244A
Wynblatt, P.	2185-2194A	Yang, Y.	813-816B	Zbib, H.M.	285-296B		2667-2676A
	1003-1007A	Yang, Y.W.	3011-3017A	Zhalelev, R.	551-559B	Zhou, Y.L.	3137-3144A
	2569-2572A	Yao, M.	1775-1778A	Zhang, B.	813-816B	Zhu, D.-P.	111-119B
Wynne, B.P.	1331-1349A	Ye, L.	897-900B	Zhang, D.	3055-3063A		121-127B
Xia, K.	467A	Yin, Z.	897-900B	Zhang, J.X.	3741-3746A	Zhu, G.	41-46B
Xiao, Y.	595-603B	Yip, T.-H.	3433-3442A	Zhang, L.-Q.	661-668B	Zhu, J.H.	3117-3120A
Xin, X.J.	2649-2658A	Yokoyama, K.	495-501A	Zhang, P.	897-900B	Zhu, S.M.	1292-1295A
Xing, Z.P.	1521-1530A	Yoo, M.H.	813-822A	Zhang, T.	1981-1989A	Zhuang, L.	3121-3126A
Xu, D.	321-324B		851-858A	Zhang, W.	443-454A	Zurek, A.K.	1509-1520A
	451-463B	Yoo, O.	1565-1569A		1805-1815A	Zwerschke, S.P.	1549-1557A



## Combined Subject Index

- Abrasive wear**  
Near-nanostructured WC-18 pct co coatings with low amounts of non-WC carbide phase: Part II. Hardness and resistance to sliding and abrasive wear. 159-164A  
Sliding wear of austenitic and austenitic-ferritic stainless steels. High stress abrasive wear mechanism of LM13-SiC composite under varying experimental conditions. 613-624A  
3031-3044A
- Absorption (material)**  
Trap-Governed Hydrogen Diffusivity and Uptake Capacity in Ultrahigh-Strength AERMET 100 Steel. 1991-2004A
- Accuracy**  
On differential thermal analyzer curves for the melting and freezing of alloys. 1779-1794A
- Acid leaching**  
Kinetics of manganese reduction leaching from weathered rare-earth mud with sodium sulfite. 41-46B
- Acoustic emission testing**  
Evolution of fiber fragmentation in a short-fiber-reinforced metal-matrix model composite during tensile creep deformation—an acoustic emission study. 1549-1557A
- Activation energy**  
Steady-state creep of  $\alpha$ -zirconium at temperatures up to 850°C. A framework for modeling creep in pure metals. 337-343A  
Rate of Interfacial Reaction between Molten  $\text{CaO-SiO}_2\text{-Al}_2\text{O}_3\text{-Fe}_2\text{O}_3$  and  $\text{CO-CO}_2$ . 363-371A  
Anisotropy of point defect diffusion in alpha-zirconium. 651-660B  
Mobility of interstitial clusters in alpha-zirconium. 777-782A  
Kinetics of Silver Leaching from Manganese-Silver Associated Ores in Sulfuric Acid Solution in the Presence of Hydrogen Peroxide. 783-789A  
The effects of test temperature, temper, and alloyed copper on the hydrogen-controlled crack growth rate of an Al-Zn-Mg-(Cu) alloy. 813-816B  
Erratum: The effects of test temperature, temper, and alloyed copper on the hydrogen-controlled crack growth rate of an Al-Zn-Mg-(Cu) alloy. 1167-1181A  
Massive transformation and the formation of the ferromagnetic  $\text{L}_{10}$  phase in manganese-aluminum-based alloys. 1297A  
2413-2423A
- Activity (chemical)**  
Oxidation state and activities of chromium oxides in  $\text{CaO-SiO}_2\text{-Cr}_2\text{O}_3$  slag system. 595-603B
- Adsorption**  
Misfit dislocations in epitaxy. 2475-2483A
- Aerospace**  
Pressure Effects on Flow and Fracture of Be-Al Alloys. 3555-3564A
- Aerospace engines, Mechanical properties**  
Effect of Prolonged Isothermal Exposure on Elevated-Temperature, Time-Dependent Fatigue-Crack Propagation in INCONEL Alloy 783. 3465-3478A
- Aging**  
Enhancement of Strength and Superplasticity in a 6061 Al Alloy Processed by Equal-Channel-Angular-Pressing. 3155-3164A
- Aging (artificial)**  
Strength of Al-Zn-Mg-Cu matrix composite reinforced with SiC particles. 455-465A  
Aging behavior of the Ti-29Nb-13Ta-4.6Zr new beta alloy for medical implants. 487-493A  
Communication: Examination of the aging and tensile properties of Al-Zn-Mg/Al<sub>3</sub>Ni eutectic composite. 707-711A  
Precipitation of austenite particles at grain boundaries during aging of Fe-Mn-Ni steel. 1057-1067A  
The effects of test temperature, temper, and alloyed copper on the hydrogen-controlled crack growth rate of an Al-Zn-Mg-(Cu) alloy. 1167-1181A  
Erratum: The effects of test temperature, temper, and alloyed copper on the hydrogen-controlled crack growth rate of an Al-Zn-Mg-(Cu) alloy. 1297A  
Age-hardening characteristics of aluminum alloy-hollow fly ash composites. 1541-1547A  
Effect of alternative aging process on the fracture and interfacial properties of particulate  $\text{Al}_2\text{O}_3$ -reinforced Al (6061) metal matrix composite. 1699-1713A  
Tensile and fatigue properties of 17-4 PH stainless steel at high temperatures. 1715-1724A  
Hydrogen-assisted deformation and fracture behaviors of Al 8090. 1755-1763A  
Effect of Fcc-Hcp Phase Transformation Produced by Isothermal Aging on the Corrosion Resistance of a Co-27Cr-5Mo-0.05C Alloy. 2229-2235A  
Fast Aging Kinetics of the AA6016 Al-Mg-Si Alloy and the Application in Forming Process. 3121-3126A
- Air cooling**  
The effect of rapid heat treatment on the high-temperature tensile behavior of superplastic Ti-6Al-4V. 83-92A
- Air pollution**  
Kinetics of formation and dissociation of  $\text{Na}_2\text{SiF}_6$ . 129-136B  
A Novel Cyclic Process using  $\text{CaSO}_4/\text{CaS}$  Pellets for Converting Sulfur Dioxide to Elemental Sulfur without Generating Secondary Pollutants: Part I. Feasibility and Kinetics of the Reduction of Sulfur Dioxide with Calcium Sulfide Pellets. 711-716B  
A Novel Cyclic Process using  $\text{CaSO}_4/\text{CaS}$  Pellets for Converting Sulfur Dioxide to Elemental Sulfur without Generating Secondary Pollutants: Part II. Hydrogen Reduction of Calcium-Sulfate Pellets to Calcium Sulfide. 717-721B
- Allotropic transformation**  
Communications: On substitutional element partitioning coefficients of two-phase alloys. 3065-3066A  
Communication: Phase Transformations in FeMnAlC Austenitic Steels with Si Addition. 3569-3573A
- Alloy development**  
Communication: Microstructures and mechanical properties of (Ir,Rh)<sub>75</sub>Nb<sub>15</sub>Ni<sub>10</sub> alloys. 1281-1283A
- Alloy steels, Phase transformations**  
Origins of internal structure in massive transformation products. 2347-2351A
- Aluminides, Bonding**  
Microstructure and Mechanical Properties of Titanium Aluminide Wide-Gap, Transient Liquid-Phase Bonds Prepared using a Slurry-Deposited Composite Interlayer. 3205-3214A
- Aluminides, Casting**  
Joining of NiAl to Iron-Based Alloys by Reactive Casting. 2073-2080A
- Aluminides, Coatings**  
Communication: Depth Profiling of Hf-Doped Aluminide Coating by Glow-Discharge Mass Spectrometry. 3578-3582A
- Aluminides, Composite materials**  
Effect of heat treatments on in-situ  $\text{Al}_2\text{O}_3/\text{TiAl}_3$  composites produced from squeeze casting of  $\text{TiO}_2/\text{A356}$  composites. 31-40B  
Intermetallic-reinforced light-metal matrix in-situ composites. 193-201A  
Reactive Infiltration of 25 Vol Pct  $\text{TiO}_2/\text{Al}$  Composites. 2155-2162A  
Microstructure/processing relationships in reaction-synthesized titanium aluminide intermetallic matrix composites. 2747-2753A  
Mechanical, Intergranular Corrosion, and Wear Behavior of Aluminum-Matrix Composite Materials Reinforced with Nickel Aluminides. 3541-3553A
- Aluminides, Mechanical properties**  
Application of a modified jogged-screw model for creep of TiAl and  $\alpha$ -Ti alloys. 329-336A  
Cracking in  $\gamma$ -TiAl due to high speed particle impact. 581-589A  
Effect of directionally solidified microstructures on the room-temperature fracture-toughness properties of Ni-33(at. pct)Al-33Cr-1 Mo and Ni-33(at. pct)Al-31 Cr-3Mo eutectic alloys grown at different solidification rates. 597-612A  
Room-temperature mechanical properties of cold-rolled thin foils of binary, stoichiometric  $\text{Ni}_3\text{Al}$ . 2607-2613A  
Crack growth in a nearly fully-lamellar gamma TiAl alloy at 650°C and 800°C under constant load conditions. 2847-2857A  
Tensile, creep, and low-cycle fatigue behavior of a cast  $\gamma$ -TiAl-based alloy for gas turbine applications. 2869-2881A  
Communication: Conducting High-Cycle Fatigue Strength Step Tests on Gamma TiAl. 3871-3874A
- Aluminides, Microstructure**  
Atomistic modeling of quaternary alloys: Ti and Cu in NiAl. 265-284B  
First-principles investigation of perfect and diffuse antiphase boundaries in hcp-based Ti-Al alloys. 735-741A  
Nonbasal deformation modes of Hcp metals and alloys: role of dislocation source and mobility. 813-822A  
Phase Separation Tendency in the As-Solidified Zr3Al-Nb Alloys Studied by Microstructural Observations and Thermodynamic Analysis. 1919-1929A  
Microstructural Analysis of Multilayered Titanium Aluminide Sheets Fabricated by Hot Rolling and Heat Treatment. 3649-3659A
- Aluminides, Phase transformations**  
Mechanisms of the massive transformation. 2285-2297A  
Origins of internal structure in massive transformation products. 2347-2351A  
Massive-parent interphase boundaries and their implications on the mechanisms of the  $\alpha \rightarrow \gamma_{\text{M}}$  massive transformation in Ti-Al alloys. 2353-2371A  
The massive transformation in titanium aluminides: initial stages of nucleation and growth. 2373-2379A  
Orientation and structure of planar facets on the  $\gamma_{\text{M}}$  massive phase in a near-TiAl alloy. 2381-2389A  
Static and in-situ high-resolution transmission electron microscopy investigations of the atomic structure and dynamics of massive transformation interfaces in a Ti-Al alloy. 2391-2411A  
Massive transformation and the formation of the ferromagnetic  $\text{L}_{10}$  phase in manganese-aluminum-based alloys. 2413-2423A  
General discussion session of the symposium on "The mechanisms of the massive transformation". 2445-2470A
- Aluminides, Powder technology**  
Grain-size control in Ti-48Al-2Cr-2Nb with yttrium additions. 2729-2736A
- Aluminizing**  
Communication: Depth Profiling of Hf-Doped Aluminide Coating by Glow-Discharge Mass Spectrometry. 3578-3582A
- Aluminum, Alloying elements**  
Communication: Effect of carbon addition on tribological properties of Fe-Al alloys. 1292-1295A  
Communication: High-cycle fatigue of an investment cast, Be-Al metal matrix composite. 1862-1865A  
Communication: Microstructure and yield behavior of a high aluminum containing Ti-Al-Nb alloy. 2763-2766A
- Aluminum, Casting**  
Mathematical modeling and computer simulation of the rotating impeller particle flotation process: Part I. Fluid flow. 297-303B

- Mathematical modeling and computer simulation of the rotating impeller particle flotation process: Part II. Particle agglomeration and flotation. 305-314B
- Communication: Physical modeling of the effects of thermal buoyancy driven flows in aluminum casters. 321-324B
- Die soldering: mechanism of the interface reaction between molten aluminum alloy and tool steel. 465-476B
- Communication: Wettability of  $Al_2O_3$ -MgO substrates by molten aluminum. 506-509B
- Constitutive Behavior of As-Cast AM 050, AA3104, and AA5182. 1971-1980A
- Two-Phase Modeling Directed Toward Hot Tearing Formation in Aluminum Direct Chill Casting. 2081-2093A
- Computer simulation of solidification processes - the evolution of a technology. 2251-2273A
- Aluminum, Composite materials**
- Effect of cyclic pressure consolidation on the uniformity of metal matrix composites. 183-191A
- Normalized Diagrams for Micromechanical Estimates of the Elastic Response of Composite Materials. 3187-3199A
- Aluminum, Dopants**
- Dopant Particle Characterization and Bubble Evolution in Aluminum-Potassium-Silicon-Doped Molybdenum Wire. 3349-3356A
- Aluminum, Mechanical properties**
- Predictive capabilities of the dislocation-network theory of Harper-Dorn creep. 231-239A
- Observations, theories, and predictions of high-temperature creep behavior. 241-248A
- Harper-Dorn creep and specimen size. 305-310A
- Dislocation microstructure and internal-stress measurements by convergent-beam electron diffraction on creep-deformed Cu and Al. 311-317A
- A framework for modeling creep in pure metals. 363-371A
- Large-Strain Softening of Aluminum in Shear at Elevated Temperature. 3145-3153A
- Aluminum, Metal working**
- Structural evolution of a strip-cast Al alloy sheet processed by continuous equal-channel angular pressing. 665-673A
- An Investigation of Microstructure and Grain-Boundary Evolution during ECA Pressing of Pure Aluminum. 2173-2184A
- Aluminum, Microstructure**
- Modeling the kinetics of grain-boundary-nucleated recrystallization processes after cold deformation. 529-537A
- Aluminum, Physical properties**
- Energy of the Pb{111} | Al{111} interface. 1003-1007A
- Effects of Macroscopic Pores on the Damping Behavior of Foamed Commercially Pure Aluminum. 3565-3568A
- Aluminum, Powder technology**
- Explicit finite element method simulation of consolidation of monolithic and composite powders. 2649-2658A
- Aluminum, Refining**
- Communication: The solubility of  $Fe_2O_3$  in cryolite-alumina melts. 140-142B
- Modeling of the solubility of alumina in the NaF-AlF<sub>3</sub> system at 1300 K. 315-319B
- Thermodynamics of liquid Al-Na alloys determined by using  $CaF_2$  solid electrolyte. 577-587B
- Aluminum, Ternary systems**
- A 500°C isothermal section for the Al-Au-Cu system. 987-993A
- Communication: On the ternary phase in the zinc-rich corner of the Zn-Fe-Al system at temperatures below 450°C. 1559-1560A
- Thermodynamic description of the Cu-Al-Sn system in the copper-rich corner. 1639-1648A
- Thermal and electrical properties of  $Nb_2AlC$ ,  $(Ti,Nb)_2AlC$  and  $Ti_3AlC$ . 2775-2779A
- On the Constitution of the System Al-Mn-Si. 3311-3319A
- Diffusion Studies in the  $\beta$  ( $B_2$ ),  $\beta'$  (Bcc), and  $\gamma$  (Fcc) Fe-Ni-Al Alloys at 1000°C. 3375-3392A
- Aluminum base alloys, Atomic properties**
- On the Partial Atomic Volume of Aluminum in Solid Solutions Based on the 3d Transition Metals and Copper. 3591-3595A
- Aluminum base alloys, Casting**
- A three-phase model of hydrogen pore formation during the equiaxed dendritic solidification of aluminum-silicon alloys. 209-221B
- Microporosity prediction in aluminum alloy castings. 243-255B
- A unified microscale parameter approach to solidification-transport process-based macrosegregation modeling for dendritic solidification. II. Numerical example computations. 451-463B
- Computer simulation of solidification processes - the evolution of a technology. 519-541B
- Time-resolved X-ray imaging of aluminum alloy solidification processes. 613-623B
- Cellular array morphology during directional solidification. 1229-1243A
- Phenomenological observations on mechanical and corrosion properties of thixoformed 357 alloys: a comparison with permanent mold cast 357 alloys. 1399-1412A
- Constitutive Behavior of As-Cast AM 050, AA3104, and AA5182. 1971-1980A
- Hydrogen Evolution during Directional Solidification and Its Effect on Porosity Formation in Aluminum Alloys. 2067-2072A
- Modeling of Microporosity, Macroporosity, and Pipe-shrinkage Formation during the Solidification of Alloys Using a Mushy-Zone Refinement Method: Applications to Aluminum Alloys. 2095-2106A
- Solidification Thermal Parameters Affecting the Columnar-to-Equiaxed Transition. 2107-2118A
- Rheology and microstructure of semi-solid aluminum alloys compressed in the drop-forge viscometer. 2737-2746A
- Aluminum base alloys, Coatings**
- Powder Eutectic Coating With  $Al_3Ti$  For Steels. 3235-3240A
- Aluminum base alloys, Composite materials**
- Intermetallic-reinforced light-metal matrix in-situ composites. 193-201A
- Strength of Al-Zn-Mg-Cu matrix composite reinforced with SiC particles. 455-465A
- In-situ formation of SiC-reinforced Al-Si alloy composites using methane gas mixtures. 543-550B
- A novel technique for manufacturing metal-bonded Nd-Fe-B magnets by squeeze casting. 637-646A
- Communication: Examination on the aging and tensile properties of Al-Zn-Mg/Al<sub>3</sub>Ni eutectic composite. 707-711A
- Communication: Comparative Welding Study of Metal Matrix Composites with the MIG Welding Process, using Direct and Indirect Electric Arc. 932-937B
- Age-hardening characteristics of aluminum alloy-hollow fly ash composites. 1541-1547A
- Effect of alternative aging process on the fracture and interfacial properties of particulate  $Al_2O_3$ -reinforced Al (6061) metal matrix composite. 1699-1713A
- Interfacial reactions in aluminosilicate short fiber-reinforced aluminum matrix composites. 2755-2761A
- High stress abrasive wear mechanism of LM13-SiC composite under varying experimental conditions. 3031-3044A
- Large Self-Thermal-Plastic Deformation in a NiTi Shape-Memory Alloy Fiber-Actuated Aluminum Metal-Matrix Composite. 3535-3540A
- Mechanical, Intergranular Corrosion, and Wear Behavior of Aluminum-Matrix Composite Materials Reinforced with Nickel Aluminides. 3541-3553A
- Strength and Plastic Flow in "In Situ" TiC Reinforced Aluminum Composites. 3831-3838A
- Effect of Overaging and Particle Size on Tensile Deformation and Fracture of Particle-Reinforced Aluminum Matrix Composites. 3861-3869A
- Aluminum base alloys, Corrosion**
- Effect of grain boundary characteristics on intergranular corrosion resistance of 6061 aluminum alloy extrusion. 2891-2898A
- Aluminum base alloys, Crystal growth**
- Coprecipitation of  $\Omega$  and  $\sigma$  Phases in Al-Cu-Mg-Mn Alloys Containing Ag and Si. 3635-3648A
- Aluminum base alloys, Extrusion**
- Electron backscatter diffraction analysis of microstructural evolution in hot-deformed 6xxx series aluminum alloys. 693-713A
- Aluminum base alloys, Heat treatment**
- Fast Aging Kinetics of the AA6016 Al-Mg-Si Alloy and the Application in Forming Process. 3121-3126A
- Aluminum base alloys, Mechanical properties**
- Denuded zones, diffusional creep, and grain boundary sliding. 219-229A
- Predictive capabilities of the dislocation-network theory of Harper-Dorn creep. 231-239A
- Creep at low stresses: an evaluation of diffusion creep and Harper-Dorn creep as viable creep mechanisms. 249-259A
- Understanding creep - a review. 291-303A
- Constitutive equations for creep and plasticity of aluminum alloys produced by powder metallurgy and aluminum-based metal matrix composites. 373-381A
- The effect of mischmetal addition on the structure and mechanical properties of a cast Al-7Si-0.3Mg alloy containing excess iron (up to 0.6 pct). 391-400A
- Effect of loading condition and stress state on damage evolution of silicon particles in an Al-Si-Mg-base cast alloy. 555-565A
- Creep and microstructure of magnesium-aluminum-calcium based alloys. 567-574A
- Toughness-strength relations in the overaged 7449 Al-based alloy. 1125-1136A
- The effects of test temperature, temper, and alloyed copper on the hydrogen-controlled crack growth rate of an Al-Zn-Mg-(Cu) alloy. 1167-1181A
- Erratum: The effects of test temperature, temper, and alloyed copper on the hydrogen-controlled crack growth rate of an Al-Zn-Mg-(Cu) alloy. 1297A
- Deformation mechanisms during low- and high-temperature superplasticity in 5083 Al-Mg alloy. 1373-1384A
- An investigation of the microstructure and strength of open-cell 6101 aluminum foams. 1413-1427A
- Hydrogen-assisted deformation and fracture behaviors of Al 8090. 1755-1763A
- Quantitative characterization of three-dimensional damage evolution in a wrought Al-alloy under tension and compression. 2599-2606A
- Low-temperature superplastic behavior of a submicrometer-grained 5083 Al alloy fabricated by severe plastic deformation. 2859-2867A
- Enhancement of Strength and Superplasticity in a 6061 Al Alloy Processed by Equal-Channel-Angular-Pressing. 3155-3164A
- Anisotropy of Intermetallic Particle Cracking Damage Evolution in an Al-Mg-Si Base Wrought Aluminum Alloy under Uniaxial Compression. 3443-3448A
- Simulation of Cavitation Processes in Superplastic Deformation. 3449-3455A
- Aluminum base alloys, Metal working**
- Elevated-temperature deformation at forming rates of  $10^{-2}$  to  $10^2$  s<sup>-1</sup>. 345-362A
- Erratum: Shear principal, and equivalent strains in equal-channel angular deformation. 467A
- Role of yield criteria and hardening laws in the prediction of forming limit diagrams. 1363-1371A
- Microstructural evolution and mechanical properties of the AA8011 alloy during the accumulative roll-bonding process. 1521-1530A
- Mechanical anisotropy and grain interaction in recrystallized aluminum. 2635-2648A
- The relationship between grain size and the surface roughness.



- ing behavior of Al-Mg alloys. 2883-2889A
- Aluminum base alloys, Microstructure**  
Deformation bands and the formation of grain boundaries in a superplastic aluminum alloy. 279-290A  
Stable quasicrystalline phase in Al-Cu-Fe-Cr coating materials. 675-679A  
Communication: On the solute field and composition of  $\gamma$  plates in an Al-22 At. Pct Ag alloy. 1561-1565A  
On the roles of clusters during intragranular nucleation in the absence of static defects. 1649-1658A  
Texture Clustering and Long-Range Disorientation Representation Methods: Application to 6022 Aluminum Sheet. 3709-3718A  
The Effect of Convection on Disorder in Primary Cellular and Dendritic Arrays. 3763-3775A
- Aluminum base alloys, Phases (state of matter)**  
Modeling of Globular Equiaxed Solidification with a Two-Phase Approach. 3673-3683A
- Aluminum base alloys, Physical properties**  
On differential thermal analyzer curves for the melting and freezing of alloys. 1779-1794A  
Communication: Thermodynamics of Hydrogen in Al-Si Alloys. 3874-3876A
- Aluminum base alloys, Powder technology**  
The Influence of the Atmosphere on the Sintering of Aluminum. Self-Propagating Reaction Induced by Ball Milling in a Mixture of  $\text{Cu}_2\text{O}$  and Al Powders. 3279-3284A  
3521-3526A
- Aluminum base alloys, Welding**  
Digital simulations of a stationary and a linear weld. 101-110B  
Characterization of a friction-stir-welded aluminum alloy 6013. Parameters controlling microstructure and hardness during friction-stir welding of precipitation-hardenable aluminum alloy 6063. 489-498B  
Investigation on the effect of laser pulse shape during Nd:YAG laser microwelding of thin Al sheet by numerical simulation. 625-635A  
1449-1459A
- Aluminum compounds, Coatings**  
Powder Eutectic Coating With  $\text{Al}_3\text{Ti}$  For Steels. 3235-3240A
- Aluminum compounds, Composite materials**  
Communication: Examination on the aging and tensile properties of Al-Zn-Mg/ $\text{Al}_3\text{Ni}$  eutectic composite. 707-711A
- Aluminum compounds, Mechanical properties**  
Use of Weibull Statistics to Quantify Property Variability in TiAl Alloys. 3127-3136A
- Aluminum compounds, Melting**  
The Critical Pressure and Impeding Pressure of Al Evaporation during Induction Skull Melting Processing of TiAl. 3249-3253A
- Aluminum killed steels, Casting**  
Formation of CaS on  $\text{Al}_2\text{O}_3$ -CaO inclusions during solidification of steels. 625-632B
- Aluminum killed steels, Microstructure**  
Study of the kinetics of the recrystallization of cold-rolled low-carbon steel. 25-31A
- Aluminum oxide, Composite materials**  
Effect of heat treatments on in-situ  $\text{Al}_2\text{O}_3/\text{TiAl}_3$  composites produced from squeeze casting of  $\text{TiO}_2/\text{A356}$  composites. 31-40B  
Effect of cyclic pressure consolidation on the uniformity of metal matrix composites. 183-191A  
Constitutive equations for creep and plasticity of aluminum alloys produced by powder metallurgy and aluminum-based metal matrix composites. 373-381A  
Creep processes in magnesium alloys and their composites. 883-889A  
Communication: Comparative Welding Study of Metal Matrix Composites with the MIG Welding Process, using Direct and Indirect Electric Arc. 932-937B  
Evolution of fiber fragmentation in a short-fiber-reinforced metal-matrix model composite during tensile creep deformation-an acoustic emission study. 1549-1557A  
Effect of alternative aging process on the fracture and interfacial properties of particulate  $\text{Al}_2\text{O}_3$ -reinforced Al (6061) metal matrix composite. 1699-1713A  
Communication: Reduced critical solidification front velocity of particle engulfment due to an interface active solute in the liquid metal. 1869-1873A  
Reactive Infiltration of 25 Vol Pct  $\text{TiO}_2/\text{Al}$  Composites. 2155-2162A
- Aluminum oxide, Solubility**  
Modeling of the solubility of alumina in the NaF- $\text{AlF}_3$  system at 1300 K. 315-319B
- Amorphous structure**  
Solid-state crystalline-glassy cyclic phase transformations of mechanically alloyed  $\text{Cu}_{33}\text{Zr}_{67}$  powders. 135-143A  
Crystallization kinetics of amorphous magnesium-rich magnesium-copper and magnesium-nickel alloys. 1041-1050A  
Thermally Enhanced and Mechanically Driven Glass Formation Reactions of Multilayered  $\text{Cu}_{33}\text{Zr}_{67}$  Powders. 2145-2153A
- Analyzing**  
Deformation twinning in polycrystalline Zr: insights from electron backscattered diffraction characterization. 955-963A
- Annealing**  
Effect of heat treatments on in-situ  $\text{Al}_2\text{O}_3/\text{TiAl}_3$  composites produced from squeeze casting of  $\text{TiO}_2/\text{A356}$  composites. 31-40B  
Deformation bands and the formation of grain boundaries in a superplastic aluminum alloy. 279-290A  
Microstructure evolution in Zr under equal channel angular pressing. 973-980A  
Evolution of microstructure and properties in alpha-brass after iterative processing. 1853-1857A  
Thermally Enhanced and Mechanically Driven Glass Formation Reactions of Multilayered  $\text{Cu}_{33}\text{Zr}_{67}$  Powders. 2145-2153A  
Formation and Annealing Behavior of Nanocrystalline Ferrite in Fe-0.89C Spheroidite Steel Produced by Ball Milling. 2195-2203A
- Structure of a Fe-Cr-Mn-Mo-N Alloy Processed by Mechanical Alloying. 3273-3278A  
Changes in Order and Texture during Annealing of Heavily Cold-Rolled  $\text{Ni}_3\text{Al}$  (B,Zr) Alloy. 3605-3618A
- Anodizing**  
Copper Electrowinning using Spouted-Bed Electrodes: Part I. Experiments with Oxygen Evolution or Matte Oxidation at the Anode. 669-676B  
Copper Electrowinning using Spouted-Bed Electrodes: Part II. Copper Electrowinning with Ferrous Ion oxidation as the Anodic Reaction. 677-683B
- Antimony, Alloying elements**  
Microstructural characteristics of Ni-Sb eutectic alloys under substantial undercooling and containerless solidification conditions. 1221-1228A  
Creep of Tin, Sb-solution-strengthened Tin, and SbSn-precipitate-strengthened tin. 1531-1539A
- AOD vessels**  
Mathematical modeling of the argon-oxygen decarburization refining process of stainless steel: Part I. Mathematical model of the process. 111-119B  
Mathematical modeling of the argon-oxygen decarburization refining process of stainless steel: Part II. Application of the model to industrial practice. 121-127B
- Arc welding**  
Communication: Comparative Welding Study of Metal Matrix Composites with the MIG Welding Process, using Direct and Indirect Electric Arc. 932-937B
- Argon oxygen decarburizing**  
Mathematical modeling of the argon-oxygen decarburization refining process of stainless steel: Part I. Mathematical model of the process. 111-119B  
Mathematical modeling of the argon-oxygen decarburization refining process of stainless steel: Part II. Application of the model to industrial practice. 121-127B
- Atomizing**  
The Influence of the Atmosphere on the Sintering of Aluminum. 3279-3284A
- Aufforming**  
Improvement of Gigacycle Fatigue Properties by Modified Ausforming in 1600 and 2000 MPA-Class Low-Alloy Steels. 3421-3431A
- Austenite**  
Comprehensive microstructural characterization in modified 9Cr-1Mo ferritic steel by ultrasonic measurements. 1617-1626A  
Austenite Decomposition to Carbide-Rich Products in Fe-030C-6.3W. 3619-3633A
- Austenite, Crystal growth**  
Static Recrystallization Mechanisms in a Coarse-Grained Nb-Microalloyed Austenite. 3089-3098A
- Austenitic stainless steels, Casting**  
Analysis and prevention of microcracking phenomenon occurring during strip casting of an AISI 304 stainless steel. 1487-1497A
- Austenitic stainless steels, Claddings**  
Sensitization behavior of type 308 stainless steel weld metals after postweld heat treatment and low-temperature aging and its relation to microstructure. 1743-1754A
- Austenitic stainless steels, Corrosion**  
Intergranular stress corrosion cracking behavior of types 308 and 316 stainless steel weld metals in a simulated boiling water reactor environment. 2907-2919A
- Austenitic stainless steels, Crystal growth**  
Evolution of Microstructure and Texture during Casting of AISI 304 Stainless Steel Strip. 3747-3754A
- Austenitic stainless steels, Joining**  
Interface nanochemistry effects on stainless steel diffusion bonding. 437-442A
- Austenitic stainless steels, Mechanical properties**  
Sliding wear of austenitic and austenitic-ferritic stainless steels. Tensile and fatigue properties of 17-4 PH stainless steel at high temperatures. 613-624A  
Comparative study of the impact response and microstructure of 304L stainless steel with and without prestrain. 1715-1724A  
Some Observations of the Influence of  $\delta$ -Ferrite Content on the Hardness, Galling Resistance, and Fracture Toughness of Selected Commercially Available Iron-Based Hardfacing Alloys. 2801-2810A  
3403-3419A
- Austenitic stainless steels, Microstructure**  
A new bcc-fcc orientation relationship observed between ferrite and austenite in solidification structures of steels. 5-15A  
Communication: Precipitation behavior of carbonitrides in type 347 stainless steels with Various C and N contents. 1565-1569A  
Why do dislocations assemble into interfaces in epitaxy as well as in crystal plasticity? To minimize free energy. 2519-2539A
- Austenitic stainless steels, Phase transformations**  
Method for Measuring Transformation Energy and Quantitative Characterization of Transformation-Induced Plasticity. 3117-3120A  
Communication: Phase Transformations in FeMnAlC Austenitic Steels with Si Addition. 3569-3573A
- Austenitic stainless steels, Powder technology**  
Sintering Densification and Microstructural Evolution of Injection Molding Grade 17-4 PH Stainless Steel Powder. 2185-2194A
- Austenitic stainless steels, Welding**  
A Study on Heat Source Equations for the Prediction of Weld Shape and Thermal Deformation in Laser Microwelding. 757-764B  
Missed Joint Induced by Thermoelectric Magnetic Field in Electron-Beam Welding Dissimilar Metals-Experiment and Scale Analysis. 765-773B

- Effects of metal vapor on electron temperature in helium gas tungsten arcs. 1183-1188A
- Dissolution Kinetics of NbC Particles in the Heat-Affected Zone of Type 347 Austenitic Stainless Steel. 2031-2042A
- A Unified Numerical Modeling of Stationary Tungsten-Inert Gas Welding Process. 2043-2052A
- Austenitizing**  
Phase transformation-induced grain refinement in rapidly solidified ultra-high-carbon steels. 2789-2799A
- Automotive components, Materials selection**  
Creep and microstructure of magnesium-aluminum-calcium based alloys. 567-574A  
Modeling  $M_{23}C_6$  Precipitation in Niobium-Alloyed Ferritic Stainless Steel. 3339-3347A
- Axial stress**  
Finite-element calculations of the lattice rotation field of a tensile-loaded nickel-based alloy multycrystal and comparison with topographical x-ray diffraction measurements. 2825-2833A
- Bainite**  
Austenite Decomposition to Carbide-Rich Products in Fe-0.30C-6.3W. 3619-3633A
- Bainitic transformations, Composition effects**  
Phase transformation and mechanical properties of Si-free CMnAl transformation-induced plasticity-aided steel. 2573-2580A
- Bake hardenable steels, Heat treatment**  
Fast Aging Kinetics of the AA6016 Al-Mg-Si Alloy and the Application in Forming Process. 3121-3126A
- Ball milling**  
Solid-state crystalline-glassy cyclic phase transformations of mechanically alloyed  $Cu_{32}Zr_{68}$  powders. 135-143A  
Fabrication and characterization of Ti-TiB<sub>2</sub> functionally graded material system. 681-685A  
Formation of a TiB<sub>2</sub>-reinforced copper-based composite by mechanical alloying and hot pressing. 1275-1280A  
Development of Austenitic Nanostructures in High-Nitrogen Steel Powders Processed by Mechanical Alloying. 2139-2144A  
Thermally Enhanced and Mechanically Driven Glass Formation Reactions of Multilayered  $Cu_{32}Zr_{68}$  Powders. 2145-2153A  
Formation and Annealing Behavior of Nanocrystalline Ferrite in Fe-0.89C Spheroidite Steel Produced by Ball Milling. 2195-2203A  
Evolution of Submicrocrystalline Iron Containing Dispersed Oxides under Mechanical Milling Followed by Consolidation. 3241-3248A  
Self-Propagating Reaction Induced by Ball Milling in a Mixture of  $Cu_2O$  and Al Powders. 3521-3526A
- Ball milling, Low temperature effects**  
Grain growth behavior of cryomilled INCONEL 625 powder during isothermal heat treatment. 125-134A
- Ballistic impact tests**  
Computational modeling of through-thickness dynamic impact response in cross-rolled Ti-6Al-4V plates. 937-947A  
Microstructural evolution of a shaped-charge liner and target materials during ballistic tests. 1069-1074A  
Control of surface carburization and improvement of dynamic fracture behavior in tungsten heavy alloys. 1213-1219A
- Banding**  
Development of microstructural banding in low-alloy steel with simulated Mn segregation. 1627-1637A
- Bearing steels, Microstructure**  
Lattice Orientation Relationship between the M<sub>23</sub>C<sub>6</sub> Carbide and the Ferrite Matrix in the M50NiL Bearing Steel. 1963-1969A
- Bend properties**  
Room-temperature mechanical properties of cold-rolled thin foils of binary, stoichiometric Ni<sub>3</sub>Al. 2607-2613A
- Bend strength**  
Effect of heat treatments on in-situ  $Al_2O_3/TiAl_3$  composites produced from squeeze casting of  $TiO_2/A356$  composites. 31-40B
- Bend tests**  
Communication: Strengthening of Virgin Martensite through Cryogenic Deformation. 3576-3578A  
Measuring the Fracture Toughness of Molybdenum-0.5 pct Titanium-0.1 pct Zirconium and Oxide Dispersion-Strengthened Molybdenum Alloys using Standard and Subsize Bend Specimens. 3685-3707A
- Beryllium base alloys, Mechanical properties**  
Communication: High-cycle fatigue of an investment cast, Be-Al metal matrix composite. 1862-1865A  
Pressure Effects on Flow and Fracture of Be-Al Alloys. 3555-3564A
- Beryllium base alloys, Powder technology**  
Equal-channel angular extrusion of beryllium. 965-972A
- Billet casting**  
Ingenuity and innovation - the hallmarks of Brimacombe's pioneering contributions to process engineering. 5-29B
- Binary systems**  
Averaged solute transport during solidification of a binary mixture: active dispersion in dendritic structures. 365-376B  
Communication: Discussion of 'coarsening of intermetallic or compound precipitates in binary systems'. 1859-1860A  
Communication: Author's reply [to 'Discussion of 'Coarsening of intermetallic or compound precipitates in binary systems'']. 1860-1862A  
Sequences of Phase Formation in Multiphase Stressed Plates. 1901-1911A
- Binary systems, Phase transformations**  
Modeling The Austenite-Ferrite Isothermal Transformation in an Fe-C Binary System and Experimental Verification. 3111-3115A
- Binary systems, Phases (state of matter)**  
Communication: The Gibbs-Thomson effect in dilute binary systems. 1283-1287A
- Metastable phases in the Ti-V system. I. Neutron diffraction study and assessment of structural properties. 1307-1317A  
Low-temperature extension of the Lehrer diagram and the iron-nitrogen phase diagram. 2593-2598A
- Binary systems, Thermal properties**  
Thermodynamic Modeling of the Indium-Palladium System. 3597-3603A
- Binder removal**  
Thermal debinding modeling of mass transport and deformation in powder-injection molding compact. 477-488B  
Effect of residual carbon on the sintering process of m2 high speed steel parts obtained by a modified metal injection molding process. 1843-1851A
- Binders (adhesives)**  
Thermal debinding modeling of mass transport and deformation in powder-injection molding compact. 477-488B
- Binders (adhesives), Materials selection**  
Effect of residual carbon on the sintering process of m2 high speed steel parts obtained by a modified metal injection molding process. 1843-1851A
- Biocompatibility**  
Recent metallic materials for biomedical applications. 477-486A  
Hydrogen embrittlement of nickel-titanium alloy in biological environment. 495-501A  
Dry-process surface modification for titanium dental implants. Effect of Fcc-Hcp Phase Transformation Produced by Isothermal Aging on the Corrosion Resistance of a Co-27Cr-5Mo-0.05C Alloy. 511-519A  
2229-2235A
- Bismuth, Ternary systems**  
Communication: Prediction of the thermodynamic properties of solutes in the Bi-based ternary dilute solution. 502-506B
- Body centered cubic lattice**  
A new bcc-fcc orientation relationship observed between ferrite and austenite in solidification structures of steels. 5-15A  
Thermodynamic description of the Cu-Al-Sn system in the copper-rich corner. 1639-1648A
- Boiling water reactors, Corrosion**  
Intergranular stress corrosion cracking behavior of types 308 and 316 stainless steel weld metals in a simulated boiling water reactor environment. 2907-2919A
- Bolts, Fabrication**  
Spheroidization cycles for medium carbon steels. 1255-1261A
- Bonding strength**  
Interface nanochemistry effects on stainless steel diffusion bonding. 437-442A  
Inertia Welding Nickel-Based Superalloy: Part I. Metallurgical Characterization. 3215-3225A
- Borides, Coatings**  
TiB Whisker Coating on Titanium Surfaces by Solid-State Diffusion: Synthesis, Microstructure, and Mechanical Properties. 3489-3498A
- Borides, Composite materials**  
Solidification paths and reinforcement morphologies in melt-processed (TiB + TiC)/Ti in situ composites. 3055-3063A
- Boriding**  
Interrupted bonding of medium-carbon steels. 1475-1485A
- Brasses, Heat treatment**  
Evolution of microstructure and properties in alpha-brass after iterative processing. 1853-1857A
- Brasses, Phase transformations**  
Massive transformations revisited. 2277-2283A
- Brazing alloys, Materials selection**  
Interfacial Segregation of Ti in the Brazing of Diamond Grits onto a Steel Substrate Using a Cu-Sn-Ti Brazing Alloy. 2163-2172A
- Brinell hardness**  
The effect of mischmetal addition on the structure and mechanical properties of a cast Al-7Si-0.3Mg alloy containing excess iron (up to 0.6 pct). 391-400A
- Brittleness**  
Crack-initiation toughness and crack-arrest toughness in advanced 9 pct Ni steel welds containing local brittle zones. 2615-2622A
- Bronzes, Powder technology**  
Density gradients formed during compaction of bronze powders: the origins of part-to-part variation. 165-170A
- Bubbles**  
An analytical self-consistent determination of a bubble with a deformed cap trapped in solid during solidification. 91-100B  
Bubble formation and detachment on nonwetted surfaces. 155-162B  
Communication: Foaming behavior of slags. 499-501B  
Dopant Particle Characterization and Bubble Evolution in Aluminum-Potassium-Silicon-Doped Molybdenum Wire. 3349-3356A
- Bubbling**  
In-situ formation of SiC-reinforced Al-Si alloy composites using methane gas mixtures. 543-550B  
Molten Wood's-Metal Flow in a Cylindrical Bath Agitated by Cold Bottom Gas Injection. 695-702B
- Bulging**  
Kinetics of biaxial dome formation by transformation superplasticity of titanium alloys and composites. 1669-1680A
- Cadmium, Microstructure**  
Effect of temperature and shear direction on yield stress by {1122}<1123> slip in hcp metals. 831-836A
- Cadmium, Ternary systems**  
Communication: Prediction of the thermodynamic properties of solutes in the Bi-based ternary dilute solution. 502-506B
- Calcium compounds, Physical properties**

- The Effect of  $\text{CaF}_2$  on the Viscosities and Structures of  $\text{CaO-SiO}_2\text{-MgO-CaF}_2$  Slags. 723-729B
- Calcium sulfate**  
A Novel Cyclic Process using  $\text{CaSO}_4/\text{CaS}$  Pellets for Converting Sulfur Dioxide to Elemental Sulfur without Generating Secondary Pollutants: Part I. Feasibility and Kinetics of the Reduction of Sulfur Dioxide with Calcium Sulfide Pellets. 711-716B
- Calcium sulfate, Reduction (chemical)**  
A Novel Cyclic Process using  $\text{CaSO}_4/\text{CaS}$  Pellets for Converting Sulfur Dioxide to Elemental Sulfur without Generating Secondary Pollutants: Part II. Hydrogen Reduction of Calcium-Sulfate Pellets to Calcium Sulfide. 717-721B
- Carbides**  
Retardation of  $\alpha$ -phase transformation in modified superalloy RR2072. 1319-1330A  
Dissolution Kinetics of NbC Particles in the Heat-Affected Zone of Type 347 Austenitic Stainless Steel. 2031-2042A
- Carbides, Coatings**  
Phase formation and microstructure in sputter-deposited Ti-Mo-C and Ti-W-C thin films. 1579-1588A
- Carbon, Additives**  
Communication: Effect of carbon addition on tribological properties of Fe-Al alloys. 1292-1295A
- Carbon, Binary systems**  
Modeling The Austenite-Ferrite Isothermal Transformation in an Fe-C Binary System and Experimental Verification. 3111-3115A
- Carbon manganese steels, Mechanical properties**  
Change of Critical Events of Cleavage Fracture with Variation of Microscopic Features of Low-Alloy Steels. 3393-3402A
- Carbon manganese steels, Powder technology**  
Explicit finite element method simulation of consolidation of monolithic and composite powders. 2649-2658A
- Carbon steels, Casting**  
A unified microscale parameter approach to solidification-transport process-based macrosegregation modeling for dendritic solidification. II. Numerical example computations. 451-463B
- Carbon steels, Coating**  
Near-nanostructured WC-18 pct co coatings with low amounts of non-WC carbide phase: Part I. Synthesis and characterization. 145-157A  
Near-nanostructured WC-18 pct co coatings with low amounts of non-WC carbide phase: Part II. Hardness and resistance to sliding and abrasive wear. 159-164A
- Carbon steels, Rolling**  
A Precision On-Line Model for the Prediction of Roll Force and Roll Power in Hot-Strip Rolling. 3255-3272A
- Carbonitriding**  
Communication: A New Hybrid Process for Surface Modification by Combining Brush Plating with Nitrocarburizing. 2240-2244A
- Carburizing**  
Control of surface carburization and improvement of dynamic fracture behavior in tungsten heavy alloys. 1213-1219A
- Case hardening**  
Surface engineering of Timet 550 with oxygen to form a rutile-based, wear-resistant coating. 1201-1211A
- Casting**  
Modeling of primary spacing selection in dendrite arrays during directional solidification. 223-233B  
Averaged solute transport during solidification of a binary mixture: active dispersion in dendritic structures. 365-376B
- Casting alloys, Physical properties**  
Communication: Thermodynamics of Hydrogen in Al-Si Alloys. 3874-3876A
- Casting defects**  
Ingenuity and innovation - the hallmarks of Brimacombe's pioneering contributions to process engineering. 5-29B  
An analytical self-consistent determination of a bubble with a deformed cap trapped in solid during solidification. 91-100B  
A three-phase model of hydrogen pore formation during the equiaxed dendritic solidification of aluminum-silicon alloys. 209-221B  
Microporosity prediction in aluminum alloy castings. 243-255B  
Die soldering: mechanism of the interface reaction between molten aluminum alloy and tool steel. 465-476B  
Formation of  $\text{CaS}$  on  $\text{Al}_2\text{O}_3\text{-CaO}$  inclusions during solidification of steels. 625-632B  
Modeling of the Continuous Casting of Steel-Past, Present, and Future. 795-812B  
Analysis and prevention of microcracking phenomenon occurring during strip casting of an AISI 304 stainless steel. 1487-1497A  
Hydrogen Evolution during Directional Solidification and Its Effect on Porosity Formation in Aluminum Alloys. 2067-2072A  
Modeling of Microporosity, Macroporosity, and Pipe-shrinkage Formation during the Solidification of Alloys Using a Mushy-Zone Refinement Method: Applications to Aluminum Alloys. 2095-2106A
- Casting defects, Deformation effects**  
An experimental study of deformation of a columnar dendritic mushy zone using a transparent succinonitrile-acetone alloy. 69-78B
- Casting machines, Design**  
Analysis and prevention of microcracking phenomenon occurring during strip casting of an AISI 304 stainless steel. 1487-1497A
- Castings, Mechanical properties**  
Modification of 27Cr Cast Iron with Alloying Yttrium for Enhanced Resistance to Sliding Wear in Corrosive Media. 1981-1989A
- Cavitation**  
Some selected topics in creep cavitation. 383-390A  
The Influence of Microstructure and Environment on the Crack Growth Behavior of Powder Metallurgy Nickel Superalloy RR1000. 3165-3172A  
Simulation of Cavitation Processes in Superplastic Deformation. 3449-3455A
- Cavitation, Vibration effects**  
Structural refinement of gray iron by electromagnetic vibrations. 3025-3030A
- Cellular structure**  
Cellular array morphology during directional solidification. Analysis of the Cu-3 Wt pct Ti cellular interphase boundary by various models. 1229-1243A  
The cellular interlamellar and growth-front interphase boundaries in Cu-3 Wt pct Ti. 2495-2505A  
Rapid Solidification of Martensitic Stainless Steel Atomized Droplets. 2507-2518A  
The Effect of Convection on Disorder in Primary Cellular and Dendritic Arrays. 3755-3760A  
3763-3775A
- Cemented carbides, Coatings**  
Near-nanostructured WC-18 pct co coatings with low amounts of non-WC carbide phase: Part I. Synthesis and characterization. 145-157A  
Near-nanostructured WC-18 pct co coatings with low amounts of non-WC carbide phase: Part II. Hardness and resistance to sliding and abrasive wear. 159-164A
- Ceramic coatings**  
Phase formation and microstructure in sputter-deposited Ti-Mo-C and Ti-W-C thin films. 1579-1588A
- Ceramic fibers, Materials selection**  
Interfacial reactions in aluminosilicate short fiber-reinforced aluminum matrix composites. 2755-2761A
- Ceramic mold casting**  
Communication: Wettability of  $\text{Al}_2\text{O}_3\text{-MgO}$  substrates by molten aluminum. 506-509B
- Ceramic powders, Coatings**  
Correlation of Microstructure with Wear and Fracture Properties of Two-Layered VC/Ti-6Al-4V Surface Composites Fabricated by High-Energy Electron-Beam Irradiation. 3173-3185A
- Charge transfer**  
On the Partial Atomic Volume of Aluminum in Solid Solutions Based on the 3d Transition Metals and Copper. 3591-3595A
- Chemical bonds**  
Effect of pressure on zone-center phonons in hexagonal-close-packed metals. 743-747A  
On the Partial Atomic Volume of Aluminum in Solid Solutions Based on the 3d Transition Metals and Copper. 3591-3595A
- Chemical composition**  
Microstructural and fracture characterization of Nb-Cr-Ti mechanically alloyed materials. 401-416A  
The Effect of  $\text{CaF}_2$  on the Viscosities and Structures of  $\text{CaO-SiO}_2\text{-MgO-CaF}_2$  Slags. 723-729B  
Communication: Microstructures and mechanical properties of  $(\text{Ir,Rh})_{75}\text{Nb}_{15}\text{Ni}_{10}$  alloys. 1281-1283A  
Communication: Precipitation behavior of carbonitrides in type 347 stainless steels with various C and N contents. 1565-1569A  
The Influence of Minor Elements on the Weldability of an INCONEL 718-Type Superalloy. 2005-2017A  
Phase transformation and mechanical properties of Si-free CMAl transformation-induced plasticity-aided steel. 2573-2580A  
Influence of Al and Ni concentration on the martensitic transformation in Cu-Al-Ni shape-memory alloys. 2581-2591A
- Chemical equilibrium**  
Communication: Manganese Deoxidation Equilibrium in Liquid Fe-36 Pct Ni Alloy at 1773 K. 930-932B
- Chill casting**  
Microporosity prediction in aluminum alloy castings. 243-255B  
Constitutive Behavior of As-Cast AM 050, AA3104, and AA5182. 1971-1980A
- Chills**  
Development of New Feeding-Distance Rules Using Casting Simulation: Part II. The New Rules. 741-755B
- Chip formation**  
Formation of white layers in steels by machining and their characteristics. 1245-1254A  
On thermoplastic shear instability in the machining of a titanium alloy (Ti-6Al-4V). 2995-3010A
- Chlorides, Reactions (chemical)**  
Recycling of magnesium alloys: chemical equilibria between magnesium-lithium-based melts and salt melts. 355-364B
- Chlorination**  
Communication: Conversion of  $\text{VOCl}_3$  to  $\text{VOCl}_2$  in liquid  $\text{TiCl}_4$ . Rare Earth Extraction and Separation from Mixed Bastnaesite-Monazite Concentrate by Stepwise Carbochlorination-Chemical Vapor Transport. 142-146B  
661-668B
- Chromium, Alloying elements**  
Phase Evolution in Laser-Deposited Titanium-Chromium Alloys. 2129-2138A  
Interphase boundary structure with irrational orientation relationship formed in grain boundary precipitation. 2327-2335A
- Chromium, Diffusion**  
Diffusion along grain and interphase boundaries in Alpha Zr and Zr-2.5 Wt Pct Nb alloy. 797-800A
- Chromium, Powder technology**  
Structure of a Fe-Cr-Mn-Mo-N Alloy Processed by Mechanical Alloying. 3273-3278A
- Chromium, Ternary systems**  
Phase equilibria of the ternary Ni-Cr-Zr system and interfacial



- reactions in the Ni-Cr/Zr couples. 995-1002A
- Chromium compounds, Reactions (chemical)**
- Oxidation state and activities of chromium oxides in CaO-SiO<sub>2</sub>-CrO<sub>2</sub> slag system. 595-603B
- Chromium iron, Mechanical properties**
- Modification of 27Cr Cast Iron with Alloying Yttrium for Enhanced Resistance to Sliding Wear in Corrosive Media. 1981-1989A
- Chromium manganese steels, Metal working**
- Hot rolling texture development in CMnCrSi dual-phase steels. 1091-1102A
- Chromium manganese steels, Microstructure**
- Development of microstructural banding in low-alloy steel with simulated Mn segregation. 1627-1637A
- Chromium manganese steels, Powder technology**
- Development of Austenitic Nanostructures in High-Nitrogen Steel Powders Processed by Mechanical Alloying. 2139-2144A
- Chromium molybdenum steels, Heat treatment**
- Toward prediction of microstructural evolution during laser surface alloying. 1189-1200A
- Chromium molybdenum steels, Mechanical properties**
- Improvement of Gigacycle Fatigue Properties by Modified Austempering in 1600 and 2000 MPA-Class Low-Alloy Steels. 3421-3431A
- Chromium molybdenum steels, Nondestructive testing**
- Comprehensive microstructural characterization in modified 9Cr-1Mo ferritic steel by ultrasonic measurements. 1617-1626A
- Chromium molybdenum steels, Sorption**
- Trap-Governed Hydrogen Diffusivity and Uptake Capacity in Ultrahigh-Strength AERMET 100 Steel. 1991-2004A
- Chromium molybdenum steels, Surface finishing**
- Communication: A New Hybrid Process for Surface Modification by Combining Brush Plating with Nitrocarburizing. 2240-2244A
- Chromium molybdenum steels, Welding**
- Communication: Thermal Scaling Behavior of Weldments of 9Cr-1Mo Steel and Its Relevance to the Life Assessment of Fossil Fuel Power Plant Components. 3296-3297A
- Chromium molybdenum vanadium steels, Mechanical properties**
- Observations, theories, and predictions of high-temperature creep behavior. 241-248A
- Chromium steels, Machining**
- Formation of white layers in steels by machining and their characteristics. 1245-1254A
- Chromium steels, Surface finishing**
- An analysis of residual stress fields caused by shot peening. 1775-1778A
- Claddings, Materials selection**
- The fracture toughness and toughening mechanisms of nickel-base wear materials. 33-56A
- Cleavage**
- Change of Critical Events of Cleavage Fracture with Variation of Microscopic Features of Low-Alloy Steels. 3393-3402A
- Clustering**
- On the roles of clusters during intragranular nucleation in the absence of static defects. 1649-1658A
- Texture Clustering and Long-Range Disorientation Representation Methods: Application to 6022 Aluminum Sheet. 3709-3718A
- Clusters**
- Numerical simulation of dendrite white spot formation during vacuum arc remelting of INCONEL718. 443-454A
- Mobility of interstitial clusters in alpha-zirconium. 783-789A
- Coarsening**
- A Discrete Approach to Grain Growth Based on Pair Interactions: Effect of Local Grain-Boundary Curvature. 3329-3337A
- Modeling M<sub>23</sub>C<sub>6</sub> Precipitation in Niobium-Alloyed Ferritic Stainless Steel. 3339-3347A
- The Coarsening Kinetics of  $\gamma'$  Particles in Nickel-Based Alloys. 3367-3373A
- Cobalt, Reduction (chemical)**
- Communication: Electroreduction of cobalt from sulfate solutions—effect of substrate and background MgSO<sub>4</sub>. 137-140B
- Cobalt base alloys, Corrosion**
- Effect of Fcc-Hcp Phase Transformation Produced by Isothermal Aging on the Corrosion Resistance of a Co-27Cr-5Mo-0.05C Alloy. 2229-2235A
- Cobalt base alloys, Mechanical properties**
- The fracture toughness and toughening mechanisms of nickel-base wear materials. 33-56A
- Some Observations of the Influence of  $\delta$ -Ferrite Content on the Hardness, Galling Resistance, and Fracture Toughness of Selected Commercially Available Iron-Based Hardfacing Alloys. 3403-3419A
- Cobalt base alloys, Reactions (chemical)**
- Interface stability during displacement reactions between Cu<sub>2</sub>O and Co<sub>1-x</sub>Fe<sub>x</sub> alloys at 1223 K. 2899-2906A
- Cobalt base alloys, Surface properties**
- Recent metallic materials for biomedical applications. 477-486A
- Codeposition**
- Phase formation and microstructure in sputter-deposited Ti-Mo-C and Ti-W-C thin films. 1579-1588A
- Coercive force**
- A novel technique for manufacturing metal-bonded Nd-Fe-B magnets by squeeze casting. 637-646A
- Coherence**
- Subnanometer-scale chemistry and structure of  $\alpha$ -iron/molybdenum nitride heterophase interfaces. 2317-2326A
- Cold pressing**
- Effect of cyclic pressure consolidation on the uniformity of metal matrix composites. 183-191A
- Cold rolling**
- Study of the kinetics of the recrystallization of cold-rolled low-carbon steel. 25-31A
- Influence of elastic and plastic anisotropy on the flow behavior in a duplex stainless steel. 57-71A
- Annealing behavior of alumina dispersion-strengthened copper strips rolled under different conditions. 1605-1616A
- Precipitate Formation in Low-Temperature Nitrided Cold-Rolled Fe<sub>93</sub>Ni<sub>4</sub>Ti<sub>2</sub> and Fe<sub>93</sub>Ni<sub>4</sub>Cr<sub>3</sub> Films. 3075-3087A
- Cold working**
- The Microstructure and Recrystallization of Flow-Formed Oxide-Dispersion-Strengthened Ferritic Alloy: Part I. Deformation Structure. 3777-3785A
- The Microstructure and Recrystallization of Flow-Formed Oxide-Dispersion-Strengthened Ferritic Alloy: Part II. Recrystallization Behavior. 3787-3794A
- Columnar structure**
- Solidification Thermal Parameters Affecting the Columnar-to-Equiaxed Transition. 2107-2118A
- Compacting**
- Density gradients formed during compaction of bronze powders: the origins of part-to-part variation. 165-170A
- Effect of cyclic pressure consolidation on the uniformity of metal matrix composites. 183-191A
- Sintering Densification and Microstructural Evolution of Injection Molding Grade 17-4 PH Stainless Steel Powder. 2185-2194A
- Explicit finite element method simulation of consolidation of monolithic and composite powders. 2649-2658A
- Compressibility (powder)**
- Density gradients formed during compaction of bronze powders: the origins of part-to-part variation. 165-170A
- Compressing**
- Effect of loading condition and stress state on damage evolution of silicon particles in an Al-Si-Mg-base cast alloy. 555-565A
- Deformation behavior of Hcp Ti-Al alloy single crystals. 837-850A
- Quantitative characterization of three-dimensional damage evolution in a wrought Al-alloy under tension and compression. 2599-2606A
- Anisotropy of Intermetallic Particle Cracking Damage Evolution in an Al-Mg-Si Base Wrought Aluminum Alloy under Uniaxial Compression. 3443-3448A
- Compression tests**
- The Effect of Grain Boundaries on the Athermal Stress of Tantalum and Tantalum-Tungsten Alloys. 3457-3464A
- Effect of the Lamellar Grain Size on Plastic Flow Behavior and Microstructure Evolution during Hot Working of a Gamma Titanium Aluminide Alloy. 3817-3830A
- Strength and Plastic Flow in "In Situ" TiC Reinforced Aluminum Composites. 3831-3838A
- Compressive strength**
- Age-hardening characteristics of aluminum alloy-hollow fly ash composites. 1541-1547A
- Compressive strength, Processing effects**
- Elevated temperature strength and room-temperature toughness of directionally solidified Ni-33Al-33Cr-1Mo. 1385-1397A
- Computer simulation**
- Digital simulations of a stationary and a linear weld. 101-110B
- Computer simulation of solidification processes - the evolution of a technology. 519-541B
- Computational fluid-dynamics modeling of the hydrodynamics of fluidization in the sand surrounding a lost-foam casting pattern. 565-575B
- Atomic-scale modeling of dislocations and related properties in the hexagonal-close-packed metals. 721-733A
- Anisotropy of point defect diffusion in alpha-zirconium. 777-782A
- Modeling of the Continuous Casting of Steel-Past, Present, and Future. 795-812B
- Twins as barriers to basal slip in hexagonal-close-packed metals. 809-812A
- Measurement and Computation of Drag Forces in Thermogravimetric Studies. 891-896B
- Computational modeling of through-thickness dynamic impact response in cross-rolled Ti-6Al-4V plates. 937-947A
- Modeling of laser keyhole welding. II. Simulation of keyhole evolution, velocity, temperature profile, and experimental verification. 1831-1842A
- On Composite-Structure Weaknesses: Part I. Simulation, Properties, and Numerical Approach. 2205-2215A
- Computer simulation of solidification processes - the evolution of a technology. 2251-2273A
- Numerical simulation of Zn coating solidification. 2685-2694A
- Finite-element calculations of the lattice rotation field of a tensile-loaded nickel-based alloy multycrystal and comparison with topographical x-ray diffraction measurements. 2825-2833A
- Residual stresses in a welded superalloy disc: characterization using synchrotron diffraction and numerical process modeling. 2921-2931A
- Modeling The Austenite-Ferrite Isothermal Transformation in an Fe-C Binary System and Experimental Verification. 3111-3115A
- The Coarsening Kinetics of  $\gamma'$  Particles in Nickel-Based Alloys. 3367-3373A
- Concentrates (ores)**
- Slags and mattes in Vanyukov's process for the extraction of copper. 551-559B
- Concentrates (ores), Reduction (chemical)**
- Thermodynamic study of the reduction of titanium magnetite concentrate with solid carbon. 633-638B



**Concentration (composition)**

- Effect of directionally solidified microstructures on the room-temperature fracture-toughness properties of Ni-33(at. pct)Al-33Cr-1 Mo and Ni-33(at. pct)Al-31 Cr-3Mo eutectic alloys grown at different solidification rates. 597-612A
- Synthesis and nanoindentation study of high-velocity oxygen fuel thermal-sprayed nanocrystalline and near-nanocrystalline Ni coatings. 647-655A
- Deoxidation of molybdenum during vacuum sintering. 657-664A
- Stable quasicrystalline phase in Al-Cu-Fe-Cr coating materials. 675-679A
- Communication: Effect of boron on the hot ductility of Nb-containing steel. 701-704A
- Thermodynamic Study of MnO-SiO<sub>2</sub>-Al<sub>2</sub>O<sub>3</sub> Slag System: Liquidus Lines and Activities of MnO at 1823 K. 915-920B

**Consolidation**

- Explicit finite element method simulation of consolidation of monolithic and composite powders. 2649-2658A
- Origin of porosity in oxide-dispersion-strengthened alloys produced by mechanical alloying. 2713-2718A
- Evolution of Submicrocrystalline Iron Containing Dispersed Oxides under Mechanical Milling Followed by Consolidation. 3241-3248A

**Contact angle**

- Bubble formation and detachment on nonwetted surfaces. 155-162B
- Energy of the Pb(111) | Al(111) interface. 1003-1007A

**Continuous annealing**

- Phase transformation and mechanical properties of Si-free CMnAl transformation-induced plasticity-aided steel. 2573-2580A

**Continuous casting**

- Ingenuity and innovation - the hallmarks of Brimacombe's pioneering contributions to process engineering. 5-29B
- An experimental study of deformation of a columnar dendritic mushy zone using a transparent succinonitrile-acetone alloy. 69-78B
- Simulation of the submerged energy nozzle-mold water model system using laser-optical and computational fluid dynamics methods. 163-172B
- A theoretical and experimental study of continuous-casting tundishes focusing on slag-steel interaction. 173-185B
- Communication: Physical modeling of the effects of thermal buoyancy driven flows in aluminum casters. 321-324B
- Modeling the formation of longitudinal facial cracks during continuous casting of hypoperitectic steel. 413-423B
- Thermal and mechanical behavior of copper molds during thin-slab casting. I. Plant trial and mathematical, modeling. 425-436B
- Thermal and mechanical behavior of copper molds during thin-slab casting. II. Mold crack formation. 437-449B
- Correction to "Simulation of the submerged energy nozzle-mold water model systems using laser optical and computational fluid dynamics methods". 639B
- Modeling of the Continuous Casting of Steel-Past, Present, and Future. 795-812B

**Controlled atmospheres**

- A new unidirectional solidification method to study gray cast iron. 235-241B
- Effects of metal vapor on electron temperature in helium gas tungsten arcs. 1183-1188A
- Pulsed Nd:YAG Laser Welding of Copper Using Oxygenated Assist Gases. 2019-2030A
- Development of Austenitic Nanostructures in High-Nitrogen Steel Powders Processed by Mechanical Alloying. 2139-2144A
- Sintering Densification and Microstructural Evolution of Injection Molding Grade 17-4 PH Stainless Steel Powder. 2185-2194A

**Convection**

- Digital simulations of a stationary and a linear weld. 101-110B
- Rayleigh-Benard convection during solidification of an eutectic solution cooled from the top. 605-612B

**Cooling rate**

- In-situ observation of the precipitation of manganese sulfide in low-carbon magnesium-killed steel. 427-436A
- In-situ measurement of continuous cooling  $\beta \rightarrow \alpha$  transformation behavior of CP-Ti. 1051-1056A
- Microstructural characteristics of Ni-Sb eutectic alloys under substantial undercooling and containerless solidification conditions. 1221-1228A
- A study on inhomogeneous distribution of temper graphite particles in strip-cast Fe-C-Si alloys. 1263-1273A
- Effect of composition and austenite deformation on the transformation characteristics of low-carbon and ultralow-carbon microalloyed steels. 1331-1349A
- Elevated temperature strength and room-temperature toughness of directionally solidified Ni-33Al-33Cr-1Mo. 1385-1397A
- Development of microstructural banding in low-alloy steel with simulated Mn segregation. 1627-1637A
- On differential thermal analyzer curves for the melting and freezing of alloys. 1779-1794A
- Dissolution Kinetics of NbC Particles in the Heat-Affected Zone of Type 347 Austenitic Stainless Steel. 2031-2042A

**Copper, Alloying additive**

- Microstructure and Mechanical Properties of Titanium Aluminum Wide-Gap, Transient Liquid-Phase Bonds Prepared using a Slurry-Deposited Composite Interlayer. 3205-3214A

**Copper, Alloying elements**

- Normal spectral emissivities of liquid Ag-Cu alloys in the visible and infrared regions. 47-54B
- Atomistic modeling of quaternary alloys: Ti and Cu in NiAl. 265-284B
- Thermally Enhanced and Mechanically Driven Glass Formation Reactions of Multilayered Cu<sub>35</sub>Zr<sub>65</sub> Powders. 2145-2153A

**Copper, Atomic properties**

- On the Partial Atomic Volume of Aluminum in Solid Solutions Based on the 3d Transition Metals and Copper. 3591-3595A

**Copper, Casting**

- Control of heat transfer and growth uniformity of solidifying copper shells through substrate temperature. 403-411B

**Copper, Composite materials**

- Formation of a TiB<sub>2</sub>-reinforced copper-based composite by mechanical alloying and hot pressing. 1275-1280A

**Copper, Crystal growth**

- The Effect of Small Deformation on Abnormal Grain Growth in Bulk Cu. 3803-3815A

**Copper, End uses**

- Thermal and mechanical behavior of copper molds during thin-slab casting. I. Plant trial and mathematical, modeling. 425-436B

**Copper, Extraction**

- Slags and mattes in Vanyukov's process for the extraction of copper. 551-559B
- Physicochemical properties of matte-slag melts taken from Vanyukov's furnace for copper extraction. 561-564B
- Copper Electrowinning using Spouted-Bed Electrodes: Part I. Experiments with Oxygen Evolution or Matte Oxidation at the Anode. 669-676B
- Copper Electrowinning using Spouted-Bed Electrodes: Part II. Copper Electrowinning with Ferrous Ion oxidation as the Anodic Reaction. 677-683B

**Copper, Irradiation**

- Localized deformation and hardening in irradiated metals: three-dimensional discrete dislocation dynamics simulations. 285-296B

**Copper, Mechanical properties**

- Observations, theories, and predictions of high-temperature creep behavior. 241-248A
- Dislocation microstructure and internal-stress measurements by convergent-beam electron diffraction on creep-deformed Cu and Al. 311-317A
- Subgrain formation during deformation: physical origin and consequences. 319-327A
- Thermal and mechanical behavior of copper molds during thin-slab casting. II. Mold crack formation. 437-449B
- Artificial Neural Network and Finite Element Modeling of Nanoindentation Tests. 1939-1947A

**Copper, Microstructure**

- Three-dimensional investigation of long-range internal stresses in a single crystal deforming by nonsymmetrical slip. 591-596A

**Copper, Ternary systems**

- A 500°C isothermal section for the Al-Au-Cu system. 987-993A
- Thermodynamic description of the Cu-Al-Sn system in the copper-rich corner. 1639-1648A
- Estimation Of Viscosity Of Ternary-Metallic Melts. 3201-3204A
- Statistical Self-Similarity in Rhines' Concept of Unique Multiphase Diffusion Paths on the Ternary Gibbs' Isotherm. 3357-3365A

**Copper, Welding**

- Pulsed Nd:YAG Laser Welding of Copper Using Oxygenated Assist Gases. 2019-2030A

**Copper base alloys, Alloy development**

- Thermodynamic description of the Cu-Al-Sn system in the copper-rich corner. 1639-1648A

**Copper base alloys, Corrosion**

- Communication: Effect of Zr Addition on Corrosion Behavior of Cu-6Ni-2Mn-2Sn-2Al Alloy. 2237-2240A

**Copper base alloys, Crystal lattices**

- Communication: A New Face-Centered-Cubic Superlattice Structure in Rapidly Solidified Cu-4 Wt Pct Ti Alloy and Its Relevance to the Ordering Process in Ni-Mo and Other 1 1/2 0 Ordering Alloys. 3573-3576A

**Copper base alloys, End uses**

- Interfacial Segregation of Ti in the Brazing of Diamond Grits onto a Steel Substrate Using a Cu-Sn-Ti Brazing Alloy. 2163-2172A

**Copper base alloys, Heat treatment**

- Annealing behavior of alumina dispersion-strengthened copper strips rolled under different conditions. 1605-1616A

**Copper base alloys, Metal working**

- Communication: Effect of Zr Addition on Hot Workability of Cu-6Ni-2Mn-2Sn-2Al Alloy. 3298-3300A

**Copper base alloys, Microstructure**

- On the roles of clusters during intragranular nucleation in the absence of static defects. 1649-1658A
- Analysis of the Cu-3 Wt pct Ti cellular interphase boundary by various models. 2495-2505A
- The cellular interlamellar and growth-front interphase boundaries in Cu-3 Wt pct Ti. 2507-2518A

**Copper base alloys, Phase transformations**

- Influence of Al and Ni concentration on the martensitic transformation in Cu-Al-Ni shape-memory alloys. 2581-2591A
- Enhancement of superelasticity in Cu-Al-Mn-Ni shape-memory alloys by texture control. 2817-2824A

**Copper compounds, Powder technology**

- Solid-state crystalline-glassy cyclic phase transformations of mechanically alloyed Cu<sub>35</sub>Zr<sub>65</sub> powders. 135-143A
- Self-Propagating Reaction Induced by Ball Milling in a Mixture of Cu<sub>2</sub>O and Al Powders. 3521-3526A

**Copper mattes, Reactions (chemical)**

- Copper Electrowinning using Spouted-Bed Electrodes: Part I. Experiments with Oxygen Evolution or Matte Oxidation at the Anode. 669-676B

**Copper steels, Mechanical properties**

- Effect of Prestrain on Stretch-Zone Formation during Ductile Fracture of Cu-Strengthened High-Strength Low-Alloy Steels. 3731-3740A

**Corrosion environments**

- Environmental aspects of near-neutral pH stress corrosion cracking of pipeline steel. 1429-1436A
- Modification of 27Cr Cast Iron with Alloying Yttrium for Enhanced Resistance to Sliding Wear in Corrosive Media. 1981-1989A
- Corrosion mechanisms**  
Corrosion behavior of austenitic alloy 690 under anodic and cathodic potentials. 1437-1447A
- Corrosion potential**  
Corrosion behavior of austenitic alloy 690 under anodic and cathodic potentials. 1437-1447A
- Corrosion resistance**  
Mechanical, Intergranular Corrosion, and Wear Behavior of Aluminum-Matrix Composite Materials Reinforced with Nickel Aluminides. 3541-3553A
- Corrosion resistance, Composition effects**  
Communication: Effect of Zr Addition on Corrosion Behavior of Cu-6Ni-2Mn-2Sn-2Al Alloy. 2237-2240A
- Corrosion resistance, Heating effects**  
Effect of Fcc-Hcp Phase Transformation Produced by Isothermal Aging on the Corrosion Resistance of a Co-27Cr-5Mo-0.05C Alloy. 2229-2235A
- Corrosion resistance, Microstructural effects**  
Communication: Precipitation behavior of carbonitrides in type 347 stainless steels with Various C and N contents. 1565-1569A  
Effect of grain boundary characteristics on intergranular corrosion resistance of 6061 aluminum alloy extrusion. 2891-2898A
- Corrosion resistance, Processing effects**  
Phenomenological observations on mechanical and corrosion properties of thixoformed 357 alloys: a comparison with permanent mold cast 357 alloys. 1399-1412A
- Crack closure**  
Shrinkage and splitting of microcracks under pressure simulated by the finite-element method. 1117-1124A
- Crack initiation**  
Fatigue crack initiation and propagation of binder-treated powder metallurgy steels. 73-81A  
The effect of constraint-induced normal stress on the failure of notched TiAl components. 417-426A  
Effect of directionally solidified microstructures on the room-temperature fracture toughness properties of Ni-33(at. pct)Al-33Cr-1 Mo and Ni-33(at. pct)Al-31 Cr-3Mo eutectic alloys grown at different solidification rates. 597-612A  
Crack-initiation toughness and crack-arrest toughness in advanced 9 pct Ni steel welds containing local brittle zones. 2615-2622A  
Evaluation of the Fatigue Behavior of Ductile Irons with Various Matrix Microstructures. 3719-3730A
- Crack opening displacement**  
Microstructural and fracture characterization of Nb-Cr-Ti mechanically alloyed materials. 401-416A
- Crack propagation**  
The fracture toughness and toughening mechanisms of nickel-base wear materials. 33-56A  
Fatigue crack initiation and propagation of binder-treated powder metallurgy steels. 73-81A  
Thermal and mechanical behavior of copper molds during thin-slab casting. II. Mold crack formation. 437-449B  
Cracking in  $\gamma$ -TiAl due to high speed particle impact. 581-589A  
Influence of microstructure on high-cycle fatigue of Ti-6Al-4V: bimodal vs. lamellar structures. 899-918A  
Anisotropic threshold stress intensity factor,  $K_{IH}$ , and crack growth rate in delayed hydride cracking of Zr-2.5Nb pressure tubes. 919-925A  
The effects of test temperature, temper, and alloyed copper on the hydrogen-controlled crack growth rate of an Al-Zn-Mg-(Cu) alloy. 1167-1181A  
Erratum: The effects of test temperature, temper, and alloyed copper on the hydrogen-controlled crack growth rate of an Al-Zn-Mg-(Cu) alloy. 1297A  
Quantitative characterization of three-dimensional damage evolution in a wrought Al-alloy under tension and compression. 2599-2606A  
Crack-initiation toughness and crack-arrest toughness in advanced 9 pct Ni steel welds containing local brittle zones. 2615-2622A  
Crack growth in a nearly fully-lamellar gamma TiAl alloy at 650°C and 800°C under constant load conditions. 2847-2857A  
The Influence of Microstructure and Environment on the Crack Growth Behavior of Powder Metallurgy Nickel Superalloy RR1000. 3165-3172A  
Communication: Thermal Scaling Behavior of Weldments of 9Cr-1Mo Steel and Its Relevance to the Life Assessment of Fossil Fuel Power Plant Components. 3296-3297A  
Change of Critical Events of Cleavage Fracture with Variation of Microscopic Features of Low-Alloy Steels. 3393-3402A  
Effect of Prolonged Isothermal Exposure on Elevated-Temperature, Time-Dependent Fatigue-Crack Propagation in INCONEL Alloy 783. 3465-3478A
- Crack propagation, Environmental effects**  
Environmentally assisted, sustained-load crack growth in powder metallurgy nickel-based superalloys. 1681-1687A
- Crack propagation, High temperature effects**  
Fatigue-Crack-Propagation Thresholds in a Nickel-Base Superalloy at High Frequencies and Temperatures. 1949-1962A
- Cracking (fracturing)**  
Modeling the formation of longitudinal facial cracks during continuous casting of hypereutectic steel. 413-423B  
Effect of loading condition and stress state on damage evolu-

- tion of silicon particles in an Al-Si-Mg-base cast alloy. 555-565A  
Communication: Effect of boron on the hot ductility of Nb-containing steel. 701-704A  
Control of surface carburization and improvement of dynamic fracture behavior in tungsten heavy alloys. 1213-1219A  
Corrosion behavior of austenitic alloy 690 under anodic and cathodic potentials. 1437-1447A  
Evolution of fiber fragmentation in a short-fiber-reinforced metal-matrix model composite during tensile creep deformation-an acoustic emission study. 1549-1557A  
Hydrogen-assisted deformation and fracture behaviors of Al 8090. 1755-1763A  
Anisotropy of Intermetallic Particle Cracking Damage Evolution in an Al-Mg-Si Base Wrought Aluminum Alloy under Uniaxial Compression. 3443-3448A
- Cracking (fracturing), Microstructural effects**  
Effect of alternative aging process on the fracture and interfacial properties of particulate  $Al_2O_3$ -reinforced Al (6061) metal matrix composite. 1699-1713A  
Effect of pearlite on the vibration-fracture behavior of spheroidal graphite cast irons under resonant conditions. 2623-2634A
- Craters**  
Microstructural evolution of a shaped-charge liner and target materials during ballistic tests. 1069-1074A
- Creep (materials)**  
Denuded zones, diffusional creep, and grain boundary sliding. Observations, theories, and predictions of high-temperature creep behavior. 219-229A  
The role of impurities during creep and superplasticity at very low stresses. 241-248A  
Understanding creep - a review. 261-278A  
Harper-Dorn creep and specimen size. 291-303A  
Dislocation microstructure and internal-stress measurements by convergent-beam electron diffraction on creep-deformed Cu and Al. 305-310A  
Application of a modified jogged-screw model for creep of TiAl and  $\alpha$ -Ti alloys. 311-317A  
Steady-state creep of  $\alpha$ -zirconium at temperatures up to 850°C. 329-336A  
A framework for modeling creep in pure metals. 337-343A  
Some selected topics in creep cavitation. 363-371A  
Unexpected transient creep behavior of tin alloys strengthened by high volume fractions of SbSn. 383-390A  
Evolution of fiber fragmentation in a short-fiber-reinforced metal-matrix model composite during tensile creep deformation-an acoustic emission study. 575-580A  
Crack growth in a nearly fully-lamellar gamma TiAl alloy at 650°C and 800°C under constant load conditions. 1549-1557A  
Tensile, creep, and low-cycle fatigue behavior of a cast  $\gamma$ -TiAl-based alloy for gas turbine applications. 2847-2857A  
Interfacial Dislocation Networks Strengthening a Fourth-Generation Single-Crystal TMS-138 Superalloy. 2869-2881A  
3741-3746A
- Creep (materials), Composition effects**  
Creep processes in magnesium alloys and their composites. 883-889A
- Creep (materials), Diffusion effects**  
Creep at low stresses: an evaluation of diffusion creep and Harper-Dorn creep as viable creep mechanisms. 249-259A
- Creep (materials), Microstructural effects**  
Creep strength of magnesium-based alloys. 875-882A  
The effect of grain size on the ambient temperature creep deformation behavior of a beta Ti-14.8V alloy. 1137-1144A
- Creep (materials), Temperature effects**  
Constitutive equations for creep and plasticity of aluminum alloys produced by powder metallurgy and aluminum-based metal matrix composites. 373-381A
- Creep life**  
Microstructural stability during creep of Mo- or W-bearing 12Cr steels. 2549-2557A  
Communication: Thermal Scaling Behavior of Weldments of 9Cr-1Mo Steel and Its Relevance to the Life Assessment of Fossil Fuel Power Plant Components. 3296-3297A
- Creep rate**  
Creep at very low rates. 213-218A  
Predictive capabilities of the dislocation-network theory of Harper-Dorn creep. 231-239A  
Observations of room-temperature creep recovery in titanium alloys. 891-898A
- Creep rate, Stress effects**  
Analysis of steady-state thermal creep of Zr-2.5Nb pressure tube material. 1103-1115A
- Creep recovery, Microstructural effects**  
Observations of room-temperature creep recovery in titanium alloys. 891-898A
- Creep strength**  
Creep and microstructure of magnesium-aluminum-calcium based alloys. 567-574A  
The Influence of Microstructure and Environment on the Crack Growth Behavior of Powder Metallurgy Nickel Superalloy RR1000. 3165-3172A  
Measuring the Fracture Toughness of Molybdenum-0.5 pct Titanium-0.1 pct Zirconium and Oxide Dispersion-Strengthened Molybdenum Alloys using Standard and Subsize Bend Specimens. 3685-3707A
- Creep strength, Composition effects**  
Creep of Tin, Sb-solution-strengthened Tin, and SbSn-precipitate-strengthened tin. 1531-1539A
- Creep tests, Size effects**  
Harper-Dorn creep and specimen size. 305-310A

- Critical pressure**  
The Critical Pressure and Impeding Pressure of Al Evaporation during Induction Skull Melting Processing of TiAl. 3249-3253A
- Critical temperature**  
Effect of composition and austenite deformation on the transformation characteristics of low-carbon and ultralow-carbon microalloyed steels. 1331-1349A
- Cross rolling**  
Computational modeling of through-thickness dynamic impact response in cross-rolled Ti-6Al-4V plates. 937-947A
- Crucibles, Reactions (chemical)**  
Communication: Solubility of Iron Magnesium-Lithium Melts. 929-930B
- Cryogenic properties**  
Communication: Strengthening of Virgin Martensite through Cryogenic Deformation. 3576-3578A
- Cryolite**  
Modeling of the solubility of alumina in the NaF-AlF<sub>3</sub> system at 1300 K. 315-319B
- Cryolite, Solubility**  
Communication: The solubility of Fe<sub>2</sub>O<sub>3</sub> in cryolite-alumina melts. 140-142B
- Crystal defects**  
Localized deformation and hardening in irradiated metals: three-dimensional discrete dislocation dynamics simulations. 285-296B
- Crystal growth**  
Communication: Discussion of 'coarsening of intermetallic or compound precipitates in binary systems'. 1859-1860A  
Communication: Author's reply to 'Discussion of 'Coarsening of intermetallic or compound precipitates in binary systems''. 1860-1862A
- Crystal lattices**  
Intergranular stresses in ZIRCALOY-2. 749-755A
- Crystal structure**  
Solid-state crystalline-glassy cyclic phase transformations of mechanically alloyed Cu<sub>32</sub>Zr<sub>67</sub> powders. 135-143A  
Atomistic modeling of quaternary alloys: Ti and Cu in NiAl. 265-284B  
Modeling the kinetics of grain-boundary-nucleated recrystallization processes after cold deformation. 529-537A  
Unexpected transient creep behavior of tin alloys strengthened by high volume fractions of SbSn. 575-580A  
Effect of directionally solidified microstructures on the room-temperature fracture-toughness properties of Ni-33(at. pct)Al-33Cr-1 Mo and Ni-33(at. pct)Al-31 Cr-3Mo eutectic alloys grown at different solidification rates. 597-612A  
Electron backscatter diffraction analysis of microstructural evolution in hot-deformed 6xxx series aluminum alloys. 693-713A  
Finite element modeling of the morphology of  $\beta$  to  $\alpha$  phase transformation in Ti-6Al-4V alloy. 1027-1040A  
In-situ measurement of continuous cooling  $\beta \rightarrow \alpha$  transformation behavior of CP-Ti. 1051-1056A  
Retardation of  $\alpha$ -phase transformation in modified superalloy RR2072. 1319-1330A  
Isothermal transformations in an Fe-9 pct Ni alloy. 2425-2431A
- Crystal structure, Composition effects**  
Effect of composition and austenite deformation on the transformation characteristics of low-carbon and ultralow-carbon microalloyed steels. 1331-1349A
- Crystal structure, Deformation effects**  
An integrated computer model with applications for austenite-to-ferrite transformation during hot deformation of Nb-microalloyed steels. 1509-1520A
- Crystal structure, Diffusion effects**  
Comparison of interfacial structure-related mechanisms in diffusional and martensitic transformations. 2541-2547A
- Crystal structure, Pressure effects**  
Effect of pressure on zone-center phonons in hexagonal-close-packed metals. 743-747A
- Crystallization**  
Crystallization kinetics of amorphous magnesium-rich magnesium-copper and magnesium-nickel alloys. 1041-1050A
- Crystallization, Impurity effects**  
Communication: Electroreduction of cobalt from sulfate solutions—effect of substrate and background MgSO<sub>4</sub>. 137-140B
- Crystallography**  
Advances in deformation twin characterization using electron backscattered diffraction data. 949-954A
- Cutting speed**  
On thermoplastic shear instability in the machining of a titanium alloy (Ti-6Al-4V). 2995-3010A
- Cyclic loads**  
Effect of cyclic pressure consolidation on the uniformity of metal matrix composites. 183-191A  
Creep of Tin, Sb-solution-strengthened Tin, and SbSn-precipitate-strengthened tin. 1531-1539A
- Damage**  
Effect of loading condition and stress state on damage evolution of silicon particles in an Al-Si-Mg-base cast alloy. 555-565A  
Quantitative characterization of three-dimensional damage evolution in a wrought Al-alloy under tension and compression. 2599-2606A  
Microscale Elastic Strain Evolution Following Damage in Ti-SiC Composites. 3839-3845A
- Damage tolerance**  
Cracking in  $\gamma$ -TiAl due to high speed particle impact. 581-589A
- Damping**  
Effect of pearlite on the vibration-fracture behavior of spheroidal graphite cast irons under resonant conditions. 2623-2634A  
Effects of Macroscopic Pores on the Damping Behavior of Foamed Commercially Pure Aluminum. 3565-3568A
- Debonding**  
Effect of loading condition and stress state on damage evolution of silicon particles in an Al-Si-Mg-base cast alloy. 555-565A
- Deformation**  
An experimental study of deformation of a columnar dendritic mushy zone using a transparent succinonitrile-acetone alloy. 69-78B  
Communication: Comments on a recent infinitesimal-deformation approach to martensite crystallography. 203A  
Author's reply [to Comments on a recent infinitesimal-deformation approach to martensite crystallography]. 204A  
Thermal and mechanical behavior of copper molds during thin-slab casting. I. Plant trial and mathematical modeling. 425-436B  
Equal-channel angular extrusion of beryllium. 965-972A  
Effect of composition and austenite deformation on the transformation characteristics of low-carbon and ultralow-carbon microalloyed steels. 1331-1349A  
Evolution of fiber fragmentation in a short-fiber-reinforced metal-matrix model composite during tensile creep deformation—an acoustic emission study. 1549-1557A  
Inferring Dynamic Recrystallization in Ferrite using the Kinetics of Static Recrystallization. 1893-1900A  
Communication: Strengthening of Virgin Martensite through Cryogenic Deformation. 3576-3578A  
The Microstructure and Recrystallization of Flow-Formed Oxide-Dispersion-Strengthened Ferritic Alloy: Part I. Deformation Structure. 3777-3785A  
The Effect of Small Deformation on Abnormal Grain Growth in Bulk Cu. 3803-3815A  
Effect of the Lamellar Grain Size on Plastic Flow Behavior and Microstructure Evolution during Hot Working of a Gamma Titanium Aluminide Alloy. 3817-3830A  
Strength and Plastic Flow in "In Situ" TiC Reinforced Aluminum Composites. 3831-3838A  
Effect of Overaging and Particle Size on Tensile Deformation and Fracture of Particle-Reinforced Aluminum Matrix Composites. 3861-3869A
- Deformation mechanisms**  
Influence of elastic and plastic anisotropy on the flow behavior in a duplex stainless steel. 57-71A  
Creep at very low rates. 213-218A  
Denuded zones, diffusional creep, and grain boundary sliding. 219-229A  
Predictive capabilities of the dislocation-network theory of Harper-Dorn creep. 231-239A  
Observations, theories, and predictions of high-temperature creep behavior. 241-248A  
Creep at low stresses: an evaluation of diffusion creep and Harper-Dorn creep as viable creep mechanisms. 249-259A  
The role of impurities during creep and superplasticity at very low stresses. 261-278A  
Deformation bands and the formation of grain boundaries in a superplastic aluminum alloy. 279-290A  
Understanding creep—a review. 291-303A  
Harper-Dorn creep and specimen size. 305-310A  
Dislocation microstructure and internal-stress measurements by convergent-beam electron diffraction on creep-deformed Cu and Al. 311-317A  
Subgrain formation during deformation: physical origin and consequences. 319-327A  
Application of a modified jogged-screw model for creep of TiAl and  $\alpha$ -Ti alloys. 329-336A  
Steady-state creep of  $\alpha$ -zirconium at temperatures up to 850°C. 337-343A  
Elevated-temperature deformation at forming rates of  $10^{-2}$  to  $10^2$  s<sup>-1</sup>. 345-362A  
A framework for modeling creep in pure metals. 363-371A  
Constitutive equations for creep and plasticity of aluminum alloys produced by powder metallurgy and aluminum-based metal matrix composites. 373-381A  
Some selected topics in creep cavitation. 383-390A  
Modeling the kinetics of grain-boundary-nucleated recrystallization processes after cold deformation. 529-537A  
Effect of loading condition and stress state on damage evolution of silicon particles in an Al-Si-Mg-base cast alloy. 555-565A  
Creep and microstructure of magnesium-aluminum-calcium based alloys. 567-574A  
Unexpected transient creep behavior of tin alloys strengthened by high volume fractions of SbSn. 575-580A  
Three-dimensional investigation of long-range internal stresses in a single crystal deforming by nonsymmetrical slip. 591-596A  
Sliding wear of austenitic and austenitic-ferritic stainless steels. 613-624A  
Structural evolution of a strip-cast Al alloy sheet processed by continuous equal-channel angular pressing. 665-673A  
Electron backscatter diffraction analysis of microstructural evolution in hot-deformed 6xxx series aluminum alloys. 693-713A  
Communication: Microstructural interpretation of negligible strain-hardening behavior of submicrometer-grained low-carbon steel during tensile deformation. 705-707A  
A study of twinning in zirconium using neutron diffraction and polycrystalline modeling. 757-763A  
Interfacial deformation mechanisms in hexagonal-close-packed metals. 801-807A  
Nonbasal deformation modes of Hcp metals and alloys: role of dislocation source and mobility. 813-822A  
Effect of temperature and shear direction on yield stress by {1122}<1123> slip in hcp metals. 831-836A  
Deformation behavior of Hcp Ti-Al alloy single crystals. 837-850A  
Transmission electron microscopy investigation of <c + a> dislocations in Mg and  $\alpha$ -solid solution Mg-Li alloys. 851-858A  
Effects of high rates of loading on the deformation behavior



- and failure mechanisms of hexagonal close-packed metals and alloys. 927-935A
- Computational modeling of through-thickness dynamic impact response in cross-rolled Ti-6Al-4V plates. 937-947A
- Deformation twinning in polycrystalline Zr: insights from electron backscattered diffraction characterization. 955-963A
- The effect of grain size on the ambient temperature creep deformation behavior of a beta Ti-14.8V alloy. 1137-1144A
- Communication: Infrared imaging during low-cycle fatigue of HR-120 alloy. 1287-1292A
- Deformation mechanisms during low- and high-temperature superplasticity in 5083 Al-Mg alloy. 1373-1384A
- An investigation of the microstructure and strength of open-cell 6101 aluminum foams. 1413-1427A
- Kinetics of biaxial dome formation by transformation superplasticity of titanium alloys and composites. 1669-1680A
- Why do dislocations assemble into interfaces in epitaxy as well as in crystal plasticity? To minimize free energy. 2519-2539A
- Microstructural stability during creep of Mo- or W-bearing 12Cr steels. 2549-2557A
- Shape Memory Behavior of FeNiCoTi Single and Polycrystals. 3661-3672A
- Deformation resistance**
- Artificial Neural Network and Finite Element Modeling of Nanoindentation Tests. 1939-1947A
- Degassing**
- Mathematical modeling and computer simulation of the rotating impeller particle flotation process: Part II. Particle agglomeration and flotation. 305-314B
- Rate of nitrogen desorption from CaO-Al<sub>2</sub>O<sub>3</sub> melts to gas phase. 393-401B
- Trap-Governed Hydrogen Diffusivity and Uptake Capacity in Ultrahigh-Strength AERMET 100 Steel. 1991-2004A
- Delaminating**
- Sliding wear of austenitic and austenitic-ferritic stainless steels. Correlation of microstructure and wear resistance of ferrous coatings fabricated by atmospheric plasma spraying. 2933-2945A
- Dendritic structure**
- A three-phase model of hydrogen pore formation during the equiaxed dendritic solidification of aluminum-silicon alloys. Modeling of primary spacing selection in dendrite arrays during directional solidification. 209-221B
- Averaged solute transport during solidification of a binary mixture: active dispersion in dendritic structures. 223-233B
- A unified microscale parameter approach to solidification-transport process-based macrosegregation modeling for dendritic solidification. II. Numerical example computations. Computer simulation of solidification processes - the evolution of a technology. 365-376B
- Time-resolved X-ray imaging of aluminum alloy solidification processes. 451-463B
- Microstructural characteristics of Ni-Sb eutectic alloys under substantial undercooling and containerless solidification conditions. 519-541B
- Cellular array morphology during directional solidification. Computer simulation of solidification processes - the evolution of a technology. 613-623B
- Primary Dendrite Distribution and Disorder during Directional Solidification of Pb-Sb Alloys. 1221-1228A
- Rapid Solidification of Martensitic Stainless Steel Atomized Droplets. 1229-1243A
- The Effect of Convection on Disorder in Primary Cellular and Dendritic Arrays. 2251-2273A
- Communication: Minimizing Segregation during the Controlled Directional Solidification of Dendritic Alloys. 3499-3510A
- Densification**
- Sintering Densification and Microstructural Evolution of Injection Molding Grade 17-4 PH Stainless Steel Powder. Explicit finite element method simulation of consolidation of monolithic and composite powders. 3755-3760A
- Grain-size control in Ti-48Al-2Cr-2Nb with yttrium additions. 3763-3775A
- Density**
- Fabrication and characterization of Ti-TiB<sub>2</sub> functionally graded material system. 3876-3881A
- An investigation of the microstructure and strength of open-cell 6101 aluminum foams. 2185-2194A
- Deoxidizing**
- Deoxidation of molybdenum during vacuum sintering. Communication: Manganese Deoxidation Equilibrium in Liquid Fe-36 Pct Ni Alloy at 1773 K. 2649-2658A
- Deposition**
- Phase Evolution in Laser-Deposited Titanium-Chromium Alloys. 2729-2736A
- Depth profiling**
- Communication: Depth Profiling of Hf-Doped Aluminate Coating by Glow-Discharge Mass Spectrometry. 681-685A
- Desorption**
- Rate of nitrogen desorption from CaO-Al<sub>2</sub>O<sub>3</sub> melts to gas phase. 1413-1427A
- Trap-Governed Hydrogen Diffusivity and Uptake Capacity in Ultrahigh-Strength AERMET 100 Steel. 657-664A
- Visualization of the hydrogen desorption process from ferrite, pearlite, and graphite by secondary ion mass spectrometry. 930-932B
- Desulfurizing**
- A Novel Cyclic Process using CaSO<sub>4</sub>/CaS Pellets for Converting Sulfur Dioxide to Elemental Sulfur without Generating Secondary Pollutants: Part I. Feasibility and Kinetics of the Reduction of Sulfur Dioxide with Calcium Sulfide Pellets. 2129-2138A
- Diamond machining**
- Interfacial Segregation of Ti in the Brazing of Diamond Grits onto a Steel Substrate Using a Cu-Sn-Ti Brazing Alloy. 2163-2172A
- Diamond pyramid hardness**
- Effect of heat treatments on in-situ Al<sub>2</sub>O<sub>3</sub>/TiAl<sub>3</sub> composites produced from squeeze casting of TiO<sub>2</sub>/A356 composites. 31-40B
- Aging behavior of the Ti-29Nb-13Ta-4.6Zr new beta alloy for medical implants. 487-493A
- Hydrogen embrittlement of nickel-titanium alloy in biological environment. 495-501A
- Communication: Effect of carbon addition on tribological properties of Fe-Al alloys. 1292-1295A
- Room-temperature mechanical properties of cold-rolled thin foils of binary, stoichiometric Ni<sub>3</sub>Al. 2607-2613A
- TiB Whisker Coating on Titanium Surfaces by Solid-State Diffusion: Synthesis, Microstructure, and Mechanical Properties. 3489-3498A
- Diamond pyramid hardness, Heating effects**
- Spheroidization cycles for medium carbon steels. 1255-1261A
- Diamonds, Brazing**
- Interfacial Segregation of Ti in the Brazing of Diamond Grits onto a Steel Substrate Using a Cu-Sn-Ti Brazing Alloy. 2163-2172A
- Die steels, Surface properties**
- Die soldering: mechanism of the interface reaction between molten aluminum alloy and tool steel. 465-476B
- Differential scanning calorimetry**
- Study of the kinetics of the recrystallization of cold-rolled low-carbon steel. 25-31A
- On the Nature of the Electrochemically Synthesized Hard Fe-0.96 Mass Pct C Alloy Film. 921-927B
- Differential thermal analysis**
- On differential thermal analyzer curves for the melting and freezing of alloys. 1779-1794A
- On the Constitution of the System Al-Mn-Si. 3311-3319A
- Diffusion coating**
- TiB Whisker Coating on Titanium Surfaces by Solid-State Diffusion: Synthesis, Microstructure, and Mechanical Properties. 3489-3498A
- Diffusion welding**
- Interface nanochemistry effects on stainless steel diffusion bonding. 437-442A
- Phase equilibria of the ternary Ni-Cr-Zr system and interfacial reactions in the Ni-Cr/Zr couples. 995-1002A
- Diffusivity**
- Solid-state reaction kinetics of the system CaO-FeO. 257-264B
- Anisotropy of point defect diffusion in alpha-zirconium. 777-782A
- Sequences of Phase Formation in Multiphase Stressed Plates. Statistical Self-Similarity in Rhines' Concept of Unique Multiphase Diffusion Paths on the Ternary Gibbs' Isotherm. 1901-1911A
- Diffusion Studies in the  $\beta$  (B<sub>2</sub>),  $\beta'$  (Bcc), and  $\gamma$  (Fcc) Fe-Ni-Al Alloys at 1000°C. 3357-3365A
- Direct chill casting**
- Two-Phase Modeling Directed Toward Hot Tearing Formation in Aluminum Direct Chill Casting. 3375-3392A
- Direct reduction**
- Process dynamics of electric arc furnace during direct reduced iron melting. 2081-2093A
- Directional solidification**
- Modeling of primary spacing selection in dendrite arrays during directional solidification. 223-233B
- A new unidirectional solidification method to study gray cast iron. 235-241B
- Cellular array morphology during directional solidification. Elevated temperature strength and room-temperature toughness of directionally solidified Ni-33Al-33Cr-1Mo. 1229-1243A
- Hydrogen Evolution during Directional Solidification and Its Effect on Porosity Formation in Aluminum Alloys. 1385-1397A
- Solidification Thermal Parameters Affecting the Columnar-to-Equiaxed Transition. 2067-2072A
- Directionally solidified eutectics**
- Effect of directionally solidified microstructures on the room-temperature fracture-toughness properties of Ni-33(at. pct)Al-33Cr-1 Mo and Ni-33(at. pct)Al-31 Cr-3Mo eutectic alloys grown at different solidification rates. 2107-2118A
- Dislocation density**
- Determination of dislocation densities in Hcp metals from X-ray diffraction line-broadening analysis. 597-612A
- Distribution of c- and a-dislocations in tubes of Zr alloys. 859-865A
- Observations of room-temperature creep recovery in titanium alloys. 867-874A
- Dislocation density, Composition effects**
- Creep strength of magnesium-based alloys. 891-898A
- Dislocation density, Deformation effects**
- Comparative study of the impact response and microstructure of 3041 stainless steel with and without prestrain. 875-882A
- Dislocation mobility**
- Grain-boundary diffusion by vacancy mechanism in  $\alpha$ -Ti and  $\alpha$ -Zr. 791-796A
- Interfacial deformation mechanisms in hexagonal-close-packed metals. 801-807A
- Twins as barriers to basal slip in hexagonal-close-packed metals. 809-812A
- Nonbasal deformation modes of Hcp metals and alloys: role of dislocation source and mobility. 813-822A
- Molecular dynamics simulation of  $\langle c+a \rangle$  dislocation core structure in hexagonal-close-packed metals. 823-829A
- Transmission electron microscopy investigation of  $\langle c+a \rangle$  dislocations in Mg and  $\alpha$ -solid solution Mg-Li alloys. 851-858A
- Origins of internal structure in massive transformation products. 2347-2351A
- Static and in-situ high-resolution transmission electron micro-



- copy investigations of the atomic structure and dynamics of massive transformation interfaces in a Ti-Al alloy.  
Jan Van Der Merwe and the theory of epitaxy  
Why do dislocations assemble into interfaces in epitaxy as well as in crystal plasticity? To minimize free energy.
- Dislocations**  
Creep and microstructure of magnesium-aluminum-calcium based alloys. 567-574A  
Three-dimensional investigation of long-range internal stresses in a single crystal deforming by nonsymmetrical slip. 591-596A  
Erratum: The Effects of deformation and pre-heat-treatment on abnormal grain growth in RENE 88 superalloy. 713A  
Atomic-scale modeling of dislocations and related properties in the hexagonal-close-packed metals. 721-733A  
First-principles investigation of perfect and diffuse antiphase boundaries in hcp-based Ti-Al alloys. 735-741A  
Subnanometer-scale chemistry and structure of  $\alpha$ -iron/molybdenum nitride heterophase interfaces. 2317-2326A  
Misfit dislocations in epitaxy. 2475-2483A  
Reciprocal-space formulation and prediction of misfit accommodation in rigid and strained epitaxial systems. 2485-2494A  
Fatigue Deformation-Induced Response in a Superduplex Stainless Steel. 3433-3442A  
Interfacial Dislocation Networks Strengthening a Fourth-Generation Single-Crystal TMS-138 Superalloy. 3741-3746A
- Dispersion**  
High Temperature SANS Experiments on Nb(C,N) and MnS Precipitates in HSLA Steel. 1883-1891A
- Dispersion hardening alloys, Heat treatment**  
Annealing behavior of alumina dispersion-strengthened copper strips rolled under different conditions. 1605-1616A
- Dispersion hardening alloys, Powder technology**  
Origin of porosity in oxide-dispersion-strengthened alloys produced by mechanical alloying. 2713-2718A
- Dissimilar materials, Joining**  
Phase equilibria of the ternary Ni-Cr-Zr system and interfacial reactions in the Ni-Cr/Zr couples. 995-1002A
- Dissimilar metals, Joining**  
Joining of NiAl to Iron-Based Alloys by Reactive Casting. 2073-2080A
- Dissimilar metals, Welding**  
Missed Joint Induced by Thermoelectric Magnetic Field in Electron-Beam Welding Dissimilar Metals-Experiment and Scale Analysis. 765-773B
- Dissociation**  
Kinetics of formation and dissociation of  $\text{Na}_2\text{SiF}_6$ . 129-136B
- Dissolution**  
Thermodynamic behavior of nickel in  $\text{CaO-SiO}_2\text{-Fe}_2\text{O}_3$  slag. Numerical simulation of dendrite white spot formation during vacuum arc remelting of INCONEL 718. 443-454A  
Dissolution Kinetics of NbC Particles in the Heat-Affected Zone of Type 347 Austenitic Stainless Steel. 2031-2042A  
Effect of Fcc-Hcp Phase Transformation Produced by Isothermal Aging on the Corrosion Resistance of a Co-27Cr-5Mo-0.05C Alloy. 2229-2235A
- Distortion**  
Thermal debinding modeling of mass transport and deformation in powder-injection molding compact. 477-488B
- Doping**  
Dopant Particle Characterization and Bubble Evolution in Aluminum-Potassium-Silicon-Doped Molybdenum Wire. 3349-3356A
- Drag (hindrance)**  
Measurement and Computation of Drag Forces in Thermo-gravimetric Studies. 891-896B
- Dual phase steels, Mechanical properties**  
Effect of Martensite Content on Friction and Oxidative Wear Behavior of 0.42 Pct Carbon Dual-Phase Steel. 3479-3488A
- Ductile fracture**  
Effect of Prestrain on Stretch-Zone Formation during Ductile Fracture of Cu-Strengthened High-Strength Low-Alloy Steels. 3731-3740A
- Ductility**  
Characterization of a friction-stir-welded aluminum alloy 6013. Hydrogen embrittlement of nickel-titanium alloy in biological environment. 489-498B  
Sliding wear of austenitic and austenitic-ferritic stainless steels. Communication: Effect of boron on the hot ductility of Nb-containing steel. 495-501A  
Communication: Microstructures and mechanical properties of  $(\text{Ir,Rh})_{75}\text{Nb}_{15}\text{Ni}_{10}$  alloys. 613-624A  
The influence of the stress state on the plasticity of transformation induced plasticity-aided steel. 701-704A  
Flow Stress and Ductility of Duplex Stainless Steel during High-Temperature Torsion Deformation. 1281-1283A  
Use of Weibull Statistics to Quantify Property Variability in TiAl Alloys. 1659-1667A  
Young's Modulus and Mechanical Properties of Ti-29Nb-13Ta-4.6Zr in Relation to  $\alpha'$  Martensite. 1931-1938A  
Pressure Effects on Flow and Fracture of Be-Al Alloys. 3127-3136A  
Communication: Strengthening of Virgin Martensite through Cryogenic Deformation. 3137-3144A  
3555-3564A  
3576-3578A
- Ductility, Environmental effects**  
Hydrogen-assisted deformation and fracture behaviors of Al 8090. 1755-1763A
- Ductility, Microstructural effects**  
Transmission electron microscopy investigation of  $\langle c + a \rangle$  dislocations in Mg and  $\alpha$ -solid solution Mg-Li alloys. 851-858A
- Ductility, Size effects**  
Communication: Specimen Size Effects and Ductile Fracture of HY 100 Steel. 3293-3295A
- Duplex stainless steels, Mechanical properties**  
Influence of elastic and plastic anisotropy on the flow behavior in a duplex stainless steel. 57-71A  
Sliding wear of austenitic and austenitic-ferritic stainless steels. Fatigue Deformation-Induced Response in a Superduplex Stainless Steel. 613-624A  
3433-3442A
- Duplex stainless steels, Metal working**  
Flow Stress and Ductility of Duplex Stainless Steel during High-Temperature Torsion Deformation. 1931-1938A
- Duplex stainless steels, Welding**  
Decomposition of ferrite in commercial superduplex stainless steel weld metals; microstructural transformations above 700°C. 1009-1018A
- Dynamic recrystallization**  
Deformation bands and the formation of grain boundaries in a superplastic aluminum alloy. 279-290A  
Elevated-temperature deformation at forming rates of  $10^{-2}$  to  $10^2 \text{ s}^{-1}$ . 345-362A  
Formation of white layers in steels by machining and their characteristics. 1245-1254A  
Inferring Dynamic Recrystallization in Ferrite using the Kinetics of Static Recrystallization. 1893-1900A  
Flow Stress and Ductility of Duplex Stainless Steel during High-Temperature Torsion Deformation. 1931-1938A
- Edge dislocations**  
Molecular dynamics simulation of  $\langle c + a \rangle$  dislocation core structure in hexagonal-close-packed metals. 823-829A
- Elastic anisotropy**  
On Composite-Structure Weaknesses: Part I. Simulation, Properties, and Numerical Approach. 2205-2215A  
On Composite-Structure Weaknesses: Part II. Computer Experiments, Identification, and Correlation. 2217-2227A
- Elastic anisotropy, Microstructural effects**  
Influence of elastic and plastic anisotropy on the flow behavior in a duplex stainless steel. 57-71A
- Elastic constants**  
Effect of pressure on zone-center phonons in hexagonal-close-packed metals. 743-747A
- Elastic deformation**  
Inertia Welding Nickel-Based Superalloy: Part II. Residual Stress Characterization. 3227-3234A
- Elasticity**  
Shape Memory Behavior of FeNiCoTi Single and Polycrystals. Microscale Elastic Strain Evolution Following Damage in Ti-SiC Composites. 3661-3672A  
3839-3845A
- Electric arc furnaces**  
Process dynamics of electric arc furnace during direct reduced iron melting. 187-199B
- Electric induction furnaces**  
A new unidirectional solidification method to study gray cast iron. 235-241B
- Electrodeposition**  
Microstructural and mechanical properties investigation of electrodeposited and annealed LIGA nickel structures. 539-554A
- Electrolysis**  
Communication: The solubility of  $\text{Fe}_2\text{O}_3$  in cryolite-alumina melts. 140-142B  
Production of Niobium Powder by Direct Electrochemical Reduction of Solid  $\text{Nb}_2\text{O}_5$  in a Eutectic  $\text{CaCl}_2\text{-NaCl}$  Melt. 685-693B
- Electrolytes**  
Thermodynamics of liquid Al-Na alloys determined by using  $\text{CaF}_2$  solid electrolyte. 577-587B
- Electromagnetic fields**  
A New Method for Three-Dimensional Numerical Simulation of Electromagnetic and Fluid-Flow Phenomena in Electromagnetic Separation of Inclusions from Liquid Metal. 775-785B
- Electron beam melting**  
Carbide formation in alloy 718 during electron-beam solid free-form fabrication. 2559-2567A
- Electron beam processing**  
Correlation of Microstructure with Wear and Fracture Properties of Two-Layered VC/Ti-6Al-4V Surface Composites Fabricated by High-Energy Electron-Beam Irradiation. 3173-3185A
- Electron beam welding**  
Missed Joint Induced by Thermoelectric Magnetic Field in Electron-Beam Welding Dissimilar Metals-Experiment and Scale Analysis. 765-773B  
Electron-beam welding behavior in Mg-Al-based alloys. The Influence of Minor Elements on the Weldability of an INCONEL 718-Type Superalloy. 1461-1473A  
Residual stresses in a welded superalloy disc: characterization using synchrotron diffraction and numerical process modeling. 2005-2017A  
2921-2931A
- Electron diffraction**  
Dislocation microstructure and internal-stress measurements by convergent-beam electron diffraction on creep-deformed Cu and Al. 311-317A  
Advances in deformation twin characterization using electron backscattered diffraction data. 949-954A  
Deformation twinning in polycrystalline Zr: insights from electron backscattered diffraction characterization. 955-963A
- Electrorefining**  
Communication: The solubility of  $\text{Fe}_2\text{O}_3$  in cryolite-alumina melts. 140-142B  
Thermodynamics of liquid Al-Na alloys determined by using

- CaF<sub>2</sub> solid electrolyte. 577-587B
- Electrowinning**
- Communication: Electroreduction of cobalt from sulfate solutions—effect of substrate and background MgSO<sub>4</sub>. 137-140B
- Copper Electrowinning using Spouted-Bed Electrodes: Part I. Experiments with Oxygen Evolution or Matte Oxidation at the Anode. 669-676B
- Copper Electrowinning using Spouted-Bed Electrodes: Part II. Copper Electrowinning with Ferrous Ion oxidation as the Anodic Reaction. 677-683B
- Elongation**
- Improvement in mechanical properties of dental cast Ti-6Al-7Nb by thermochemical processing. 503-510A
- Communication: Examination on the aging and tensile properties of Al-Zn-Mg/Al<sub>3</sub>Ni eutectic composite. 707-711A
- Symmetry-breaking transitions in equilibrium shapes of coherent precipitates: effect of elastic anisotropy and inhomogeneity. 1083-1090A
- Large Self-Thermal-Plastic Deformation in a NiTi Shape-Memory Alloy Fiber-Actuated Aluminum Metal-Matrix Composite. 3535-3540A
- Embedding**
- A study of the Pb/Al (100) interfacial energy. 2569-2572A
- Embrittlement**
- Deoxidation of molybdenum during vacuum sintering. 657-664A
- Intergranular stress corrosion cracking behavior of types 308 and 316 stainless steel weld metals in a simulated boiling water reactor environment. 2907-2919A
- Energy consumption**
- Copper Electrowinning using Spouted-Bed Electrodes: Part I. Experiments with Oxygen Evolution or Matte Oxidation at the Anode. 669-676B
- Engine components, Materials selection**
- The effect of constraint-induced normal stress on the failure of notched TiAl components. 417-426A
- Epitaxial growth**
- Misfit dislocations in epitaxy. 2475-2483A
- Reciprocal-space formulation and prediction of misfit accommodation in rigid and strained epitaxial systems. 2485-2494A
- Epitaxy**
- Jan Van Der Merwe and the theory of epitaxy. 2473-2474A
- Analysis of the Cu-3 Wt pct Ti cellular interphase boundary by various models. 2495-2505A
- The cellular interlamellar and growth-front interphase boundaries in Cu-3 Wt pct Ti. 2507-2518A
- Why do dislocations assemble into interfaces in epitaxy as well as in crystal plasticity? To minimize free energy. 2519-2539A
- Equal channel angular extrusion**
- Equal-channel angular extrusion of beryllium. 965-972A
- Equal channel angular pressing**
- Erratum: Shear principal, and equivalent strains in equal-channel angular deformation. 467A
- Structural evolution of a strip-cast Al alloy sheet processed by continuous equal-channel angular pressing. 665-673A
- Microstructure evolution in Zr under equal channel angular pressing. 973-980A
- Communication: Thermal stability and microstructural evolution in ultrafine-grained nickel after equal-channel angular pressing (ECAP). 1865-1868A
- An Investigation of Microstructure and Grain-Boundary Evolution during ECA Pressing of Pure Aluminum. 2173-2184A
- Enhancement of Strength and Superplasticity in a 6061 Al Alloy Processed by Equal-Channel-Angular-Pressing. 3155-3164A
- Equiaxed structure**
- A three-phase model of hydrogen pore formation during the equiaxed dendritic solidification of aluminum-silicon alloys. 209-221B
- The production of ultrafine ferrite in low-carbon steel by strain-induced transformation. 1019-1026A
- Symmetry-breaking transitions in equilibrium shapes of coherent precipitates: effect of elastic anisotropy and inhomogeneity. 1083-1090A
- Solidification Thermal Parameters Affecting the Columnar-to-Equiaxed Transition. 2107-2118A
- The Kinetics of Static Globularization of Ti-6Al-4V. 3527-3534A
- Eutectic reactions**
- Production of Niobium Powder by Direct Electrochemical Reduction of Solid Nb<sub>2</sub>O<sub>5</sub> in a Eutectic CaCl<sub>2</sub>-NaCl Melt. 685-693B
- Eutectics**
- Rayleigh-Benard convection during solidification of an eutectic solution cooled from the top. 605-612B
- Time-resolved X-ray imaging of aluminum alloy solidification processes. 613-623B
- Microstructural characteristics of Ni-Sb eutectic alloys under substantial undercooling and containerless solidification conditions. 1221-1228A
- Eutectics, Directional solidification**
- Communication: Minimizing Segregation during the Controlled Directional Solidification of Dendritic Alloys. 3876-3881A
- Evaporation**
- The Critical Pressure and Impeding Pressure of Al Evaporation during Induction Skull Melting Processing of TiAl. 3249-3253A
- Exothermic reactions**
- Joining of NiAl to Iron-Based Alloys by Reactive Casting. 2073-2080A
- Microstructure/processing relationships in reaction-synthesized titanium aluminum intermetallic matrix composites. 2747-2753A
- Extractive metallurgy**
- Kinetics of formation and dissociation of Na<sub>2</sub>SIF<sub>6</sub>. 129-136B
- Rare Earth Extraction and Separation from Mixed Bastnaesite-Monazite Concentrate by Stepwise Carbochlorination-Chemical Vapor Transport. 661-668B
- Extrusions, Corrosion**
- Effect of grain boundary characteristics on intergranular corrosion resistance of 6061 aluminum alloy extrusion. 2891-2898A
- Extrusions, Mechanical properties**
- Quantitative characterization of three-dimensional damage evolution in a wrought Al-alloy under tension and compression. 2599-2606A
- Face centered cubic lattice**
- A new bcc-fcc orientation relationship observed between ferrite and austenite in solidification structures of steels. 5-15A
- Communication: Comments on a recent infinitesimal-deformation approach to martensite crystallography. 203A
- Author's reply [to Comments on a recent infinitesimal-deformation approach to martensite crystallography]. 204A
- Thermodynamic description of the Cu-Al-Sn system in the copper-rich corner. 1639-1648A
- Communication: A New Face-Centered-Cubic Superlattice Structure in Rapidly Solidified Cu-4 Wt Pct Ti Alloy and Its Relevance to the Ordering Process in Ni-Mo and Other 1/2 0 Ordering Alloys. 3573-3576A
- Rapid Solidification of Martensitic Stainless Steel Atomized Droplets. 3755-3760A
- Failure analysis**
- The effect of constraint-induced normal stress on the failure of notched TiAl components. 417-426A
- Effects of high rates of loading on the deformation behavior and failure mechanisms of hexagonal close-packed metals and alloys. 927-935A
- Computational modeling of through-thickness dynamic impact response in cross-rolled Ti-6Al-4V plates. 937-947A
- Toughness-strength relations in the overaged 7449 Al-based alloy. 1125-1136A
- Fatigue (materials)**
- The fracture toughness and toughening mechanisms of nickel-base wear materials. 33-56A
- Fatigue crack initiation and propagation of binder-treated powder metallurgy steels. 73-81A
- Phenomenological observations on mechanical and corrosion properties of thixoformed 357 alloys: a comparison with permanent mold cast 357 alloys. 1399-1412A
- Fatigue-Crack-Propagation Thresholds in a Nickel-Base Superalloy at High Frequencies and Temperatures. 1949-1962A
- Effect of Prolonged Isothermal Exposure on Elevated-Temperature, Time-Dependent Fatigue-Crack Propagation in INCONEL Alloy 783. 3465-3478A
- Evaluation of the Fatigue Behavior of Ductile Irons with Various Matrix Microstructures. 3719-3730A
- Fatigue (materials), Composition effects**
- Microstructural and fracture characterization of Nb-Cr-Ti mechanically alloyed materials. 401-416A
- Fatigue failure**
- Communication: Conducting High-Cycle Fatigue Strength Step Tests on Gamma TiAl. 3871-3874A
- Fatigue life**
- Improvement in mechanical properties of dental cast Ti-6Al-7Nb by thermochemical processing. 503-510A
- Communication: Infrared imaging during low-cycle fatigue of HR-120 alloy. 1287-1292A
- Carbide formation in alloy 718 during electron-beam solid free-form fabrication. 2559-2567A
- Fatigue limit**
- Communication: High-cycle fatigue of an investment cast, Be-Al metal matrix composite. 1862-1865A
- Improvement of Gigacycle Fatigue Properties by Modified Ausforming in 1600 and 2000 MPA-Class Low-Alloy Steels. 3421-3431A
- Fatigue strength**
- Communication: Conducting High-Cycle Fatigue Strength Step Tests on Gamma TiAl. 3871-3874A
- Fatigue strength, Heating effects**
- Tensile and fatigue properties of 17-4 PH stainless steel at high temperatures. 1715-1724A
- Fatigue strength, Microstructural effects**
- Influence of microstructure on high-cycle fatigue of Ti-6Al-4V: bimodal vs. lamellar structures. 899-918A
- Fatigue tests**
- Improvement of Gigacycle Fatigue Properties by Modified Ausforming in 1600 and 2000 MPA-Class Low-Alloy Steels. 3421-3431A
- Evaluation of the Fatigue Behavior of Ductile Irons with Various Matrix Microstructures. 3719-3730A
- Feeding**
- Development of New Feeding-Distance Rules Using Casting Simulation: Part I. Methodology. 731-740B
- Development of New Feeding-Distance Rules Using Casting Simulation: Part II. The New Rules. 741-755B
- Ferrite**
- The production of ultrafine ferrite in low-carbon steel by strain-induced transformation. 1019-1026A
- Comprehensive microstructural characterization in modified 9Cr-1Mo ferritic steel by ultrasonic measurements. 1617-1626A
- Inferring Dynamic Recrystallization in Ferrite using the Kinetics of Static Recrystallization. 1893-1900A
- Lattice Orientation Relationship between the M2C Carbide and the Ferrite Matrix in the M50NiL Bearing Steel. 1963-1969A
- Formation and Annealing Behavior of Nanocrystalline Ferrite in Fe-0.89C Spheroidite Steel Produced by Ball Milling. 2195-2203A

- The production of ultrafine ferrite during hot torsion testing of a 0.11 Wt pct C steel. 2985-2993A
- Ferritic stainless steels, Casting**  
Texture enhancement by inoculation during casting of ferritic stainless steel strip. 1499-1507A
- Ferritic stainless steels, Phase transformations**  
Modeling  $M_{23}C_6$  Precipitation in Niobium-Alloyed Ferritic Stainless Steel. 3339-3347A
- Ferritic transformations**  
Hot rolling texture development in CMnCrSi dual-phase steels. An integrated computer model with applications for austenite-to-ferrite transformation during hot deformation of Nb-microalloyed steels. 1091-1102A  
Isothermal transformations in an Fe-9 pct Ni alloy. The production of ultrafine ferrite during hot torsion testing of a 0.11 Wt pct C steel. 1509-1520A  
Modeling The Austenite-Ferrite Isothermal Transformation in an Fe-C Binary System and Experimental Verification. 2425-2431A  
Austenite Decomposition to Carbide-Rich Products in Fe-0.30C-6.3W. 2985-2993A  
3111-3115A  
3619-3633A
- Ferromagnetism**  
Massive transformation and the formation of the ferromagnetic  $L_{12}$  phase in manganese-aluminum-based alloys. 2413-2423A
- Ferrous alloys, Casting**  
Joining of NiAl to Iron-Based Alloys by Reactive Casting. 2073-2080A
- Ferrous alloys, Chemical analysis**  
On the Nature of the Electrochemically Synthesized Hard Fe-0.96 Mass Pct C Alloy Film. 921-927B
- Ferrous alloys, Coatings**  
Correlation of microstructure and wear resistance of ferrous coatings fabricated by atmospheric plasma spraying. 2933-2945A
- Ferrous alloys, Composite materials**  
A novel technique for manufacturing metal-bonded Nd-Fe-B magnets by squeeze casting. 637-646A  
Communication: Reduced critical solidification front velocity of particle engulfment due to an interface active solute in the liquid metal. 1869-1873A
- Ferrous alloys, Crystal growth**  
The Microstructure and Recrystallization of Flow-Formed Oxide-Dispersion-Strengthened Ferritic Alloy: Part II. Recrystallization Behavior. 3787-3794A
- Ferrous alloys, Mechanical properties**  
Fatigue crack initiation and propagation of binder-treated powder metallurgy steels. 73-81A  
Communication: Effect of carbon addition on tribological properties of Fe-Al alloys. 1292-1295A  
Some Observations of the Influence of  $\delta$ -Ferrite Content on the Hardness, Galling Resistance, and Fracture Toughness of Selected Commercially Available Iron-Based Hardfacing Alloys. 3403-3419A  
Shape Memory Behavior of FeNiCoTi Single and Polycrystals The Microstructure and Recrystallization of Flow-Formed Oxide-Dispersion-Strengthened Ferritic Alloy: Part I. Deformation Structure. 3661-3672A  
3777-3785A
- Ferrous alloys, Microstructure**  
A new bcc-fcc orientation relationship observed between ferrite and austenite in solidification structures of steels. 5-15A  
Subnanometer-scale chemistry and structure of  $\alpha$ -iron/molybdenum nitride heterophase interfaces. 2317-2326A
- Ferrous alloys, Phase transformations**  
Communication: Comments on a recent infinitesimal-deformation approach to martensite crystallography. 203A  
Author's reply [to Comments on a recent infinitesimal-deformation approach to martensite crystallography]. 204A  
Relationship between Austenite Dislocation Density Introduced during Thermal Cycling and  $M_s$  Temperature in an Fe-17 Wt Pct Mn Alloy. 1913-1917A  
Mechanisms of the massive transformation. 2285-2297A  
Critical limit for massive transformation. 2299-2308A  
Simulation of ferrite growth in continuously cooled low-carbon iron alloys. 2309-2316A  
Massive transformation and absolute stability. 2337-2345A  
Isothermal transformations in an Fe-9 pct Ni alloy. 2425-2431A  
Comparison of interfacial structure-related mechanisms in diffusional and martensitic transformations. 2541-2547A  
Precipitate Formation in Low-Temperature Nitrided Cold-Rolled Fe<sub>94</sub>Ni<sub>4</sub>Ti<sub>2</sub> and Fe<sub>93</sub>Ni<sub>4</sub>Cr<sub>3</sub> Films. 3075-3087A  
Austenite Decomposition to Carbide-Rich Products in Fe-0.30C-6.3W. 3619-3633A
- Ferrous alloys, Phases (state of matter)**  
Diffusion Studies in the  $\beta$  ( $B_{27}$ ),  $\beta'$  (Bcc), and  $\gamma$  (Fcc) Fe-Ni-Al Alloys at 1000°C. 3375-3392A
- Ferrous alloys, Powder technology**  
Origin of porosity in oxide-dispersion-strengthened alloys produced by mechanical alloying. 2713-2718A  
Evolution of Submicrocrystalline Iron Containing Dispersed Oxides under Mechanical Milling Followed by Consolidation. 3241-3248A  
Structure of a Fe-Cr-Mn-Mo-N Alloy Processed by Mechanical Alloying. 3273-3278A
- Ferrous alloys, Reactions (chemical)**  
Communication: Manganese Deoxidation Equilibrium in Liquid Fe-36 Pct Ni Alloy at 1773 K. 930-932B
- Ferrous alloys, Welding**  
Modeling of laser keyhole welding. I. Mathematical modeling, numerical methodology, role of recoil pressure, multiple reflections, and free surface evolution. 1817-1830A
- Fiber composites, Casting**  
Interfacial reactions in aluminosilicate short fiber-reinforced aluminum matrix composites. 2755-2761A
- Fiber composites, Mechanical properties**  
Creep processes in magnesium alloys and their composites. 883-889A  
Evolution of fiber fragmentation in a short-fiber-reinforced metal-matrix model composite during tensile creep deformation-an acoustic emission study. 1549-1557A  
On Composite-Structure Weaknesses: Part I. Simulation, Properties, and Numerical Approach. 2205-2215A  
On Composite-Structure Weaknesses: Part II. Computer Experiments, Identification, and Correlation. 2217-2227A  
Micromechanical modeling of unidirectional continuous sigma fiber-reinforced Ti-6Al-4V subjected to transverse tensile loading. 3045-3054A  
Normalized Diagrams for Micromechanical Estimates of the Elastic Response of Composite Materials. 3187-3199A  
Large Self-Thermal-Plastic Deformation in a NiTi Shape-Memory Alloy Fiber-Actuated Aluminum Metal-Matrix Composite. 3535-3540A
- Filler metal, Materials selection**  
Infrared repair brazing of 403 stainless steel with a nickel-based braze alloy. 1765-1773A
- Finite element method**  
Bubble formation and detachment on nonwetted surfaces. 155-162B  
A Study on Heat Source Equations for the Prediction of Weld Shape and Thermal Deformation in Laser Microwelding. 757-764B  
A New Method for Three-Dimensional Numerical Simulation of Electromagnetic and Fluid-Flow Phenomena in Electromagnetic Separation of Inclusions from Liquid Metal. 775-785B  
Finite element modeling of the morphology of  $\beta$  to  $\alpha$  phase transformation in Ti-6Al-4V alloy. 1027-1040A  
Shrinkage and splitting of microcracks under pressure simulated by the finite-element method. 1117-1124A  
Artificial Neural Network and Finite Element Modeling of Nanoindentation Tests. 1939-1947A  
Residual stresses in a welded superalloy disc: characterization using synchrotron diffraction and numerical process modeling. 2921-2931A  
A Precision On-Line Model for the Prediction of Roll Force and Roll Power in Hot-Strip Rolling. 3255-3272A  
Change of Critical Events of Cleavage Fracture with Variation of Microscopic Features of Low-Alloy Steels. 3393-3402A  
The Kinetics of Static Globularization of Ti-6Al-4V. 3527-3534A
- Flame spraying**  
Near-nanostructured WC-18 pct co coatings with low amounts of non-WC carbide phase: Part I. Synthesis and characterization. 145-157A  
Near-nanostructured WC-18 pct co coatings with low amounts of non-WC carbide phase: Part II. Hardness and resistance to sliding and abrasive wear. 159-164A
- Flotation**  
Bubble formation and detachment on nonwetted surfaces. 155-162B  
Mathematical modeling and computer simulation of the rotating impeller particle flotation process: Part I. Fluid flow. 297-303B  
Mathematical modeling and computer simulation of the rotating impeller particle flotation process: Part II. Particle agglomeration and flotation. 305-314B
- Flow**  
Structural evolution of a strip-cast Al alloy sheet processed by continuous equal-channel angular pressing. 665-673A
- Flow, Pressure effects**  
Pressure Effects on Flow and Fracture of Be-Al Alloys. 3555-3564A
- Flow rate**  
Molten Wood's-Metal Flow in a Cylindrical Bath Agitated by Cold Bottom Gas Injection. 695-702B
- Fluid dynamics**  
Simulation of the submerged energy nozzle-mold water model system using laser-optical and computational fluid dynamics methods. 163-172B  
Computational fluid-dynamics modeling of the hydrodynamics of fluidization in the sand surrounding a lost-foam casting pattern. 565-575B  
Correction to "Simulation of the submerged energy nozzle-mold water model systems using laser optical and computational fluid dynamics methods" 639B
- Fluid flow**  
Mathematical modeling and computer simulation of the rotating impeller particle flotation process: Part I. Fluid flow. 297-303B  
Communication: Physical modeling of the effects of thermal buoyancy driven flows in aluminum casters. 321-324B  
Rayleigh-Benard convection during solidification of an eutectic solution cooled from the top. 605-612B  
A New Method for Three-Dimensional Numerical Simulation of Electromagnetic and Fluid-Flow Phenomena in Electromagnetic Separation of Inclusions from Liquid Metal. 775-785B  
Rheology and microstructure of semi-solid aluminum alloys compressed in the drop-forge viscometer. 2737-2746A
- Fluidized bed electrodes**  
Copper Electrowinning using Spouted-Bed Electrodes: Part I. Experiments with Oxygen Evolution or Matte Oxidation at the Anode. 669-676B  
Copper Electrowinning using Spouted-Bed Electrodes: Part II. Copper Electrowinning with Ferrous Ion oxidation as the Anodic Reaction. 677-683B
- Fluorination**  
Rare Earth Extraction and Separation from Mixed Bastnaesite-Monazite Concentrate by Stepwise Carbochlorination-Chemical Vapor Transport. 661-668B
- Fluorite**



- The Effect of  $\text{CaF}_2$  on the Viscosities and Structures of  $\text{CaO-SiO}_2\text{-MgO-CaF}_2$  Slags. 723-729B
- Fluxes**
- Stability of silico-ferrite of calcium and aluminum (SFCA) in air-solid solution limits between 1240°C and 1390°C and phase relationships within the  $\text{Fe}_2\text{O}_3\text{-CaO-Al}_2\text{O}_3\text{-SiO}_2$  (FCAS) system. 79-89B
- Fly ash, Composite materials**
- Age-hardening characteristics of aluminum alloy-hollow fly ash composites. 1541-1547A
- Foamed metals**
- An investigation of the microstructure and strength of open-cell 6101 aluminum foams. 1413-1427A
- Foamed metals, Phases (state of matter)**
- The Optimum Wetting Angle for the Stabilization of Liquid-Metal Foams by Ceramic Particles: Experimental Simulations. 3285-3292A
- Foamed metals, Physical properties**
- Effects of Macroscopic Pores on the Damping Behavior of Foamed Commercially Pure Aluminum. 3565-3568A
- Foaming**
- Communication: Foaming behavior of slags. 499-501B
- In-situ formation of SiC-reinforced Al-Si alloy composites using methane gas mixtures. 543-550B
- Foil, Mechanical properties**
- Room-temperature mechanical properties of cold-rolled thin foils of binary, stoichiometric  $\text{Ni}_3\text{Al}$ . 2607-2613A
- Formability**
- Structural evolution of a strip-cast Al alloy sheet processed by continuous equal-channel angular pressing. 665-673A
- Communication: Effect of boron on the hot ductility of Nb-containing steel. 701-704A
- Role of yield criteria and hardening laws in the prediction of forming limit diagrams. 1363-1371A
- Communication: Interpretation of flow instability using dynamic material modeling. 1569-1572A
- Flow Stress and Ductility of Duplex Stainless Steel during High-Temperature Torsion Deformation. 1931-1938A
- Mechanical anisotropy and grain interaction in recrystallized aluminum. 2635-2648A
- Forming**
- The relationship between grain size and the surface roughening behavior of Al-Mg alloys. 2883-2889A
- Forming dies, Design**
- Microstructural gradients in the superplastic forming of Ti-6Al-4V. 93-100A
- Foundry practice**
- Mathematical modeling and computer simulation of the rotating impeller particle flotation process: Part I. Fluid flow. 297-303B
- Mathematical modeling and computer simulation of the rotating impeller particle flotation process: Part II. Particle agglomeration and flotation. 305-314B
- Development of New Feeding-Distance Rules Using Casting Simulation: Part I. Methodology. 731-740B
- Development of New Feeding-Distance Rules Using Casting Simulation: Part II. The New Rules. 741-755B
- Modeling of the Continuous Casting of Steel-Past, Present, and Future. 795-812B
- Foundry sands**
- Computational fluid-dynamics modeling of the hydrodynamics of fluidization in the sand surrounding a lost-foam casting pattern. 565-575B
- Fractography**
- Cracking in  $\gamma\text{-TiAl}$  due to high speed particle impact. 581-589A
- Fatigue-Crack-Propagation Thresholds in a Nickel-Base Superalloy at High Frequencies and Temperatures. 1949-1962A
- Effect of Overaging and Particle Size on Tensile Deformation and Fracture of Particle-Reinforced Aluminum Matrix Composites. 3861-3869A
- Fracture mechanics**
- The Influence of Microstructure and Environment on the Crack Growth Behavior of Powder Metallurgy Nickel Superalloy RR1000. 3165-3172A
- Fracture strength**
- The effect of constraint-induced normal stress on the failure of notched TiAl components. 417-426A
- Fracture toughness**
- The fracture toughness and toughening mechanisms of nickel-base wear materials. 33-56A
- Microstructural and fracture characterization of Nb-Cr-Ti mechanically alloyed materials. 401-416A
- Effect of directionally solidified microstructures on the room-temperature fracture-toughness properties of Ni-33(at. pct)Al-33Cr-1 Mo and Ni-33(at. pct)Al-31 Cr-3Mo eutectic alloys grown at different solidification rates. 597-612A
- Toughness-strength relations in the overaged 7449 Al-based alloy. 1125-1136A
- Crack-initiation toughness and crack-arrest toughness in advanced 9 pct Ni steel welds containing local brittle zones. 2615-2622A
- Correlation of Microstructure with Wear and Fracture Properties of Two-Layered VC/Ti-6Al-4V Surface Composites Fabricated by High-Energy Electron-Beam Irradiation. 3173-3185A
- Some Observations of the Influence of  $\delta\text{-Ferrite}$  Content on the Hardness, Galling Resistance, and Fracture Toughness of Selected Commercially Available Iron-Based Hardfacing Alloys. 3403-3419A
- Measuring the Fracture Toughness of Molybdenum-0.5 pct Titanium-0.1 pct Zirconium and Oxide Dispersion-Strengthened Molybdenum Alloys using Standard and Subsize Bend Specimens. 3685-3707A
- Effect of Prestrain on Stretch-Zone Formation during Ductile Fracture of Cu-Strengthened High-Strength Low-Alloy Steels. 3731-3740A
- Fracture toughness, Environmental effects**
- Fracture toughness of alloy 690 and EN52 welds in air and water. 1725-1735A
- Fracture toughness, Heating effects**
- Hydrogen-assisted deformation and fracture behaviors of Al 8090. 1755-1763A
- Fractures**
- Microscale Elastic Strain Evolution Following Damage in Ti-SiC Composites. 3839-3845A
- Fracturing**
- Improvement of Gigacycle Fatigue Properties by Modified Austempering in 1600 and 2000 MPA-Class Low-Alloy Steels. 3421-3431A
- Effect of Overaging and Particle Size on Tensile Deformation and Fracture of Particle-Reinforced Aluminum Matrix Composites. 3861-3869A
- Fracturing, Pressure effects**
- Pressure Effects on Flow and Fracture of Be-Al Alloys. 3555-3564A
- Freeform fabrication**
- Carbide formation in alloy 718 during electron-beam solid free-form fabrication. 2559-2567A
- Friction**
- Effect of Martensite Content on Friction and Oxidative Wear Behavior of 0.42 Pct Carbon Dual-Phase Steel. 3479-3488A
- Friction stir welding**
- Characterization of a friction-stir-welded aluminum alloy 6013. Parameters controlling microstructure and hardness during friction-stir welding of precipitation-hardenable aluminum alloy 6063. 489-498B
- 625-635A
- Functionally gradient materials, Powder technology**
- Fabrication and characterization of Ti-TiB<sub>2</sub> functionally graded material system. 681-685A
- Fused salts**
- Interrupted bonding of medium-carbon steels. 1475-1485A
- Fusion bonding**
- Joining of NiAl to Iron-Based Alloys by Reactive Casting. 2073-2080A
- Fusion welding**
- Communication: Comparative Welding Study of Metal Matrix Composites with the MIG Welding Process, using Direct and Indirect Electric Arc. 932-937B
- Electron-beam welding behavior in Mg-Al-based alloys. 1461-1473A
- Galling**
- Some Observations of the Influence of  $\delta\text{-Ferrite}$  Content on the Hardness, Galling Resistance, and Fracture Toughness of Selected Commercially Available Iron-Based Hardfacing Alloys. 3403-3419A
- Galvanizing**
- Communication: On the ternary phase in the zinc-rich corner of the Zn-Fe-Al system at temperatures below 450°C. 1559-1560A
- Gas evolution**
- Hydrogen Evolution during Directional Solidification and Its Effect on Porosity Formation in Aluminum Alloys. 2067-2072A
- Gas flow**
- Communication: On the Estimation of Plume Rise Velocity in Gas-Stirred Ladles. 937-941B
- Gas tungsten arc welding**
- Digital simulations of a stationary and a linear weld. Decomposition of ferrite in commercial superduplex stainless steel weld metals; microstructural transformations above 700°C. 101-110B
- Effects of metal vapor on electron temperature in helium gas tungsten arcs. 1009-1018A
- A Unified Numerical Modeling of Stationary Tungsten-InertGas Welding Process. 1183-1188A
- 2043-2052A
- Gating and risering**
- Development of New Feeding-Distance Rules Using Casting Simulation: Part II. The New Rules. 741-755B
- Gettering**
- The Influence of the Atmosphere on the Sintering of Aluminum. 3279-3284A
- Glissile dislocations**
- Effect of temperature and shear direction on yield stress by  $\{112\}\langle 112 \rangle$  slip in hcp metals. 831-836A
- Gold, Ternary systems**
- A 500°C isothermal section for the Al-Au-Cu system. 987-993A
- Estimation Of Viscosity Of Ternary-Metallic Melts. 3201-3204A
- Gold base alloys, Casting**
- A 500°C isothermal section for the Al-Au-Cu system. 987-993A
- Gold plating**
- Effects of Au plating on small-scale resistance spot welding of thin-sheet nickel. 2667-2676A
- Grain boundaries**
- Deformation bands and the formation of grain boundaries in a superplastic aluminum alloy. 279-290A
- Modeling the kinetics of grain-boundary-nucleated recrystallization processes after cold deformation. 529-537A
- Erratum: The Effects of deformation and pre-heat-treatment on abnormal grain growth in RENE 88 superalloy. 713A
- Atomic-scale modeling of dislocations and related properties in the hexagonal-close-packed metals. 721-733A
- Bulk and interface boundary diffusion in group IV hexagonal close-packed metals and alloys. 765-775A



- Grain-boundary diffusion by vacancy mechanism in  $\alpha$ -Ti and  $\alpha$ -Zr 791-796A
- Diffusion along grain and interphase boundaries in Alpha Zr and Zr-2.5 Wt Pct Nb alloy 797-800A
- Twins as barriers to basal slip in hexagonal-close-packed metals 809-812A
- Distribution of c- and a-dislocations in tubes of Zr alloys 867-874A
- Shrinkage and splitting of microcracks under pressure simulated by the finite-element method 1117-1124A
- Visualization of the hydrogen desorption process from ferrite, pearlite, and graphite by secondary ion mass spectrometry 2659-2665A
- Effect of grain boundary characteristics on intergranular corrosion resistance of 6061 aluminum alloy extrusion 2891-2898A
- Static Recrystallization Mechanisms in a Coarse-Grained Nb-Microalloyed Austenite 3089-3098A
- A Discrete Approach to Grain Growth Based on Pair Interactions: Effect of Local Grain-Boundary Curvature 3329-3337A
- The Effect of Grain Boundaries on the Athermal Stress of Tantalum and Tantalum-Tungsten Alloys 3457-3464A
- The Effect of Small Deformation on Abnormal Grain Growth in Bulk Cu 3803-3815A
- Grain boundary migration**
- Finite element modeling of the morphology of  $\beta$  to  $\alpha$  phase transformation in Ti-6Al-4V alloy 1027-1040A
- Grain boundary sliding**
- Creep and microstructure of magnesium-aluminum-calcium based alloys 567-574A
- Deformation mechanisms during low- and high-temperature superplasticity in 5083 Al-Mg alloy 1373-1384A
- Low-temperature superplastic behavior of a submicrometer-grained 5083 Al alloy fabricated by severe plastic deformation 2859-2867A
- Tensile, creep, and low-cycle fatigue behavior of a cast  $\gamma$ -TiAl-based alloy for gas turbine applications 2869-2881A
- Grain growth**
- Grain growth behavior of cryomilled INCONEL 625 powder during isothermal heat treatment 125-134A
- A three-phase model of hydrogen pore formation during the equiaxed dendritic solidification of aluminum-silicon alloys 209-221B
- Modeling of primary spacing selection in dendrite arrays during directional solidification 223-233B
- A new unidirectional solidification method to study gray cast iron 235-241B
- Microstructure evolution in Zr under equal channel angular pressing 973-980A
- Finite element modeling of the morphology of  $\beta$  to  $\alpha$  phase transformation in Ti-6Al-4V alloy 1027-1040A
- Theory for growth of needle-shaped particles in multicomponent systems 1075-1081A
- Microstructural characteristics of Ni-Sb eutectic alloys under substantial undercooling and containerless solidification conditions 1221-1228A
- Cellular array morphology during directional solidification 1229-1243A
- Dislocation-disclination model of heterogeneous martensite nucleation in transformation-induced-plasticity steels 1351-1362A
- Elevated temperature strength and room-temperature toughness of directionally solidified Ni-33Al-33Cr-1Mo 1385-1397A
- Texture enhancement by inoculation during casting of ferritic stainless steel strip 1499-1507A
- Communication: On the solute field and composition of  $\gamma$  plates in an Al-22 At. Pct Ag alloy 1561-1565A
- On the roles of clusters during intragranular nucleation in the absence of static defects 1649-1658A
- Tree-ring formation during vacuum arc remelting of INCONEL 718. I. Experimental investigation 1795-1804A
- Communication: Discussion of 'coarsening of intermetallic or compound precipitates in binary systems' 1859-1860A
- Communication: Author's reply [to 'Discussion of 'Coarsening of intermetallic or compound precipitates in binary systems'] 1860-1862A
- Massive transformations revisited 2277-2283A
- Simulation of ferrite growth in continuously cooled low-carbon iron alloys 2309-2316A
- Massive transformation and the formation of the ferromagnetic  $L_{12}$  phase in manganese-aluminum-based alloys 2413-2423A
- Comparison of interfacial structure-related mechanisms in diffusional and martensitic transformations 2541-2547A
- Evolution of Microstructure and Texture during Casting of AISI 304 Stainless Steel Strip 3747-3754A
- The Effect of Small Deformation on Abnormal Grain Growth in Bulk Cu 3803-3815A
- Grain growth, Heating effects**
- Erratum: The Effects of deformation and pre-heat-treatment on abnormal grain growth in RENE 88 superalloy 713A
- Grain orientation**
- Texture Clustering and Long-Range Disorientation Representation Methods: Application to 6022 Aluminum Sheet 3709-3718A
- Evolution of Microstructure and Texture during Casting of AISI 304 Stainless Steel Strip 3747-3754A
- The Microstructure and Recrystallization of Flow-Formed Oxide-Dispersion-Strengthened Ferritic Alloy: Part II. Recrystallization Behavior 3787-3794A
- Grain refinement**
- Equal-channel angular extrusion of beryllium 965-972A
- High Temperature SANS Experiments on Nb(C,N) and MnS Precipitates in HSLA Steel 1883-1891A
- Phase transformation-induced grain refinement in rapidly solidified ultra-high-carbon steels 2789-2799A
- Structural refinement of gray iron by electromagnetic vibrations 3025-3030A
- Solidification Behavior of Sn-15 Wt Pct Pb Alloy under a High Shear Rate and High Intensity of Turbulence during Semi-solid Processing 3511-3520A
- Grain refinement, Deformation effects**
- Communication: Thermal stability and microstructural evolution in ultrafine-grained nickel after equal-channel angular pressing (ECAP) 1865-1868A
- Grain size**
- Grain growth behavior of cryomilled INCONEL 625 powder during isothermal heat treatment 125-134A
- Deformation bands and the formation of grain boundaries in a superplastic aluminum alloy 279-290A
- Parameters controlling microstructure and hardness during friction-stir welding of precipitation-hardenable aluminum alloy 6063 625-635A
- Stable quasicrystalline phase in Al-Cu-Fe-Cr coating materials 675-679A
- Direct measurements of grain size in low-carbon steels using the laser ultrasonic technique 687-691A
- Communication: Microstructural interpretation of negligible strain-hardening behavior of submicrometer-grained low-carbon steel during tensile deformation 705-707A
- Communication: Examination on the aging and tensile properties of Al-Zn-Mg/Al<sub>3</sub>Ni eutectic composite 707-711A
- Distribution of c- and a-dislocations in tubes of Zr alloys 867-874A
- The production of ultrafine ferrite in low-carbon steel by strain-induced transformation 1019-1026A
- The effect of grain size on the ambient temperature creep deformation behavior of a beta Ti-14.8V alloy 1137-1144A
- Microstructural evolution and mechanical properties of the AA8011 alloy during the accumulative roll-bonding process 1521-1530A
- Comprehensive microstructural characterization in modified 9Cr-1Mo ferritic steel by ultrasonic measurements 1617-1626A
- An Investigation of Microstructure and Grain-Boundary Evolution during ECA Pressing of Pure Aluminum 2173-2184A
- Grain-size control in Ti-48Al-2Cr-2Nb with yttrium additions 2729-2736A
- The relationship between grain size and the surface roughening behavior of Al-Mg alloys 2883-2889A
- Static Recrystallization Mechanisms in a Coarse-Grained Nb-Microalloyed Austenite 3089-3098A
- Young's Modulus and Mechanical Properties of Ti-29Nb-13Ta-4.6Zr in Relation to  $\alpha'$  Martensite 3137-3144A
- Inertia Welding Nickel-Based Superalloy: Part I. Metallurgical Characterization 3215-3225A
- Evolution of Submicrocrystalline Iron Containing Dispersed Oxides under Mechanical Milling Followed by Consolidation 3241-3248A
- The Effect of Small Deformation on Abnormal Grain Growth in Bulk Cu 3803-3815A
- Grain size, Pressure effects**
- Microstructural evolution of a shaped-charge liner and target materials during ballistic tests 1069-1074A
- Grain size distribution**
- A Discrete Approach to Grain Growth Based on Pair Interactions: Effect of Local Grain-Boundary Curvature 3329-3337A
- Grain structure**
- Subgrain formation during deformation: physical origin and consequences 319-327A
- Improvement in mechanical properties of dental cast Ti-6Al-7Nb by thermochemical processing 503-510A
- Electron-beam welding behavior in Mg-Al-based alloys 1461-1473A
- Texture enhancement by inoculation during casting of ferritic stainless steel strip 1499-1507A
- Tree-ring formation during vacuum arc remelting of INCONEL 718. I. Experimental investigation 1795-1804A
- Evolution of microstructure and properties in alpha-brass after iterative processing 1853-1857A
- Development of Austenitic Nanostructures in High-Nitrogen Steel Powders Processed by Mechanical Alloying 2139-2144A
- The Microstructure and Recrystallization of Flow-Formed Oxide-Dispersion-Strengthened Ferritic Alloy: Part II. Recrystallization Behavior 3787-3794A
- Grain structure, Processing effects**
- Tree-ring formation during vacuum arc remelting of INCONEL 718. II. Mathematical modeling 1805-1815A
- Granular materials**
- Computational fluid-dynamics modeling of the hydrodynamics of fluidization in the sand surrounding a lost-foam casting pattern 565-575B
- Graphic methods**
- Observations, theories, and predictions of high-temperature creep behavior 241-248A
- Graphitization**
- A study on inhomogeneous distribution of temper graphite particles in strip-cast Fe-C-Si alloys 1263-1273A
- Gray iron, Casting**
- A new unidirectional solidification method to study gray cast iron 235-241B
- Gray iron, Microstructure**
- Structural refinement of gray iron by electromagnetic vibrations 3025-3030A
- Grinding wheels, Fabrication**
- Interfacial Segregation of Ti in the Brazing of Diamond Grits onto a Steel Substrate Using a Cu-Sn-Ti Brazing Alloy 2163-2172A
- Growth rate**
- The Coarsening Kinetics of  $\gamma$  Particles in Nickel-Based Alloys 3367-3373A
- Hafnium, Dopants**
- Communication: Depth Profiling of Hf-Doped Aluminide Coating by Glow-Discharge Mass Spectrometry 3578-3582A
- Hafnium, Mechanical properties**
- Effects of high rates of loading on the deformation behavior and failure mechanisms of hexagonal close-packed metals

- and alloys. 927-935A
- Hafnium, Microstructure**  
Bulk and interface boundary diffusion in group IV hexagonal close-packed metals and alloys. 765-775A
- Hall Heroult process**  
Modeling of the solubility of alumina in the NaF-AlF<sub>3</sub> system at 1300 K. 315-319B
- Hard surfacing**  
The fracture toughness and toughening mechanisms of nickel-base wear materials. 33-56A
- Hardenability**  
Effect of composition and austenite deformation on the transformation characteristics of low-carbon and ultralow-carbon microalloyed steels. 1331-1349A
- Hardening, Heating effects**  
Precipitation of austenite particles at grain boundaries during aging of Fe-Mn-Ni steel. 1057-1067A
- Hardness**  
Microstructural and mechanical properties investigation of electrodeposited and annealed LIGA nickel structures. Parameters controlling microstructure and hardness during friction-stir welding of precipitation-hardenable aluminum alloy 6063. 539-554A  
Synthesis and nanoindentation study of high-velocity oxygen fuel thermal-sprayed nanocrystalline and near-nanocrystalline Ni coatings. 647-655A  
Fabrication and characterization of Ti-TiB<sub>2</sub> functionally graded material system. 681-685A  
Age-hardening characteristics of aluminum alloy-hollow fly ash composites. 1541-1547A  
Correlation of Microstructure with Wear and Fracture Properties of Two-Layered VC/Ti-6Al-4V Surface Composites Fabricated by High-Energy Electron-Beam Irradiation. 3173-3185A  
Inertia Welding Nickel-Based Superalloy: Part I. Metallurgical Characterization. 3215-3225A
- Hardness tests**  
Artificial Neural Network and Finite Element Modeling of Nanoindentation Tests. 1939-1947A
- HCP metals, Diffusion**  
Bulk and interface boundary diffusion in group IV hexagonal close-packed metals and alloys. 765-775A
- HCP metals, Metallography**  
Advances in deformation twin characterization using electron backscattered diffraction data. 949-954A
- HCP metals, Microstructure**  
Atomic-scale modeling of dislocations and related properties in the hexagonal-close-packed metals. 721-733A  
First-principles investigation of perfect and diffuse antiphase boundaries in hcp-based Ti-Al alloys. 735-741A  
Effect of pressure on zone-center phonons in hexagonal-close-packed metals. 743-747A  
Mobility of interstitial clusters in alpha-zirconium. 783-789A  
Interfacial deformation mechanisms in hexagonal-close-packed metals. 801-807A  
Twins as barriers to basal slip in hexagonal-close-packed metals. 809-812A  
Nonbasal deformation modes of Hcp metals and alloys: role of dislocation source and mobility. 813-822A  
Molecular dynamics simulation of  $\langle c + a \rangle$  dislocation core structure in hexagonal-close-packed metals. 823-829A
- Heat affected zone**  
Inertia Welding Nickel-Based Superalloy: Part II. Residual Stress Characterization. 3227-3234A
- Heat affected zone, Microstructure**  
Dissolution Kinetics of NbC Particles in the Heat-Affected Zone of Type 347 Austenitic Stainless Steel. 2031-2042A
- Heat exchanger tubes, Materials selection**  
Corrosion behavior of austenitic alloy 690 under anodic and cathodic potentials. 1437-1447A
- Heat of formation**  
Solubility of Some Transition Metal Oxides in Cryolite-Alumina Melts: Part I. Solubility of FeO, FeAl<sub>2</sub>O<sub>4</sub>, NiO, and NiAl<sub>2</sub>O<sub>4</sub>. Phase Separation Tendency in the As-Solidified ZrAl-Nb Alloys Studied by Microstructural Observations and Thermodynamic Analysis. 901-908B  
Thermally Enhanced and Mechanically Driven Glass Formation Reactions of Multilayered Cu<sub>33</sub>Zr<sub>67</sub> Powders. 1919-1929A  
On the Partial Atomic Volume of Aluminum in Solid Solutions Based on the 3d Transition Metals and Copper. 2145-2153A  
3591-3595A
- Heat of solution**  
Solubility of Some Transition Metal Oxides in Cryolite-Alumina Melts: Part II. Solubility of TiO<sub>2</sub>. 909-913B
- Heat resistant steels, Phase transformations**  
Modeling M<sub>23</sub>C<sub>6</sub> Precipitation in Niobium-Alloyed Ferritic Stainless Steel. 3339-3347A
- Heat transfer**  
Control of heat transfer and growth uniformity of solidifying copper shells through substrate temperature. 403-411B  
Thermal and mechanical behavior of copper molds during thin-slab casting. I. Plant trial and mathematical modeling. 425-436B  
Thermal and mechanical behavior of copper molds during thin-slab casting. II. Mold crack formation. 437-449B  
Molten Wood's-Metal Flow in a Cylindrical Bath Agitated by Cold Bottom Gas Injection. 695-702B  
A Study on Heat Source Equations for the Prediction of Weld Shape and Thermal Deformation in Laser Microwelding. 757-764B  
A study on inhomogeneous distribution of temper graphite particles in strip-cast Fe-C-Si alloys. 1263-1273A
- Modeling of laser keyhole welding. I. Mathematical modeling, numerical methodology, role of recoil pressure, multiple reflections, and free surface evolution.** 1817-1830A
- A Unified Numerical Modeling of Stationary Tungsten-Inert Gas Welding Process.** 2043-2052A
- Joining of NiAl to Iron-Based Alloys by Reactive Casting.** 2073-2080A
- Heating rate**  
The effect of rapid heat treatment on the high-temperature tensile behavior of superplastic Ti-6Al-4V. 83-92A
- Hexagonal lattice**  
Atomic-scale modeling of dislocations and related properties in the hexagonal-close-packed metals. 721-733A  
First-principles investigation of perfect and diffuse antiphase boundaries in hcp-based Ti-Al alloys. 735-741A  
A study of twinning in zirconium using neutron diffraction and polycrystalline modeling. 757-763A  
Grain-boundary diffusion by vacancy mechanism in  $\alpha$ -Ti and  $\alpha$ -Zr. 791-796A  
Effect of temperature and shear direction on yield stress by  $\{112\} \langle 112 \rangle$  slip in hcp metals. 831-836A  
Creep strength of magnesium-based alloys. 875-882A
- High alloy steels, Sorption**  
Trap-Governed Hydrogen Diffusivity and Uptake Capacity in Ultrahigh-Strength AERMET 100 Steel. 1991-2004A
- High carbon steels, Mechanical properties**  
A critical-strain criterion for hydrogen embrittlement of cold-drawn, ultrafine pearlitic steel. 1151-1166A
- High carbon steels, Phase transformations**  
Phase transformation-induced grain refinement in rapidly solidified ultra-high-carbon steels. 2789-2799A
- High cycle fatigue**  
Influence of microstructure on high-cycle fatigue of Ti-6Al-4V: bimodal vs. lamellar structures. 899-918A  
Tensile and fatigue properties of 17-4 PH stainless steel at high temperatures. 1715-1724A  
Communication: High-cycle fatigue of an investment cast, Be-Al metal matrix composite. 1862-1865A  
Communication: Conducting High-Cycle Fatigue Strength Step Tests on Gamma TiAl. 3871-3874A
- High pressure**  
Effect of pressure on zone-center phonons in hexagonal-close-packed metals. 743-747A
- High speed tool steels, Microstructure**  
Lattice Orientation Relationship between the M<sub>2</sub>C Carbide and the Ferrite Matrix in the M50NiL Bearing Steel. 1963-1969A
- High speed tool steels, Powder technology**  
Effect of residual carbon on the sintering process of m2 high speed steel parts obtained by a modified metal injection molding process. 1843-1851A
- High strength low alloy steels, Corrosion**  
Environmental aspects of near-neutral pH stress corrosion cracking of pipeline steel. 1429-1436A
- High strength low alloy steels, Mechanical properties**  
Carbide precipitation and high-temperature strength of hot-rolled high-strength, low-alloy steels containing Nb and Mo. Communication: Specimen Size Effects and Ductile Fracture of HY 100 Steel. 1689-1698A  
Change of Critical Events of Cleavage Fracture with Variation of Microscopic Features of Low-Alloy Steels. 3293-3295A  
Effect of Prestrain on Stretch-Zone Formation during Ductile Fracture of Cu-Strengthened High-Strength Low-Alloy Steels. 3393-3402A  
3731-3740A
- High strength low alloy steels, Microstructure**  
High Temperature SANS Experiments on Nb(C,N) and MnS Precipitates in HSLA Steel. 1883-1891A
- High strength low alloy steels, Phase transformations**  
An integrated computer model with applications for austenite-to-ferrite transformation during hot deformation of Nb-microalloyed steels. 1509-1520A  
Titanium Nitride Precipitation Behavior in Thin-Slab Cast High-Strength Low-Alloy Steels. 3099-3110A
- High strength steels, Crystal growth**  
Titanium Nitride Precipitation Behavior in Thin-Slab Cast High-Strength Low-Alloy Steels. 3099-3110A
- High strength steels, Heat treatment**  
Toward prediction of microstructural evolution during laser surface alloying. 1189-1200A
- High strength steels, Sorption**  
Trap-Governed Hydrogen Diffusivity and Uptake Capacity in Ultrahigh-Strength AERMET 100 Steel. 1991-2004A
- High temperature**  
Observations, theories, and predictions of high-temperature creep behavior. 241-248A  
Creep at low stresses: an evaluation of diffusion creep and Harper-Dorn creep as viable creep mechanisms. 249-259A  
The role of impurities during creep and superplasticity at very low stresses. 261-278A  
Steady-state creep of  $\alpha$ -zirconium at temperatures up to 850°C. 337-343A  
Elevated-temperature deformation at forming rates of  $10^{-2}$  to  $10^2$  s<sup>-1</sup>. 345-362A  
Some selected topics in creep cavitation. 383-390A  
The effect of mischmetal addition on the structure and mechanical properties of a cast Al-7Si-0.3Mg alloy containing excess iron (up to 0.6 pct). 391-400A  
Creep strength of magnesium-based alloys. 875-882A
- Historical metallurgy**

- Ingenuity and innovation - the hallmarks of Brimacombe's pioneering contributions to process engineering. 5-29B  
Modeling of the Continuous Casting of Steel-Past, Present, and Future. 795-812B  
Computer simulation of solidification processes - the evolution of a technology. 2251-2273A  
Jan Van Der Merwe and the theory of epitaxy 2473-2474A
- Hot dip galvanizing**  
Numerical simulation of Zn coating solidification. 2685-2694A  
Orientation domains and texture in hot-dipped galvanized coatings. 2695-2701A
- Hot forming**  
Communication: Interpretation of flow instability using dynamic material modeling. 1569-1572A
- Hot isostatic pressing**  
Grain-size control in Ti-48Al-2Cr-2Nb with yttrium additions. 2729-2736A
- Hot pressing**  
Fabrication and characterization of Ti-TiB<sub>2</sub> functionally graded material system. 681-685A  
Formation of a TiB<sub>2</sub>-reinforced copper-based composite by mechanical alloying and hot pressing. 1275-1280A
- Hot rolling**  
The production of ultrafine ferrite in low-carbon steel by strain-induced transformation. 1019-1026A  
Hot rolling texture development in CMnCrSi dual-phase steels. 1091-1102A  
Effect of composition and austenite deformation on the transformation characteristics of low-carbon and ultra-low-carbon microalloyed steels. 1331-1349A  
Texture and microstructure development during intercritical rolling of low-carbon steels. 1589-1603A  
Carbide precipitation and high-temperature strength of hot-rolled high-strength, low-alloy steels containing Nb and Mo. 1689-1698A  
A Precision On-Line Model for the Prediction of Roll Force and Roll Power in Hot-Strip Rolling. 3255-3272A  
Microstructural Analysis of Multilayered Titanium Aluminide Sheets Fabricated by Hot Rolling and Heat Treatment. 3649-3659A
- Hot upsetting**  
The Kinetics of Static Globularization of Ti-6Al-4V. 3527-3534A
- Hot workability**  
Constitutive equations for creep and plasticity of aluminum alloys produced by powder metallurgy and aluminum-based metal matrix composites. 373-381A
- Hot workability, Alloying effects**  
Communication: Effect of Zr Addition on Hot Workability of Cu-6Ni-2Mn-2Sn-2Al Alloy. 3298-3300A
- Hot working**  
Elevated-temperature deformation at forming rates of  $10^{-2}$  to  $10^2$  s<sup>-1</sup>. 345-362A  
An integrated computer model with applications for austenite-to-ferrite transformation during hot deformation of Nb-microalloyed steels. 1509-1520A  
Flow Stress and Ductility of Duplex Stainless Steel during High-Temperature Torsion Deformation. 1931-1938A  
Communication: Effect of Zr Addition on Corrosion Behavior of Cu-6Ni-2Mn-2Sn-2Al Alloy. 2237-2240A  
Self-consistent modeling of the flow behavior of wrought alpha/beta titanium alloys under isothermal and nonisothermal hot-working conditions. 2719-2727A  
Effect of the Lamellar Grain Size on Plastic Flow Behavior and Microstructure Evolution during Hot Working of a Gamma Titanium Aluminide Alloy. 3817-3830A
- Hydration**  
Solid-state reaction kinetics of the system CaO-FeO. 257-264B
- Hydrocarbons, Reactions (chemical)**  
In-situ formation of SiC-reinforced Al-Si alloy composites using methane gas mixtures. 543-550B
- Hydrogen, Diffusion**  
Trap-Governed Hydrogen Diffusivity and Uptake Capacity in Ultrahigh-Strength AERMET 100 Steel. 1991-2004A  
Visualization of the hydrogen desorption process from ferrite, pearlite, and graphite by secondary ion mass spectrometry. 2659-2665A
- Hydrogen embrittlement**  
Hydrogen embrittlement of nickel-titanium alloy in biological environment. 495-501A  
A critical-strain criterion for hydrogen embrittlement of cold-drawn, ultrafine pearlitic steel. 1151-1166A  
Hydrogen-assisted deformation and fracture behaviors of Al 8090. 1755-1763A  
Trap-Governed Hydrogen Diffusivity and Uptake Capacity in Ultrahigh-Strength AERMET 100 Steel. 1991-2004A
- Hydrogen embrittlement, Heating effects**  
The effects of test temperature, temper, and alloyed copper on the hydrogen-controlled crack growth rate of an Al-Zn-Mg-(Cu) alloy. 1167-1181A  
Erratum: The effects of test temperature, temper, and alloyed copper on the hydrogen-controlled crack growth rate of an Al-Zn-Mg-(Cu) alloy. 1297A
- Hydrogen reduction**  
A Novel Cyclic Process using CaSO<sub>4</sub>/CaS Pellets for Converting Sulfur Dioxide to Elemental Sulfur without Generating Secondary Pollutants: Part II. Hydrogen Reduction of Calcium-Sulfate Pellets to Calcium Sulfide. 717-721B
- Hydrogenation**  
Two-way shape memory effect of TiNi alloys induced by hydrogenation. 17-23A  
Improvement in mechanical properties of dental cast Ti-6Al-7Nb by thermochemical processing. 503-510A
- Anisotropic threshold stress intensity factor, K<sub>IK</sub> and crack growth rate in delayed hydride cracking of Zr-2.5Nb pressure tubes. 919-925A
- Hydrometallurgy**  
Bubble formation and detachment on nonwetted surfaces. 155-162B
- Hydrostatic pressure**  
The influence of the stress state on the plasticity of transformation induced plasticity-aided steel. 1659-1667A
- Hydroxyapatite, Coatings**  
Dry-process surface modification for titanium dental implants. 511-519A
- Image analysis**  
Direct measurements of grain size in low-carbon steels using the laser ultrasonic technique. 687-691A  
Advances in deformation twin characterization using electron backscattered diffraction data. 949-954A  
Communication: Infrared imaging during low-cycle fatigue of HR-120 alloy. 1287-1292A
- Impact strength**  
Cracking in  $\gamma$ -TiAl due to high speed particle impact. 581-589A  
Phenomenological observations on mechanical and corrosion properties of thixoformed 357 alloys: a comparison with permanent mold cast 357 alloys. 1399-1412A  
Crack-initiation toughness and crack-arrest toughness in advanced 9 pct Ni steel welds containing local brittle zones. 2615-2622A
- Incandescent lamps, Materials selection**  
Dopant Particle Characterization and Bubble Evolution in Aluminum-Potassium-Silicon-Doped Molybdenum Wire. 3349-3356A
- Inclusions**  
A theoretical and experimental study of continuous-casting tundishes focusing on slag-steel interaction. 173-185B  
Mathematical modeling and computer simulation of the rotating impeller particle flotation process: Part I. Fluid flow. 297-303B  
Mathematical modeling and computer simulation of the rotating impeller particle flotation process: Part II. Particle agglomeration and flotation. 305-314B  
In-situ observation of the precipitation of manganese sulfide in low-carbon magnesium-killed steel. 427-436A  
Numerical simulation of dendrite white spot formation during vacuum arc remelting of INCONEL718. 443-454A  
Thermodynamics on the Formation of Spinel (MgO-Al<sub>2</sub>O<sub>3</sub>) Inclusion in Liquid Iron Containing Chromium. 703-709B  
A New Method for Three-Dimensional Numerical Simulation of Electromagnetic and Fluid-Flow Phenomena in Electromagnetic Separation of Inclusions from Liquid Metal. 775-785B  
Communication: Specimen Size Effects and Ductile Fracture of HY 100 Steel. 3293-3295A  
Dopant Particle Characterization and Bubble Evolution in Aluminum-Potassium-Silicon-Doped Molybdenum Wire. 3349-3356A
- Indentation**  
Artificial Neural Network and Finite Element Modeling of Nanoindentation Tests. 1939-1947A
- Indium, Binary systems**  
Thermodynamic Modeling of the Indium-Palladium System. 3597-3603A
- Indium, Ternary systems**  
Communication: Prediction of the thermodynamic properties of solutes in the Bi-based ternary dilute solution. 502-506B
- Induction melting**  
Intermetallic-reinforced light-metal matrix in-situ composites. 193-201A
- Infiltration**  
Reactive Infiltration of 25 Vol Pct TiO<sub>2</sub>/Al Composites. 2155-2162A
- Infrared brazing**  
Infrared repair brazing of 403 stainless steel with a nickel-based braze alloy. 1765-1773A
- Ingot casting**  
Ingenuity and innovation - the hallmarks of Brimacombe's pioneering contributions to process engineering. 5-29B  
Numerical simulation of dendrite white spot formation during vacuum arc remelting of INCONEL718. 443-454A  
Constitutive Behavior of As-Cast AM 050, AA3104, and AA5182. 1971-1980A
- Ingot, Phases (state of matter)**  
Modeling of Globular Equiaxed Solidification with a Two-Phase Approach. 3673-3683A
- Inhibition**  
A Discrete Approach to Grain Growth Based on Pair Interactions: Effect of Local Grain-Boundary Curvature. 3329-3337A
- Injection**  
A water model and numerical study of the spout height in a gas-stirred vessel. 377-384B
- Injection molding**  
Thermal debinding modeling of mass transport and deformation in powder-injection molding compact. 477-488B  
Effect of residual carbon on the sintering process of m2 high speed steel parts obtained by a modified metal injection molding process. 1843-1851A  
Sintering Densification and Microstructural Evolution of Injection Molding Grade 17-4 PH Stainless Steel Powder. 2185-2194A  
The microstructural development of Mg-9 pct Al-1 pct Zn alloy during injection molding. 2963-2972A
- Inoculation**  
Texture enhancement by inoculation during casting of ferritic stainless steel strip. 1499-1507A
- Interatomic distance**  
Effect of pressure on zone-center phonons in hexagonal-close-packed metals. 743-747A  
Metastable phases in the Ti-V system. I. Neutron diffraction



- study and assessment of structural properties. 1307-1317A
- Interdendritic structure**  
Primary Dendrite Distribution and Disorder during Directional Solidification of Pb-Sb Alloys. 3499-3510A
- Interface reactions**  
Die soldering: mechanism of the interface reaction between molten aluminum alloy and tool steel. 465-476B  
Rate of Interfacial Reaction between Molten  $\text{CaO-SiO}_2\text{-Al}_2\text{O}_3\text{-Fe}_2\text{O}_3$  and  $\text{CO-CO}_2$ . 651-660B  
Phase equilibria of the ternary Ni-Cr-Zr system and interfacial reactions in the Ni-Cr/Zr couples. 995-1002A  
Interfacial Segregation of Ti in the Brazing of Diamond Grits onto a Steel Substrate Using a Cu-Sn-Ti Brazing Alloy. 2163-2172A  
Interfacial reactions in aluminosilicate short fiber-reinforced aluminum matrix composites. 2755-2761A  
Interface stability during displacement reactions between  $\text{Cu}_2\text{O}$  and  $\text{Co}_{1-x}\text{Fe}_x$  alloys at 1223 K. 2899-2906A  
Statistical Self-Similarity in Rhines' Concept of Unique Multiphase Diffusion Paths on the Ternary Gibbs' Isotherm. 3357-3365A  
Microstructural Analysis of Multilayered Titanium Aluminide Sheets Fabricated by Hot Rolling and Heat Treatment. 3649-3659A  
Interfacial Dislocation Networks Strengthening a Fourth-Generation Single-Crystal TMS-138 Superalloy. 3741-3746A
- Interfaces**  
A theoretical and experimental study of continuous-casting tundishes focusing on slag-steel interaction. 173-185B  
Energy of the  $\text{Pb}(111)/\text{Al}(111)$  interface. 1003-1007A  
Finite element modeling of the morphology of  $\beta$  to  $\alpha$  phase transformation in Ti-6Al-4V alloy. 1027-1040A  
Modeling of laser keyhole welding. I. Mathematical modeling, numerical methodology, role of recoil pressure, multiple reflections, and free surface evolution. 1817-1830A  
Communication: Reduced critical solidification front velocity of particle engulfment due to an interface active solute in the liquid metal. 1869-1873A  
Subnanometer-scale chemistry and structure of  $\alpha$ -iron/molybdenum nitride heterophase interfaces. 2317-2326A  
Analysis of the Cu-3 Wt pct Ti cellular interphase boundary by various models. 2495-2505A  
The cellular interlamellar and growth-front interphase boundaries in Cu-3 Wt pct Ti. 2507-2518A  
A study of the Pb/Al (100) interfacial energy. 2569-2572A  
Visualization of the hydrogen desorption process from ferrite, pearlite, and graphite by secondary ion mass spectrometry. 2659-2665A
- Interfaces, Stress effects**  
Sequences of Phase Formation in Multiphase Stressed Plates. 1901-1911A
- Intergranular corrosion**  
Sensitization behavior of type 308 stainless steel weld metals after postweld heat treatment and low-temperature aging and its relation to microstructure. 1743-1754A  
Effect of grain boundary characteristics on intergranular corrosion resistance of 6061 aluminum alloy extrusion. 2891-2898A  
Intergranular stress corrosion cracking behavior of types 308 and 316 stainless steel weld metals in a simulated boiling water reactor environment. 2907-2919A  
Mechanical, Intergranular Corrosion, and Wear Behavior of Aluminum-Matrix Composite Materials Reinforced with Nickel Aluminides. 3541-3553A
- Intergranular fracture**  
The Influence of Microstructure and Environment on the Crack Growth Behavior of Powder Metallurgy Nickel Superalloy RR1000. 3165-3172A
- Intergranular structure**  
Deformation bands and the formation of grain boundaries in a superplastic aluminum alloy. 279-290A  
Some selected topics in creep cavitation. 383-390A  
Intergranular stresses in ZIRCALOY-2. 749-755A  
Determination of dislocation densities in Hcp metals from X-ray diffraction line-broadening analysis. 859-865A  
Precipitation of austenite particles at grain boundaries during aging of Fe-Mn-Ni steel. 1057-1067A  
Interphase boundary structure with irrational orientation relationship formed in grain boundary precipitation. 2327-2335A  
Origins of internal structure in massive transformation products. 2347-2351A
- Intergranular structure, Deformation effects**  
Denuded zones, diffusional creep, and grain boundary sliding. 219-229A
- Intergranular structure, Processing effects**  
Evolution of microstructure and properties in alpha-brass after iterative processing. 1853-1857A
- Intermetallic phases**  
Grain growth behavior of cryomilled INCONEL 625 powder during isothermal heat treatment. 125-134A  
Die soldering: mechanism of the interface reaction between molten aluminum alloy and tool steel. 465-476B  
A 500°C isothermal section for the Al-Au-Cu system. 987-993A  
Decomposition of ferrite in commercial superduplex stainless steel weld metals; microstructural transformations above 700°C. 1009-1018A  
Crystallization kinetics of amorphous magnesium-rich magnesium-copper and magnesium-nickel alloys. 1041-1050A  
Communication: On the ternary phase in the zinc-rich corner of the Zn-Fe-Al system at temperatures below 450°C. 1559-1560A  
Thermodynamic description of the Cu-Al-Sn system in the copper-rich corner. 1639-1648A  
Communication: Discussion of 'coarsening of intermetallic or compound precipitates in binary systems'. 1859-1860A  
Communication: Author's reply [to 'Discussion of 'Coarsening of intermetallic or compound precipitates in binary systems'']. 1860-1862A
- Phase Separation Tendency in the As-Solidified Zr3Al-Nb Alloys Studied by Microstructural Observations and Thermodynamic Analysis. 1919-1929A  
Massive-parent interphase boundaries and their implications on the mechanisms of the  $\alpha \rightarrow \gamma_{\text{M}}$  massive transformation in Ti-Al alloys. 2353-2371A  
Massive transformation and the formation of the ferromagnetic  $\text{L}_{10}$  phase in manganese-aluminum-based alloys. 2413-2423A
- Intermetallic phases, Physical properties**  
Thermal and electrical properties of  $\text{Nb}_2\text{AlC}$ ,  $(\text{Ti,Nb})_2\text{AlC}$  and  $\text{Ti}_2\text{AlC}$ . 2775-2779A
- Intermetallics**  
Cracking in  $\gamma$ -TiAl due to high speed particle impact. 581-589A
- Intermetallics, Bonding**  
Microstructure and Mechanical Properties of Titanium Aluminide Wide-Gap, Transient Liquid-Phase Bonds Prepared using a Slurry-Deposited Composite Interlayer. 3205-3214A
- Intermetallics, Casting**  
Joining of NiAl to Iron-Based Alloys by Reactive Casting. 2073-2080A
- Intermetallics, Coatings**  
Powder Eutectic Coating With  $\text{Al}_3\text{Ti}$  For Steels. 3235-3240A  
Communication: Depth Profiling of Hf-Doped Aluminide Coating by Glow-Discharge Mass Spectrometry. 3578-3582A
- Intermetallics, Composite materials**  
Effect of heat treatments on in-situ  $\text{Al}_2\text{O}_3\text{-TiAl}_3$  composites produced from squeeze casting of  $\text{TiO}_2\text{-Al}_3\text{Si}_5$  composites. 31-40B  
Intermetallic-reinforced light-metal matrix in-situ composites. 193-201A  
Communication: Examination on the aging and tensile properties of Al-Zn-Mg/ $\text{Al}_3\text{Ni}$  eutectic composite. 707-711A  
Reactive Infiltration of 25 Vol Pct  $\text{TiO}_2\text{-Al}$  Composites. 2155-2162A  
Microstructure/processing relationships in reaction-synthesized titanium aluminide intermetallic matrix composites. 2747-2753A  
Large Self-Thermal-Plastic Deformation in a NiTi Shape-Memory Alloy Fiber-Actuated Aluminum Metal-Matrix Composite. 3535-3540A
- Intermetallics, Mechanical properties**  
Two-way shape memory effect of TiNi alloys induced by hydro-generation. 17-23A  
Application of a modified jogged-screw model for creep of TiAl and  $\alpha$ -Ti alloys. 329-336A  
The effect of constraint-induced normal stress on the failure of notched TiAl components. 417-426A  
Hydrogen embrittlement of nickel-titanium alloy in biological environment. 495-501A  
Room-temperature mechanical properties of cold-rolled thin foils of binary, stoichiometric  $\text{Ni}_3\text{Al}$ . 2607-2613A  
Crack growth in a nearly fully-lamellar gamma TiAl alloy at 650°C and 800°C under constant load conditions. 2847-2857A  
Tensile, creep, and low-cycle fatigue behavior of a cast  $\gamma$ -TiAl-based alloy for gas turbine applications. 2869-2881A  
Use of Weibull Statistics to Quantify Property Variability in TiAl Alloys. 3127-3136A  
Communication: Conducting High-Cycle Fatigue Strength Step Tests on Gamma TiAl. 3871-3874A
- Intermetallics, Melting**  
The Critical Pressure and Impeding Pressure of Al Evaporation during Induction Skull Melting Processing of TiAl. 3249-3253A
- Intermetallics, Microstructure**  
Atomistic modeling of quaternary alloys: Ti and Cu in NiAl. 265-284B  
First-principles investigation of perfect and diffuse antiphase boundaries in hcp-based Ti-Al alloys. 735-741A  
Nonbasal deformation modes of Hcp metals and alloys: role of dislocation source and mobility. 813-822A  
Phase Separation Tendency in the As-Solidified Zr3Al-Nb Alloys Studied by Microstructural Observations and Thermodynamic Analysis. 1919-1929A  
Microstructural Analysis of Multilayered Titanium Aluminide Sheets Fabricated by Hot Rolling and Heat Treatment. 3649-3659A  
The Effect of Convection on Disorder in Primary Cellular and Dendritic Arrays. 3763-3775A
- Intermetallics, Phase transformations**  
Massive transformation and the formation of the ferromagnetic  $\text{L}_{10}$  phase in manganese-aluminum-based alloys. 2413-2423A  
General discussion session of the symposium on "The mechanisms of the massive transformation". 2445-2470A
- Intermetallics, Powder technology**  
Solid-state crystalline-glassy cyclic phase transformations of mechanically alloyed  $\text{Cu}_{33}\text{Zr}_{67}$  powders. 135-143A  
Reduction of  $\text{Fe}_2\text{MoO}_4$  by hydrogen gas. 589-594B  
Grain-size control in Ti-48Al-2Cr-2Nb with yttrium additions. 2729-2736A
- Intermetallics, Thermal properties**  
Thermodynamic Modeling of the Indium-Palladium System. 3597-3603A
- Interstitial free steels, Metal working**  
Texture and microstructure development during intercritical rolling of low-carbon steels. 1589-1603A
- Interstitial impurities, Diffusion**  
Bulk and interface boundary diffusion in group IV hexagonal close-packed metals and alloys. 765-775A
- Investment castings**  
Communication: High-cycle fatigue of an investment cast, Be-Al metal matrix composite. 1862-1865A
- Ionization**  
Production of Niobium Powder by Direct Electrochemical Reduction of Solid  $\text{Nb}_2\text{O}_5$  in a Eutectic  $\text{CaCl}_2\text{-NaCl}$  Melt. 685-693B
- Iridium base alloys, Mechanical properties**  
Communication: Microstructures and mechanical properties of  $(\text{Ir,Rh})_{75}\text{Nb}_{15}\text{Ni}_{10}$  alloys. 1281-1283A
- Iron, Binary systems**



- Low-temperature extension of the Lehrer diagram and the iron-nitrogen phase diagram. 2593-2598A
- Modeling The Austenite-Ferrite Isothermal Transformation in an Fe-C Binary System and Experimental Verification. 3111-3115A
- Iron, Extraction**
- Stability of silico-ferrite of calcium and aluminum (SFCA) in air-solid solution limits between 1240°C and 1390°C and phase relationships within the  $\text{Fe}_2\text{O}_3\text{-CaO-Al}_2\text{O}_3\text{-SiO}_2$  (FCAS) system. 79-89B
- Thermodynamic study of the reduction of titanium magnetite concentrate with solid carbon. 633-638B
- Iron, Impurities**
- The effect of mischmetal addition on the structure and mechanical properties of a cast Al-7Si-0.3Mg alloy containing excess iron (up to 0.6 pct). 391-400A
- In-situ measurement of continuous cooling  $\beta \rightarrow \alpha$  transformation behavior of CP-Ti. 1051-1056A
- Iron, Powder technology**
- Thermal debinding modeling of mass transport and deformation in powder-injection molding compact. 477-488B
- Iron, Reactions (chemical)**
- Thermodynamics on the Formation of Spinell ( $\text{MgO-Al}_2\text{O}_3$ ) Inclusion in Liquid Iron Containing Chromium. 703-709B
- Communication: Solubility of Iron Magnesium-Lithium Melts. 929-930B
- Iron, Refining**
- Solid-state reaction kinetics of the system  $\text{CaO-FeO}$ . 257-264B
- The reaction behavior of Fe-C-S droplets in  $\text{CaO-SiO}_2\text{-MgO-FeO}$  slags. 335-344B
- Determination of Gibbs energies of formation of  $\text{CaFe}_2\text{O}_4$  and  $\text{Ca}_2\text{Fe}_2\text{O}_5$  from solid-state emf measurements using  $\text{CaF}_2$  as solid electrolyte. 385-392B
- Communication: Foaming behavior of slags. 499-501B
- Iron, Ternary systems**
- Communication: On the ternary phase in the zinc-rich corner of the Zn-Fe-Al system at temperatures below 450°C. 1559-1560A
- Diffusion Studies in the  $\beta$  ( $\text{B}_2$ ),  $\beta'$  (Bcc), and  $\gamma$  (Fcc) Fe-Ni-Al Alloys at 1000°C. 3375-3392A
- Iron and steel making**
- A water model and numerical study of the spout height in a gas-stirred vessel. 377-384B
- Communication: On the Estimation of Plume Rise Velocity in Gas-Stirred Ladles. 937-941B
- Iron compounds, Powder technology**
- Reduction of  $\text{Fe}_2\text{MoO}_4$  by hydrogen gas. 589-594B
- Iron compounds, Reactions (chemical)**
- Solubility of Some Transition Metal Oxides in Cryolite-Alumina Melts: Part I. Solubility of  $\text{FeO}$ ,  $\text{FeAl}_2\text{O}_4$ ,  $\text{NiO}$ , and  $\text{NiAl}_2\text{O}_4$ . 901-908B
- Iron ores, Extraction**
- Stability of silico-ferrite of calcium and aluminum (SFCA) in air-solid solution limits between 1240°C and 1390°C and phase relationships within the  $\text{Fe}_2\text{O}_3\text{-CaO-Al}_2\text{O}_3\text{-SiO}_2$  (FCAS) system. 79-89B
- Iron oxides, Reduction (chemical)**
- Process dynamics of electric arc furnace during direct reduced iron melting. 187-199B
- The reaction behavior of Fe-C-S droplets in  $\text{CaO-SiO}_2\text{-MgO-FeO}$  slags. 335-344B
- Rate of Interfacial Reaction between Molten  $\text{CaO-SiO}_2\text{-Al}_2\text{O}_3\text{-Fe}_2\text{O}_3$  and  $\text{CO-CO}_2$ . 651-660B
- Iron oxides, Solubility**
- Communication: The solubility of  $\text{Fe}_2\text{O}_3$  in cryolite-alumina melts. 140-142B
- Isothermal annealing**
- Aging behavior of the Ti-29Nb-13Ta-4.6Zr new beta alloy for medical implants. 487-493A
- Annealing behavior of alumina dispersion-strengthened copper strips rolled under different conditions. 1605-1616A
- Isothermal treatment**
- Grain growth behavior of cryomilled INCONEL 625 powder during isothermal heat treatment. 125-134A
- Jewelry, Materials selection**
- A 500°C isothermal section for the Al-Au-Cu system. 987-993A
- Killed steels, Microstructure**
- In-situ observation of the precipitation of manganese sulfide in low-carbon magnesium-killed steel. 427-436A
- High Temperature SANS Experiments on Nb(C,N) and MnS Precipitates in HSLA Steel. 1883-1891A
- Kinetics**
- Study of the kinetics of the recrystallization of cold-rolled low-carbon steel. 25-31A
- Kinetics of manganese reduction leaching from weathered rare-earth mud with sodium sulfite. 41-46B
- Diffusion-based model for isothermal solidification kinetics during transient liquid-phase sintering. 117-124A
- Rate of nitrogen desorption from  $\text{CaO-Al}_2\text{O}_3$  melts to gas phase. 393-401B
- Modeling the kinetics of grain-boundary-nucleated recrystallization processes after cold deformation. 529-537A
- Time-resolved X-ray imaging of aluminum alloy solidification processes. 613-623B
- Crystallization kinetics of amorphous magnesium-rich magnesium-copper and magnesium-nickel alloys. 1041-1050A
- Theory for growth of needle-shaped particles in multicomponent systems. 1075-1081A
- An integrated computer model with applications for austenite-to-ferrite transformation during hot deformation of Nb-microalloyed steels. 1509-1520A
- Age-hardening characteristics of aluminum alloy-hollow fly ash composites. 1541-1547A
- Inferring Dynamic Recrystallization in Ferrite using the Kinetics of Static Recrystallization. 1893-1900A
- Massive transformation and absolute stability. 2337-2345A
- Massive transformation and the formation of the ferromagnetic  $\text{L}_{10}$  phase in manganese-aluminum-based alloys. 2413-2423A
- Microstructural stability during creep of Mo- or W-bearing 12Cr steels. 2549-2557A
- Ladle additions**
- A water model and numerical study of the spout height in a gas-stirred vessel. 377-384B
- Ladle metallurgy**
- A theoretical and experimental study of continuous-casting tundishes focusing on slag-steel interaction. 173-185B
- A water model and numerical study of the spout height in a gas-stirred vessel. 377-384B
- Communication: On the Estimation of Plume Rise Velocity in Gas-Stirred Ladles. 937-941B
- Lamellar structure**
- Influence of microstructure on high-cycle fatigue of Ti-6Al-4V: bimodal vs. lamellar structures. 899-918A
- Analysis of the Cu-3 Wt pct Ti cellular interphase boundary by various models. 2495-2505A
- The cellular interlamellar and growth-front interphase boundaries in Cu-3 Wt pct Ti. 2507-2518A
- The Kinetics of Static Globularization of Ti-6Al-4V. 3527-3534A
- Laser beam cladding**
- Processing and microstructures of fiber Bragg grating sensors embedded in stainless steel. 3019-3024A
- Laser beam heating**
- Toward prediction of microstructural evolution during laser surface alloying. 1189-1200A
- Laser beam welding**
- A Study on Heat Source Equations for the Prediction of Weld Shape and Thermal Deformation in Laser Microwelding. 757-764B
- Investigation on the effect of laser pulse shape during Nd:YAG laser microwelding of thin Al sheet by numerical simulation. 1449-1459A
- Modeling of laser keyhole welding. I. Mathematical modeling, numerical methodology, role of recoil pressure, multiple reflections, and free surface evolution. 1817-1830A
- Modeling of laser keyhole welding. II. Simulation of keyhole evolution, velocity, temperature profile, and experimental verification. 1831-1842A
- Pulsed Nd:YAG Laser Welding of Copper Using Oxygenated Assist Gases. 2019-2030A
- Laser processing**
- Phase Evolution in Laser-Deposited Titanium-Chromium Alloys. 2129-2138A
- Lasers**
- Simulation of the submerged energy nozzle-mold water model system using laser-optical and computational fluid dynamics methods. 163-172B
- Correction to "Simulation of the submerged energy nozzle-mold water model systems using laser optical and computational fluid dynamics methods" 639B
- Lattice parameters**
- Atomistic modeling of quaternary alloys: Ti and Cu in NiAl. 265-284B
- Improvement in mechanical properties of dental cast Ti-6Al-7Nb by thermochemical processing. 503-510A
- Metastable phases in the Ti-V system. I. Neutron diffraction study and assessment of structural properties. 1307-1317A
- Misfit dislocations in epitaxy. 2475-2483A
- Reciprocal-space formulation and prediction of misfit accommodation in rigid and strained epitaxial systems. 2485-2494A
- Why do dislocations assemble into interfaces in epitaxy as well as in crystal plasticity? To minimize free energy. 2519-2539A
- Communication: A New Face-Centered-Cubic Superlattice Structure in Rapidly Solidified Cu-4 Wt Pct Ti Alloy and Its Relevance to the Ordering Process in Ni-Mo and Other 1/2 0 Ordering Alloys. 3573-3576A
- Lattice vacancies**
- Bulk and interface boundary diffusion in group IV hexagonal close-packed metals and alloys. 765-775A
- Anisotropy of point defect diffusion in alpha-zirconium. 777-782A
- Grain-boundary diffusion by vacancy mechanism in  $\alpha$ -Ti and  $\alpha$ -Zr. 791-796A
- On the roles of clusters during intragranular nucleation in the absence of static defects. 1649-1658A
- Laves phase**
- Microstructural stability during creep of Mo- or W-bearing 12Cr steels. 2549-2557A
- Layers**
- Sequences of Phase Formation in Multiphase Stressed Plates. 1901-1911A
- Carbide formation in alloy 718 during electron-beam solid free-form fabrication. 2559-2567A
- Leaching**
- Kinetics of Silver Leaching from Manganese-Silver Associated Ores in Sulfuric Acid Solution in the Presence of Hydrogen Peroxide. 813-816B
- Lead (metal), Coatings**
- Energy of the Pb{111} | Al{111} interface. 1003-1007A
- Lead (metal), Composite materials**
- Evolution of fiber fragmentation in a short-fiber-reinforced metal-matrix model composite during tensile creep deformation-an acoustic emission study. 1549-1557A
- Lead (metal), Extraction**

- Experimental Study of Phase Equilibria in the PbO-ZnO-Fe<sub>2</sub>O<sub>3</sub>-CaO-SiO<sub>2</sub> System in Air for High Lead Smelting Slags (CaO/SiO<sub>2</sub> = 0.35 and PbO/(CaO+SiO<sub>2</sub>) = 5.0 by Weight). 817-825B
- Experimental Liquidus in the PbO-ZnO-Fe<sub>2</sub>O<sub>3</sub>-(CaO + SiO<sub>2</sub>) System in Air, with CaO/SiO<sub>2</sub> = 0.35 and PbO/(CaO + SiO<sub>2</sub>) = 3.2. 851-863B
- Lead (metal), Physical properties**  
A study of the Pb/Al (100) interfacial energy. 2569-2572A
- Lead (metal), Ternary systems**  
Communication: Prediction of the thermodynamic properties of solutes in the Bi-based ternary dilute solution. 502-506B
- Lead base alloys, Casting**  
Cellular array morphology during directional solidification. 1229-1243A
- Lead base alloys, Directional solidification**  
Primary Dendrite Distribution and Disorder during Directional Solidification of Pb-Sb Alloys. 3499-3510A  
Communication: Minimizing Segregation during the Controlled Directional Solidification of Dendritic Alloys. 3876-3881A
- Lead base alloys, Microstructure**  
The Effect of Convection on Disorder in Primary Cellular and Dendritic Arrays 3763-3775A
- Lead base alloys, Powder technology**  
Diffusion-based model for isothermal solidification kinetics during transient liquid-phase sintering. 117-124A
- Lead compounds, Phases (state of matter)**  
Experimental Study of Phase Equilibria in the "FeO"-ZnO(CaO + SiO<sub>2</sub>) System with the CaO/SiO<sub>2</sub> Weight Ratio of 0.71 at Metallic Iron Saturation. 865-876B  
Experimental Study of Phase Equilibria in the "FeO"-ZnO(CaO + SiO<sub>2</sub>) System with CaO/SiO<sub>2</sub> Weight Ratios of 0.33, 0.93, and 1.2 in Equilibrium with Metallic Iron. 877-890B
- Levitation casting**  
Communication: Physical modeling of the effects of thermal buoyancy driven flows in aluminum casters. 321-324B
- Levitation melting**  
Communication: Manganese Deoxidation Equilibrium in Liquid Fe-36 Pct Ni Alloy at 1773 K. 930-932B  
Direct observation of the crystal-growth transition in under-cooled silicon. 2947-2953A
- Life cycle assessment**  
Communication: Thermal Scaling Behavior of Weldments of 9Cr-1Mo Steel and Its Relevance to the Life Assessment of Fossil Fuel Power Plant Components. 3296-3297A
- Liquid flow**  
Molten Wood's-Metal Flow in a Cylindrical Bath Agitated by Cold Bottom Gas Injection. 695-702B
- Liquid metals**  
The equilibrium partitioning of titanium between Ti<sup>3+</sup> and Ti<sup>4+</sup> valency states in CaO-SiO<sub>2</sub>-TiO<sub>2</sub> slags. 61-67B  
In-situ formation of SiC-reinforced Al-Si alloy composites using methane gas mixtures. 543-550B  
Communication: Reduced critical solidification front velocity of particle engulfment due to an interface active solute in the liquid metal. 1869-1873A  
Reactive Infiltration of 25 Vol Pct TiO<sub>2</sub>/Al Composites. 2155-2162A  
Carbide formation in alloy 718 during electron-beam solid free-form fabrication. 2559-2567A  
Interfacial reactions in aluminosilicate short fiber-reinforced aluminum matrix composites. 2755-2761A
- Liquid metals, Magnetic properties**  
A New Method for Three-Dimensional Numerical Simulation of Electromagnetic and Fluid-Flow Phenomena in Electromagnetic Separation of Inclusions from Liquid Metal. 775-785B
- Liquid metals, Physical properties**  
Molten Wood's-Metal Flow in a Cylindrical Bath Agitated by Cold Bottom Gas Injection. 695-702B  
Estimation Of Viscosity Of Ternary-Metallic Melts. 3201-3204A
- Liquid metals, Reactions (chemical)**  
Thermodynamics on the Formation of Spinel (MgO-Al<sub>2</sub>O<sub>3</sub>) Inclusion in Liquid Iron Containing Chromium. 703-709B
- Liquid phase sintering**  
Diffusion-based model for isothermal solidification kinetics during transient liquid-phase sintering. 117-124A
- Liquid phases**  
Experimental Study of Phase Equilibria in the "FeO"-ZnO(CaO + SiO<sub>2</sub>) System with the CaO/SiO<sub>2</sub> Weight Ratio of 0.71 at Metallic Iron Saturation. 865-876B
- Liquidus**  
Phase Equilibrium Studies in the "MnO"-Al<sub>2</sub>O<sub>3</sub>-SiO<sub>2</sub> System. Phase Equilibrium Data and Liquidus for the System "MnO"-CaO-(Al<sub>2</sub>O<sub>3</sub> + SiO<sub>2</sub>) at Al<sub>2</sub>O<sub>3</sub>/SiO<sub>2</sub> = 0.41. 827-838B  
Experimental Liquidus in the PbO-ZnO-Fe<sub>2</sub>O<sub>3</sub>-(CaO + SiO<sub>2</sub>) System in Air, with CaO/SiO<sub>2</sub> = 0.35 and PbO/(CaO + SiO<sub>2</sub>) = 3.2. 851-863B  
Experimental Study of Phase Equilibria in the "FeO"-ZnO(CaO + SiO<sub>2</sub>) System with the CaO/SiO<sub>2</sub> Weight Ratio of 0.71 at Metallic Iron Saturation. 865-876B  
Experimental Study of Phase Equilibria in the "FeO"-ZnO(CaO + SiO<sub>2</sub>) System with CaO/SiO<sub>2</sub> Weight Ratios of 0.33, 0.93, and 1.2 in Equilibrium with Metallic Iron. 877-890B  
Thermodynamic Study of MnO-SiO<sub>2</sub>-Al<sub>2</sub>O<sub>3</sub> Slag System: Liquidus Lines and Activities of MnO at 1823 K. 915-920B  
On differential thermal analyzer curves for the melting and freezing of alloys. 1779-1794A  
On the Constitution of the System Al-Mn-Si. 3311-3319A
- Lithium, Alloying elements**  
Recycling of magnesium alloys: chemical equilibria between magnesium-lithium-based melts and salt melts. 355-364B
- Lost foam casting**  
Computational fluid-dynamics modeling of the hydrodynamics of fluidization in the sand surrounding a lost-foam casting pattern. 565-575B
- Low alloy steels, Casting**  
Development of New Feeding-Distance Rules Using Casting Simulation: Part I. Methodology. 731-740B  
Development of New Feeding-Distance Rules Using Casting Simulation: Part II. The New Rules. 741-755B
- Low alloy steels, Welding**  
Sensitization behavior of type 308 stainless steel weld metals after postweld heat treatment and low-temperature aging and its relation to microstructure. 1743-1754A
- Low carbon steels, Casting**  
A theoretical and experimental study of continuous-casting tundishes focusing on slag-steel interaction. 173-185B
- Low carbon steels, Coating**  
Correlation of microstructure and wear resistance of ferrous coatings fabricated by atmospheric plasma spraying. 2933-2945A
- Low carbon steels, Mechanical properties**  
Change of Critical Events of Cleavage Fracture with Variation of Microscopic Features of Low-Alloy Steels. 3393-3402A
- Low carbon steels, Metal working**  
The production of ultrafine ferrite in low-carbon steel by strain-induced transformation. 1019-1026A  
Texture and microstructure development during intercritical rolling of low-carbon steels. 1589-1603A
- Low carbon steels, Microstructure**  
In-situ observation of the precipitation of manganese sulfide in low-carbon magnesium-killed steel. 427-436A  
Microstructural evolution of a shaped-charge liner and target materials during ballistic tests. 1069-1074A
- Low carbon steels, Nondestructive testing**  
Direct measurements of grain size in low-carbon steels using the laser ultrasonic technique. 687-691A
- Low carbon steels, Phase transformations**  
Effect of composition and austenite deformation on the transformation characteristics of low-carbon and ultra-low-carbon microalloyed steels. 1331-1349A  
Simulation of ferrite growth in continuously cooled low-carbon iron alloys. 2309-2316A
- Low carbon steels, Structural hardening**  
Communication: Microstructural interpretation of negligible strain-hardening behavior of submicrometer-grained low-carbon steel during tensile deformation. 705-707A
- Low carbon steels, Welding**  
Missed Joint Induced by Thermoelectric Magnetic Field in Electron-Beam Welding Dissimilar Metals-Experiment and Scale Analysis. 765-773B
- Low cycle fatigue**  
Communication: Infrared imaging during low-cycle fatigue of Ti-12Al alloy. 1287-1292A  
Tensile, creep, and low-cycle fatigue behavior of a cast γ-TiAl-based alloy for gas turbine applications. 2869-2881A
- Low temperature**  
Low-temperature extension of the Lehrer diagram and the iron-nitrogen phase diagram. 2593-2598A
- Lutetium, Extraction**  
Communication: Removal of phosphorus-based extractant contamination from lutetium oxalate produced by precipitation stripping. 146-147B
- Macroporosity**  
Effects of Macroscopic Pores on the Damping Behavior of Foamed Commercially Pure Aluminum. 3565-3568A
- Magnesium, Microstructure**  
Nonbasal deformation modes of Hcp metals and alloys: role of dislocation source and mobility. 813-822A  
Effect of temperature and shear direction on yield stress by {112̄}<112̄> slip in hcp metals. 831-836A  
Transmission electron microscopy investigation of <c + a> dislocations in Mg and α-solid solution Mg-Li alloys. 851-858A
- Magnesium, Reactions (chemical)**  
Communication: Manganese Deoxidation Equilibrium in Liquid Fe-36 Pct Ni Alloy at 1773 K. 930-932B
- Magnesium, Welding**  
Electron-beam welding behavior in Mg-Al-based alloys. 1461-1473A
- Magnesium base alloys, Crystal growth**  
The microstructural development of Mg-9 pct Al-1 pct Zn alloy during injection molding. 2963-2972A
- Magnesium base alloys, Materials substitution**  
Creep and microstructure of magnesium-aluminum-calcium based alloys. 567-574A
- Magnesium base alloys, Mechanical properties**  
Denuded zones, diffusional creep, and grain boundary sliding. Creep strength of magnesium-based alloys. 219-229A  
Creep processes in magnesium alloys and their composites. 875-882A  
883-889A
- Magnesium base alloys, Microstructure**  
Transmission electron microscopy investigation of <c + a> dislocations in Mg and α-solid solution Mg-Li alloys. 851-858A  
Crystallization kinetics of amorphous magnesium-rich magnesium-copper and magnesium-nickel alloys. 1041-1050A
- Magnesium base alloys, Reactions (chemical)**

- Communication: Solubility of Iron Magnesium-Lithium Melts. 929-930B
- Magnesium base alloys, Recycling**  
Recycling of magnesium alloys: chemical equilibria between magnesium-lithium-based melts and salt melts. 355-364B
- Magnesium base alloys, Welding**  
Electron-beam welding behavior in Mg-Al-based alloys. 1461-1473A
- Magnetic fields**  
Missed Joint Induced by Thermoelectric Magnetic Field in Electron-Beam Welding Dissimilar Metals-Experiment and Scale Analysis. 765-773B
- Magnetic measurements**  
On the Nature of the Electrochemically Synthesized Hard Fe-0.96 Mass Pct C Alloy Film. 921-927B
- Magnetization**  
A novel technique for manufacturing metal-bonded Nd-Fe-B magnets by squeeze casting. 637-646A
- Magnetohydrodynamics**  
A New Method for Three-Dimensional Numerical Simulation of Electromagnetic and Fluid-Flow Phenomena in Electromagnetic Separation of Inclusions from Liquid Metal. 775-785B
- Manganese, Diffusion**  
In-situ observation of the precipitation of manganese sulfide in low-carbon magnesium-killed steel. 427-436A
- Manganese, Powder technology**  
Structure of a Fe-Cr-Mn-Mo-N Alloy Processed by Mechanical Alloying. 3273-3278A
- Manganese, Ternary systems**  
On the Constitution of the System Al-Mn-Si. 3311-3319A
- Manganese base alloys, Reactions (chemical)**  
Kinetics of Silver Leaching from Manganese-Silver Associated Ores in Sulfuric Acid Solution in the Presence of Hydrogen Peroxide. 813-816B
- Manganese compounds, Phase transformations**  
Massive transformation and the formation of the ferromagnetic  $L_{10}$  phase in manganese-aluminum-based alloys. 2413-2423A
- Manganese compounds, Phases (state of matter)**  
Phase Equilibrium Studies in the  $MnO-Al_2O_3-SiO_2$  System. Phase Equilibrium Data and Liquidus for the System  $MnO-CaO-(Al_2O_3 + SiO_2)$  at  $Al_2O_3/SiO_2 = 0.41$ . 827-838B  
839-849B
- Manganese compounds, Reactions (chemical)**  
Thermodynamic Study of  $MnO-SiO_2-Al_2O_3$  Slag System: Liquidus Lines and Activities of  $MnO$  at 1823 K. 915-920B
- Manganese compounds, Reduction (chemical)**  
Kinetics of manganese reduction leaching from weathered rare-earth mud with sodium sulfite. 41-46B
- Manganese ores, Reactions (chemical)**  
Kinetics of Silver Leaching from Manganese-Silver Associated Ores in Sulfuric Acid Solution in the Presence of Hydrogen Peroxide. 813-816B
- Manganese steels, Heat treatment**  
Precipitation of austenite particles at grain boundaries during aging of Fe-Mn-Ni steel. 1057-1067A
- Manganese steels, Mechanical properties**  
Carbide precipitation and high-temperature strength of hot-rolled high-strength, low-alloy steels containing Nb and Mo. 1689-1698A
- Manganese steels, Phase transformations**  
The production of ultrafine ferrite during hot torsion testing of a 0.11 Wt pct C steel. 2985-2993A
- Martensite**  
Effect of Martensite Content on Friction and Oxidative Wear Behavior of 0.42 Pct Carbon Dual-Phase Steel. 3479-3488A
- Martensite, Crystal growth**  
Method for Measuring Transformation Energy and Quantitative Characterization of Transformation-Induced Plasticity. 3117-3120A
- Martensite, Mechanical properties**  
Shape Memory Behavior of FeNiCoTi Single and Polycrystals 3661-3672A
- Martensitic stainless steels, Brazing**  
Infrared repair brazing of 403 stainless steel with a nickel-based braze alloy. 1765-1773A
- Martensitic stainless steels, Mechanical properties**  
Microstructural stability during creep of Mo- or W-bearing 12Cr steels. 2549-2557A  
Communication: Strengthening of Virgin Martensite through Cryogenic Deformation. 3576-3578A
- Martensitic stainless steels, Microstructure**  
Rapid Solidification of Martensitic Stainless Steel Atomized Droplets. 3755-3760A
- Martensitic transformations**  
Communication: Comments on a recent infinitesimal-deformation approach to martensite crystallography. 203A  
Author's reply [to Comments on a recent infinitesimal-deformation approach to martensite crystallography]. 204A  
In-situ measurement of continuous cooling  $\beta \rightarrow \alpha$  transformation behavior of CP-Ti. 1051-1056A  
Microstructural evolution of a shaped-charge liner and target materials during ballistic tests. 1069-1074A  
Dislocation-disclination model of heterogeneous martensite nucleation in transformation-induced-plasticity steels. 1351-1362A  
Relationship between Austenite Dislocation Density Introduced during Thermal Cycling and  $M_s$  Temperature in an Fe-17 Wt Pct Mn Alloy. 1913-1917A  
Comparison of interfacial structure-related mechanisms in diffusional and martensitic transformations. 2541-2547A  
Influence of Al and Ni concentration on the martensitic transformation in Cu-Al-Ni shape-memory alloys. 2581-2591A  
Enhancement of superelasticity in Cu-Al-Mn-Ni shape-memory alloys by texture control. 2817-2824A  
Young's Modulus and Mechanical Properties of Ti-29Nb-13Ta-4.6Zr in Relation to  $\alpha'$  Martensite. 3137-3144A
- Mass transfer**  
Averaged solute transport during solidification of a binary mixture: active dispersion in dendritic structures. 365-376B  
A unified microscale parameter approach to solidification-transport process-based macrosegregation modeling for dendritic solidification. II. Numerical example computations. 451-463B  
Thermal debinding modeling of mass transport and deformation in powder-injection molding compact. 477-488B  
Anisotropy of point defect diffusion in alpha-zirconium. 777-782A  
Mobility of interstitial clusters in alpha-zirconium. 783-789A  
Diffusion along grain and interphase boundaries in Alpha Zr and Zr-2.5 Wt Pct Nb alloy. 797-800A  
Modeling of Globular Equiaxed Solidification with a Two-Phase Approach. 3673-3683A
- Massive type transformation**  
Massive transformations revisited. 2277-2283A  
Mechanisms of the massive transformation. 2285-2297A  
Critical limit for massive transformation. 2299-2308A  
Simulation of ferrite growth in continuously cooled low-carbon iron alloys. 2309-2316A  
Massive transformation and absolute stability. 2337-2345A  
Origins of internal structure in massive transformation products. 2347-2351A  
Massive-parent interphase boundaries and their implications on the mechanisms of the  $\alpha \rightarrow \gamma_M$  massive transformation in Ti-Al alloys. 2353-2371A  
The massive transformation in titanium aluminides: initial stages of nucleation and growth. 2373-2379A  
Orientation and structure of planar facets on the  $\gamma_m$  massive phase in a near-TiAl alloy. 2381-2389A  
Static and in-situ high-resolution transmission electron microscopy investigations of the atomic structure and dynamics of massive transformation interfaces in a Ti-Al alloy. 2391-2411A  
Massive transformation and the formation of the ferromagnetic  $L_{10}$  phase in manganese-aluminum-based alloys. 2413-2423A  
Isothermal transformations in an Fe-9 pct Ni alloy. 2425-2431A  
General discussion session of the symposium on "The mechanisms of the massive transformation" 2445-2470A
- Mathematical models**  
The fracture toughness and toughening mechanisms of nickel-base wear materials. 33-56A  
An analytical self-consistent determination of a bubble with a deformed cap trapped in solid during solidification. 91-100B  
Mathematical modeling of the argon-oxygen decarburization refining process of stainless steel: Part I. Mathematical model of the process. 111-119B  
Diffusion-based model for isothermal solidification kinetics during transient liquid-phase sintering. 117-124A  
Mathematical modeling of the argon-oxygen decarburization refining process of stainless steel: Part II. Application of the model to industrial practice. 121-127B  
Kinetics of formation and dissociation of  $Na_2SiF_6$  bubbles formation and detachment on nonwetting surfaces. 129-136B  
Simulation of the submerged energy nozzle-mold water model system using laser-optical and computational fluid dynamics methods. 155-162B  
163-172B  
Communication: Comments on a recent infinitesimal-deformation approach to martensite crystallography. 203A  
Author's reply [to Comments on a recent infinitesimal-deformation approach to martensite crystallography]. 204A  
A three-phase model of hydrogen pore formation during the equiaxed dendritic solidification of aluminum-silicon alloys. 209-221B  
Creep at very low rates. 213-218A  
Modeling of primary spacing selection in dendrite arrays during directional solidification. 223-233B  
Predictive capabilities of the dislocation-network theory of Harper-Dorn creep. 231-239A  
Observations, theories, and predictions of high-temperature creep behavior. 241-248A  
Creep at low stresses: an evaluation of diffusion creep and Harper-Dorn creep as viable creep mechanisms. 249-259A  
Atomistic modeling of quaternary alloys: Ti and Cu in NiAl. 265-284B  
Understanding creep - a review. 291-303A  
Mathematical modeling and computer simulation of the rotating impeller particle flotation process: Part I. Fluid flow. 297-303B  
Mathematical modeling and computer simulation of the rotating impeller particle flotation process: Part II. Particle agglomeration and flotation. 305-314B  
Harper-Dorn creep and specimen size. 305-310A  
Subgrain formation during deformation: physical origin and consequences. 319-327A  
Communication: Physical modeling of the effects of thermal buoyancy driven flows in aluminum casters. 321-324B  
Application of a modified jogged-screw model for creep of TiAl and  $\alpha$ -Ti alloys. 329-336A  
A framework for modeling creep in pure metals. 363-371A  
Averaged solute transport during solidification of a binary mixture: active dispersion in dendritic structures. 365-376B  
Constitutive equations for creep and plasticity of aluminum alloys produced by powder metallurgy and aluminum-based metal matrix composites. 373-381A  
A water model and numerical study of the spout height in a gas-stirred vessel. 377-384B  
Some selected topics in creep cavitation. 383-390A  
Rate of nitrogen desorption from  $CaO-Al_2O_3$  melts to gas phase. 393-401B  
Control of heat transfer and growth uniformity of solidifying



copper shells through substrate temperature.	403-411B	Welding Process.	2043-2052A
Thermal and mechanical behavior of copper molds during thin-slab casting. I. Plant trial and mathematical modeling.	425-436B	Hydrogen Evolution during Directional Solidification and Its Effect on Porosity Formation in Aluminum Alloys.	2067-2072A
Numerical simulation of dendrite white spot formation during vacuum arc remelting of INCONEL718.	443-454A	Two-Phase Modeling Directed Toward Hot Tearing Formation in Aluminum Direct Chill Casting.	2081-2093A
A unified microscale parameter approach to solidification-transport process-based macrosegregation modeling for dendritic solidification. II. Numerical example computations.	451-463B	Modeling of Microporosity, Macroporosity, and Pipe-shrinkage Formation during the Solidification of Alloys Using a Mushy-Zone Refinement Method: Applications to Aluminum Alloys.	2095-2106A
Erratum: Shear principal, and equivalent strains in equal-channel angular deformation.	467A	Solidification Thermal Parameters Affecting the Columnar-to-Equiaxed Transition.	2107-2118A
Thermal debinding modeling of mass transport and deformation in powder-injection molding compact.	477-488B	On Composite-Structure Weaknesses: Part II. Computer Experiments, Identification, and Correlation.	2217-2227A
Communication: Foaming behavior of slags.	499-501B	Misfit dislocations in epitaxy.	2475-2483A
Communication: Prediction of the thermodynamic properties of solutes in the Bi-based ternary dilute solution.	502-506B	Reciprocal-space formulation and prediction of misfit accommodation in rigid and strained epitaxial systems.	2485-2494A
Modeling the kinetics of grain-boundary-nucleated recrystallization processes after cold deformation.	529-537A	Analysis of the Cu-3 Wt pct Ti cellular interphase boundary by various models.	2495-2505A
Computational fluid-dynamics modeling of the hydrodynamics of fluidization in the sand surrounding a lost-foam casting pattern.	565-575B	The cellular interlamellar and growth-front interphase boundaries in Cu-3 Wt pct Ti.	2507-2518A
Thermodynamics of liquid Al-Na alloys determined by using CaF <sub>2</sub> solid electrolyte.	577-587B	Residual stresses in a welded superalloy disc: characterization using synchrotron diffraction and numerical process modeling.	2921-2931A
Three-dimensional investigation of long-range internal stresses in a single crystal deforming by nonsymmetrical slip.	591-596A		
Rayleigh-Benard convection during solidification of an eutectic solution cooled from the top.	605-612B	<b>Mattes</b>	
Correction to "Simulation of the submerged energy nozzle-mold water model systems using laser optical and computational fluid dynamics methods"	639B	Slags and mattes in Vanyukov's process for the extraction of copper.	551-559B
Molten Wood's-Metal Flow in a Cylindrical Bath Agitated by Cold Bottom Gas Injection.	695-702B	Physicochemical properties of matte-slag melts taken from Vanyukov's furnace for copper extraction.	561-564B
First-principles investigation of perfect and diffuse antiphase boundaries in hcp-based Ti-Al alloys.	735-741A		
Intergranular stresses in ZIRCALOY-2.	749-755A	<b>Mechanical alloying</b>	
A study of twinning in zirconium using neutron diffraction and polycrystalline modeling.	757-763A	Solid-state crystalline-glassy cyclic phase transformations of mechanically alloyed Cu <sub>35</sub> Zr <sub>65</sub> powders.	135-143A
A New Method for Three-Dimensional Numerical Simulation of Electromagnetic and Fluid-Flow Phenomena in Electromagnetic Separation of Inclusions from Liquid Metal.	775-785B	Microstructural and fracture characterization of Nb-Cr-Ti mechanically alloyed materials.	401-416A
Modeling of the Continuous Casting of Steel-Past, Present, and Future.	795-812B	Formation of a TiB <sub>2</sub> -reinforced copper-based composite by mechanical alloying and hot pressing.	1275-1280A
Communication: On the Estimation of Plume Rise Velocity in Gas-Stirred Ladles.	937-941B	Development of Austenitic Nanostructures in High-Nitrogen Steel Powders Processed by Mechanical Alloying.	2139-2144A
Energy of the Pb{111}   Al{111} interface.	1003-1007A	Thermally Enhanced and Mechanically Driven Glass Formation Reactions of Multilayered Cu <sub>35</sub> Zr <sub>65</sub> Powders.	2145-2153A
Finite element modeling of the morphology of $\beta$ to $\alpha$ phase transformation in Ti-6Al-4V alloy.	1027-1040A	Origin of porosity in oxide-dispersion-strengthened alloys produced by mechanical alloying.	2713-2718A
Theory for growth of needle-shaped particles in multicomponent systems.	1075-1081A	Grain-size control in Ti-48Al-2Cr-2Nb with yttrium additions.	2729-2736A
Symmetry-breaking transitions in equilibrium shapes of coherent precipitates: effect of elastic anisotropy and inhomogeneity.	1083-1090A	Evolution of Submicrocrystalline Iron Containing Dispersed Oxides under Mechanical Milling Followed by Consolidation.	3241-3248A
Analysis of steady-state thermal creep of Zr-2.5Nb pressure tube material.	1103-1115A	Structure of a Fe-Cr-Mn-Mo-N Alloy Processed by Mechanical Alloying.	3273-3278A
Shrinkage and splitting of microcracks under pressure simulated by the finite-element method.	1117-1124A	Mechanical, Intergranular Corrosion, and Wear Behavior of Aluminum-Matrix Composite Materials Reinforced with Nickel Aluminides.	3541-3553A
Toughness-strength relations in the overaged 7449 Al-based alloy.	1125-1136A		
A critical-strain criterion for hydrogen embrittlement of cold-drawn, ultrafine pearlitic steel.	1151-1166A	<b>Mechanisms</b>	
Toward prediction of microstructural evolution during laser surface alloying.	1189-1200A	The fracture toughness and toughening mechanisms of nickel-base wear materials.	33-56A
Communication: The Gibbs-Thomson effect in dilute binary systems.	1283-1287A	Fatigue crack initiation and propagation of binder-treated powder metallurgy steels.	73-81A
Metastable phases in the Ti-V system. I. Neutron diffraction study and assessment of structural properties.	1307-1317A	Diffusion-based model for isothermal solidification kinetics during transient liquid-phase sintering.	117-124A
Dislocation-clincination model of heterogeneous martensite nucleation in transformation-induced-plasticity steels.	1351-1362A	Averaged solute transport during solidification of a binary mixture: active dispersion in dendritic structures.	365-376B
Role of yield criteria and hardening laws in the prediction of forming limit diagrams.	1363-1371A	Modeling the formation of longitudinal facial cracks during continuous casting of hypopercutic steel.	413-423B
An integrated computer model with applications for austenite-to-ferrite transformation during hot deformation of Nb-microalloyed steels.	1509-1520A	Anisotropy of point defect diffusion in alpha-zirconium.	777-782A
Communication: Interpretation of flow instability using dynamic material modeling.	1569-1572A	Mobility of interstitial clusters in alpha-zirconium.	783-789A
Tree-ring formation during vacuum arc remelting of INCONEL 718. I. Experimental investigation.	1795-1804A	Grain-boundary diffusion by vacancy mechanism in $\alpha$ -Ti and $\alpha$ -Zr.	791-796A
Tree-ring formation during vacuum arc remelting of INCONEL 718. II. Mathematical modeling.	1805-1815A	Diffusion along grain and interphase boundaries in Alpha Zr and Zr-2.5 Wt Pct Nb alloy.	797-800A
Modeling of laser keyhole welding. I. Mathematical modeling, numerical methodology, role of recoil pressure, multiple reflections, and free surface evolution.	1817-1830A	Observations of room-temperature creep recovery in titanium alloys.	891-898A
Modeling of laser keyhole welding. II. Simulation of keyhole evolution, velocity, temperature profile, and experimental verification.	1831-1842A	Crystallization kinetics of amorphous magnesium-rich magnesium-copper and magnesium-nickel alloys.	1041-1050A
Communication: Discussion of "coarsening of intermetallic or compound precipitates in binary systems".	1859-1860A	Theory for growth of needle-shaped particles in multicomponent systems.	1075-1081A
Communication: Author's reply to "Discussion of 'Coarsening of intermetallic or compound precipitates in binary systems'".	1860-1862A	Shrinkage and splitting of microcracks under pressure simulated by the finite-element method.	1117-1124A
Communication: Reduced critical solidification front velocity of particle engulfment due to an interface active solute in the liquid metal.	1869-1873A	A critical-strain criterion for hydrogen embrittlement of cold-drawn, ultrafine pearlitic steel.	1151-1166A
Inferring Dynamic Recrystallization in Ferrite using the Kinetics of Static Recrystallization.	1893-1900A	Dislocation-clincination model of heterogeneous martensite nucleation in transformation-induced-plasticity steels.	1351-1362A
Sequences of Phase Formation in Multiphase Stressed Plates. Relationship between $\lambda$ -ustenite Dislocation Density Introduced during Thermal Cycling and $M_s$ Temperature in an Fe-17 Wt Pct Mn Alloy.	1901-1911A	Texture and microstructure development during intercritical rolling of low-carbon steels.	1589-1603A
Artificial Neural Network and Finite Element Modeling of Nanoindentation Tests.	1913-1917A	On the roles of clusters during intragranular nucleation in the absence of static defects.	1649-1658A
Constitutive Behavior of As-Cast AM 050, AA3104, and AA5182.	1939-1947A	Fracture toughness of alloy 690 and EN52 welds in air and water.	1725-1735A
A Unified Numerical Modeling of Stationary Tungsten-InertGas	1971-1980A	Modeling of laser keyhole welding. I. Mathematical modeling, numerical methodology, role of recoil pressure, multiple reflections, and free surface evolution.	1817-1830A



- on the mechanisms of the  $\alpha \rightarrow \gamma_M$  massive transformation in Ti-Al alloys. 2353-2371A
- The massive transformation in titanium aluminides: initial stages of nucleation and growth. 2373-2379A
- Orientation and structure of planar facets on the  $\gamma_M$  massive phase in a near-TiAl alloy. 2381-2389A
- Isothermal transformations in an Fe-9 pct Ni alloy. 2425-2431A
- General discussion session of the symposium on "The mechanisms of the massive transformation" 2445-2470A
- Comparison of interfacial structure-related mechanisms in diffusional and martensitic transformations. 2541-2547A
- Quantitative characterization of three-dimensional damage evolution in a wrought Al-alloy under tension and compression. 2599-2606A
- Visualization of the hydrogen desorption process from ferrite, pearlite, and graphite by secondary ion mass spectrometry. 2659-2665A
- Effects of Au plating on small-scale resistance spot welding of thin-sheet nickel. 2667-2676A
- Medium carbon steels, Coating**
- Powder Eutectic Coating With  $Al_3Ti$  For Steels. 3235-3240A
- Medium carbon steels, Composite materials**
- The incorporation of self-propagating, high-temperature synthesis-formed Fe-TiB<sub>2</sub> into ferrous melts. 2973-2983A
- Medium carbon steels, Heat treatment**
- Spheroidization cycles for medium carbon steels. 1255-1261A
- Interrupted bonding of medium-carbon steels. 1475-1485A
- Melt spinning**
- Crystallization kinetics of amorphous magnesium-rich magnesium-copper and magnesium-nickel alloys. 1041-1050A
- Melting**
- Recycling of magnesium alloys: chemical equilibria between magnesium-lithium-based melts and salt melts. 355-364B
- Modeling of Globular Equiaxed Solidification with a Two-Phase Approach. 3673-3683A
- Melting points**
- Communication: Microstructures and mechanical properties of (Ir,Rh)<sub>75</sub>Nb<sub>15</sub>Ni<sub>10</sub> alloys. 1281-1283A
- On differential thermal analyzer curves for the melting and freezing of alloys. 1779-1794A
- A study of the Pb/Al (100) interfacial energy. 2569-2572A
- Melts**
- Communication: Physical modeling of the effects of thermal buoyancy driven flows in aluminum casters. 321-324B
- Metal matrix composites, Casting**
- Intermetallic-reinforced light-metal matrix in-situ composites. A novel technique for manufacturing metal-bonded Nd-Fe-B magnets by squeeze casting. 193-201A
- 637-646A
- Metal matrix composites, Mechanical properties**
- Microscale Elastic Strain Evolution Following Damage in Ti-SiC Composites. 3839-3845A
- Effect of Overaging and Particle Size on Tensile Deformation and Fracture of Particle-Reinforced Aluminum Matrix Composites. 3861-3869A
- Metal matrix composites, Metal working**
- Kinetics of biaxial dome formation by transformation superplasticity of titanium alloys and composites. 1669-1680A
- Metal matrix composites, Powder technology**
- Solidification paths and reinforcement morphologies in melt-processed (TiB + TiC)/Ti in situ composites. 3055-3063A
- Metal matrix composites, Synthesis**
- Reactive Infiltration of 25 Vol Pct TiO<sub>2</sub>/Al Composites. 2155-2162A
- Metal matrix composites, Welding**
- Communication: Comparative Welding Study of Metal Matrix Composites with the MIG Welding Process, using Direct and Indirect Electric Arc. 932-937B
- Metallic glasses**
- Thermally Enhanced and Mechanically Driven Glass Formation Reactions of Multilayered Cu<sub>33</sub>Zr<sub>67</sub> Powders. 2145-2153A
- Metallic glasses, Composite materials**
- A novel technique for manufacturing metal-bonded Nd-Fe-B magnets by squeeze casting. 637-646A
- Metastable phases**
- Solid-state crystalline-glassy cyclic phase transformations of mechanically alloyed Cu<sub>33</sub>Zr<sub>67</sub> powders. 135-143A
- Crystallization kinetics of amorphous magnesium-rich magnesium-copper and magnesium-nickel alloys. 1041-1050A
- Metastable phases in the Ti-V system. I. Neutron diffraction study and assessment of structural properties. 1307-1317A
- Sequences of Phase Formation in Multiphase Stressed Plates. 1901-1911A
- Microalloying**
- Effect of composition and austenite deformation on the transformation characteristics of low-carbon and ultralow-carbon microalloyed steels. 1331-1349A
- Microcracks**
- Shrinkage and splitting of microcracks under pressure simulated by the finite-element method. 1117-1124A
- Correlation of Microstructure with Wear and Fracture Properties of Two-Layered VC/Ti-6Al-4V Surface Composites Fabricated by High-Energy Electron-Beam Irradiation. 3173-3185A
- Microelectromechanical systems, Fabrication**
- Microstructural and mechanical properties investigation of electrodeposited and annealed LIGA nickel structures. 539-554A
- Microhardness**
- Characterization of a friction-stir-welded aluminum alloy 6013. 489-498B
- Microstructural evolution of a shaped-charge liner and target materials during ballistic tests. 1069-1074A
- An investigation of the microstructure and strength of open-cell 6101 aluminum foams. 1413-1427A
- Infrared repair brazing of 403 stainless steel with a nickel-based braze alloy. 1765-1773A
- Communication: Thermal stability and microstructural evolution in ultrafine-grained nickel after equal-channel angular pressing (ECAP). 1865-1868A
- Formation and Annealing Behavior of Nanocrystalline Ferrite in Fe-0.89C Spheroidite Steel Produced by Ball Milling. 2195-2203A
- Communication: Strengthening of Virgin Martensite through Cryogenic Deformation. 3576-3578A
- Microminiaturization**
- Artificial Neural Network and Finite Element Modeling of Nanoindentation Tests. 1939-1947A
- Microporosity**
- Microporosity prediction in aluminum alloy castings. 243-255B
- Microstrain**
- Intergranular stresses in ZIRCALOY-2. 749-755A
- Determination of dislocation densities in Hcp metals from X-ray diffraction line-broadening analysis. 859-865A
- Distribution of c- and a-dislocations in tubes of Zr alloys. 867-874A
- Symmetry-breaking transitions in equilibrium shapes of coherent precipitates: effect of elastic anisotropy and inhomogeneity. 1083-1090A
- On the Influence of N on Residual Microstrain in Cryomilled Ni. 3795-3801A
- Microstructural analysis**
- Comprehensive microstructural characterization in modified 9Cr-1Mo ferritic steel by ultrasonic measurements. 1617-1626A
- Effects of Macroscopic Pores on the Damping Behavior of Foamed Commercially Pure Aluminum. 3565-3568A
- Microstructural analysis, Automation**
- Advances in deformation twin characterization using electron backscattered diffraction data. 949-954A
- Microwelding**
- A Study on Heat Source Equations for the Prediction of Weld Shape and Thermal Deformation in Laser Microwelding. 757-764B
- Milling (machining)**
- On the Influence of N on Residual Microstrain in Cryomilled Ni. 3795-3801A
- Mischmetal, Additives**
- The effect of mischmetal addition on the structure and mechanical properties of a cast Al-7Si-0.3Mg alloy containing excess iron (up to 0.6 pct). 391-400A
- Miscibility**
- Phase Separation Tendency in the As-Solidified Zr3Al-Nb Alloys Studied by Microstructural Observations and Thermodynamic Analysis. 1919-1929A
- Mobility**
- Diffusion along grain and interphase boundaries in Alpha Zr and Zr-2.5 Wt Pct Nb alloy. 797-800A
- Modulus of elasticity**
- Young's Modulus and Mechanical Properties of Ti-29Nb-13Ta-4.6Zr in Relation to  $\alpha'$  Martensite. 3137-3144A
- Normalized Diagrams for Micromechanical Estimates of the Elastic Response of Composite Materials. 3187-3199A
- Molds, Materials selection**
- Thermal and mechanical behavior of copper molds during thin-slab casting. I. Plant trial and mathematical, modeling. 425-436B
- Molds, Mechanical properties**
- Thermal and mechanical behavior of copper molds during thin-slab casting. II. Mold crack formation. 437-449B
- Molds, Surface properties**
- Die soldering: mechanism of the interface reaction between molten aluminum alloy and tool steel. 465-476B
- Communication: Wettability of Al<sub>2</sub>O<sub>3</sub>-MgO substrates by molten aluminum. 506-509B
- Molecular dynamics**
- Static and in-situ high-resolution transmission electron microscopy investigations of the atomic structure and dynamics of massive transformation interfaces in a Ti-Al alloy. 2391-2411A
- Molybdenum, Alloying elements**
- Carbide precipitation and high-temperature strength of hot-rolled high-strength, low-alloy steels containing Nb and Mo. 1689-1698A
- Molybdenum, Powder technology**
- Deoxidation of molybdenum during vacuum sintering. 657-664A
- Structure of a Fe-Cr-Mn-Mo-N Alloy Processed by Mechanical Alloying. 3273-3278A
- Molybdenum, Surface properties**
- Dopant Particle Characterization and Bubble Evolution in Aluminum-Potassium-Silicon-Doped Molybdenum Wire. 3349-3356A
- Molybdenum base alloys, Mechanical properties**
- Measuring the Fracture Toughness of Molybdenum-0.5 pct Titanium-0.1 pct Zirconium and Oxide Dispersion-Strengthened Molybdenum Alloys using Standard and Subsize Bend Specimens. 3685-3707A
- Molybdenum compounds, Powder technology**
- Reduction of Fe<sub>2</sub>MoO<sub>4</sub> by hydrogen gas. 589-594B
- Molybdenum steels, Microstructure**
- Theory for growth of needle-shaped particles in multicomponent systems. 1075-1081A
- Monitoring**
- Simulation of the submerged energy nozzle-mold water model system using laser-optical and computational fluid dynamics methods. 163-172B
- A new unidirectional solidification method to study gray cast iron. 235-241B

- Time-resolved X-ray imaging of aluminum alloy solidification processes. 613-623B
- Correction to "Simulation of the submerged energy nozzle-mold water model systems using laser optical and computational fluid dynamics methods" 639B
- Communication: Infrared imaging during low-cycle fatigue of HR-120 alloy. 1287-1292A
- Morphology**
- Effect of heat treatments on in-situ  $\text{Al}_2\text{O}_3/\text{TiAl}_3$  composites produced from squeeze casting of  $\text{TiO}_2/\text{A356}$  composites. 31-40B
- Effect of cyclic pressure consolidation on the uniformity of metal matrix composites. 183-191A
- Strength of Al-Zn-Mg-Cu matrix composite reinforced with SiC particles. 455-465A
- Characterization of a friction-stir-welded aluminum alloy 6013. 489-498B
- Effect of loading condition and stress state on damage evolution of silicon particles in an Al-Si-Mg-base cast alloy. 555-565A
- Unexpected transient creep behavior of tin alloys strengthened by high volume fractions of SbSn. 575-580A
- Theory for growth of needle-shaped particles in multicomponent systems. 1075-1081A
- The effect of grain size on the ambient temperature creep deformation behavior of a beta Ti-14.8V alloy. 1137-1144A
- A critical-strain criterion for hydrogen embrittlement of cold-drawn, ultrafine pearlitic steel. 1151-1166A
- Communication: Microstructures and mechanical properties of  $(\text{Ir,Rh})_{75}\text{Nb}_{15}\text{Ni}_{10}$  alloys. 1281-1283A
- Elevated temperature strength and room-temperature toughness of directionally solidified Ni-33Al-33Cr-1Mo. 1385-1397A
- Phenomenological observations on mechanical and corrosion properties of thixoformed 357 alloys: a comparison with permanent mold cast 357 alloys. 1399-1412A
- An investigation of the microstructure and strength of open-cell 6101 aluminum foams. 1413-1427A
- Age-hardening characteristics of aluminum alloy-hollow fly ash composites. 1541-1547A
- Effect of residual carbon on the sintering process of m2 high speed steel parts obtained by a modified metal injection molding process. 1843-1851A
- Phase Evolution in Laser-Deposited Titanium-Chromium Alloys. 2129-2138A
- Sintering Densification and Microstructural Evolution of Injection Molding Grade 17-4 PH Stainless Steel Powder. 2185-2194A
- On Composite-Structure Weaknesses: Part I. Simulation, Properties, and Numerical Approach. 2205-2215A
- On Composite-Structure Weaknesses: Part II. Computer Experiments, Identification, and Correlation. 2217-2227A
- General discussion session of the symposium on "The mechanisms of the massive transformation" 2445-2470A
- Carbide formation in alloy 718 during electron-beam solid free-form fabrication. 2559-2567A
- Effect of pearlite on the vibration-fracture behavior of spheroidal graphite cast irons under resonant conditions. 2623-2634A
- Grain-size control in Ti-48Al-2Cr-2Nb with yttrium additions. 2729-2736A
- Microstructure/processing relationships in reaction-synthesized titanium aluminide intermetallic matrix composites. 2747-2753A
- Segregation and morphological instability due to double-diffusive convection in rotational directional solidification. 3011-3017A
- Solidification Behavior of Sn-15 Wt Pct Pb Alloy under a High Shear Rate and High Intensity of Turbulence during Semi-solid Processing. 3511-3520A
- Morphology, Composition effects**
- The effect of mischmetal addition on the structure and mechanical properties of a cast Al-7Si-0.3Mg alloy containing excess iron (up to 0.6 pct). 391-400A
- Carbide precipitation and high-temperature strength of hot-rolled high-strength, low-alloy steels containing Nb and Mo. 1689-1698A
- Phase Separation Tendency in the As-Solidified Zr3Al-Nb Alloys Studied by Microstructural Observations and Thermodynamic Analysis. 1919-1929A
- Morphology, Cooling effects**
- Development of microstructural banding in low-alloy steel with simulated Mn segregation. 1627-1637A
- Morphology, Deformation effects**
- The production of ultrafine ferrite in low-carbon steel by strain-induced transformation. 1019-1026A
- Microstructural evolution of a shaped-charge liner and target materials during ballistic tests. 1069-1074A
- Microstructural evolution and mechanical properties of the AA8011 alloy during the accumulative roll-bonding process. 1521-1530A
- Comparative study of the impact response and microstructure of 304L stainless steel with and without prestrain. 2801-2810A
- Morphology, Heating effects**
- Precipitation of austenite particles at grain boundaries during aging of Fe-Mn-Ni steel. 1057-1067A
- Annealing behavior of alumina dispersion-strengthened copper strips rolled under different conditions. 1605-1616A
- Comprehensive microstructural characterization in modified 9Cr-1Mo ferritic steel by ultrasonic measurements. 1617-1626A
- Morphology, Pressure effects**
- The influence of the stress state on the plasticity of transformation induced plasticity-aided steel. 1659-1667A
- Morphology, Processing effects**
- Microstructural gradients in the superplastic forming of Ti-6Al-4V. 93-100A
- Microstructure evolution in Zr under equal channel angular pressing. 973-980A
- Formation of white layers in steels by machining and their characteristics. 1245-1254A
- A study on inhomogeneous distribution of temper graphite particles in strip-cast Fe-C-Si alloys. 1263-1273A
- Development of Austenitic Nanostructures in High-Nitrogen Steel Powders Processed by Mechanical Alloying. 2139-2144A
- An Investigation of Microstructure and Grain-Boundary Evolution during ECA Pressing of Pure Aluminum. 2173-2184A
- Morphology, Vibration effects**
- Structural refinement of gray iron by electromagnetic vibrations. 3025-3030A
- Mossbauer spectroscopy**
- On the Nature of the Electrochemically Synthesized Hard Fe-0.96 Mass Pct C Alloy Film. 921-927B
- Mud, Extraction**
- Kinetics of manganese reduction leaching from weathered rare-earth mud with sodium sulfite. 41-46B
- Multilayers, Microstructure**
- Microstructural Analysis of Multilayered Titanium Aluminide Sheets Fabricated by Hot Rolling and Heat Treatment. 3649-3659A
- Nanomaterials**
- A study of the Pb/Al (100) interfacial energy. 2569-2572A
- Nanostructure**
- Grain growth behavior of cryomilled INCONEL 625 powder during isothermal heat treatment. 125-134A
- Near-nanostructured WC-18 pct co coatings with low amounts of non-WC carbide phase: Part I. Synthesis and characterization. 145-157A
- Synthesis and nanoindentation study of high-velocity oxygen fuel thermal-sprayed nanocrystalline and near-nanocrystalline Ni coatings. 647-655A
- Subnanometer-scale chemistry and structure of  $\alpha$ -iron/molybdenum nitride heterophase interfaces. 2317-2326A
- Nanostructure, Processing effects**
- Solid-state crystalline-glassy cyclic phase transformations of mechanically alloyed  $\text{Cu}_{33}\text{Zr}_{67}$  powders. 135-143A
- Formation and Annealing Behavior of Nanocrystalline Ferrite in Fe-0.89C Spherulite Steel Produced by Ball Milling. 2195-2203A
- Nanostructure, Radiation effects**
- Localized deformation and hardening in irradiated metals: three-dimensional discrete dislocation dynamics simulations. 285-296B
- Near net shaping**
- Phase Evolution in Laser-Deposited Titanium-Chromium Alloys. 2129-2138A
- Neural networks**
- Artificial Neural Network and Finite Element Modeling of Nanoindentation Tests. 1939-1947A
- Neutrons**
- Localized deformation and hardening in irradiated metals: three-dimensional discrete dislocation dynamics simulations. 285-296B
- Nickel, Alloying elements**
- Isothermal transformations in an Fe-9 pct Ni alloy. 2425-2431A
- Nickel, Mechanical properties**
- Some selected topics in creep cavitation. 383-390A
- Nickel, Metal working**
- Communication: Thermal stability and microstructural evolution in ultrafine-grained nickel after equal-channel angular pressing (ECAP). 1865-1868A
- Nickel, Physical properties**
- On differential thermal analyzer curves for the melting and freezing of alloys. 1779-1794A
- Nickel, Solubility**
- Thermodynamic behavior of nickel in  $\text{CaO-SiO}_2\text{-Fe}_2\text{O}_3$  slag. 55-59B
- Nickel, Ternary systems**
- Phase equilibria of the ternary Ni-Cr-Zr system and interfacial reactions in the Ni-Cr/Zr couples. 995-1002A
- Statistical Self-Similarity in Rhines' Concept of Unique Multiphase Diffusion Paths on the Ternary Gibbs' Isotherm. 3357-3365A
- Diffusion Studies in the  $\beta$  ( $\text{B}_2$ ),  $\beta'$  (Bcc), and  $\gamma$  (Fcc) Fe-Ni-Al Alloys at 1000°C. 3375-3392A
- Nickel, Welding**
- Effects of Au plating on small-scale resistance spot welding of thin-sheet nickel. 2667-2676A
- Nickel base alloys, Casting**
- Microstructural characteristics of Ni-Sb eutectic alloys under substantial undercooling and containerless solidification conditions. 1221-1228A
- Elevated temperature strength and room-temperature toughness of directionally solidified Ni-33Al-33Cr-1Mo. 1385-1397A
- Tree-ring formation during vacuum arc remelting of INCONEL 718. I. Experimental investigation. 1795-1804A
- Tree-ring formation during vacuum arc remelting of INCONEL 718. II. Mathematical modeling. 1805-1815A
- Carbide formation in alloy 718 during electron-beam solid free-form fabrication. 2559-2567A
- Nickel base alloys, Coating**
- Phase formation and microstructure in sputter-deposited Ti-Mo-C and Ti-W-C thin films. 1579-1588A
- Communication: Depth Profiling of Hf-Doped Aluminide Coating by Glow-Discharge Mass Spectrometry. 3578-3582A
- Nickel base alloys, Composite materials**
- Large Self-Thermal-Plastic Deformation in a NiTi Shape-Memory Alloy Fiber-Actuated Aluminum Metal-Matrix Composite. 3535-3540A
- Nickel base alloys, Corrosion**
- Corrosion behavior of austenitic alloy 690 under anodic and cathodic potentials. 1437-1447A
- Nickel base alloys, Crystal growth**
- The Coarsening Kinetics of  $\gamma$  Particles in Nickel-Based Alloys. 3367-3373A

**Nickel base alloys, Crystal lattices**

Finite-element calculations of the lattice rotation field of a tensile-loaded nickel-based alloy multycrystal and comparison with topographical x-ray diffraction measurements.

2825-2833A

Communication: A New Face-Centered-Cubic Superlattice Structure in Rapidly Solidified Cu-4 Wt Pct Ti Alloy and Its Relevance to the Ordering Process in Ni-Mo and Other 1/2 0 Ordering Alloys.

3573-3576A

**Nickel base alloys, End uses**

Infrared repair brazing of 403 stainless steel with a nickel-based braze alloy.

1765-1773A

**Nickel base alloys, Joining**

Phase equilibria of the ternary Ni-Cr-Zr system and interfacial reactions in the Ni-Cr/Zr couples.

995-1002A

**Nickel base alloys, Materials substitution**

The effect of constraint-induced normal stress on the failure of notched TiAl components.

417-426A

**Nickel base alloys, Mechanical properties**

The fracture toughness and toughening mechanisms of nickel-base wear materials.

33-56A

Denuded zones, diffusional creep, and grain boundary sliding. Hydrogen embrittlement of nickel-titanium alloy in biological environment.

219-229A

Effect of directionally solidified microstructures on the room-temperature fracture-toughness properties of Ni-33(at. pct)Al-33Cr-1 Mo and Ni-33(at. pct)Al-31 Cr-3Mo eutectic alloys grown at different solidification rates.

495-501A

Communication: Infrared imaging during low-cycle fatigue of HR-120 alloy.

597-612A

Environmentally assisted, sustained-load crack growth in powder metallurgy nickel-based superalloys.

1287-1292A

Fracture toughness of alloy 690 and EN52 welds in air and water.

1681-1687A

Fatigue-Crack-Propagation Thresholds in a Nickel-Base Superalloy at High Frequencies and Temperatures.

1725-1735A

The Influence of Microstructure and Environment on the Crack Growth Behavior of Powder Metallurgy Nickel Superalloy RR1000.

1949-1962A

Some Observations of the Influence of  $\delta$ -Ferrite Content on the Hardness, Galling Resistance, and Fracture Toughness of Selected Commercially Available Iron-Based Hardfacing Alloys.

3165-3172A

Effect of Prolonged Isothermal Exposure on Elevated-Temperature, Time-Dependent Fatigue-Crack Propagation in INCONEL Alloy 783.

3403-3419A

On the Influence of N on Residual Microstrain in Cryomilled Ni.

3465-3478A

**Nickel base alloys, Melting**

Numerical simulation of dendrite white spot formation during vacuum arc remelting of INCONEL718.

3795-3801A

**Nickel base alloys, Microstructure**

Atomistic modeling of quaternary alloys: Ti and Cu in NiAl. Erratum: The Effects of deformation and pre-heat-treatment on abnormal grain growth in RENE 88 superalloy.

265-284B

Symmetry-breaking transitions in equilibrium shapes of coherent precipitates: effect of elastic anisotropy and inhomogeneity.

713A

Interphase boundary structure with irrational orientation relationship formed in grain boundary precipitation.

1083-1090A

**Nickel base alloys, Phase transformations**

Retardation of  $\alpha$ -phase transformation in modified superalloy RR2072.

2327-2335A

The production of ultrafine ferrite during hot torsion testing of a 0.11 Wt pct C steel.

1319-1330A

Changes in Order and Texture during Annealing of Heavily Cold-Rolled Ni<sub>3</sub>Al (B,Zr) Alloy

2985-2993A

**Nickel base alloys, Phases (state of matter)**

Diffusion Studies in the  $\beta$  (B<sub>2</sub>),  $\beta'$  (Bcc), and  $\gamma$  (Fcc) Fe-Ni-Al Alloys at 1000°C.

3605-3618A

**Nickel base alloys, Powder technology**

Grain growth behavior of cryomilled INCONEL 625 powder during isothermal heat treatment.

3375-3392A

**Nickel base alloys, Welding**

Missed Joint Induced by Thermoelectric Magnetic Field in Electron-Beam Welding Dissimilar Metals-Experiment and Scale Analysis.

125-134A

The Influence of Minor Elements on the Weldability of an INCONEL 718-Type Superalloy.

765-773B

Residual stresses in a welded superalloy disc: characterization using synchrotron diffraction and numerical process modeling.

2005-2017A

Inertia Welding Nickel-Based Superalloy: Part I. Metallurgical Characterization.

2921-2931A

Inertia Welding Nickel-Based Superalloy: Part II. Residual Stress Characterization.

3215-3225A

**Nickel chromium molybdenum steels, Mechanical properties**

Communication: Specimen Size Effects and Ductile Fracture of HY 100 Steel.

3227-3234A

**Nickel chromium steels, Steel making**

Mathematical modeling of the argon-oxygen decarburization refining process of stainless steel: Part II. Application of the model to industrial practice.

3293-3295A

**Nickel compounds, Casting**

Joining of NiAl to Iron-Based Alloys by Reactive Casting.

121-127B

**Nickel compounds, Coatings**

Communication: Depth Profiling of Hf-Doped Aluminate Coating by Glow-Discharge Mass Spectrometry.

2073-2080A

**Nickel compounds, Composite materials**

3578-3582A

Communication: Examination on the aging and tensile properties of Al-Zn-Mg/Al<sub>3</sub>Ni eutectic composite.

707-711A

Large Self-Thermal-Plastic Deformation in a NiTi Shape-Memory Alloy Fiber-Actuated Aluminum Metal-Matrix Composite.

3535-3540A

Mechanical, Intergranular Corrosion, and Wear Behavior of Aluminum-Matrix Composite Materials Reinforced with Nickel Aluminides.

3541-3553A

**Nickel compounds, Mechanical properties**

Two-way shape memory effect of TiNi alloys induced by hydrogenation.

17-23A

Hydrogen embrittlement of nickel-titanium alloy in biological environment.

495-501A

Room-temperature mechanical properties of cold-rolled thin foils of binary, stoichiometric Ni<sub>3</sub>Al.

2607-2613A

**Nickel compounds, Reactions (chemical)**

Solubility of Some Transition Metal Oxides in Cryolite-Alumina Melts: Part I. Solubility of FeO, FeAl<sub>2</sub>O<sub>4</sub>, NiO, and NiAl<sub>2</sub>O<sub>4</sub>.

901-908B

**Nickel plating**

Microstructural and mechanical properties investigation of electrodeposited and annealed LIGA nickel structures.

539-554A

Communication: A New Hybrid Process for Surface Modification by Combining Brush Plating with Nitrocarburizing.

2240-2244A

Processing and microstructures of fiber Bragg grating sensors embedded in stainless steel.

3019-3024A

**Nickel steels, Heat treatment**

Precipitation of austenite particles at grain boundaries during aging of Fe-Mn-Ni steel.

1057-1067A

**Nickel steels, Mechanical properties**

Crack-initiation toughness and crack-arrest toughness in advanced 9 pct Ni steel welds containing local brittle zones.

2615-2622A

**Niobium, Additives**

Communication: Precipitation behavior of carbonitrides in type 347 stainless steels with Various C and N contents.

1565-1569A

Environmentally assisted, sustained-load crack growth in powder metallurgy nickel-based superalloys.

1681-1687A

High Temperature SANS Experiments on Nb(C,N) and MnS Precipitates in HSLA Steel.

1883-1891A

Phase Separation Tendency in the As-Solidified Zr3Al-Nb Alloys Studied by Microstructural Observations and Thermodynamic Analysis.

1919-1929A

**Niobium, Alloying elements**

Carbide precipitation and high-temperature strength of hot-rolled high-strength, low-alloy steels containing Nb and Mo.

1689-1698A

Communication: Microstructure and yield behavior of a high aluminum containing Ti-Al-Nb alloy.

2763-2766A

**Niobium, Extraction**

Production of Niobium Powder by Direct Electrochemical Reduction of Solid Nb<sub>2</sub>O<sub>5</sub> in a Eutectic CaCl<sub>2</sub>-NaCl Melt.

685-693B

**Niobium, Ternary systems**

Thermal and electrical properties of Nb<sub>2</sub>AlC, (Ti,Nb)<sub>2</sub>AlC and Ti<sub>2</sub>AlC.

2775-2779A

**Niobium base alloys, Mechanical properties**

Microstructural and fracture characterization of Nb-Cr-Ti mechanically alloyed materials.

401-416A

**Niobium compounds, Reduction (chemical)**

Production of Niobium Powder by Direct Electrochemical Reduction of Solid Nb<sub>2</sub>O<sub>5</sub> in a Eutectic CaCl<sub>2</sub>-NaCl Melt.

685-693B

**Nitriding**

Precipitate Formation in Low-Temperature Nitrided Cold-Rolled Fe<sub>93</sub>Ni<sub>4</sub>Ti<sub>2</sub> and Fe<sub>93</sub>Ni<sub>4</sub>Cr<sub>3</sub> Films.

3075-3087A

**Nitrogen, Binary systems**

Low-temperature extension of the Lehrer diagram and the iron-nitrogen phase diagram.

2593-2598A

**Nitrogen, Sorption**

Rate of nitrogen desorption from CaO-Al<sub>2</sub>O<sub>3</sub> melts to gas phase.

393-401B

Development of Austenitic Nanostructures in High-Nitrogen Steel Powders Processed by Mechanical Alloying.

2139-2144A

**Nodular graphitic structure**

Evaluation of the Fatigue Behavior of Ductile Irons with Various Matrix Microstructures.

3719-3730A

**Nodular iron, Mechanical properties**

Effect of pearlite on the vibration-fracture behavior of spheroidal graphite cast irons under resonant conditions.

2623-2634A

Evaluation of the Fatigue Behavior of Ductile Irons with Various Matrix Microstructures.

3719-3730A

**Nodular iron, Microstructure**

Visualization of the hydrogen desorption process from ferrite, pearlite, and graphite by secondary ion mass spectrometry.

2659-2665A

**Nonmetallic inclusions**

Formation of CaS on Al<sub>2</sub>O<sub>3</sub>-CaO inclusions during solidification of steels.

625-632B

**Normalizing (heat treatment)**

Comprehensive microstructural characterization in modified 9Cr-1Mo ferritic steel by ultrasonic measurements.

1617-1626A

**Notch strength**

The effect of constraint-induced normal stress on the failure of notched TiAl components.

417-426A

**Nuclear reactor components**

Sensitization behavior of type 308 stainless steel weld metals after postweld heat treatment and low-temperature aging

1743-1754A

and its relation to microstructure.

**Nuclear reactor components, Corrosion**

Intergranular stress corrosion cracking behavior of types 308 and 316 stainless steel weld metals in a simulated boiling



- water reactor environment. 2907-2919A
- Nuclear reactor components, Materials selection**
- Steady-state creep of  $\alpha$ -zirconium at temperatures up to 850°C. 337-343A
- Distribution of c- and a-dislocations in tubes of Zr alloys. 867-874A
- Anisotropic threshold stress intensity factor,  $K_{IH}$  and crack growth rate in delayed hydride cracking of Zr-2.5Nb pressure tubes. 919-925A
- Analysis of steady-state thermal creep of Zr-2.5Nb pressure tube material. 1103-1115A
- Corrosion behavior of austenitic alloy 690 under anodic and cathodic potentials. 1437-1447A
- Fracture toughness of alloy 690 and EN52 welds in air and water. 1725-1735A
- Nucleation**
- A new unidirectional solidification method to study gray cast iron. 235-241B
- Modeling the kinetics of grain-boundary-nucleated recrystallization processes after cold deformation. 529-537A
- Finite element modeling of the morphology of  $\beta$  to  $\alpha$  phase transformation in Ti-6Al-4V alloy. 1027-1040A
- Microstructural characteristics of Ni-Sb eutectic alloys under substantial undercooling and containerless solidification conditions. 1221-1228A
- Dislocation-disclination model of heterogeneous martensite nucleation in transformation-induced-plasticity steels. 1351-1362A
- On the roles of clusters during intragranular nucleation in the absence of static defects. 1649-1658A
- Static Recrystallization Mechanisms in a Coarse-Grained Nb-Microalloyed Austenite. 3089-3098A
- Solidification Behavior of Sn-15 Wt Pct Pb Alloy under a High Shear Rate and High Intensity of Turbulence during Semi-solid Processing. 3511-3520A
- Coprecipitation of  $\Omega$  and  $\sigma$  Phases in Al-Cu-Mg-Mn Alloys Containing Ag and Si. 3635-3648A
- Evolution of Microstructure and Texture during Casting of AISI 304 Stainless Steel Strip. 3747-3754A
- Numerical analysis**
- Investigation on the effect of laser pulse shape during Nd:YAG laser microwelding of thin Al sheet by numerical simulation. 1449-1459A
- Oil quenching**
- Comprehensive microstructural characterization in modified 9Cr-1Mo ferritic steel by ultrasonic measurements. 1617-1626A
- Optical measurements**
- Simulation of the submerged energy nozzle-mold water model system using laser-optical and computational fluid dynamics methods. 163-172B
- Correction to "Simulation of the submerged energy nozzle-mold water model systems using laser optical and computational fluid dynamics methods" 639B
- Optimization**
- Mathematical modeling of the argon-oxygen decarburization refining process of stainless steel: Part II. Application of the model to industrial practice. 121-127B
- Process dynamics of electric arc furnace during direct reduced iron melting. 187-199B
- Ores, Beneficiation**
- Bubble formation and detachment on nonwetted surfaces. 155-162B
- Orientation**
- Subgrain formation during deformation: physical origin and consequences. 319-327A
- Electron backscatter diffraction analysis of microstructural evolution in hot-deformed 6xxx series aluminum alloys. 693-713A
- Deformation behavior of Hcp Ti-Al alloy single crystals. 837-850A
- Texture enhancement by inoculation during casting of ferritic stainless steel strip. 1499-1507A
- Orientation relationships**
- A new bcc-fcc orientation relationship observed between ferrite and austenite in solidification structures of steels. 5-15A
- Advances in deformation twin characterization using electron backscattered diffraction data. 949-954A
- Hot rolling texture development in CMnCrSi dual-phase steels. 1091-1102A
- Lattice Orientation Relationship between the M2C Carbide and the Ferrite Matrix in the M50NiL Bearing Steel. 1963-1969A
- Interphase boundary structure with irrational orientation relationship formed in grain boundary precipitation. 2327-2335A
- Massive-parent interphase boundaries and their implications on the mechanisms of the  $\alpha \rightarrow \gamma_M$  massive transformation in Ti-Al alloys. 2353-2371A
- Orientation and structure of planar facets on the  $\gamma_M$  massive phase in a near-TiAl alloy. 2381-2389A
- Static and in-situ high-resolution transmission electron microscopy investigations of the atomic structure and dynamics of massive transformation interfaces in a Ti-Al alloy. 2391-2411A
- Misfit dislocations in epitaxy. 2475-2483A
- Analysis of the Cu-3 Wt pct Ti cellular interphase boundary by various models. 2495-2505A
- The cellular interlamellar and growth-front interphase boundaries in Cu-3 Wt pct Ti. 2507-2518A
- Why do dislocations assemble into interfaces in epitaxy as well as in crystal plasticity? To minimize free energy. 2519-2539A
- Finite-element calculations of the lattice rotation field of a tensile-loaded nickel-based alloy multycrystal and comparison with topographical x-ray diffraction measurements. 2825-2833A
- Ostwald ripening**
- Microstructural stability during creep of Mo- or W-bearing 12Cr steels. 2549-2557A
- Overaging**
- Toughness-strength relations in the overaged 7449 Al-based alloy. 1125-1136A
- The effects of test temperature, temper, and alloyed copper on the hydrogen-controlled crack growth rate of an Al-Zn-Mg-(Cu) alloy. 1167-1181A
- Erratum: The effects of test temperature, temper, and alloyed copper on the hydrogen-controlled crack growth rate of an Al-Zn-Mg-(Cu) alloy. 1297A
- Oxidation rate**
- Rate of Interfacial Reaction between Molten  $\text{CaO-SiO}_2\text{-Al}_2\text{O}_3\text{-Fe}_2\text{O}_3$  and  $\text{CO-CO}_2$ . 651-660B
- Oxidation resistance**
- Communication: Phase Transformations in FeMnAlC Austenitic Steels with Si Addition. 3569-3573A
- Oxide coatings**
- Surface engineering of Timet 550 with oxygen to form a rutile-based, wear-resistant coating. 1201-1211A
- Oxides, Reactions (chemical)**
- Oxidation state and activities of chromium oxides in  $\text{CaO-SiO}_2\text{-Cr}_2\text{O}_3$  slag system. 595-603B
- Oxides, Reduction (chemical)**
- Reduction of  $\text{Fe}_2\text{MoO}_4$  by hydrogen gas. 589-594B
- Oxidizing atmospheres**
- Surface engineering of Timet 550 with oxygen to form a rutile-based, wear-resistant coating. 1201-1211A
- Environmentally assisted, sustained-load crack growth in powder metallurgy nickel-based superalloys. 1681-1687A
- Pack cementation**
- Interrupted bonding of medium-carbon steels. 1475-1485A
- Palladium, Binary systems**
- Thermodynamic Modeling of the Indium-Palladium System. 3597-3603A
- Particle shape**
- Bubble formation and detachment on nonwetted surfaces. 155-162B
- Symmetry-breaking transitions in equilibrium shapes of coherent precipitates: effect of elastic anisotropy and inhomogeneity. 1083-1090A
- Particle size**
- Near-nanostructured WC-18 pct co coatings with low amounts of non-WC carbide phase: Part I. Synthesis and characterization. 145-157A
- Effect of loading condition and stress state on damage evolution of silicon particles in an Al-Si-Mg-base cast alloy. 555-565A
- Reduction of  $\text{Fe}_2\text{MoO}_4$  by hydrogen gas. 589-594B
- Synthesis and nanoindentation study of high-velocity oxygen fuel thermal-sprayed nanocrystalline and near-nanocrystalline Ni coatings. 647-655A
- Communication: Precipitation behavior of carbonitrides in type 347 stainless steels with Various C and N contents. 1565-1569A
- High Temperature SANS Experiments on Nb(C,N) and MnS Precipitates in HSLA Steel. 1883-1891A
- Rapid Solidification of Martensitic Stainless Steel Atomized Droplets. 3755-3760A
- Particulate composites, Casting**
- Effect of heat treatments on in-situ  $\text{Al}_2\text{O}_3\text{-TiAl}_3$  composites produced from squeeze casting of  $\text{TiO}_2\text{-Al}_3\text{Si}_5$  composites. 31-40B
- In-situ formation of SiC-reinforced Al-Si alloy composites using methane gas mixtures. 543-550B
- Communication: Reduced critical solidification front velocity of particle engulfment due to an interface active solute in the liquid metal. 1869-1873A
- Particulate composites, Corrosion**
- Mechanical, Intergranular Corrosion, and Wear Behavior of Aluminum-Matrix Composite Materials Reinforced with Nickel Aluminides. 3541-3553A
- Particulate composites, Heat treatment**
- Age-hardening characteristics of aluminum alloy-hollow fly ash composites. 1541-1547A
- Effect of alternative aging process on the fracture and interfacial properties of particulate  $\text{Al}_2\text{O}_3$ -reinforced Al (6061) metal matrix composite. 1699-1713A
- Particulate composites, Mechanical properties**
- Constitutive equations for creep and plasticity of aluminum alloys produced by powder metallurgy and aluminum-based metal matrix composites. 373-381A
- Strength of Al-Zn-Mg-Cu matrix composite reinforced with SiC particles. 455-465A
- Communication: Examination on the aging and tensile properties of Al-Zn-Mg/ $\text{Al}_3\text{Ni}$  eutectic composite. 707-711A
- High stress abrasive wear mechanism of LM13-SiC composite under varying experimental conditions. 3031-3044A
- Strength and Plastic Flow in "In Situ" TiC Reinforced Aluminum Composites. 3831-3838A
- Particulate composites, Powder technology**
- Effect of cyclic pressure consolidation on the uniformity of metal matrix composites. 183-191A
- Formation of a TiB<sub>2</sub>-reinforced copper-based composite by mechanical alloying and hot pressing. 1275-1280A
- Microstructure/processing relationships in reaction-synthesized titanium aluminide intermetallic matrix composites. 2747-2753A
- The incorporation of self-propagating, high-temperature synthesis-formed Fe-TiB<sub>2</sub> into ferrous melts. 2973-2983A
- Solidification paths and reinforcement morphologies in melt-processed (TiB + TiC)/Ti in situ composites. 3055-3063A
- Passivation**
- Corrosion behavior of austenitic alloy 690 under anodic and cathodic potentials. 1437-1447A
- Passivation, Alloying effects**
- Modification of 27Cr Cast Iron with Alloying Yttrium for



- Enhanced Resistance to Sliding Wear in Corrosive Media. 1981-1989A
- Pearlite**  
A critical-strain criterion for hydrogen embrittlement of cold-drawn, ultrafine pearlitic steel. 1151-1166A  
Effect of pearlite on the vibration-fracture behavior of spheroidal graphite cast irons under resonant conditions. 2623-2634A
- Penetration**  
Microstructural evolution of a shaped-charge liner and target materials during ballistic tests. 1069-1074A  
A Unified Numerical Modeling of Stationary Tungsten-Inert Gas Welding Process. 2043-2052A
- Peritectic reactions**  
Modeling the formation of longitudinal facial cracks during continuous casting of hypoperitectic steel. 413-423B
- Permanent magnets**  
A novel technique for manufacturing metal-bonded Nd-Fe-B magnets by squeeze casting. 637-646A
- Permanent mold casting**  
Intermetallic-reinforced light-metal matrix in-situ composites. Die soldering: mechanism of the interface reaction between molten aluminum alloy and tool steel. 193-201A  
Phenomenological observations on mechanical and corrosion properties of thixoformed 357 alloys: a comparison with permanent mold cast 357 alloys. 465-476B  
1399-1412A
- Phase boundary**  
First-principles investigation of perfect and diffuse antiphase boundaries in hcp-based Ti-Al alloys. 735-741A  
Bulk and interface boundary diffusion in group IV hexagonal close-packed metals and alloys. 765-775A  
Diffusion along grain and interphase boundaries in Alpha Zr and Zr-2.5 Wt Pct Nb alloy. 797-800A  
Twins as barriers to basal slip in hexagonal-close-packed metals. 809-812A  
Critical limit for massive transformation. 2299-2308A  
Simulation of ferrite growth in continuously cooled low-carbon iron alloys. 2309-2316A  
Interphase boundary structure with irrational orientation relationship formed in grain boundary precipitation. 2327-2335A  
Massive-parent interphase boundaries and their implications on the mechanisms of the  $\alpha \rightarrow \gamma_m$  massive transformation in Ti-Al alloys. 2353-2371A  
Orientation and structure of planar facets on the  $\gamma_m$  massive phase in a near-TiAl alloy. 2381-2389A  
Static and in-situ high-resolution transmission electron microscopy investigations of the atomic structure and dynamics of massive transformation interfaces in a Ti-Al alloy. 2391-2411A  
Massive transformation and the formation of the ferromagnetic  $L_{10}$  phase in manganese-aluminum-based alloys. 2413-2423A  
Jan Van Der Merwe and the theory of epitaxy. 2473-2474A  
The cellular interlamellar and growth-front interphase boundaries in Cu-3 Wt pct Ti. 2507-2518A
- Phase decomposition**  
Formation of white layers in steels by machining and their characteristics. 1245-1254A  
An integrated computer model with applications for austenite-to-ferrite transformation during hot deformation of Nb-microalloyed steels. 1509-1520A  
Communication: Phase Transformations in FeMnAlC Austenitic Steels with Si Addition. 3569-3573A  
Austenite Decomposition to Carbide-Rich Products in Fe-0.30C-6.3W. 3619-3633A
- Phase decomposition, High temperature effects**  
Decomposition of ferrite in commercial superduplex stainless steel weld metals; microstructural transformations above 700°C. 1009-1018A
- Phase decomposition, Stress effects**  
Communication: Microstructure and yield behavior of a high aluminum containing Ti-Al-Nb alloy. 2763-2766A
- Phase diagram reactions**  
Stability of silico-ferrite of calcium and aluminum (SFCA) in air-solid solution limits between 1240°C and 1390°C and phase relationships within the  $\text{Fe}_2\text{O}_3\text{-CaO-Al}_2\text{O}_3\text{-SiO}_2$  (FCAS) system. 79-89B  
Metastable phases in the Ti-V system. I. Neutron diffraction study and assessment of structural properties. 1307-1317A  
Communication: On the solute field and composition of  $\gamma$  plates in an Al-22 At. Pct Ag alloy. 1561-1565A
- Phase diagrams**  
Phase Equilibrium Studies in the "MnO"- $\text{Al}_2\text{O}_3\text{-SiO}_2$  System. Phase Equilibrium Data and Liquidus for the System "MnO"- $\text{CaO}(\text{Al}_2\text{O}_3 + \text{SiO}_2)$  at  $\text{Al}_2\text{O}_3/\text{SiO}_2 = 0.41$ . 827-838B  
A 500°C isothermal section for the Al-Au-Cu system. 839-849B  
Phase equilibria of the ternary Ni-Cr-Zr system and interfacial reactions in the Ni-Cr/Zr couples. 987-993A  
Equilibrium solid solubility of silicon in silver. 995-1002A  
Communication: On the ternary phase in the zinc-rich corner of the Zn-Fe-Al system at temperatures below 450°C. 1145-1150A  
Thermodynamic description of the Cu-Al-Sn system in the copper-rich corner. 1559-1560A  
Phase Separation Tendency in the As-Solidified Zr3Al-Nb Alloys Studied by Microstructural Observations and Thermodynamic Analysis. 1639-1648A  
Low-temperature extension of the Lehrer diagram and the iron-nitrogen phase diagram. 1919-1929A  
Evaluation of the thermodynamic properties and phase equilibria of the Re-Ta-W system. 2593-2598A  
2781-2787A
- Phase ratio**  
Determination of Gibbs energies of formation of  $\text{CaFe}_2\text{O}_4$  and  $\text{Ca}_2\text{Fe}_2\text{O}_5$  from solid-state emf measurements using  $\text{CaF}_2$  as solid electrolyte. 385-392B  
General discussion session of the symposium on "The mechanisms of the massive transformation" 2445-2470A
- Phase rule**  
Statistical Self-Similarity in Rhines' Concept of Unique Multiphase Diffusion Paths on the Ternary Gibbs' Isotherm. 3357-3365A
- Phase separation**  
Hot rolling texture development in CMnCrSi dual-phase steels. Communication: The Gibbs-Thomson effect in dilute binary systems. 1091-1102A  
Communication: High-cycle fatigue of an investment cast, Be-Al metal matrix composite. 1283-1287A  
Phase Separation Tendency in the As-Solidified Zr3Al-Nb Alloys Studied by Microstructural Observations and Thermodynamic Analysis. 1862-1865A  
1919-1929A
- Phase stability**  
Aging behavior of the Ti-29Nb-13Ta-4.6Zr new beta alloy for medical implants. 487-493A  
Communication: Prediction of the thermodynamic properties of solutes in the Bi-based ternary dilute solution. 502-506B  
Stable quasicrystalline phase in Al-Cu-Fe-Cr coating materials. Fabrication and characterization of Ti-TiB<sub>2</sub> functionally graded material system. 675-679A  
Communication: Effect of boron on the hot ductility of Nb-containing steel. 681-685A  
Phase Equilibrium Data and Liquidus for the System "MnO"- $\text{CaO}(\text{Al}_2\text{O}_3 + \text{SiO}_2)$  at  $\text{Al}_2\text{O}_3/\text{SiO}_2 = 0.41$ . 701-704A  
Phase equilibria of the ternary Ni-Cr-Zr system and interfacial reactions in the Ni-Cr/Zr couples. 839-849B  
Decomposition of ferrite in commercial superduplex stainless steel weld metals; microstructural transformations above 700°C. 995-1002A  
Massive transformation and absolute stability. 1009-1018A  
The Optimum Wetting Angle for the Stabilization of Liquid-Metal Foams by Ceramic Particles: Experimental Simulations. 2337-2345A  
3285-3292A
- Phase stability, Composition effects**  
Communication: Microstructure and yield behavior of a high aluminum containing Ti-Al-Nb alloy. 2763-2766A
- Photoelectron spectroscopy**  
On the Nature of the Electrochemically Synthesized Hard Fe-0.96 Mass Pct C Alloy Film. 921-927B
- Physical simulation**  
An experimental study of deformation of a columnar dendritic mushy zone using a transparent succinonitrile-acetone alloy. 69-78B  
Modeling of primary spacing selection in dendrite arrays during directional solidification. 223-233B  
Segregation and morphological instability due to double-diffusive convection in rotational directional solidification. 3011-3017A  
The Optimum Wetting Angle for the Stabilization of Liquid-Metal Foams by Ceramic Particles: Experimental Simulations. 3285-3292A
- Pipelines, Corrosion**  
Environmental aspects of near-neutral pH stress corrosion cracking of pipeline steel. 1429-1436A
- Pipelines, Mechanical properties**  
Fatigue Deformation-Induced Response in a Superduplex Stainless Steel. 3433-3442A
- Pitting (corrosion)**  
Corrosion behavior of austenitic alloy 690 under anodic and cathodic potentials. 1437-1447A
- Plasma (physics)**  
Effects of metal vapor on electron temperature in helium gas tungsten arcs. 1183-1188A
- Plasma spraying**  
Dry-process surface modification for titanium dental implants. Correlation of microstructure and wear resistance of ferrous coatings fabricated by atmospheric plasma spraying. 511-519A  
2933-2945A
- Plastic deformation**  
Subgrain formation during deformation: physical origin and consequences. 319-327A  
A framework for modeling creep in pure metals. 363-371A  
Constitutive equations for creep and plasticity of aluminum alloys produced by powder metallurgy and aluminum-based metal matrix composites. 373-381A  
Why do dislocations assemble into interfaces in epitaxy as well as in crystal plasticity? To minimize free energy. 2519-2539A  
Mechanical anisotropy and grain interaction in recrystallized aluminum. 2635-2648A  
Self-consistent modeling of the flow behavior of wrought alpha/beta titanium alloys under isothermal and nonisothermal hot-working conditions. 2719-2727A  
Comparative study of the impact response and microstructure of 304L stainless steel with and without prestrain. 2801-2810A  
Low-temperature superplastic behavior of a submicrometer-grained 5083 Al alloy fabricated by severe plastic deformation. 2859-2867A  
The relationship between grain size and the surface roughening behavior of Al-Mg alloys. 2883-2889A  
The production of ultrafine ferrite during hot torsion testing of a 0.11 Wt pct C steel. 2985-2993A  
Use of Weibull Statistics to Quantify Property Variability in TiAl Alloys. 3127-3136A  
Fatigue Deformation-Induced Response in a Superduplex Stainless Steel. 3433-3442A  
Simulation of Cavitation Processes in Superplastic Deformation. 3449-3455A  
Large Self-Thermal-Plastic Deformation in a NiTi Shape-Memory Alloy Fiber-Actuated Aluminum Metal-Matrix Composite. 3535-3540A

**Plastic deformation, Anisotropy**

Influence of elastic and plastic anisotropy on the flow behavior in a duplex stainless steel. 57-71A

**Plastic deformation, Stress effects**

The influence of the stress state on the plasticity of transformation induced plasticity-aided steel. 1659-1667A

**Plastic flow**

Communication: Interpretation of flow instability using dynamic material modeling. 1569-1572A

Self-consistent modeling of the flow behavior of wrought alpha/beta titanium alloys under isothermal and nonisothermal hot-working conditions. 2719-2727A

Effect of the Lamellar Grain Size on Plastic Flow Behavior and Microstructure Evolution during Hot Working of a Gamma Titanium Aluminide Alloy. 3817-3830A

Strength and Plastic Flow in "In Situ" TiC Reinforced Aluminum Composites. 3831-3838A

**Plasticity**

An investigation of the microstructure and strength of open-cell 6101 aluminum foams. 1413-1427A

Effect of thermomechanical processing on the retained austenite content in a Si-Mn transformation-induced-plasticity steel. 2811-2816A

Method for Measuring Transformation Energy and Quantitative Characterization of Transformation-Induced Plasticity. 3117-3120A

**Plate metal, Mechanical properties**

Toughness-strength relations in the overaged 7449 Al-based alloy. 1125-1136A

**Plating baths**

Microstructural and mechanical properties investigation of electrodeposited and annealed LIGA nickel structures. 539-554A

Communication: On the ternary phase in the zinc-rich corner of the Zn-Fe-Al system at temperatures below 450°C. 1559-1560A

**Platinum base alloys, Mechanical properties**

Measurement and Computation of Drag Forces in Thermo-gravimetric Studies. 891-896B

**Platinum base alloys, Reactions (chemical)**

Thermodynamic Study of MnO-SiO<sub>2</sub>-Al<sub>2</sub>O<sub>3</sub> Slag System: Liquidus Lines and Activities of MnO at 1823 K. 915-920B

**Poissons ratio**

Simulation of Cavitation Processes in Superplastic Deformation. 3449-3455A

**Pole figures**

Deformation bands and the formation of grain boundaries in a superplastic aluminum alloy. 279-290A

Microstructural and mechanical properties investigation of electrodeposited and annealed LIGA nickel structures. 539-554A

Electron backscatter diffraction analysis of microstructural evolution in hot-deformed 6xxx series aluminum alloys. 693-713A

Intergranular stresses in ZIRCALOY-2. 749-755A

A study of twinning in zirconium using neutron diffraction and polycrystalline modeling. 757-763A

Transmission electron microscopy investigation of <c + a> dislocations in Mg and  $\alpha$ -solid solution Mg-Li alloys. 851-858A

Determination of dislocation densities in Hcp metals from X-ray diffraction line-broadening analysis. 859-865A

Distribution of c- and a-dislocations in tubes of Zr alloys. 867-874A

Anisotropic threshold stress intensity factor, K<sub>th</sub>, and crack growth rate in delayed hydride cracking of Zr-2.5Nb pressure tubes. 919-925A

Computational modeling of through-thickness dynamic impact response in cross-rolled Ti-6Al-4V plates. 937-947A

Advances in deformation twin characterization using electron backscattered diffraction data. 949-954A

Deformation twinning in polycrystalline Zr: insights from electron backscattered diffraction characterization. 955-963A

Equal-channel angular extrusion of beryllium. 965-972A

Microstructure evolution in Zr under equal channel angular pressing. 973-980A

Electron-beam welding behavior in Mg-Al-based alloys. 1461-1473A

Texture enhancement by inoculation during casting of ferritic stainless steel strip. 1499-1507A

Annealing behavior of alumina dispersion-strengthened copper strips rolled under different conditions. 1605-1616A

Tree-ring formation during vacuum arc remelting of INCONEL 718. I. Experimental investigation. 1795-1804A

Phase Evolution in Laser-Deposited Titanium-Chromium Alloys. 2129-2138A

An Investigation of Microstructure and Grain-Boundary Evolution during ECA Pressing of Pure Aluminum. 2173-2184A

Room-temperature mechanical properties of cold-rolled thin foils of binary, stoichiometric Ni<sub>3</sub>Al. 2607-2613A

Mechanical anisotropy and grain interaction in recrystallized aluminum. 2635-2648A

Orientation domains and texture in hot-dipped galvanized coatings. 2695-2701A

**Pollution abatement**

A Novel Cyclic Process using CaSO<sub>3</sub>/CaS Pellets for Converting Sulfur Dioxide to Elemental Sulfur without Generating Secondary Pollutants: Part I. Feasibility and Kinetics of the Reduction of Sulfur Dioxide with Calcium Sulfide Pellets. 711-716B

A Novel Cyclic Process using CaSO<sub>3</sub>/CaS Pellets for Converting Sulfur Dioxide to Elemental Sulfur without Generating Secondary Pollutants: Part II. Hydrogen Reduction of Calcium-Sulfate Pellets to Calcium Sulfide. 717-721B

Polycrystals 213-218A

Creep at very low rates. 311-317A

Dislocation microstructure and internal-stress measurements by convergent-beam electron diffraction on creep-deformed Cu and Al.

**Polycrystals, Crystal growth**

A Discrete Approach to Grain Growth Based on Pair Interactions: Effect of Local Grain-Boundary Curvature. 3329-3337A

**Porosity**

An analytical self-consistent determination of a bubble with a deformed cap trapped in solid during solidification. 91-100B

A three-phase model of hydrogen pore formation during the equiaxed dendritic solidification of aluminum-silicon alloys. 209-221B

Origin of porosity in oxide-dispersion-strengthened alloys produced by mechanical alloying. 2713-2718A

Communication: Thermodynamics of Hydrogen in Al-Si Alloys. 3874-3876A

**Porous materials**

An investigation of the microstructure and strength of open-cell 6101 aluminum foams. 1413-1427A

**Postheating**

Characterization of a friction-stir-welded aluminum alloy 6013. Sensitization behavior of type 308 stainless steel weld metals after postweld heat treatment and low-temperature aging and its relation to microstructure. 1743-1754A

**Potassium, Dopants**

Dopant Particle Characterization and Bubble Evolution in Aluminum-Potassium-Silicon-Doped Molybdenum Wire. 3349-3356A

**Powder blending**

Effect of cyclic pressure consolidation on the uniformity of metal matrix composites. 183-191A

Formation of a TiB<sub>3</sub>-reinforced copper-based composite by mechanical alloying and hot pressing. 1275-1280A

Phase Evolution in Laser-Deposited Titanium-Chromium Alloys. 2129-2138A

Thermally Enhanced and Mechanically Driven Glass Formation Reactions of Multilayered Cu<sub>35</sub>Zr<sub>65</sub> Powders. 2145-2153A

Microstructure/processing relationships in reaction-synthesized titanium aluminide intermetallic matrix composites. 2747-2753A

**Powder coatings, Microstructure**

Powder Eutectic Coating With Al<sub>3</sub>Ti For Steels. 3235-3240A

**Powder compacts, Reactions (chemical)**

The Influence of the Atmosphere on the Sintering of Aluminum. 3279-3284A

**Powder metallurgy**

Structure of a Fe-Cr-Mn-Mo-N Alloy Processed by Mechanical Alloying. 3273-3278A

**Powder metallurgy parts**

Environmentally assisted, sustained-load crack growth in powder metallurgy nickel-based superalloys. 1681-1687A

**Powder metallurgy parts, Mechanical properties**

Fatigue crack initiation and propagation of binder-treated powder metallurgy steels. 73-81A

Fatigue-Crack-Propagation Thresholds in a Nickel-Base Superalloy at High Frequencies and Temperatures. 1949-1962A

The Influence of Microstructure and Environment on the Crack Growth Behavior of Powder Metallurgy Nickel Superalloy RR1000. 3165-3172A

**Precipitate free zone**

Effect of grain boundary characteristics on intergranular corrosion resistance of 6061 aluminum alloy extrusion. 2891-2898A

**Precipitates**

Grain growth behavior of cryomilled INCONEL 625 powder during isothermal heat treatment. 125-134A

Communication: Removal of phosphorus-based extractant contamination from lutetium oxalate produced by precipitation stripping. 146-147B

In-situ observation of the precipitation of manganese sulfide in low-carbon magnesium-killed steel. 427-436A

Parameters controlling microstructure and hardness during friction-stir welding of precipitation-hardenable aluminum alloy 6063. 625-635A

Symmetry-breaking transitions in equilibrium shapes of coherent precipitates: effect of elastic anisotropy and inhomogeneity. 1083-1090A

Retardation of  $\sigma$ -phase transformation in modified superalloy RR202. 1319-1330A

High Temperature SANS Experiments on Nb(C,N) and MnS Precipitates in HSLA Steel. 1883-1891A

Lattice Orientation Relationship between the M2C Carbide and the Ferrite Matrix in the M50NiL Bearing Steel. 1963-1969A

Dissolution Kinetics of NbC Particles in the Heat-Affected Zone of Type 347 Austenitic Stainless Steel. 2031-2042A

Phase Evolution in Laser-Deposited Titanium-Chromium Alloys. 2129-2138A

Subnanometer-scale chemistry and structure of  $\alpha$ -iron/molybdenum nitride heterophase interfaces. 2317-2326A

Carbide formation in alloy 718 during electron-beam solid free-form fabrication. 2559-2567A

Visualization of the hydrogen desorption process from ferrite, pearlite, and graphite by secondary ion mass spectrometry. 2659-2665A

**Precipitates, Composition effects**

Communication: Precipitation behavior of carbonitrides in type 347 stainless steels with Various C and N contents. 1565-1569A

**Precipitates, Crystal growth**

Precipitate Formation in Low-Temperature Nitrided Cold-Rolled Fe<sub>34</sub>Ni<sub>66</sub>Ti<sub>2</sub> and Fe<sub>93</sub>Ni<sub>4</sub>Cr<sub>3</sub> Films. 3075-3087A

**Precipitation**

Study of the kinetics of the recrystallization of cold-rolled low-carbon steel. 25-31A

Aging behavior of the Ti-29Nb-13Ta-4.6Zr new beta alloy for medical implants. 487-493A

Precipitation of austenite particles at grain boundaries during aging of Fe-Mn-Ni steel. 1057-1067A

Communication: The Gibbs-Thomson effect in dilute binary

- systems.  
On the roles of clusters during intragranular nucleation in the absence of static defects.  
Communication: Discussion of 'coarsening of intermetallic or compound precipitates in binary systems'.  
Communication: Author's reply to "Discussion of 'Coarsening of intermetallic or compound precipitates in binary systems'".  
Interphase boundary structure with irrational orientation relationship formed in grain boundary precipitation.  
Microstructural stability during creep of Mo- or W-bearing 12Cr steels.  
Precipitate Formation in Low-Temperature Nitrided Cold-Rolled  $\text{Fe}_{94}\text{Ni}_4\text{Ti}_2$  and  $\text{Fe}_{93}\text{Ni}_4\text{Cr}_3$  Films.  
Titanium Nitride Precipitation Behavior in Thin-Slab Cast High-Strength Low-Alloy Steels.  
Modeling  $\text{M}_6\text{C}$  Precipitation in Niobium-Alloyed Ferritic Stainless Steel.  
Austenite Decomposition to Carbide-Rich Products in Fe-0.30C-6.3W.  
Cocprecipitation of  $\Omega$  and  $\alpha$  Phases in Al-Cu-Mg-Mn Alloys Containing Ag and Si.
- Precipitation hardening**  
Unexpected transient creep behavior of tin alloys strengthened by high volume fractions of SbSn.  
Tensile and fatigue properties of 17-4 PH stainless steel at high temperatures.
- Precipitation hardening alloys, Mechanical properties**  
Creep at very low rates.  
Denuded zones, diffusional creep, and grain boundary sliding.
- Preforming**  
Effect of heat treatments on in-situ  $\text{Al}_2\text{O}_3/\text{TiAl}_3$  composites produced from squeeze casting of  $\text{TiO}_2/\text{A356}$  composites.  
Reactive Infiltration of 25 Vol Pct  $\text{TiO}_2/\text{Al}$  Composites.
- Pressure vessels, Materials selection**  
Analysis of steady-state thermal creep of Zr-2.5Nb pressure tube material.
- Prestraining**  
Comparative study of the impact response and microstructure of 304L stainless steel with and without prestrain.  
Effect of Prestrain on Stretch-Zone Formation during Ductile Fracture of Cu-Strengthened High-Strength Low-Alloy Steels.
- Process parameters**  
Intermetallic-reinforced light-metal matrix in-situ composites.  
Mathematical modeling of the argon-oxygen decarburization refining process of stainless steel: Part II. Application of the model to industrial practice.  
Control of heat transfer and growth uniformity of solidifying copper shells through substrate temperature.  
A novel technique for manufacturing metal-bonded Nd-Fe-B magnets by squeeze casting.  
Deoxidation of molybdenum during vacuum sintering.  
Structural evolution of a strip-cast Al alloy sheet processed by continuous equal-channel angular pressing.  
Development of New Feeding-Distance Rules Using Casting Simulation: Part I. Methodology.  
Communication: On the Estimation of Plume Rise Velocity in Gas-Stirred Ladles.  
Surface engineering of Timet 550 with oxygen to form a rutile-based, wear-resistant coating.  
Spheroidization cycles for medium carbon steels.  
Interrupted bonding of medium-carbon steels.  
Texture and microstructure development during intercritical rolling of low-carbon steels.  
Effect of alternative aging process on the fracture and interfacial properties of particulate  $\text{Al}_2\text{O}_3$ -reinforced Al (6061) metal matrix composite.  
Modeling of laser keyhole welding. II. Simulation of keyhole evolution, velocity, temperature profile, and experimental verification.  
Pulsed Nd:YAG Laser Welding of Copper Using Oxygenated Assist Gases.  
Effect of Fcc-Hcp Phase Transformation Produced by Isothermal Aging on the Corrosion Resistance of a Co-27Cr-5Mo-0.05C Alloy.  
A Precision On-Line Model for the Prediction of Roll Force and Roll Power in Hot-Strip Rolling.
- Pulsation**  
Pulsed Nd:YAG Laser Welding of Copper Using Oxygenated Assist Gases.
- Punching**  
Role of yield criteria and hardening laws in the prediction of forming limit diagrams.
- Purification**  
Communication: Conversion of  $\text{VOCl}_3$  to  $\text{VOCl}_2$  in liquid  $\text{TiCl}_4$ .  
A theoretical and experimental study of continuous-casting tundishes focusing on slag-steel interaction.  
Mathematical modeling and computer simulation of the rotating impeller particle flotation process: Part I. Fluid flow.  
Mathematical modeling and computer simulation of the rotating impeller particle flotation process: Part II. Particle agglomeration and flotation.  
Numerical simulation of dendrite white spot formation during vacuum arc remelting of INCONEL718.
- Purity**  
Communication: Removal of phosphorus-based extractant contamination from lutetium oxalate produced by precipitation stripping.
- Pyrometallurgy**  
Stability of silico-ferrite of calcium and aluminum (SFCA) in air-
- 1283-1287A  
1649-1658A  
1859-1860A  
1860-1862A  
2327-2335A  
2549-2557A  
3075-3087A  
3099-3110A  
3339-3347A  
3619-3633A  
3635-3648A  
575-580A  
1715-1724A  
213-218A  
219-229A  
31-40B  
2155-2162A  
1103-1115A  
2801-2810A  
3731-3740A  
193-201A  
121-127B  
403-411B  
637-646A  
657-664A  
665-673A  
731-740B  
937-941B  
1201-1211A  
1255-1261A  
1475-1485A  
1589-1603A  
1699-1713A  
1831-1842A  
2019-2030A  
2229-2235A  
3255-3272A  
2019-2030A  
1363-1371A  
142-146B  
173-185B  
297-303B  
305-314B  
443-454A  
146-147B
- solid solution limits between 1240°C and 1390°C and phase relationships within the  $\text{Fe}_2\text{O}_3$ -CaO- $\text{Al}_2\text{O}_3$ - $\text{SiO}_2$  (FCAS) system.  
Slags and mattes in Vanyukov's process for the extraction of copper.  
Physicochemical properties of matte-slag melts taken from Vanyukov's furnace for copper extraction.  
Rate of Interfacial Reaction between Molten CaO- $\text{SiO}_2$ - $\text{Al}_2\text{O}_3$ - $\text{Fe}_2\text{O}_3$  and CO- $\text{CO}_2$ .  
Rare Earth Extraction and Separation from Mixed Bastnaesite-Monazite Concentrate by Stepwise Carbochlorination-Chemical Vapor Transport.  
**Pyrometry**  
Normal spectral emissivities of liquid Ag-Cu alloys in the visible and infrared regions.  
**Quantitative analysis**  
Inertia Welding Nickel-Based Superalloy: Part I. Metallurgical Characterization.  
**Quasicrystals**  
Stable quasicrystalline phase in Al-Cu-Fe-Cr coating materials.  
**Radiation damage**  
Localized deformation and hardening in irradiated metals: three-dimensional discrete dislocation dynamics simulations.  
Atomic-scale modeling of dislocations and related properties in the hexagonal-close-packed metals.  
**Raman spectroscopy**  
Effect of pressure on zone-center phonons in hexagonal-close-packed metals.  
**Rapid solidification**  
Microstructural characteristics of Ni-Sb eutectic alloys under substantial undercooling and containerless solidification conditions.  
Communication: A New Face-Centered-Cubic Superlattice Structure in Rapidly Solidified Cu-4 Wt Pct Ti Alloy and Its Relevance to the Ordering Process in Ni-Mo and Other 1/2 0 Ordering Alloys.  
Rapid Solidification of Martensitic Stainless Steel Atomized Droplets.  
**Rare earth metal ores, Extraction**  
Communication: Removal of phosphorus-based extractant contamination from lutetium oxalate produced by precipitation stripping.  
**Rare earth metals, Extraction**  
Kinetics of manganese reduction leaching from weathered rare-earth mud with sodium sulfite.  
Rare Earth Extraction and Separation from Mixed Bastnaesite-Monazite Concentrate by Stepwise Carbochlorination-Chemical Vapor Transport.  
**Rare earth metals, Microstructure**  
Effect of pressure on zone-center phonons in hexagonal-close-packed metals.  
**Raw materials**  
Deoxidation of molybdenum during vacuum sintering.  
**Reaction kinetics**  
Kinetics of formation and dissociation of  $\text{Na}_2\text{SiF}_6$ .  
The reaction behavior of Fe-C-S droplets in CaO- $\text{SiO}_2$ -MgO-FeO slags.  
In-situ formation of SiC-reinforced Al-Si alloy composites using methane gas mixtures.  
Reduction of  $\text{Fe}_2\text{MoO}_4$  by hydrogen gas.  
Production of Niobium Powder by Direct Electrochemical Reduction of Solid  $\text{Nb}_2\text{O}_5$  in a Eutectic  $\text{CaCl}_2$ -NaCl Melt.  
A Novel Cyclic Process using  $\text{CaSO}_4/\text{CaS}$  Pellets for Converting Sulfur Dioxide to Elemental Sulfur without Generating Secondary Pollutants: Part I. Feasibility and Kinetics of the Reduction of Sulfur Dioxide with Calcium Sulfide Pellets.  
A Novel Cyclic Process using  $\text{CaSO}_4/\text{CaS}$  Pellets for Converting Sulfur Dioxide to Elemental Sulfur without Generating Secondary Pollutants: Part II. Hydrogen Reduction of Calcium-Sulfate Pellets to Calcium Sulfide.  
Kinetics of Silver Leaching from Manganese-Silver Associated Ores in Sulfuric Acid Solution in the Presence of Hydrogen Peroxide.  
Interface stability during displacement reactions between  $\text{Cu}_2\text{O}$  and  $\text{Co}_{1-x}\text{Fe}_x$  alloys at 1223 K.  
Fast Aging Kinetics of the AA6016 Al-Mg-Si Alloy and the Application in Forming Process.  
**Reaction mechanisms**  
The equilibrium partitioning of titanium between  $\text{Ti}^{3+}$  and  $\text{Ti}^{4+}$  valency states in CaO- $\text{SiO}_2$ - $\text{TiO}_2$  slags.  
Recycling of magnesium alloys: chemical equilibria between magnesium-lithium-based melts and salt melts.  
Reactive Infiltration of 25 Vol Pct  $\text{TiO}_2/\text{Al}$  Composites.  
**Reactive processing**  
Effect of heat treatments on in-situ  $\text{Al}_2\text{O}_3/\text{TiAl}_3$  composites produced from squeeze casting of  $\text{TiO}_2/\text{A356}$  composites.  
In-situ formation of SiC-reinforced Al-Si alloy composites using methane gas mixtures.  
Reduction of  $\text{Fe}_2\text{MoO}_4$  by hydrogen gas.  
Formation of a  $\text{TiB}_2$ -reinforced copper-based composite by mechanical alloying and hot pressing.  
Joining of NiAl to Iron-Based Alloys by Reactive Casting.  
Reactive Infiltration of 25 Vol Pct  $\text{TiO}_2/\text{Al}$  Composites.  
Microstructure/processing relationships in reaction-synthesized titanium aluminide intermetallic matrix composites.  
**Reactivity**  
The Oxidation Behavior of Unactivated and Mechanically Activated Sphalerite.
- 79-89B  
551-559B  
561-564B  
651-660B  
661-668B  
47-54B  
3215-3225A  
675-679A  
285-296B  
721-733A  
743-747A  
1221-1228A  
3573-3576A  
3755-3760A  
146-147B  
41-46B  
661-668B  
743-747A  
657-664A  
129-136B  
335-344B  
543-550B  
589-594B  
685-693B  
711-716B  
717-721B  
813-816B  
2899-2906A  
3121-3126A  
61-67B  
355-364B  
2155-2162A  
31-40B  
543-550B  
589-594B  
1275-1280A  
2073-2080A  
2155-2162A  
2747-2753A  
897-900B



<b>Reactors</b>		
Experimental Study of Phase Equilibria in the PbO-ZnO-Fe <sub>2</sub> O <sub>3</sub> -CaO-SiO <sub>2</sub> System in Air for High Lead Smelting Slags (CaO/SiO <sub>2</sub> = 0.35 and PbO/(CaO+SiO <sub>2</sub> ) = 5.0 by Weight).	817-825B	
<b>Reagents</b>		
Communication: Conversion of VOCl <sub>3</sub> to VOCl <sub>2</sub> in liquid TiCl <sub>4</sub> .	142-146B	
<b>Recalcification</b>		
Direct observation of the crystal-growth transition in under-cooled silicon.	2947-2953A	
<b>Recovery</b>		
Communication: Microstructural interpretation of negligible strain-hardening behavior of submicrometer-grained low-carbon steel during tensile deformation.	705-707A	
Changes in Order and Texture during Annealing of Heavily Cold-Rolled Ni <sub>3</sub> Al (B,Zr) Alloy	3605-3618A	
<b>Recrystallization</b>		
Study of the kinetics of the recrystallization of cold-rolled low-carbon steel.	25-31A	
Modeling the kinetics of grain-boundary-nucleated recrystallization processes after cold deformation.	529-537A	
Hot rolling texture development in CMnCrSi dual-phase steels.	1091-1102A	
Texture and microstructure development during intercritical rolling of low-carbon steels.	1589-1603A	
Annealing behavior of alumina dispersion-strengthened copper strips rolled under different conditions.	1605-1616A	
Evolution of microstructure and properties in alpha-brass after iterative processing.	1853-1857A	
Formation and Annealing Behavior of Nanocrystalline Ferrite in Fe-0.89C Spheroidite Steel Produced by Ball Milling.	2195-2203A	
Static Recrystallization Mechanisms in a Coarse-Grained Nb-Microalloyed Austenite.	3089-3098A	
Changes in Order and Texture during Annealing of Heavily Cold-Rolled Ni <sub>3</sub> Al (B,Zr) Alloy	3605-3618A	
The Microstructure and Recrystallization of Flow-Formed Oxide-Dispersion-Strengthened Ferritic Alloy: Part II. Recrystallization Behavior.	3787-3794A	
<b>Reducing agents</b>		
Thermodynamic study of the reduction of titanium magnetite concentrate with solid carbon.	633-638B	
A Novel Cyclic Process using CaSO <sub>4</sub> /CaS Pellets for Converting Sulfur Dioxide to Elemental Sulfur without Generating Secondary Pollutants: Part I. Feasibility and Kinetics of the Reduction of Sulfur Dioxide with Calcium Sulfide Pellets.	711-716B	
A Novel Cyclic Process using CaSO <sub>4</sub> /CaS Pellets for Converting Sulfur Dioxide to Elemental Sulfur without Generating Secondary Pollutants: Part II. Hydrogen Reduction of Calcium-Sulfate Pellets to Calcium Sulfide.	717-721B	
<b>Reduction</b>		
Rare Earth Extraction and Separation from Mixed Bastnaesite-Monazite Concentrate by Stepwise Carbochlorination-Chemical Vapor Transport.	661-668B	
<b>Reduction (chemical)</b>		
Communication: Conversion of VOCl <sub>3</sub> to VOCl <sub>2</sub> in liquid TiCl <sub>4</sub> .	142-146B	
<b>Reduction (metal working)</b>		
Mechanical anisotropy and grain interaction in recrystallized aluminum.	2635-2648A	
<b>Remanence</b>		
A novel technique for manufacturing metal-bonded Nd-Fe-B magnets by squeeze casting.	637-646A	
<b>Repairing</b>		
Infrared repair brazing of 403 stainless steel with a nickel-based braze alloy.	1765-1773A	
<b>Research</b>		
Ingenuity and innovation - the hallmarks of Brimacombe's pioneering contributions to process engineering.	5-29B	
<b>Residual stress</b>		
Three-dimensional investigation of long-range internal stresses in a single crystal deforming by nonsymmetrical slip.	591-596A	
Inertia Welding Nickel-Based Superalloy: Part II. Residual Stress Characterization.	3227-3234A	
Evaluation of the Fatigue Behavior of Ductile Irons with Various Matrix Microstructures.	3719-3730A	
On the Influence of N on Residual Microstrain in Cryomilled Ni.	3795-3801A	
<b>Residual stress, Deformation effects</b>		
Dislocation microstructure and internal-stress measurements by convergent-beam electron diffraction on creep-deformed Cu and Al.	311-317A	
<b>Residual stress, Processing effects</b>		
An analysis of residual stress fields caused by shot peening.	1775-1778A	
<b>Residual stress, Welding effects</b>		
Residual stresses in a welded superalloy disc: characterization using synchrotron diffraction and numerical process modeling.	2921-2931A	
<b>Resistance heating</b>		
The effect of rapid heat treatment on the high-temperature tensile behavior of superplastic Ti-6Al-4V.	83-92A	
In-situ measurement of continuous cooling $\beta \rightarrow \alpha$ transformation behavior of CP-Ti.	1051-1056A	
<b>Resistance spot welding, Coating effects</b>		
Effects of Au plating on small-scale resistance spot welding of thin-sheet nickel.	2667-2676A	
<b>Resistance welding</b>		
Inertia Welding Nickel-Based Superalloy: Part I. Metallurgical Characterization.	3215-3225A	
Inertia Welding Nickel-Based Superalloy: Part II. Residual Stress Characterization.	3227-3234A	
<b>Resistivity</b>		
Thermal and electrical properties of Nb <sub>2</sub> AlC, (Ti,Nb) <sub>2</sub> AlC and Ti <sub>2</sub> AlC.	2775-2779A	
<b>Resistivity, Composition effects</b>		
Equilibrium solid solubility of silicon in silver.	1145-1150A	
<b>Retained austenite</b>		
Effect of thermomechanical processing on the retained austenite content in a Si-Mn transformation-induced-plasticity steel.	2811-2816A	
<b>Reviews</b>		
Understanding creep - a review.	291-303A	
Nonbasal deformation modes of Hcp metals and alloys: role of dislocation source and mobility.	813-822A	
<b>Rhenium, Ternary systems</b>		
Evaluation of the thermodynamic properties and phase equilibria of the Re-Ta-W system.	2781-2787A	
<b>Rhodium base alloys, Mechanical properties</b>		
Communication: Microstructures and mechanical properties of (Ir,Rh) <sub>75</sub> Nb <sub>15</sub> Ni <sub>10</sub> alloys.	1281-1283A	
<b>Risers</b>		
Development of New Feeding-Distance Rules Using Casting Simulation: Part II. The New Rules.	741-755B	
<b>Roll bonding</b>		
Microstructural evolution and mechanical properties of the AA8011 alloy during the accumulative roll-bonding process.	1521-1530A	
<b>Roll load</b>		
A Precision On-Line Model for the Prediction of Roll Force and Roll Power in Hot-Strip Rolling.	3255-3272A	
<b>Rolling texture</b>		
Influence of elastic and plastic anisotropy on the flow behavior in a duplex stainless steel.	57-71A	
Computational modeling of through-thickness dynamic impact response in cross-rolled Ti-6Al-4V plates.	937-947A	
Hot rolling texture development in CMnCrSi dual-phase steels.	1091-1102A	
Texture and microstructure development during intercritical rolling of low-carbon steels.	1589-1603A	
Annealing behavior of alumina dispersion-strengthened copper strips rolled under different conditions.	1605-1616A	
Room-temperature mechanical properties of cold-rolled thin foils of binary, stoichiometric Ni <sub>3</sub> Al.	2607-2613A	
Mechanical anisotropy and grain interaction in recrystallized aluminum.	2635-2648A	
<b>Roughness, Size effects</b>		
The relationship between grain size and the surface roughening behavior of Al-Mg alloys.	2883-2889A	
<b>S N diagrams</b>		
Improvement in mechanical properties of dental cast Ti-6Al-7Nb by thermochemical processing.	503-510A	
<b>Salt water, Environment</b>		
Communication: Effect of Zr Addition on Corrosion Behavior of Cu-6Ni-2Mn-2Sn-2Al Alloy.	2237-2240A	
<b>Sand casting</b>		
Microporosity prediction in aluminum alloy castings.	243-255B	
<b>Scale (corrosion)</b>		
Communication: Thermal Scaling Behavior of Weldments of 9Cr-1Mo Steel and Its Relevance to the Life Assessment of Fossil Fuel Power Plant Components.	3296-3297A	
<b>Scanning electron microscopy</b>		
On the Nature of the Electrochemically Synthesized Hard Fe-0.96 Mass Pct C Alloy Film.	921-927B	
<b>Screw dislocations</b>		
Molecular dynamics simulation of <c + a> dislocation core structure in hexagonal-close-packed metals.	823-829A	
<b>Secondary recrystallization</b>		
The Effect of Small Deformation on Abnormal Grain Growth in Bulk Cu.	3803-3815A	
<b>Sedimentation</b>		
Modeling of Globular Equiaxed Solidification with a Two-Phase Approach.	3673-3683A	
<b>Seebeck effect</b>		
Missed Joint Induced by Thermoelectric Magnetic Field in Electron-Beam Welding Dissimilar Metals-Experiment and Scale Analysis.	765-773B	
<b>Segregations</b>		
An experimental study of deformation of a columnar dendritic mushy zone using a transparent succinonitrile-acetone alloy.	69-78B	
A unified microscale parameter approach to solidification-transport process-based macrosegregation modeling for dendritic solidification. II. Numerical example computations.	451-463B	
Diffusion along grain and interphase boundaries in Alpha Zr and Zr-2.5 Wt Pct Nb alloy.	797-800A	
Precipitation of austenite particles at grain boundaries during aging of Fe-Mn-Ni steel.	1057-1067A	
Retardation of $\alpha$ -phase transformation in modified superalloy RR2072.	1319-1330A	
Development of microstructural banding in low-alloy steel with simulated Mn segregation.	1627-1637A	
Interfacial Segregation of Ti in the Brazing of Diamond Grits onto a Steel Substrate Using a Cu-Sn-Ti Brazing Alloy.	2163-2172A	
Subnanometer-scale chemistry and structure of $\alpha$ -iron/molybdenum nitride heterophase interfaces.	2317-2326A	
Segregation and morphological instability due to double-diffusive convection in rotational directional solidification.	3011-3017A	
Communication: Minimizing Segregation during the Controlled Directional Solidification of Dendritic Alloys.	3876-3881A	



- Self-interstitials**  
Atomic-scale modeling of dislocations and related properties in the hexagonal-close-packed metals. 721-733A  
Anisotropy of point defect diffusion in alpha-zirconium. 777-782A  
Mobility of interstitial clusters in alpha-zirconium. 783-789A
- Self-propagating synthesis**  
The incorporation of self-propagating, high-temperature synthesis-formed Fe-TiB<sub>2</sub> into ferrous melts. 2973-2983A  
Solidification paths and reinforcement morphologies in melt-processed (TiB + TiC)/Ti in situ composites. 3055-3063A  
Self-Propagating Reaction Induced by Ball Milling in a Mixture of Cu<sub>2</sub>O and Al Powders. 3521-3526A  
Microstructural Analysis of Multilayered Titanium Aluminide Sheets Fabricated by Hot Rolling and Heat Treatment. 3649-3659A
- Semi-solid processing**  
Rheology and microstructure of semi-solid aluminum alloys compressed in the drop-forge viscometer. 2737-2746A
- Sensitizing**  
Sensitization behavior of type 308 stainless steel weld metals after postweld heat treatment and low-temperature aging and its relation to microstructure. 1743-1754A
- Sensors**  
Processing and microstructures of fiber Bragg grating sensors embedded in stainless steel. 3019-3024A
- Separation**  
Kinetics of manganese reduction leaching from weathered rare-earth mud with sodium sulfite. 41-46B  
Rare Earth Extraction and Separation from Mixed Bastnaesite-Monazite Concentrate by Stepwise Carbochlorination-Chemical Vapor Transport. 661-668B  
A New Method for Three-Dimensional Numerical Simulation of Electromagnetic and Fluid-Flow Phenomena in Electromagnetic Separation of Inclusions from Liquid Metal. 775-785B
- Sessile dislocations**  
Interfacial deformation mechanisms in hexagonal-close-packed metals. 801-807A  
Molecular dynamics simulation of <c + a> dislocation core structure in hexagonal-close-packed metals. 823-829A  
Effect of temperature and shear direction on yield stress by {1122}<1123> slip in hcp metals. 831-836A
- Shape memory**  
Shape Memory Behavior of FeNiCoTi Single and Polycrystals 3661-3672A
- Shape memory, Composition effects**  
Two-way shape memory effect of TiNi alloys induced by hydrogenation. 17-23A
- Shape memory alloys**  
Hydrogen embrittlement of nickel-titanium alloy in biological environment. 495-501A  
Large Self-Thermal-Plastic Deformation in a NiTi Shape-Memory Alloy Fiber-Actuated Aluminum Metal-Matrix Composite. 3535-3540A
- Shape memory alloys, Phase transformations**  
Influence of Al and Ni concentration on the martensitic transformation in Cu-Al-Ni shape-memory alloys. 2581-2591A  
Enhancement of superelasticity in Cu-Al-Mn-Ni shape-memory alloys by texture control. 2817-2824A
- Shear deformation**  
Rheology and microstructure of semi-solid aluminum alloys compressed in the drop-forge viscometer. 2737-2746A  
Large-Strain Softening of Aluminum in Shear at Elevated Temperature. 3145-3153A
- Shear stress**  
Erratum: Shear principal, and equivalent strains in equal-channel angular deformation. 467A  
The influence of the stress state on the plasticity of transformation induced plasticity-aided steel. 1659-1667A  
On thermoplastic shear instability in the machining of a titanium alloy (Ti-6Al-4V). 2995-3010A
- Sheet metal**  
Role of yield criteria and hardening laws in the prediction of forming limit diagrams. 1363-1371A
- Sheet metal, Coatings**  
Orientation domains and texture in hot-dipped galvanized coatings. 2695-2701A
- Sheet metal, Metal working**  
The influence of the stress state on the plasticity of transformation induced plasticity-aided steel. 1659-1667A
- Sheet metal, Rolling**  
Mechanical anisotropy and grain interaction in recrystallized aluminum. 2635-2648A
- Sheet metal, Welding**  
Investigation on the effect of laser pulse shape during Nd:YAG laser microwelding of thin Al sheet by numerical simulation. 1449-1459A  
Effects of Au plating on small-scale resistance spot welding of thin-sheet nickel. 2667-2676A
- Shielded metal arc welding**  
Dissolution Kinetics of NbC Particles in the Heat-Affected Zone of Type 347 Austenitic Stainless Steel. 2031-2042A
- Short range order**  
First-principles investigation of perfect and diffuse antiphase boundaries in hcp-based Ti-Al alloys. 735-741A
- Shot peening**  
An analysis of residual stress fields caused by shot peening. 1775-1778A
- Shrinkage**  
Development of New Feeding-Distance Rules Using Casting Simulation: Part I. Methodology. 731-740B
- Silicates, Composite materials**  
Interfacial reactions in aluminosilicate short fiber-reinforced aluminum matrix composites. 2755-2761A
- Silicon, Alloying additive**  
Communication: Phase Transformations in FeMnAlC Austenitic Steels with Si Addition. 3569-3573A
- Silicon, Alloying elements**  
A three-phase model of hydrogen pore formation during the equiaxed dendritic solidification of aluminum-silicon alloys. 209-221B
- Silicon, Coating**  
Phase formation and microstructure in sputter-deposited Ti-Mo-C and Ti-W-C thin films. 1579-1588A
- Silicon, Crystal growth**  
Direct observation of the crystal-growth transition in under-cooled silicon. 2947-2953A
- Silicon, Dopants**  
Dopant Particle Characterization and Bubble Evolution in Aluminum-Potassium-Silicon-Doped Molybdenum Wire. 3349-3356A
- Silicon, Solubility**  
Equilibrium solid solubility of silicon in silver. 1145-1150A
- Silicon, Ternary systems**  
On the Constitution of the System Al-Mn-Si. 3311-3319A
- Silicon carbide**  
Communication: Comparative Welding Study of Metal Matrix Composites with the MIG Welding Process, using Direct and Indirect Electric Arc. 932-937B
- Silicon carbide, Composite materials**  
Strength of Al-Zn-Mg-Cu matrix composite reinforced with SiC particles. 455-465A  
In-situ formation of SiC-reinforced Al-Si alloy composites using methane gas mixtures. 543-550B  
High stress abrasive wear mechanism of LM13-SiC composite under varying experimental conditions. 3031-3044A  
Micromechanical modeling of unidirectional continuous sigma fiber-reinforced Ti-6Al-4V subjected to transverse tensile loading. 3045-3054A  
Microscale Elastic Strain Evolution Following Damage in Ti-SiC Composites. 3839-3845A  
Effect of Overaging and Particle Size on Tensile Deformation and Fracture of Particle-Reinforced Aluminum Matrix Composites. 3861-3869A
- Silicon manganese steels, Phase transformations**  
Effect of thermomechanical processing on the retained austenite content in a Si-Mn transformation-induced-plasticity steel. 2811-2816A
- Silver, Alloying elements**  
Communication: On the solute field and composition of  $\gamma$  plates in an Al-22 At. Pct Ag alloy. 1561-1565A
- Silver, Reactions (chemical)**  
Kinetics of Silver Leaching from Manganese-Silver Associated Ores in Sulfuric Acid Solution in the Presence of Hydrogen Peroxide. 813-816B
- Silver, Ternary systems**  
Estimation Of Viscosity Of Ternary-Metallic Melts. 3201-3204A
- Silver base alloys, Electrical properties**  
Equilibrium solid solubility of silicon in silver. 1145-1150A
- Silver base alloys, Physical properties**  
Normal spectral emissivities of liquid Ag-Cu alloys in the visible and infrared regions. 47-54B
- Simulation**  
Simulation of Cavitation Processes in Superplastic Deformation. 3449-3455A
- Single crystals**  
Localized deformation and hardening in irradiated metals: three-dimensional discrete dislocation dynamics simulations. 285-296B  
Dislocation microstructure and internal-stress measurements by convergent-beam electron diffraction on creep-deformed Cu and Al. 311-317A  
Deformation behavior of Hcp Ti-Al alloy single crystals. 837-850A
- Single crystals, Directional solidification**  
Segregation and morphological instability due to double-diffusive convection in rotational directional solidification. 3011-3017A
- Single crystals, Microstructure**  
Three-dimensional investigation of long-range internal stresses in a single crystal deforming by nonsymmetrical slip. 591-596A
- Single crystals, Surface properties**  
Misfit dislocations in epitaxy. 2475-2483A  
Reciprocal-space formulation and prediction of misfit accommodation in rigid and strained epitaxial systems. 2485-2494A
- Sintered compacts, Mechanical properties**  
Fatigue crack initiation and propagation of binder-treated powder metallurgy steels. 73-81A
- Sintering (powder metallurgy)**  
Effect of residual carbon on the sintering process of m2 high speed steel parts obtained by a modified metal injection molding process. 1843-1851A  
Sintering Densification and Microstructural Evolution of Injection Molding Grade 17-4 PH Stainless Steel Powder. 2185-2194A  
The Influence of the Atmosphere on the Sintering of Aluminum. 3279-3284A
- Sintering (roasting)**  
Stability of silico-ferrite of calcium and aluminum (SFCA) in air-solid solution limits between 1240°C and 1390°C and phase relationships within the Fe<sub>2</sub>O<sub>3</sub>-CaO-Al<sub>2</sub>O<sub>3</sub>-SiO<sub>2</sub> (FCAS) system. 79-89B
- Skull melting**  
The Critical Pressure and Impeding Pressure of Al Evaporation

- during Induction Skull Melting Processing of TiAl. 3249-3253A
- Slab casting**
- Simulation of the submerged energy nozzle-mold water model system using laser-optical and computational fluid dynamics methods. 163-172B
- Correction to "Simulation of the submerged energy nozzle-mold water model systems using laser optical and computational fluid dynamics methods". 639B
- Modeling of the Continuous Casting of Steel-Past, Present, and Future. 795-812B
- Titanium Nitride Precipitation Behavior in Thin-Slab Cast High-Strength Low-Alloy Steels. 3099-3110A
- Slags**
- The equilibrium partitioning of titanium between  $Ti^{3+}$  and  $Ti^{4+}$  valency states in  $CaO-SiO_2-TiO_2$  slags. 61-67B
- Kinetics of formation and dissociation of  $Na_2SiF_6$ . 129-136B
- A theoretical and experimental study of continuous-casting tundishes focusing on slag-steel interaction. 173-185B
- Process dynamics of electric arc furnace during direct reduced iron melting. 187-199B
- The reaction behavior of Fe-C-S droplets in  $CaO-SiO_2-MgO-FeO$  slags. 335-344B
- Recycling of magnesium alloys: chemical equilibria between magnesium-lithium-based melts and salt melts. 355-364B
- Determination of Gibbs energies of formation of  $CaFe_2O_4$  and  $Ca_2Fe_2O_5$  from solid-state emf measurements using  $CaF_2$  as solid electrolyte. 385-392B
- Rate of nitrogen desorption from  $CaO-Al_2O_3$  melts to gas phase. 393-401B
- Communication: Foaming behavior of slags. 499-501B
- Slags and mattes in Vanyukov's process for the extraction of copper. 551-559B
- Physicochemical properties of matte-slag melts taken from Vanyukov's furnace for copper extraction. 561-564B
- Oxidation state and activities of chromium oxides in  $CaO-SiO_2-Cr_2O_3$  slag system. 595-603B
- Rate of Interfacial Reaction between Molten  $CaO-SiO_2-Al_2O_3-Fe_2O_3$  and  $CO-CO_2$ . 651-660B
- Experimental Study of Phase Equilibria in the  $PbO-ZnO-Fe_2O_3-CaO-SiO_2$  System in Air for High Lead Smelting Slags ( $CaO/SiO_2 = 0.35$  and  $PbO/(CaO+SiO_2) = 5.0$  by Weight). 817-825B
- Experimental Liquidus in the  $PbO-ZnO-Fe_2O_3-(CaO+SiO_2)$  System in Air, with  $CaO/SiO_2 = 0.35$  and  $PbO/(CaO+SiO_2) = 3.2$ . 851-863B
- Thermodynamic Study of  $MnO-SiO_2-Al_2O_3$  Slag System: Liquidus Lines and Activities of  $MnO$  at 1823 K. 915-920B
- Slags, Physical properties**
- The Effect of  $CaF_2$  on the Viscosities and Structures of  $CaO-SiO_2(MgO)-CaF_2$  Slags. 723-729B
- Slags, Reactions (chemical)**
- Communication: Solubility of Iron Magnesium-Lithium Melts. 929-930B
- Slags, Recycling**
- Solid-state reaction kinetics of the system  $CaO-FeO$ . 257-264B
- Slags, Solubility**
- Thermodynamic behavior of nickel in  $CaO-SiO_2-FeO$  slag. 55-59B
- Sliding friction**
- Near-nanostructured WC-18 pct co coatings with low amounts of non-WC carbide phase: Part II. Hardness and resistance to sliding and abrasive wear. 159-164A
- Sliding wear of austenitic and austenitic-ferritic stainless steels. Surface engineering of Timet 550 with oxygen to form a rutile-based, wear-resistant coating. 613-624A
- Communication: Effect of carbon addition on tribological properties of Fe-Al alloys. 1201-1211A
- 1292-1295A
- Slip bands**
- On thermoplastic shear instability in the machining of a titanium alloy (Ti-6Al-4V). 2995-3010A
- The Microstructure and Recrystallization of Flow-Formed Oxide-Dispersion-Strengthened Ferritic Alloy: Part I. Deformation Structure. 3777-3785A
- Slip planes**
- First-principles investigation of perfect and diffuse antiphase boundaries in hcp-based Ti-Al alloys. 735-741A
- Interfacial deformation mechanisms in hexagonal-close-packed metals. 801-807A
- Twins as barriers to basal slip in hexagonal-close-packed metals. 809-812A
- Nonbasal deformation modes of Hcp metals and alloys: role of dislocation source and mobility. 813-822A
- Effect of temperature and shear direction on yield stress by (1122)<1123> slip in hcp metals. 831-836A
- Deformation behavior of Hcp Ti-Al alloy single crystals. 837-850A
- Transmission electron microscopy investigation of <c + a> dislocations in Mg and  $\alpha$ -solid solution Mg-Li alloys. 851-858A
- Slipping**
- Three-dimensional investigation of long-range internal stresses in a single crystal deforming by nonsymmetrical slip. 591-596A
- Slurrying**
- Microstructure and Mechanical Properties of Titanium Aluminum Wide-Gap, Transient Liquid-Phase Bonds Prepared using a Slurry-Deposited Composite Interlayer. 3205-3214A
- Smelting**
- Slags and mattes in Vanyukov's process for the extraction of copper. 551-559B
- Physicochemical properties of matte-slag melts taken from Vanyukov's furnace for copper extraction. 561-564B
- A Novel Cyclic Process using  $CaSO_4/CaS$  Pellets for Converting Sulfur Dioxide to Elemental Sulfur without Generating Secondary Pollutants: Part I. Feasibility and Kinetics of the Reduction of Sulfur Dioxide with Calcium Sulfide Pellets. 711-716B
- A Novel Cyclic Process using  $CaSO_4/CaS$  Pellets for Converting Sulfur Dioxide to Elemental Sulfur without Generating Secondary Pollutants: Part II. Hydrogen Reduction of Calcium-Sulfate Pellets to Calcium Sulfide. 717-721B
- Experimental Study of Phase Equilibria in the  $PbO-ZnO-Fe_2O_3-CaO-SiO_2$  System in Air for High Lead Smelting Slags ( $CaO/SiO_2 = 0.35$  and  $PbO/(CaO+SiO_2) = 5.0$  by Weight). 817-825B
- Experimental Liquidus in the  $PbO-ZnO-Fe_2O_3-(CaO+SiO_2)$  System in Air, with  $CaO/SiO_2 = 0.35$  and  $PbO/(CaO+SiO_2) = 3.2$ . 851-863B
- Softening**
- Fatigue Deformation-Induced Response in a Superduplex Stainless Steel. 3433-3442A
- Soil (material)**
- Environmental aspects of near-neutral pH stress corrosion cracking of pipeline steel. 1429-1436A
- Soldering**
- Creep of Tin, Sb-solution-strengthened Tin, and SbSn-precipitate-strengthened tin. 1531-1539A
- Solders, Development**
- Creep of Tin, Sb-solution-strengthened Tin, and SbSn-precipitate-strengthened tin. 1531-1539A
- Solid solubility**
- Equilibrium solid solubility of silicon in silver. 1145-1150A
- Communication: The Gibbs-Thomson effect in dilute binary systems. 1283-1287A
- Solid solutions**
- Transmission electron microscopy investigation of <c + a> dislocations in Mg and  $\alpha$ -solid solution Mg-Li alloys. 851-858A
- Experimental Study of Phase Equilibria in the "FeO"-ZnO( $CaO+SiO_2$ ) System with the  $CaO/SiO_2$  Weight Ratio of 0.71 at Metallic Iron Saturation. 865-876B
- Creep strength of magnesium-based alloys. 875-882A
- Experimental Study of Phase Equilibria in the "FeO"-ZnO( $CaO+SiO_2$ ) System with  $CaO/SiO_2$  Weight Ratios of 0.33, 0.93, and 1.2 in Equilibrium with Metallic Iron. 877-890B
- Equilibrium solid solubility of silicon in silver. 1145-1150A
- Modeling  $M_{23}C_6$  Precipitation in Niobium-Alloyed Ferritic Stainless Steel. 3339-3347A
- Coprecipitation of  $\Omega$  and  $\sigma$  Phases in Al-Cu-Mg-Mn Alloys Containing Ag and Si. 3635-3648A
- Solid solutions, Atomic properties**
- On the Partial Atomic Volume of Aluminum in Solid Solutions Based on the 3d Transition Metals and Copper. 3591-3595A
- Solid solutions, Phase transformations**
- Communications: On substitutional element partitioning coefficients of two-phase alloys. 3065-3066A
- Solid state**
- Solid-state reaction kinetics of the system  $CaO-FeO$ . 257-264B
- Solidification**
- An experimental study of deformation of a columnar dendritic mushy zone using a transparent succinonitrile-acetone alloy. 69-78B
- An analytical self-consistent determination of a bubble with a deformed cap trapped in solid during solidification. 91-100B
- A three-phase model of hydrogen pore formation during the equiaxed dendritic solidification of aluminum-silicon alloys. 209-221B
- Microporosity prediction in aluminum alloy castings. 243-255B
- Averaged solute transport during solidification of a binary mixture: active dispersion in dendritic structures. 365-376B
- A unified microscale parameter approach to solidification-transport process-based macrosegregation modeling for dendritic solidification. II. Numerical example computations. 451-463B
- Computer simulation of solidification processes - the evolution of a technology. 519-541B
- Rayleigh-Benard convection during solidification of an eutectic solution cooled from the top. 605-612B
- Time-resolved X-ray imaging of aluminum alloy solidification processes. 613-623B
- Formation of  $CaS$  on  $Al_2O_3-CaO$  inclusions during solidification of steels. 625-632B
- A 500°C isothermal section for the Al-Au-Cu system. 987-993A
- Analysis and prevention of microcracking phenomenon occurring during strip casting of an AISI 304 stainless steel. 1487-1497A
- Texture enhancement by inoculation during casting of ferritic stainless steel strip. 1499-1507A
- Communication: On the solute field and composition of  $\gamma$  plates in an Al-22 At. Pct Ag alloy. 1561-1565A
- Development of microstructural banding in low-alloy steel with simulated Mn segregation. 1627-1637A
- On differential thermal analyzer curves for the melting and freezing of alloys. 1779-1794A
- Tree-ring formation during vacuum arc remelting of INCONEL 718. I. Experimental investigation. 1795-1804A
- Tree-ring formation during vacuum arc remelting of INCONEL 718. II. Mathematical modeling. 1805-1815A
- Communication: Reduced critical solidification front velocity of particle engulfment due to an interface active solute in the liquid metal. 1869-1873A
- Constitutive Behavior of As-Cast AM 050, AA3104, and AA5182. 1971-1980A
- Two-Phase Modeling Directed Toward Hot Tearing Formation in Aluminum Direct Chill Casting. 2081-2093A
- Modeling of Microporosity, Macroporosity, and Pipe-shrinkage Formation during the Solidification of Alloys Using a Mushy-Zone Refinement Method: Applications to Aluminum Alloys. 2095-2106A
- Computer simulation of solidification processes - the evolution

- of a technology.  
Carbide formation in alloy 718 during electron-beam solid free-form fabrication. 2251-2273A  
Numerical simulation of Zn coating solidification. 2559-2567A  
The microstructural development of Mg-9 pct Al-1 pct Zn alloy during injection molding. 2685-2694A  
Modeling of Globular Equiaxed Solidification with a Two-Phase Approach. 2963-2972A  
Evolution of Microstructure and Texture during Casting of AISI 304 Stainless Steel Strip. 3673-3683A  
Communication: Thermodynamics of Hydrogen in Al-Si Alloys. 3747-3754A  
3874-3876A
- Solidification, Diffusion effects**  
Diffusion-based model for isothermal solidification kinetics during transient liquid-phase sintering. 117-124A
- Solubility**  
Communication: Prediction of the thermodynamic properties of solutes in the Bi-based ternary dilute solution. 502-506B  
Solubility of Some Transition Metal Oxides in Cryolite-Alumina Melts: Part I. Solubility of FeO, FeAl<sub>2</sub>O<sub>4</sub>, NiO, and NiAl<sub>2</sub>O<sub>4</sub>. 901-908B  
Solubility of Some Transition Metal Oxides in Cryolite-Alumina Melts: Part II. Solubility of TiO<sub>2</sub>. 909-913B  
Communication: Solubility of Iron Magnesium-Lithium Melts. 929-930B  
Communication: Thermodynamics of Hydrogen in Al-Si Alloys. 3874-3876A
- Solutes**  
Modeling of the solubility of alumina in the NaF-AlF<sub>3</sub> system at 1300 K. 315-319B  
Communication: Minimizing Segregation during the Controlled Directional Solidification of Dendritic Alloys. 3876-3881A
- Solution annealing**  
Age-hardening characteristics of aluminum alloy-hollow fly ash composites. 1541-1547A
- Solution heat treatment**  
Aging behavior of the Ti-29Nb-13Ta-4.6Zr new beta alloy for medical implants. 487-493A  
Effect of alternative aging process on the fracture and interfacial properties of particulate Al<sub>2</sub>O<sub>3</sub>-reinforced Al (6061) metal matrix composite. 1699-1713A
- Solvent extraction**  
Communication: Removal of phosphorus-based extractant contamination from lutetium oxalate produced by precipitation stripping. 146-147B
- Specimen preparation**  
Harper-Dorn creep and specimen size. 305-310A
- Spectral emissivity, Composition effects**  
Normal spectral emissivities of liquid Ag-Cu alloys in the visible and infrared regions. 47-54B
- Sphalerite, Oxidation**  
The Oxidation Behavior of Unactivated and Mechanically Activated Sphalerite. 897-900B
- Spheroidizing**  
Spheroidization cycles for medium carbon steels. 1255-1261A
- Spinel, Reactions (chemical)**  
Thermodynamics on the Formation of Spinel (MgO-Al<sub>2</sub>O<sub>3</sub>) Inclusion in Liquid Iron Containing Chromium. 703-709B
- Sprayed coatings, Mechanical properties**  
Synthesis and nanoindentation study of high-velocity oxygen fuel thermal-sprayed nanocrystalline and near-nanocrystalline Ni coatings. 647-655A
- Sputtered coatings**  
Energy of the Pb(111) | Al(111) interface. 1003-1007A
- Sputtered films, Microstructure**  
Stable quasicrystalline phase in Al-Cu-Fe-Cr coating materials. 675-679A
- Sputtering**  
Phase formation and microstructure in sputter-deposited Ti-Mo-C and Ti-W-C thin films. 1579-1588A  
Processing and microstructures of fiber Bragg grating sensors embedded in stainless steel. 3019-3024A
- Squeeze casting**  
Effect of heat treatments on in-situ Al<sub>2</sub>O<sub>3</sub>/TiAl<sub>3</sub> composites produced from squeeze casting of TiO<sub>2</sub>/A356 composites. 31-40B  
A novel technique for manufacturing metal-bonded Nd-Fe-B magnets by squeeze casting. 637-646A  
Evolution of fiber fragmentation in a short-fiber-reinforced metal-matrix model composite during tensile creep deformation-an acoustic emission study. 1549-1557A
- Stability**  
Method for Measuring Transformation Energy and Quantitative Characterization of Transformation-Induced Plasticity. 3117-3120A
- Stabilization**  
The Optimum Wetting Angle for the Stabilization of Liquid-Metal Foams by Ceramic Particles: Experimental Simulations. 3285-3292A
- Stacking fault energy**  
Method for Measuring Transformation Energy and Quantitative Characterization of Transformation-Induced Plasticity. 3117-3120A
- Stacking faults**  
Transmission electron microscopy investigation of <c + a> dislocations in Mg and  $\alpha$ -solid solution Mg-Li alloys. 851-858A
- Stainless steels, Coating**  
Processing and microstructures of fiber Bragg grating sensors embedded in stainless steel. 3019-3024A
- Stainless steels, Composite materials**  
Normalized Diagrams for Micromechanical Estimates of the Elastic Response of Composite Materials. 3187-3199A
- Stainless steels, Steel making**
- Mathematical modeling of the argon-oxygen decarburization refining process of stainless steel: Part I. Mathematical model of the process. 111-119B  
Mathematical modeling of the argon-oxygen decarburization refining process of stainless steel: Part II. Application of the model to industrial practice. 121-127B  
Oxidation state and activities of chromium oxides in CaO-SiO<sub>2</sub>-Cr<sub>2</sub>O<sub>3</sub> slag system. 595-603B
- Stainless steels, Surface properties**  
Recent metallic materials for biomedical applications. 477-486A
- Steel constituents**  
Development of microstructural banding in low-alloy steel with simulated Mn segregation. 1627-1637A  
Simulation of ferrite growth in continuously cooled low-carbon iron alloys. 2309-2316A
- Steel making**  
Ingenuity and innovation - the hallmarks of Brimacombe's pioneering contributions to process engineering. 5-29B  
Thermodynamic behavior of nickel in CaO-SiO<sub>2</sub>-FeO slag. 55-59B  
The equilibrium partitioning of titanium between Ti<sup>3+</sup> and Ti<sup>4+</sup> valency states in CaO-SiO<sub>2</sub>-TiO<sub>2</sub> slags. 61-67B  
Process dynamics of electric arc furnace during direct reduced iron melting. 187-199B  
Rate of nitrogen desorption from CaO-Al<sub>2</sub>O<sub>3</sub> melts to gas phase. 393-401B
- Steels, Casting**  
Ingenuity and innovation - the hallmarks of Brimacombe's pioneering contributions to process engineering. 5-29B  
An experimental study of deformation of a columnar dendritic mushy zone using a transparent succinonitrile-acetone alloy. 69-78B  
Modeling the formation of longitudinal facial cracks during continuous casting of hypoperitectic steel. 413-423B  
Thermal and mechanical behavior of copper molds during thin-slab casting. I. Plant trial and mathematical modeling. 425-436B  
Thermal and mechanical behavior of copper molds during thin-slab casting. II. Mold crack formation. 437-449B  
Modeling of the Continuous Casting of Steel-Past, Present, and Future. 795-812B
- Steels, Coating**  
Numerical simulation of Zn coating solidification. 2685-2694A  
Orientation domains and texture in hot-dipped galvanized coatings. 2695-2701A
- Steels, Crystal growth**  
Static Recrystallization Mechanisms in a Coarse-Grained Nb-Microalloyed Austenite. 3089-3098A
- Steels, Joining**  
Interfacial Segregation of Ti in the Brazing of Diamond Grits onto a Steel Substrate Using a Cu-Sn-Ti Brazing Alloy. 2163-2172A
- Steels, Mechanical properties**  
Communication: Effect of boron on the hot ductility of Nb-containing steel. 701-704A
- Steels, Microstructure**  
Inferring Dynamic Recrystallization in Ferrite using the Kinetics of Static Recrystallization. 1893-1900A
- Steels, Phase transformations**  
Modeling The Austenite-Ferrite Isothermal Transformation in an Fe-C Binary System and Experimental Verification. 3111-3115A
- Steels, Powder technology**  
Formation and Annealing Behavior of Nanocrystalline Ferrite in Fe-0.89C Spheroidite Steel Produced by Ball Milling. 2195-2203A
- Steels, Welding**  
Modeling of laser keyhole welding. II. Simulation of keyhole evolution, velocity, temperature profile, and experimental verification. 1831-1842A
- Stiffness, Microstructural effects**  
On Composite-Structure Weaknesses: Part I. Simulation, Properties, and Numerical Approach. 2205-2215A  
On Composite-Structure Weaknesses: Part II. Computer Experiments, Identification, and Correlation. 2217-2227A
- Stirring**  
A water model and numerical study of the spout height in a gas-stirred vessel. 377-384B  
Interfacial reactions in aluminosilicate short fiber-reinforced aluminum matrix composites. 2755-2761A
- Stoichiometry**  
Thermodynamic Modeling of the Indium-Palladium System. 3597-3603A
- Storage tanks, Materials selection**  
Crack-initiation toughness and crack-arrest toughness in advanced 9 pct Ni steel welds containing local brittle zones. 2615-2622A
- Strain**  
Erratum: Shear principal, and equivalent strains in equal-channel angular deformation. 467A  
Communication: Infrared imaging during low-cycle fatigue of HR-120 alloy. 1287-1292A  
Role of yield criteria and hardening laws in the prediction of forming limit diagrams. 1363-1371A  
Microstructural evolution and mechanical properties of the AA8011 alloy during the accumulative roll-bonding process. 1521-1530A  
Sequences of Phase Formation in Multiphase Stressed Plates. 1901-1911A  
Quantitative characterization of three-dimensional damage evolution in a wrought Al-alloy under tension and compression. 2599-2606A  
Effect of the Lamellar Grain Size on Plastic Flow Behavior and Microstructure Evolution during Hot Working of a Gamma Titanium Aluminum Alloy. 3817-3830A
- Strain, Anisotropy**  
Mechanical anisotropy and grain interaction in recrystallized



- aluminum. 2635-2648A
- Strain aging**  
Analysis of steady-state thermal creep of Zr-2.5Nb pressure tube material. 1103-1115A
- Strain hardenability**  
Phase transformation and mechanical properties of Si-free CMnAl transformation-induced plasticity-aided steel. 2573-2580A
- Strain hardening**  
Subgrain formation during deformation: physical origin and consequences. 319-327A  
Communication: Microstructural interpretation of negligible strain-hardening behavior of submicrometer-grained low-carbon steel during tensile deformation. 705-707A  
Anisotropic threshold stress intensity factor,  $K_{IH}$ , and crack growth rate in delayed hydride cracking of Zr-2.5Nb pressure tubes. 919-925A  
Fatigue Deformation-Induced Response in a Superalloy Stainless Steel. 3433-3442A
- Strain rate**  
Microstructural gradients in the superplastic forming of Ti-6Al-4V. 93-100A  
Elevated-temperature deformation at forming rates of  $10^{-2}$  to  $10^2$  s $^{-1}$ . 345-362A  
Constitutive equations for creep and plasticity of aluminum alloys produced by powder metallurgy and aluminum-based metal matrix composites. 373-381A  
A study of twinning in zirconium using neutron diffraction and polycrystalline modeling. 757-763A  
Effects of high rates of loading on the deformation behavior and failure mechanisms of hexagonal close-packed metals and alloys. 927-935A  
Deformation mechanisms during low- and high-temperature superplasticity in 5083 Al-Mg alloy. 1373-1384A  
Communication: Interpretation of flow instability using dynamic material modeling. 1569-1572A  
Inferring Dynamic Recrystallization in Ferrite using the Kinetics of Static Recrystallization. 1893-1900A  
Flow Stress and Ductility of Duplex Stainless Steel during High-Temperature Torsion Deformation. 1931-1938A  
Self-consistent modeling of the flow behavior of wrought alpha/beta titanium alloys under isothermal and nonisothermal hot-working conditions. 2719-2727A  
Comparative study of the impact response and microstructure of 3041 stainless steel with and without prestrain. 2801-2810A  
Low-temperature superplastic behavior of a submicrometer-grained 5083 Al alloy fabricated by severe plastic deformation. 2859-2867A  
Strength and Plastic Flow in "In Situ" TiC Reinforced Aluminum Composites. 3831-3838A
- Strain softening**  
Flow Stress and Ductility of Duplex Stainless Steel during High-Temperature Torsion Deformation. 1931-1938A  
Large-Strain Softening of Aluminum in Shear at Elevated Temperature. 3145-3153A
- Strength to weight ratio**  
Communication: Microstructures and mechanical properties of (Ir,Rh)<sub>75</sub>Nb<sub>15</sub>Ni<sub>10</sub> alloys. 1281-1283A
- Stress analysis**  
Three-dimensional investigation of long-range internal stresses in a single crystal deforming by nonsymmetrical slip. 591-596A  
An analysis of residual stress fields caused by shot peening. 1775-1778A  
Constitutive Behavior of As-Cast AM 050, AA3104, and AA5182. 1971-1980A
- Stress corrosion cracking**  
Environmental aspects of near-neutral pH stress corrosion cracking of pipeline steel. 1429-1436A  
Fracture toughness of alloy 690 and EN52 welds in air and water. 1725-1735A  
Sensitization behavior of type 308 stainless steel weld metals after postweld heat treatment and low-temperature aging and its relation to microstructure. 1743-1754A  
Communication: Effect of Zr Addition on Corrosion Behavior of Cu-6Ni-2Mn-25Sn-2Al Alloy. 2237-2240A  
Intergranular stress corrosion cracking behavior of types 308 and 316 stainless steel weld metals in a simulated boiling water reactor environment. 2907-2919A
- Stress intensity**  
The effects of test temperature, temper, and alloyed copper on the hydrogen-controlled crack growth rate of an Al-Zn-Mg-(Cu) alloy. 1167-1181A  
Erratum: The effects of test temperature, temper, and alloyed copper on the hydrogen-controlled crack growth rate of an Al-Zn-Mg-(Cu) alloy. 1297A  
Environmentally assisted, sustained-load crack growth in powder metallurgy nickel-based superalloys. 1681-1687A
- Stress intensity, Microstructural effects**  
Anisotropic threshold stress intensity factor,  $K_{IH}$ , and crack growth rate in delayed hydride cracking of Zr-2.5Nb pressure tubes. 919-925A
- Stress strain curves**  
The effect of rapid heat treatment on the high-temperature tensile behavior of superplastic Ti-6Al-4V. 83-92A  
Hydrogen embrittlement of nickel-titanium alloy in biological environment. 495-501A  
Microstructural and mechanical properties investigation of electrodeposited and annealed LIGA nickel structures. 539-554A  
Communication: Microstructural interpretation of negligible strain-hardening behavior of submicrometer-grained low-carbon steel during tensile deformation. 705-707A
- A study of twinning in zirconium using neutron diffraction and polycrystalline modeling. 757-763A  
Elevated temperature strength and room-temperature toughness of directionally solidified Ni-33Al-33Cr-1Mo. 1385-1397A  
An investigation of the microstructure and strength of open-cell 6101 aluminum foams. 1413-1427A  
Artificial Neural Network and Finite Element Modeling of Nanoindentation Tests. 1939-1947A  
Room-temperature mechanical properties of cold-rolled thin foils of binary, stoichiometric Ni<sub>3</sub>Al. 2607-2613A  
Fatigue Deformation-Induced Response in a Superalloy Stainless Steel. 3433-3442A  
Evaluation of the Fatigue Behavior of Ductile Irons with Various Matrix Microstructures. 3719-3730A
- Stress transfer**  
Creep processes in magnesium alloys and their composites. 883-889A
- Stresses**  
On Composite-Structure Weaknesses: Part I. Simulation, Properties, and Numerical Approach. 2205-2215A  
On Composite-Structure Weaknesses: Part II. Computer Experiments, Identification, and Correlation. 2217-2227A
- Stretching**  
Role of yield criteria and hardening laws in the prediction of forming limit diagrams. 1363-1371A
- Strip, Rolling**  
The production of ultrafine ferrite in low-carbon steel by strain-induced transformation. 1019-1026A
- Strip casting**  
Control of heat transfer and growth uniformity of solidifying copper shells through substrate temperature. 403-411B  
A study on inhomogeneous distribution of temper graphite particles in strip-cast Fe-C-Si alloys. 1263-1273A  
Analysis and prevention of microcracking phenomenon occurring during strip casting of an AISI 304 stainless steel. 1487-1497A  
Texture enhancement by inoculation during casting of ferritic stainless steel strip. 1499-1507A
- Submerged arc welding**  
Sensitization behavior of type 308 stainless steel weld metals after postweld heat treatment and low-temperature aging and its relation to microstructure. 1743-1754A
- Substitutional solid solutions**  
Atomistic modeling of quaternary alloys: Ti and Cu in NiAl. 265-284B
- Substructures (crystalline)**  
Evolution of Submicrocrystalline Iron Containing Dispersed Oxides under Mechanical Milling Followed by Consolidation. 3241-3248A
- Sulfates, Impurities**  
Communication: Electroreduction of cobalt from sulfate solutions—effect of substrate and background MgSO<sub>4</sub>. 137-140B
- Sulfides**  
A Novel Cyclic Process using CaSO<sub>4</sub>/CaS Pellets for Converting Sulfur Dioxide to Elemental Sulfur without Generating Secondary Pollutants: Part I. Feasibility and Kinetics of the Reduction of Sulfur Dioxide with Calcium Sulfide Pellets. 711-716B  
A Novel Cyclic Process using CaSO<sub>4</sub>/CaS Pellets for Converting Sulfur Dioxide to Elemental Sulfur without Generating Secondary Pollutants: Part II. Hydrogen Reduction of Calcium-Sulfate Pellets to Calcium Sulfide. 717-721B
- Sulfur dioxide, Reduction (chemical)**  
A Novel Cyclic Process using CaSO<sub>4</sub>/CaS Pellets for Converting Sulfur Dioxide to Elemental Sulfur without Generating Secondary Pollutants: Part I. Feasibility and Kinetics of the Reduction of Sulfur Dioxide with Calcium Sulfide Pellets. 711-716B  
A Novel Cyclic Process using CaSO<sub>4</sub>/CaS Pellets for Converting Sulfur Dioxide to Elemental Sulfur without Generating Secondary Pollutants: Part II. Hydrogen Reduction of Calcium-Sulfate Pellets to Calcium Sulfide. 717-721B
- Superalloys**  
Interfacial Dislocation Networks Strengthening a Fourth-Generation Single-Crystal TMS-138 Superalloy. 3741-3746A
- Superalloys, Casting**  
Tree-ring formation during vacuum arc remelting of INCONEL 718. I. Experimental investigation. 1795-1804A  
Tree-ring formation during vacuum arc remelting of INCONEL 718. II. Mathematical modeling. 1805-1815A  
Carbide formation in alloy 718 during electron-beam solid free-form fabrication. 2559-2567A
- Superalloys, Coating**  
Phase formation and microstructure in sputter-deposited Ti-Mo-C and Ti-W-C thin films. 1579-1588A  
Communication: Depth Profiling of Hf-Doped Aluminide Coating by Glow-Discharge Mass Spectrometry. 3578-3582A
- Superalloys, Corrosion**  
Corrosion behavior of austenitic alloy 690 under anodic and cathodic potentials. 1437-1447A
- Superalloys, Crystal growth**  
The Coarsening Kinetics of  $\gamma$  Particles in Nickel-Based Alloys. The Microstructure and Recrystallization of Flow-Formed Oxide-Dispersion-Strengthened Ferritic Alloy: Part II. Recrystallization Behavior. 3367-3373A  
3787-3794A
- Superalloys, Joining**  
Phase equilibria of the ternary Ni-Cr-Zr system and interfacial reactions in the Ni-Cr/Zr couples. 995-1002A
- Superalloys, Materials substitution**  
The effect of constraint-induced normal stress on the failure of notched TiAl components. 417-426A
- Superalloys, Mechanical properties**

- The fracture toughness and toughening mechanisms of nickel-base wear materials. 33-56A
- Communication: Infrared imaging during low-cycle fatigue of HR-120 alloy. 1287-1292A
- Environmentally assisted, sustained-load crack growth in powder metallurgy nickel-based superalloys. 1681-1687A
- Fracture toughness of alloy 690 and EN52 welds in air and water. 1725-1735A
- Fatigue-Crack-Propagation Thresholds in a Nickel-Base Superalloy at High Frequencies and Temperatures. 1949-1962A
- Some Observations of the Influence of  $\delta$ -Ferrite Content on the Hardness, Galling Resistance, and Fracture Toughness of Selected Commercially Available Iron-Based Hardfacing Alloys. 3403-3419A
- Effect of Prolonged Isothermal Exposure on Elevated-Temperature, Time-Dependent Fatigue-Crack Propagation in INCONEL Alloy 783. 3465-3478A
- The Microstructure and Recrystallization of Flow-Formed Oxide-Dispersion-Strengthened Ferritic Alloy: Part I. Deformation Structure. 3777-3785A
- Superalloys, Melting**
- Numerical simulation of dendrite white spot formation during vacuum arc remelting of INCONEL718. 443-454A
- Superalloys, Microstructure**
- Erratum: The Effects of deformation and pre-heat-treatment on abnormal grain growth in RENE 88 superalloy. 713A
- Superalloys, Phase transformations**
- Retardation of  $\alpha$ -phase transformation in modified superalloy RR2072. 1319-1330A
- Superalloys, Powder technology**
- Grain growth behavior of cryomilled INCONEL 625 powder during isothermal heat treatment. 125-134A
- Superalloys, Welding**
- The Influence of Minor Elements on the Weldability of an INCONEL 718-Type Superalloy. 2005-2017A
- Residual stresses in a welded superalloy disc: characterization using synchrotron diffraction and numerical process modeling. 2921-2931A
- Supercooling**
- In-situ observation of the precipitation of manganese sulfide in low-carbon magnesium-killed steel. 427-436A
- Microstructural characteristics of Ni-Sb eutectic alloys under substantial undercooling and containerless solidification conditions. 1221-1228A
- Numerical simulation of Zn coating solidification. 2685-2694A
- Direct observation of the crystal-growth transition in under-cooled silicon. 2947-2953A
- Solidification Behavior of Sn-15 Wt Pct Pb Alloy under a High Shear Rate and High Intensity of Turbulence during Semi-solid Processing. 3511-3520A
- Superelasticity**
- Enhancement of superelasticity in Cu-Al-Mn-Ni shape-memory alloys by texture control. 2817-2824A
- Superheating**
- Communication: Physical modeling of the effects of thermal buoyancy driven flows in aluminum casters. 321-324B
- A study of the Pb/Al (100) interfacial energy. 2569-2572A
- Superplastic forming**
- Microstructural gradients in the superplastic forming of Ti-6Al-4V. 93-100A
- Deformation bands and the formation of grain boundaries in a superplastic aluminum alloy. 279-290A
- Kinetics of biaxial dome formation by transformation superplasticity of titanium alloys and composites. 1669-1680A
- Phase transformation-induced grain refinement in rapidly solidified ultra-high-carbon steels. 2789-2799A
- Simulation of Cavitation Processes in Superplastic Deformation. 3449-3455A
- Superplasticity**
- Communication: Interpretation of flow instability using dynamic material modeling. 1569-1572A
- Low-temperature superplastic behavior of a submicrometer-grained 5083 Al alloy fabricated by severe plastic deformation. 2859-2867A
- Enhancement of Strength and Superplasticity in a 6061 Al Alloy Processed by Equal-Channel-Angular-Pressing. 3155-3164A
- Superplasticity, Heating effects**
- The effect of rapid heat treatment on the high-temperature tensile behavior of superplastic Ti-6Al-4V. 83-92A
- Superplasticity, Impurity effects**
- The role of impurities during creep and superplasticity at very low stresses. 261-278A
- Superplasticity, Temperature effects**
- Deformation mechanisms during low- and high-temperature superplasticity in 5083 Al-Mg alloy. 1373-1384A
- Supersaturation**
- Communication: On the solute field and composition of  $\gamma$  plates in an Al-22 At. Pct Ag alloy. 1561-1565A
- Statistical Self-Similarity in Rhines' Concept of Unique Multiphase Diffusion Paths on the Ternary Gibbs' Isotherm. 3357-3365A
- Coprecipitation of  $\Omega$  and  $\sigma$  Phases in Al-Cu-Mg-Mn Alloys Containing Ag and Si. 3635-3648A
- Surface alloying**
- Toward prediction of microstructural evolution during laser surface alloying. 1189-1200A
- Control of surface carburization and improvement of dynamic fracture behavior in tungsten heavy alloys. 1213-1219A
- Surface chemistry**
- Recent metallic materials for biomedical applications. 477-486A
- Dry-process surface modification for titanium dental implants. 511-519A
- Surface defects**
- Infrared repair brazing of 403 stainless steel with a nickel-based braze alloy. 1765-1773A
- Surface energy**
- Energy of the Pb(111) | Al(111) interface. 1003-1007A
- A study of the Pb/Al (100) interfacial energy. 2569-2572A
- The Coarsening Kinetics of  $\gamma$  Particles in Nickel-Based Alloys. 3367-3373A
- Surface hardness**
- Near-nanostructured WC-18 pct co coatings with low amounts of non-WC carbide phase: Part II. Hardness and resistance to sliding and abrasive wear. 159-164A
- Control of surface carburization and improvement of dynamic fracture behavior in tungsten heavy alloys. 1213-1219A
- Phase formation and microstructure in sputter-deposited Ti-Mo-C and Ti-W-C thin films. 1579-1588A
- Surface pretreatments**
- Interface nanochemistry effects on stainless steel diffusion bonding. 437-442A
- Surface structure**
- Near-nanostructured WC-18 pct co coatings with low amounts of non-WC carbide phase: Part I. Synthesis and characterization. 145-157A
- Recent metallic materials for biomedical applications. 477-486A
- Sliding wear of austenitic and austenitic-ferritic stainless steels. 613-624A
- Toward prediction of microstructural evolution during laser surface alloying. 1189-1200A
- Surface engineering of Timet 550 with oxygen to form a rutile-based, wear-resistant coating. 1201-1211A
- Control of surface carburization and improvement of dynamic fracture behavior in tungsten heavy alloys. 1213-1219A
- Corrosion behavior of austenitic alloy 690 under anodic and cathodic potentials. 1437-1447A
- Interrupted bonding of medium-carbon steels. 1475-1485A
- Phase formation and microstructure in sputter-deposited Ti-Mo-C and Ti-W-C thin films. 1579-1588A
- Jan Van Der Merwe and the theory of epitaxy. 2473-2474A
- Misfit dislocations in epitaxy. 2475-2483A
- Reciprocal-space formulation and prediction of misfit accommodation in rigid and strained epitaxial systems. 2485-2494A
- Orientation domains and texture in hot-dipped galvanized coatings. 2695-2701A
- Surgical implants**
- Recent metallic materials for biomedical applications. 477-486A
- Aging behavior of the Ti-29Nb-13Ta-4.6Zr new beta alloy for medical implants. 487-493A
- Hydrogen embrittlement of nickel-titanium alloy in biological environment. 495-501A
- Improvement in mechanical properties of dental cast Ti-6Al-7Nb by thermochemical processing. 503-510A
- Surgical implants, Materials selection**
- Dry-process surface modification for titanium dental implants. 511-519A
- Effect of Fcc-Hcp Phase Transformation Produced by Isothermal Aging on the Corrosion Resistance of a Co-27Cr-5Mo-0.05C Alloy. 2229-2235A
- Synchrotrons**
- Time-resolved X-ray imaging of aluminum alloy solidification processes. 613-623B
- Tantalum, Ternary systems**
- Evaluation of the thermodynamic properties and phase equilibria of the Re-Ta-W system. 2781-2787A
- Tantalum base alloys, Mechanical properties**
- The Effect of Grain Boundaries on the Athermal Stress of Tantalum and Tantalum-Tungsten Alloys. 3457-3464A
- Tearing**
- Two-Phase Modeling Directed Toward Hot Tearing Formation in Aluminum Direct Chill Casting. 2081-2093A
- Temperature gradient**
- Cellular array morphology during directional solidification. 1229-1243A
- Tensile properties**
- Characterization of a friction-stir-welded aluminum alloy 6013. 489-498B
- Microstructural and mechanical properties investigation of electrodeposited and annealed LIGA nickel structures. 539-554A
- Toughness-strength relations in the overaged 7449 Al-based alloy. 1125-1136A
- Phenomenological observations on mechanical and corrosion properties of thixoformed 357 alloys: a comparison with permanent mold cast 357 alloys. 1399-1412A
- Microstructural evolution and mechanical properties of the AA8011 alloy during the accumulative roll-bonding process. 1521-1530A
- Communication: High-cycle fatigue of an investment cast, Be-Al metal matrix composite. 1862-1865A
- Effect of Fcc-Hcp Phase Transformation Produced by Isothermal Aging on the Corrosion Resistance of a Co-27Cr-5Mo-0.05C Alloy. 2229-2235A
- Room-temperature mechanical properties of cold-rolled thin foils of binary, stoichiometric Ni<sub>3</sub>Al. 2607-2613A
- Tensile, creep, and low-cycle fatigue behavior of a cast  $\gamma$ -TiAl-based alloy for gas turbine applications. 2869-2881A
- Effect of Overaging and Particle Size on Tensile Deformation and Fracture of Particle-Reinforced Aluminum Matrix Composites. 3861-3869A
- Tensile properties, Composition effects**
- The effect of mischmetal addition on the structure and mechanical properties of a cast Al-7Si-0.3Mg alloy containing excess iron (up to 0.6 pct). 391-400A

**Tensile properties, Heating effects**

Effect of alternative aging process on the fracture and interfacial properties of particulate  $Al_2O_3$ -reinforced Al (6061) metal matrix composite.

1699-1713A

**Tensile properties, Temperature effects**

Tensile and fatigue properties of 17-4 PH stainless steel at high temperatures.

1715-1724A

**Tensile strength**

Hydrogen embrittlement of nickel-titanium alloy in biological environment.

495-501A

Improvement in mechanical properties of dental cast Ti-6Al-7Nb by thermochemical processing.

503-510A

Creep and microstructure of magnesium-aluminum-calcium based alloys.

567-574A

Communication: Examination on the aging and tensile properties of Al-Zn-Mg/Al<sub>3</sub>Ni eutectic composite.

707-711A

Precipitation of austenite particles at grain boundaries during aging of Fe-Mn-Ni steel.

1057-1067A

Micromechanical modeling of unidirectional continuous sigma fiber-reinforced Ti-6Al-4V subjected to transverse tensile loading.

3045-3054A

Enhancement of Strength and Superplasticity in a 6061 Al Alloy Processed by Equal-Channel-Angular-Pressing.

3155-3164A

Improvement of Gigacycle Fatigue Properties by Modified Austempering in 1600 and 2000 MPA-Class Low-Alloy Steels.

3421-3431A

**Tensile strength, Alloying effects**

Carbide precipitation and high-temperature strength of hot-rolled high-strength, low-alloy steels containing Nb and Mo.

1689-1698A

**Tensile strength, Composition effects**

Strength of Al-Zn-Mg-Cu matrix composite reinforced with SiC particles.

455-465A

**Tensile stress**

The influence of the stress state on the plasticity of transformation induced plasticity-aided steel.

1659-1667A

Quantitative characterization of three-dimensional damage evolution in a wrought Al-alloy under tension and compression.

2599-2606A

Change of Critical Events of Cleavage Fracture with Variation of Microscopic Features of Low-Alloy Steels.

3393-3402A

Microscale Elastic Strain Evolution Following Damage in Ti-SiC Composites.

3839-3845A

**Tension tests**

Finite-element calculations of the lattice rotation field of a tensile-loaded nickel-based alloy multycrystal and comparison with topographical x-ray diffraction measurements.

2825-2833A

Micromechanical modeling of unidirectional continuous sigma fiber-reinforced Ti-6Al-4V subjected to transverse tensile loading.

3045-3054A

Use of Weibull Statistics to Quantify Property Variability in TiAl Alloys.

3127-3136A

Measuring the Fracture Toughness of Molybdenum-0.5 pct Titanium-0.1 pct Zirconium and Oxide Dispersion-Strengthened Molybdenum Alloys using Standard and Subsize Bend Specimens.

3685-3707A

**Ternary systems, Phases (state of matter)**

Communication: Prediction of the thermodynamic properties of solutes in the Bi-based ternary dilute solution.

502-506B

A 500°C isothermal section for the Al-Au-Cu system.

987-993A

Phase equilibria of the ternary Ni-Cr-Zr system and interfacial reactions in the Ni-Cr/Zr couples.

995-1002A

Communication: On the ternary phase in the zinc-rich corner of the Zn-Fe-Al system at temperatures below 450°C.

1559-1560A

Thermodynamic description of the Cu-Al-Sn system in the copper-rich corner.

1639-1648A

Thermal and electrical properties of Nb<sub>2</sub>AlC, (Ti,Nb)<sub>2</sub>AlC and Ti<sub>3</sub>AlC.

2775-2779A

Evaluation of the thermodynamic properties and phase equilibria of the Re-Ta-W system.

2781-2787A

On the Constitution of the System Al-Mn-Si.

3311-3319A

Statistical Self-Similarity in Rhines' Concept of Unique Multiphase Diffusion Paths on the Ternary Gibbs' Isotherm.

3357-3365A

Diffusion Studies in the  $\beta$  (B<sub>2</sub>),  $\beta'$  (Bcc), and  $\gamma$  (Fcc) Fe-Ni-Al Alloys at 1000°C.

3375-3392A

**Ternary systems, Physical properties**

Estimation Of Viscosity Of Ternary-Metallic Melts.

3201-3204A

**Testing equipment, Design**

A new unidirectional solidification method to study gray cast iron.

235-241B

**Texture**

Electron backscatter diffraction analysis of microstructural evolution in hot-deformed 6xxx series aluminum alloys.

693-713A

Intergranular stresses in ZIRCALOY-2.

749-755A

A study of twinning in zirconium using neutron diffraction and polycrystalline modeling.

757-763A

Transmission electron microscopy investigation of  $\langle c + a \rangle$  dislocations in Mg and  $\alpha$ -solid solution Mg-Li alloys.

851-858A

Determination of dislocation densities in Hcp metals from X-ray diffraction line-broadening analysis.

859-865A

Distribution of c- and a-dislocations in tubes of Zr alloys.

867-874A

Anisotropic threshold stress intensity factor,  $K_{IH}$ , and crack growth rate in delayed hydride cracking of Zr-2.5Nb pressure tubes.

919-925A

Deformation twinning in polycrystalline Zr: insights from electron backscattered diffraction characterization.

955-963A

Microstructure evolution in Zr under equal channel angular pressing.

973-980A

Electron-beam welding behavior in Mg-Al-based alloys.

1461-1473A

An Investigation of Microstructure and Grain-Boundary Evolution during ECA Pressing of Pure Aluminum.

2173-2184A

Orientation domains and texture in hot-dipped galvanized coatings.

2695-2701A

Changes in Order and Texture during Annealing of Heavily Cold-Rolled Ni<sub>3</sub>Al (B,Zr) Alloy

3605-3618A

Evolution of Microstructure and Texture during Casting of AISI 304 Stainless Steel Strip.

3747-3754A

**Texture, Processing effects**

Elevated-temperature deformation at forming rates of  $10^{-2}$  to  $10^2$  s<sup>-1</sup>.

345-362A

Equal-channel angular extrusion of beryllium.

965-972A

**Thermal conductivity**

Thermal and electrical properties of Nb<sub>2</sub>AlC, (Ti,Nb)<sub>2</sub>AlC and Ti<sub>3</sub>AlC.

2775-2779A

**Thermal cycling**

Two-way shape memory effect of TiNi alloys induced by hydro-generation.

17-23A

Kinetics of biaxial dome formation by transformation superplasticity of titanium alloys and composites.

1669-1680A

Infrared repair brazing of 403 stainless steel with a nickel-based braze alloy.

1765-1773A

Relationship between Austenite Dislocation Density Introduced during Thermal Cycling and  $M_s$  Temperature in an Fe-17 Wt Pct Mn Alloy.

1913-1917A

On Composite-Structure Weaknesses: Part I. Simulation, Properties, and Numerical Approach.

2205-2215A

**Thermal expansion**

Large Self-Thermal-Plastic Deformation in a NiTi Shape-Memory Alloy Fiber-Actuated Aluminum Metal-Matrix Composite.

3535-3540A

**Thermal fatigue**

Thermal and mechanical behavior of copper molds during thin-slab casting. II. Mold crack formation.

437-449B

**Thermal spraying**

Synthesis and nanoindentation study of high-velocity oxygen fuel thermal-sprayed nanocrystalline and near-nanocrystalline Ni coatings.

647-655A

**Thermal stresses**

Thermal and mechanical behavior of copper molds during thin-slab casting. II. Mold crack formation.

437-449B

Analysis of steady-state thermal creep of Zr-2.5Nb pressure tube material.

1103-1115A

The Effect of Grain Boundaries on the Athermal Stress of Tantalum and Tantalum-Tungsten Alloys.

3457-3464A

**Thermodynamics**

Thermodynamic behavior of nickel in CaO-SiO<sub>2</sub>-Fe<sub>2</sub>O<sub>3</sub> slag. Kinetics of formation and dissociation of Na<sub>2</sub>SiF<sub>6</sub>.

55-59B

Determination of Gibbs energies of formation of CaFe<sub>2</sub>O<sub>4</sub> and Ca<sub>2</sub>Fe<sub>2</sub>O<sub>5</sub> from solid-state emf measurements using CaF<sub>2</sub> as solid electrolyte.

129-136B

In-situ observation of the precipitation of manganese sulfide in low-carbon magnesium-killed steel.

385-392B

Communication: Prediction of the thermodynamic properties of solutes in the Bi-based ternary dilute solution.

427-436A

Thermodynamics of liquid Al-Na alloys determined by using CaF<sub>2</sub> solid electrolyte.

502-506B

Oxidation state and activities of chromium oxides in CaO-SiO<sub>2</sub>-Cr<sub>2</sub>O<sub>3</sub> slag system.

577-587B

Thermodynamic study of the reduction of titanium magnetite concentrate with solid carbon.

595-603B

Phase equilibria of the ternary Ni-Cr-Zr system and interfacial reactions in the Ni-Cr/Zr couples.

633-638B

Decomposition of ferrite in commercial superduplex stainless steel weld metals; microstructural transformations above 700°C.

995-1002A

Equilibrium solid solubility of silicon in silver.

1009-1018A

Communication: The Gibbs-Thomson effect in dilute binary systems.

1145-1150A

Relationship between Austenite Dislocation Density Introduced during Thermal Cycling and  $M_s$  Temperature in an Fe-17 Wt Pct Mn Alloy.

1283-1287A

Reactive Infiltration of 25 Vol Pct TiO<sub>2</sub>/Al Composites.

1913-1917A

Why do dislocations assemble into interfaces in epitaxy as well as in crystal plasticity? To minimize free energy.

2155-2162A

Thermodynamic Modeling of the Indium-Palladium System.

2519-2539A

**Thermography**

Communication: Infrared imaging during low-cycle fatigue of HR-120 alloy.

3597-3603A

**Thermogravimetric analysis**

Rate of Interfacial Reaction between Molten CaO-SiO<sub>2</sub>-Al<sub>2</sub>O<sub>3</sub>-Fe<sub>2</sub>O<sub>3</sub> and CO-CO<sub>2</sub>.

1287-1292A

Measurement and Computation of Drag Forces in Thermogravimetric Studies.

651-660B

The Oxidation Behavior of Unactivated and Mechanically Activated Sphalerite.

891-896B

**Thermomechanical treatment**

Deformation bands and the formation of grain boundaries in a superplastic aluminum alloy.

897-900B

Evolution of microstructure and properties in alpha-brass after iterative processing.

279-290A

High Temperature SANS Experiments on Nb(C,N) and MnS Precipitates in HSLA Steel.

1853-1857A

Inferring Dynamic Recrystallization in Ferrite using the Kinetics of Static Recrystallization.

1883-1891A

Effect of thermomechanical processing on the retained austenite content in a Si-Mn transformation-induced-plasticity steel.

1893-1900A

Enhancement of superelasticity in Cu-Al-Mn-Ni shape-memory alloys by texture control.

2811-2816A

**Thixoforming**

Phenomenological observations on mechanical and corrosion properties of thixoformed 357 alloys: a comparison with per-

2817-2824A



- manent mold cast 357 alloys. 1399-1412A
- Tin, Mechanical properties**  
Unexpected transient creep behavior of tin alloys strengthened by high volume fractions of SbSn. 575-580A
- Tin, Ternary systems**  
Communication: Prediction of the thermodynamic properties of solutes in the Bi-based ternary dilute solution. 502-506B  
Thermodynamic description of the Cu-Al-Sn system in the copper-rich corner. 1639-1648A  
Estimation Of Viscosity Of Ternary-Metallic Melts. 3201-3204A
- Tin base alloys, Directional solidification**  
Solidification Behavior of Sn-15 Wt Pct Pb Alloy under a High Shear Rate and High Intensity of Turbulence during Semi-solid Processing. 3511-3520A
- Tin base alloys, Mechanical properties**  
Unexpected transient creep behavior of tin alloys strengthened by high volume fractions of SbSn. 575-580A  
Creep of Tin, Sb-solution-strengthened Tin, and SbSn-precipitate-strengthened tin. 1531-1539A
- Tin base alloys, Phase transformations**  
Solidification Thermal Parameters Affecting the Columnar-to-Equiaxed Transition. 2107-2118A
- Titanium, Alloying elements**  
Atomistic modeling of quaternary alloys: Ti and Cu in NiAl. 265-284B
- Titanium, Binary systems**  
Metastable phases in the Ti-V system. I. Neutron diffraction study and assessment of structural properties. 1307-1317A
- Titanium, Coating**  
TiB Whisker Coating on Titanium Surfaces by Solid-State Diffusion: Synthesis, Microstructure, and Mechanical Properties. 3489-3498A
- Titanium, Composite materials**  
Fabrication and characterization of Ti-TiB<sub>2</sub> functionally graded material system. 681-685A
- Titanium, Extraction**  
Communication: Conversion of VOCl<sub>3</sub> to VOCl<sub>2</sub> in liquid TiCl<sub>4</sub>. Thermodynamic study of the reduction of titanium magnetite concentrate with solid carbon. 142-146B  
633-638B
- Titanium, Mechanical properties**  
Effects of high rates of loading on the deformation behavior and failure mechanisms of hexagonal close-packed metals and alloys. 927-935A
- Titanium, Metal working**  
Kinetics of biaxial dome formation by transformation superplasticity of titanium alloys and composites. 1669-1680A
- Titanium, Microstructure**  
Effect of pressure on zone-center phonons in hexagonal-close-packed metals. 743-747A  
Bulk and interface boundary diffusion in group IV hexagonal close-packed metals and alloys. 765-775A  
Grain-boundary diffusion by vacancy mechanism in  $\alpha$ -Ti and  $\alpha$ -Zr. 791-796A  
Nonbasal deformation modes of Hcp metals and alloys: role of dislocation source and mobility. 813-822A
- Titanium, Phase transformations**  
In-situ measurement of continuous cooling  $\beta \rightarrow \alpha$  transformation behavior of CP-Ti. 1051-1056A
- Titanium, Surface properties**  
Dry-process surface modification for titanium dental implants. 511-519A
- Titanium, Ternary systems**  
Thermal and electrical properties of Nb<sub>2</sub>AlC, (Ti,Nb)<sub>2</sub>AlC and Ti<sub>2</sub>AlC. 2775-2779A
- Titanium base alloys, Composite materials**  
Micromechanical modeling of unidirectional continuous sigma fiber-reinforced Ti-6Al-4V subjected to transverse tensile loading. 3045-3054A  
Solidification paths and reinforcement morphologies in melt-processed (TiB + TiC)/Ti in situ composites. 3055-3063A  
Microscale Elastic Strain Evolution Following Damage in Ti-SiC Composites. 3839-3845A
- Titanium base alloys, End uses**  
The effect of constraint-induced normal stress on the failure of notched TiAl components. 417-426A
- Titanium base alloys, Heat treatment**  
The effect of rapid heat treatment on the high-temperature tensile behavior of superplastic Ti-6Al-4V. 83-92A  
Aging behavior of the Ti-29Nb-13Ta-4.6Zr new beta alloy for medical implants. 487-493A  
Surface engineering of Timet 550 with oxygen to form a rutile-based, wear-resistant coating. 1201-1211A
- Titanium base alloys, Machining**  
On thermoplastic shear instability in the machining of a titanium alloy (Ti-6Al-4V). 2995-3010A
- Titanium base alloys, Mechanical properties**  
Understanding creep - a review. 291-303A  
Application of a modified jogged-screw model for creep of TiAl and  $\alpha$ -Ti alloys. 329-336A  
Improvement in mechanical properties of dental cast Ti-6Al-7Nb by thermochemical processing. 503-510A  
Cracking in  $\gamma$ -TiAl due to high speed particle impact. 581-589A  
Deformation behavior of Hcp Ti-Al alloy single crystals. 837-850A  
Observations of room-temperature creep recovery in titanium alloys. 891-898A  
Influence of microstructure on high-cycle fatigue of Ti-6Al-4V: bimodal vs. lamellar structures. 899-918A  
Effects of high rates of loading on the deformation behavior and failure mechanisms of hexagonal close-packed metals and alloys. 927-935A
- Titanium base alloys, Melting**  
The Critical Pressure and Impeding Pressure of Al Evaporation during Induction Skull Melting Processing of TiAl. 3249-3253A
- Titanium base alloys, Metal working**  
Microstructural gradients in the superplastic forming of Ti-6Al-4V. 93-100A  
Kinetics of biaxial dome formation by transformation superplasticity of titanium alloys and composites. 1669-1680A  
Self-consistent modeling of the flow behavior of wrought alpha/beta titanium alloys under isothermal and nonisothermal hot-working conditions. 2719-2727A
- Titanium base alloys, Microstructure**  
First-principles investigation of perfect and diffuse antiphase boundaries in hcp-based Ti-Al alloys. 735-741A  
Nonbasal deformation modes of Hcp metals and alloys: role of dislocation source and mobility. 813-822A  
Metastable phases in the Ti-V system. I. Neutron diffraction study and assessment of structural properties. 1307-1317A  
The Kinetics of Static Globularization of Ti-6Al-4V. 3527-3534A  
Microstructural Analysis of Multilayered Titanium Aluminide Sheets Fabricated by Hot Rolling and Heat Treatment. 3649-3659A
- Titanium base alloys, Phase transformations**  
Finite element modeling of the morphology of  $\beta$  to  $\alpha$  phase transformation in Ti-6Al-4V alloy. 1027-1040A  
Mechanisms of the massive transformation. 2285-2297A  
Origins of internal structure in massive transformation products. 2347-2351A  
Massive-parent interphase boundaries and their implications on the mechanisms of the  $\alpha \rightarrow \gamma_M$  massive transformation in Ti-Al alloys. 2353-2371A  
The massive transformation in titanium aluminides: initial stages of nucleation and growth. 2373-2379A  
Orientation and structure of planar facets on the  $\gamma_M$  massive phase in a near-TiAl alloy. 2381-2389A  
Static and in-situ high-resolution transmission electron microscopy investigations of the atomic structure and dynamics of massive transformation interfaces in a Ti-Al alloy. 2391-2411A  
Communication: Microstructure and yield behavior of a high aluminum containing Ti-Al-Nb alloy. 2763-2766A
- Titanium base alloys, Powder technology**  
Phase Evolution in Laser-Deposited Titanium-Chromium Alloys. 2129-2138A
- Titanium base alloys, Surface properties**  
Recent metallic materials for biomedical applications. 477-486A  
Dry-process surface modification for titanium dental implants. 511-519A
- Titanium carbide, Composite materials**  
Communication: Comparative Welding Study of Metal Matrix Composites with the MIG Welding Process, using Direct and Indirect Electric Arc. 932-937B  
Kinetics of biaxial dome formation by transformation superplasticity of titanium alloys and composites. 1669-1680A  
Solidification paths and reinforcement morphologies in melt-processed (TiB + TiC)/Ti in situ composites. 3055-3063A  
Strength and Plastic Flow in "In Situ" TiC Reinforced Aluminum Composites. 3831-3838A
- Titanium compounds, Bonding**  
Microstructure and Mechanical Properties of Titanium Aluminide Wide-Gap, Transient Liquid-Phase Bonds Prepared using a Slurry-Deposited Composite Interlayer. 3205-3214A
- Titanium compounds, Coatings**  
Powder Eutectic Coating With Al<sub>3</sub>Ti For Steels. 3235-3240A  
TiB Whisker Coating on Titanium Surfaces by Solid-State Diffusion: Synthesis, Microstructure, and Mechanical Properties. 3489-3498A
- Titanium compounds, Composite materials**  
Effect of heat treatments on in-situ Al<sub>2</sub>O<sub>3</sub>/TiAl<sub>3</sub> composites produced from squeeze casting of TiO<sub>2</sub>/A356 composites. 31-40B  
Intermetallic-reinforced light-metal matrix in-situ composites. 193-201A  
Reactive Infiltration of 25 Vol Pct TiO<sub>2</sub>/Al Composites. 2155-2162A  
Microstructure/processing relationships in reaction-synthesized titanium aluminide intermetallic matrix composites. 2747-2753A  
Large Self-Thermal-Plastic Deformation in a NiTi Shape-Memory Alloy Fiber-Actuated Aluminum Metal-Matrix Composite. 3535-3540A
- Titanium compounds, Mechanical properties**  
Two-way shape memory effect of TiNi alloys induced by hydrogenation. 17-23A  
Application of a modified jogged-screw model for creep of TiAl

- and  $\alpha$ -Ti alloys. 329-336A
- Hydrogen embrittlement of nickel-titanium alloy in biological environment. 495-501A
- Crack growth in a nearly fully-lamellar gamma TiAl alloy at 650°C and 800°C under constant load conditions. 2847-2857A
- Tensile, creep, and low-cycle fatigue behavior of a cast  $\gamma$ -TiAl-based alloy for gas turbine applications. 2869-2881A
- Use of Weibull Statistics to Quantify Property Variability in TiAl Alloys. 3127-3136A
- Communication: Conducting High-Cycle Fatigue Strength Step Tests on Gamma TiAl. 3871-3874A
- Titanium compounds, Melting**
- The Critical Pressure and Impeding Pressure of Al Evaporation during Induction Skull Melting Processing of TiAl. 3249-3253A
- Titanium compounds, Microstructure**
- Microstructural Analysis of Multilayered Titanium Aluminide Sheets Fabricated by Hot Rolling and Heat Treatment. 3649-3659A
- Titanium compounds, Phase transformations**
- General discussion session of the symposium on "The mechanisms of the massive transformation" 2445-2470A
- Titanium compounds, Powder technology**
- Grain-size control in Ti-48Al-2Cr-2Nb with yttrium additions. 2729-2736A
- Titanium compounds, Reactions (chemical)**
- Solubility of Some Transition Metal Oxides in Cryolite-Alumina Melts: Part II. Solubility of TiO<sub>2</sub>. 909-913B
- Titanium diboride, Composite materials**
- Fabrication and characterization of Ti-TiB<sub>2</sub> functionally graded material system. 681-685A
- Formation of a TiB<sub>2</sub>-reinforced copper-based composite by mechanical alloying and hot pressing. 1275-1280A
- Kinetics of biaxial dome formation by transformation superplasticity of titanium alloys and composites. 1669-1680A
- Microstructure/processing relationships in reaction-synthesized titanium aluminide intermetallic matrix composites. 2747-2753A
- The incorporation of self-propagating, high-temperature synthesis-formed Fe-TiB<sub>2</sub> into ferrous melts. 2973-2983A
- Titanium nitride, Crystal growth**
- Titanium Nitride Precipitation Behavior in Thin-Slab Cast High-Strength Low-Alloy Steels. 3099-3110A
- Titanium ores, Extraction**
- Communication: Conversion of VOCl<sub>3</sub> to VOCl<sub>2</sub> in liquid TiCl<sub>4</sub>. 142-146B
- Tomography**
- Density gradients formed during compaction of bronze powders: the origins of part-to-part variation. 165-170A
- Tool steels, Machining**
- Formation of white layers in steels by machining and their characteristics. 1245-1254A
- Topography**
- Dry-process surface modification for titanium dental implants. 511-519A
- Topology**
- Normalized Diagrams for Micromechanical Estimates of the Elastic Response of Composite Materials. 3187-3199A
- Torsion**
- Flow Stress and Ductility of Duplex Stainless Steel during High-Temperature Torsion Deformation. 1931-1938A
- Torsion tests**
- The production of ultrafine ferrite during hot torsion testing of a 0.11 Wt pct C steel. 2985-2993A
- Toughness**
- Elevated temperature strength and room-temperature toughness of directionally solidified Ni-33Al-33Cr-1Mo. 1385-1397A
- Effect of pearlite on the vibration-fracture behavior of spherical graphite cast irons under resonant conditions. 2623-2634A
- Transformation temperature**
- Communication: Microstructure and yield behavior of a high aluminum containing Ti-Al-Nb alloy. 2763-2766A
- Transformation temperature, Composition effects**
- Influence of Al and Ni concentration on the martensitic transformation in Cu-Al-Ni shape-memory alloys. 2581-2591A
- Transmission electron microscopy**
- On the Nature of the Electrochemically Synthesized Hard Fe-0.96 Mass Pct C Alloy Film. 921-927B
- Static and in-situ high-resolution transmission electron microscopy investigations of the atomic structure and dynamics of massive transformation interfaces in a Ti-Al alloy. 2391-2411A
- Tribology**
- Communication: Effect of carbon addition on tribological properties of Fe-Al alloys. 1292-1295A
- Effect of Martensite Content on Friction and Oxidative Wear Behavior of 0.42 Pct Carbon Dual-Phase Steel. 3479-3488A
- TRIP steels, Heat treatment**
- Phase transformation and mechanical properties of Si-free CMnAl transformation-induced plasticity-aided steel. 2573-2580A
- TRIP steels, Mechanical properties**
- The influence of the stress state on the plasticity of transformation induced plasticity-aided steel. 1659-1667A
- TRIP steels, Phase transformations**
- Dislocation-disclination model of heterogeneous martensite nucleation in transformation-induced-plasticity steels. 1351-1362A
- Effect of thermomechanical processing on the retained austenite content in a Si-Mn transformation-induced-plasticity steel. 2811-2816A
- Method for Measuring Transformation Energy and Quantitative Characterization of Transformation-Induced Plasticity. 3117-3120A
- TTT curves**
- In-situ measurement of continuous cooling  $\beta \rightarrow \alpha$  transformation behavior of CP-Ti. 1051-1056A
- Effect of composition and austenite deformation on the transformation characteristics of low-carbon and ultralow-carbon microalloyed steels. 1331-1349A
- Tube joints, Microstructure**
- Inertia Welding Nickel-Based Superalloy: Part I. Metallurgical Characterization. 3215-3225A
- Inertia Welding Nickel-Based Superalloy: Part II. Residual Stress Characterization. 3227-3234A
- Tubes, X ray analysis**
- Distribution of c- and a-dislocations in tubes of Zr alloys. 867-874A
- Tungsten, Ternary systems**
- Evaluation of the thermodynamic properties and phase equilibria of the Re-Ta-W system. 2781-2787A
- Tungsten base alloys, Heat treatment**
- Control of surface carburization and improvement of dynamic fracture behavior in tungsten heavy alloys. 1213-1219A
- Tungsten carbide, Coatings**
- Toward prediction of microstructural evolution during laser surface alloying. 1189-1200A
- Turbine blades**
- Cracking in  $\gamma$ -TiAl due to high speed particle impact. 581-589A
- Turbine blades, Materials selection**
- Infrared repair brazing of 403 stainless steel with a nickel-based braze alloy. 1765-1773A
- Turbine blades, Mechanical properties**
- Communication: Conducting High-Cycle Fatigue Strength Step Tests on Gamma TiAl. 3871-3874A
- Turbine disks, Fabrication**
- Tree-ring formation during vacuum arc remelting of INCONEL 718. I. Experimental investigation. 1795-1804A
- Turbines, Mechanical properties**
- Effect of Prolonged Isothermal Exposure on Elevated-Temperature, Time-Dependent Fatigue-Crack Propagation in INCONEL Alloy 783. 3465-3478A
- Turbines, Service life**
- Creep at very low rates. 213-218A
- Turbulent flow**
- Simulation of the submerged energy nozzle-mold water model system using laser-optical and computational fluid dynamics methods. 163-172B
- Correction to "Simulation of the submerged energy nozzle-mold water model systems using laser optical and computational fluid dynamics methods" 639B
- Turning (machining)**
- Formation of white layers in steels by machining and their characteristics. 1245-1254A
- Twinning**
- A study of twinning in zirconium using neutron diffraction and polycrystalline modeling. 757-763A
- Grain-boundary diffusion by vacancy mechanism in  $\alpha$ -Ti and  $\alpha$ -Zr. 791-796A
- Interfacial deformation mechanisms in hexagonal-close-packed metals. 801-807A
- Twins as barriers to basal slip in hexagonal-close-packed metals. 809-812A
- Nonbasal deformation modes of Hcp metals and alloys: role of dislocation source and mobility. 813-822A
- Molecular dynamics simulation of  $\langle c + a \rangle$  dislocation core structure in hexagonal-close-packed metals. 823-829A
- Deformation behavior of Hcp Ti-Al alloy single crystals. 837-850A
- Transmission electron microscopy investigation of  $\langle c + a \rangle$  dislocations in Mg and  $\alpha$ -solid solution Mg-Li alloys. 851-858A
- Advances in deformation twin characterization using electron backscattered diffraction data. 949-954A
- Microstructure evolution in Zr under equal channel angular pressing. 973-980A
- Twinning, Deformation effects**
- Atomic-scale modeling of dislocations and related properties in the hexagonal-close-packed metals. 721-733A
- Deformation twinning in polycrystalline Zr: insights from electron backscattered diffraction characterization. 955-963A
- Ultrasonic testing**
- Direct measurements of grain size in low-carbon steels using the laser ultrasonic technique. 687-691A
- Comprehensive microstructural characterization in modified 9Cr-1Mo ferritic steel by ultrasonic measurements. 1617-1626A
- Underground corrosion**
- Environmental aspects of near-neutral pH stress corrosion cracking of pipeline steel. 1429-1436A
- Uniform attack (corrosion)**
- Communication: Effect of Zr Addition on Corrosion Behavior of Cu-6Ni-2Mn-2Sn-2Al Alloy. 2237-2240A
- Vacuum arc melting**
- Numerical simulation of dendrite white spot formation during vacuum arc remelting of INCONEL718. 443-454A
- Tree-ring formation during vacuum arc remelting of INCONEL 718. I. Experimental investigation. 1795-1804A
- Tree-ring formation during vacuum arc remelting of INCONEL 718. II. Mathematical modeling. 1805-1815A
- Vacuum melting**
- Intermetallic-reinforced light-metal matrix in-situ composites. 193-201A
- Vacuum sintering**
- Deoxidation of molybdenum during vacuum sintering. 657-664A
- Valence**

- The equilibrium partitioning of titanium between  $Ti^{3+}$  and  $Ti^{4+}$  valency states in  $CaO-SiO_2-TiO_x$  slags. 61-67B
- Vanadium, Binary systems**  
Metastable phases in the Ti-V system. I. Neutron diffraction study and assessment of structural properties. 1307-1317A
- Vanadium, Extraction**  
Thermodynamic study of the reduction of titanium magnetite concentrate with solid carbon. 633-638B
- Vanadium carbide, Coatings**  
Correlation of Microstructure with Wear and Fracture Properties of Two-Layered VC/Ti-6Al-4V Surface Composites Fabricated by High-Energy Electron-Beam Irradiation. 3173-3185A
- Vanadium compounds, Impurities**  
Communication: Conversion of  $VOCl_3$  to  $VOCl_2$  in liquid  $TiCl_4$ . 142-146B
- Vaporizing**  
Kinetics of formation and dissociation of  $Na_2SiF_6$ . 129-136B
- Variability**  
Density gradients formed during compaction of bronze powders: the origins of part-to-part variation.  
Effect of cyclic pressure consolidation on the uniformity of metal matrix composites. 165-170A  
A study on inhomogeneous distribution of temper graphite particles in strip-cast Fe-C-Si alloys. 183-191A  
Communication: Minimizing Segregation during the Controlled Directional Solidification of Dendritic Alloys. 1263-1273A  
3876-3881A
- Vertical shaft furnaces**  
Measurement and Computation of Drag Forces in Thermo-gravimetric Studies. 891-896B
- Vibration**  
Effect of pearlite on the vibration-fracture behavior of spheroidal graphite cast irons under resonant conditions. 2623-2634A
- Viscosity**  
The Effect of  $CaF_2$  on the Viscosities and Structures of  $CaO-SiO_2-(MgO)-CaF_2$  Slags. 723-729B  
Estimation Of Viscosity Of Ternary-Metallic Melts. 3201-3204A
- Viscosity, Deformation effects**  
Rheology and microstructure of semi-solid aluminum alloys compressed in the drop-forge viscometer. 2737-2746A
- Viscous flow**  
The Effect of  $CaF_2$  on the Viscosities and Structures of  $CaO-SiO_2-(MgO)-CaF_2$  Slags. 723-729B
- Voils**  
Communication: Specimen Size Effects and Ductile Fracture of HY 100 Steel. 3293-3295A
- Volume**  
On the Partial Atomic Volume of Aluminum in Solid Solutions Based on the 3d Transition Metals and Copper. 3591-3595A
- Volume fraction**  
Communication: Examination on the aging and tensile properties of Al-Zn-Mg/Al<sub>3</sub>Ni eutectic composite. 707-711A  
Modeling The Austenite-Ferrite Isothermal Transformation in an Fe-C Binary System and Experimental Verification. 3111-3115A  
Normalized Diagrams for Micromechanical Estimates of the Elastic Response of Composite Materials. 3187-3199A  
Evolution of Submicrocrystalline Iron Containing Dispersed Oxides under Mechanical Milling Followed by Consolidation. 3241-3248A
- Water, Environment**  
Fracture toughness of alloy 690 and EN52 welds in air and water. 1725-1735A
- Water quenching**  
The effect of rapid heat treatment on the high-temperature tensile behavior of superplastic Ti-6Al-4V. 83-92A  
Age-hardening characteristics of aluminum alloy-hollow fly ash composites. 1541-1547A
- Wavelengths**  
Normal spectral emissivities of liquid Ag-Cu alloys in the visible and infrared regions. 47-54B
- Wear**  
Mechanical, Intergranular Corrosion, and Wear Behavior of Aluminum-Matrix Composite Materials Reinforced with Nickel Aluminides. 3541-3553A
- Wear mechanisms**  
High stress abrasive wear mechanism of LM13-SiC composite under varying experimental conditions. 3031-3044A
- Wear rate**  
Correlation of microstructure and wear resistance of ferrous coatings fabricated by atmospheric plasma spraying. 2933-2945A
- Wear resistance**  
Surface engineering of Timet 550 with oxygen to form a rutile-based, wear-resistant coating. 1201-1211A  
Infrared repair brazing of 403 stainless steel with a nickel-based braze alloy. 1765-1773A  
Correlation of microstructure and wear resistance of ferrous coatings fabricated by atmospheric plasma spraying. 2933-2945A  
Correlation of Microstructure with Wear and Fracture Properties of Two-Layered VC/Ti-6Al-4V Surface Composites Fabricated by High-Energy Electron-Beam Irradiation. 3173-3185A  
Some Observations of the Influence of  $\delta$ -Ferrite Content on the Hardness, Galling Resistance, and Fracture Toughness of Selected Commercially Available Iron-Based Hardfacing Alloys. 3403-3419A  
Effect of Martensite Content on Friction and Oxidative Wear Behavior of 0.42 Pct Carbon Dual-Phase Steel. 3479-3488A  
TiB Whisker Coating on Titanium Surfaces by Solid-State Diffusion: Synthesis, Microstructure, and Mechanical Properties. 3489-3498A
- Wear resistance, Alloying effects**  
Modification of 27Cr Cast Iron with Alloying Yttrium for Enhanced Resistance to Sliding Wear in Corrosive Media. 1981-1989A
- Wear resistance, Coating effects**  
Near-nanostructured WC-18 pct co coatings with low amounts of non-WC carbide phase: Part II. Hardness and resistance to sliding and abrasive wear. 159-164A
- Wear resistance, Composition effects**  
Communication: Effect of carbon addition on tribological properties of Fe-Al alloys. 1292-1295A
- Wear resistance, Processing effects**  
Communication: A New Hybrid Process for Surface Modification by Combining Brush Plating with Nitrocarburizing. 2240-2244A
- Weibull modulus**  
Use of Weibull Statistics to Quantify Property Variability in TiAl Alloys. 3127-3136A
- Weld cladding**  
Sensitization behavior of type 308 stainless steel weld metals after postweld heat treatment and low-temperature aging and its relation to microstructure. 1743-1754A
- Weld defects**  
Missed Joint Induced by Thermoelectric Magnetic Field in Electron-Beam Welding Dissimilar Metals-Experiment and Scale Analysis. 765-773B
- Weld deposited coatings, Mechanical properties**  
Some Observations of the Influence of  $\delta$ -Ferrite Content on the Hardness, Galling Resistance, and Fracture Toughness of Selected Commercially Available Iron-Based Hardfacing Alloys. 3403-3419A
- Weld metal, Corrosion**  
Intergranular stress corrosion cracking behavior of types 308 and 316 stainless steel weld metals in a simulated boiling water reactor environment. 2907-2919A
- Weld metal pool**  
Digital simulations of a stationary and a linear weld. 101-110B  
Investigation on the effect of laser pulse shape during Nd:YAG laser microwelding of thin Al sheet by numerical simulation. 1449-1459A
- Weldability**  
Communication: Comparative Welding Study of Metal Matrix Composites with the MIG Welding Process, using Direct and Indirect Electric Arc. 932-937B  
Inertia Welding Nickel-Based Superalloy: Part I. Metallurgical Characterization. 3215-3225A
- Weldability, Composition effects**  
The Influence of Minor Elements on the Weldability of an INCONEL 718-Type Superalloy. 2005-2017A
- Welded joints, Corrosion**  
Communication: Thermal Scaling Behavior of Weldments of 9Cr-1Mo Steel and Its Relevance to the Life Assessment of Fossil Fuel Power Plant Components. 3296-3297A
- Welded joints, Mechanical properties**  
Fracture toughness of alloy 690 and EN52 welds in air and water. 1725-1735A  
Crack-initiation toughness and crack-arrest toughness in advanced 9 pct Ni steel welds containing local brittle zones. 2615-2622A  
Residual stresses in a welded superalloy disc: characterization using synchrotron diffraction and numerical process modeling. 2921-2931A
- Welded joints, Microstructure**  
A new bcc-fcc orientation relationship observed between ferrite and austenite in solidification structures of steels. 5-15A  
Decomposition of ferrite in commercial superduplex stainless steel weld metals; microstructural transformations above 700°C. 1009-1018A  
Electron-beam welding behavior in Mg-Al-based alloys. 1461-1473A  
Inertia Welding Nickel-Based Superalloy: Part I. Metallurgical Characterization. 3215-3225A  
Inertia Welding Nickel-Based Superalloy: Part II. Residual Stress Characterization. 3227-3234A
- Welding parameters**  
Parameters controlling microstructure and hardness during friction-stir welding of precipitation-hardenable aluminum alloy 6063. 625-635A  
Communication: Comparative Welding Study of Metal Matrix Composites with the MIG Welding Process, using Direct and Indirect Electric Arc. 932-937B  
Investigation on the effect of laser pulse shape during Nd:YAG laser microwelding of thin Al sheet by numerical simulation. 1449-1459A
- Weldments, Corrosion**  
Communication: Thermal Scaling Behavior of Weldments of 9Cr-1Mo Steel and Its Relevance to the Life Assessment of Fossil Fuel Power Plant Components. 3296-3297A
- Wettability**  
Bubble formation and detachment on nonwetted surfaces. 155-162B  
Communication: Wettability of  $Al_2O_3-MgO$  substrates by molten aluminum. 506-509B
- Wetting**  
Die soldering: mechanism of the interface reaction between molten aluminum alloy and tool steel. 465-476B  
The Optimum Wetting Angle for the Stabilization of Liquid-Metal Foams by Ceramic Particles: Experimental Simulations. 3285-3292A
- Whiskers (nonmetals), Coatings**  
TiB Whisker Coating on Titanium Surfaces by Solid-State Diffusion: Synthesis, Microstructure, and Mechanical Properties. 3489-3498A
- White iron, Casting**



- A study on inhomogeneous distribution of temper graphite particles in strip-cast Fe-C-Si alloys. 1263-1273A
- Wire, Surface properties**  
Dopant Particle Characterization and Bubble Evolution in Aluminum-Potassium-Silicon-Doped Molybdenum Wire. 3349-3356A
- Workability**  
Communication: Effect of Zr Addition on Corrosion Behavior of Cu-6Ni-2Mn-2Sn-2Al Alloy. 2237-2240A
- X ray analysis**  
Density gradients formed during compaction of bronze powders: the origins of part-to-part variation. 165-170A  
Development of New Feeding-Distance Rules Using Casting Simulation: Part I. Methodology. 731-740B
- X ray diffraction**  
Study of the kinetics of the recrystallization of cold-rolled low-carbon steel. 25-31A  
Dislocation microstructure and internal-stress measurements by convergent-beam electron diffraction on creep-deformed Cu and Al. 311-317A  
Determination of dislocation densities in Hcp metals from X-ray diffraction line-broadening analysis. 859-865A  
Distribution of c- and a-dislocations in tubes of Zr alloys. 867-874A  
On the Nature of the Electrochemically Synthesized Hard Fe-0.96 Mass Pct C Alloy Film. 921-927B  
Finite-element calculations of the lattice rotation field of a tensile-loaded nickel-based alloy multycrystal and comparison with topographical x-ray diffraction measurements. 2825-2833A  
Residual stresses in a welded superalloy disc: characterization using synchrotron diffraction and numerical process modeling. 2921-2931A  
On the Constitution of the System Al-Mn-Si. 3311-3319A
- X ray scattering**  
Time-resolved X-ray imaging of aluminum alloy solidification processes. 613-623B
- Yield strength**  
Influence of elastic and plastic anisotropy on the flow behavior in a duplex stainless steel. 57-71A  
Microstructural gradients in the superplastic forming of Ti-6Al-4V. 93-100A  
Communication: Examination on the aging and tensile properties of Al-Zn-Mg/Al<sub>3</sub>Ni eutectic composite. 707-711A  
The effect of grain size on the ambient temperature creep deformation behavior of a beta Ti-14.8V alloy. 1137-1144A  
A critical-strain criterion for hydrogen embrittlement of cold-drawn, ultrafine pearlitic steel. 1151-1166A  
Communication: Microstructures and mechanical properties of (Ir,Rh)<sub>75</sub>Nb<sub>15</sub>Ni<sub>10</sub> alloys. 1281-1283A  
Carbide precipitation and high-temperature strength of hot-rolled high-strength, low-alloy steels containing Nb and Mo. 1689-1698A  
Flow Stress and Ductility of Duplex Stainless Steel during High-Temperature Torsion Deformation. 1931-1938A  
Large-Strain Softening of Aluminum in Shear at Elevated Temperature. 3145-3153A  
Enhancement of Strength and Superplasticity in a 6061 Al Alloy Processed by Equal-Channel-Angular-Pressing. 3155-3164A  
The Effect of Grain Boundaries on the Athermal Stress of Tantalum and Tantalum-Tungsten Alloys. 3457-3464A  
Strength and Plastic Flow in "In Situ" TiC Reinforced Aluminum Composites. 3831-3838A
- Yield strength, Microstructural effects**  
Localized deformation and hardening in irradiated metals: three-dimensional discrete dislocation dynamics simulations. 285-296B  
Molecular dynamics simulation of <c + a> dislocation core structure in hexagonal-close-packed metals. 823-829A  
Effect of temperature and shear direction on yield stress by {1122}<1123> slip in hcp metals. 831-836A
- Yield strength, Temperature effects**  
Effects of high rates of loading on the deformation behavior and failure mechanisms of hexagonal close-packed metals and alloys. 927-935A  
Self-consistent modeling of the flow behavior of wrought alpha/beta titanium alloys under isothermal and nonisothermal hot-working conditions. 2719-2727A
- Yttrium, Additives**  
Grain-size control in Ti-48Al-2Cr-2Nb with yttrium additions. 2729-2736A
- Yttrium, Alloying elements**  
Modification of 27Cr Cast Iron with Alloying Yttrium for Enhanced Resistance to Sliding Wear in Corrosive Media. 1981-1989A
- Zinc, Alloying elements**  
Creep strength of magnesium-based alloys. 875-882A
- Zinc, Coatings**  
Numerical simulation of Zn coating solidification. 2685-2694A
- Zinc, Extraction**  
Experimental Liquidus in the PbO-ZnO-Fe<sub>2</sub>O<sub>3</sub>-(CaO + SiO<sub>2</sub>) System in Air, with CaO/SiO<sub>2</sub> = 0.35 and PbO/(CaO + SiO<sub>2</sub>) = 3.2. 851-863B
- Zinc, Microstructure**  
Effect of temperature and shear direction on yield stress by {1122}<1123> slip in hcp metals. 831-836A
- Zinc, Ternary systems**  
Communication: Prediction of the thermodynamic properties of solutes in the Bi-based ternary dilute solution. 502-506B  
Communication: On the ternary phase in the zinc-rich corner of the Zn-Fe-Al system at temperatures below 450°C. 1559-1560A  
Statistical Self-Similarity in Rhines' Concept of Unique Multiphase Diffusion Paths on the Ternary Gibbs' Isotherm. 3357-3365A
- Zinc base alloys, Coatings**  
Orientation domains and texture in hot-dipped galvanized coatings. 2695-2701A
- Zinc base alloys, Composite materials**  
A novel technique for manufacturing metal-bonded Nd-Fe-B magnets by squeeze casting. 637-646A
- Zinc base alloys, Mechanical properties**  
The role of impurities during creep and superplasticity at very low stresses. 261-278A
- Zirconium, Additives**  
Communication: Effect of Zr Addition on Corrosion Behavior of Cu-6Ni-2Mn-2Sn-2Al Alloy. 2237-2240A
- Zirconium, Alloying additive**  
Communication: Effect of Zr Addition on Hot Workability of Cu-6Ni-2Mn-2Sn-2Al Alloy. 3298-3300A
- Zirconium, Metal working**  
Microstructure evolution in Zr under equal channel angular pressing. 973-980A
- Zirconium, Metallography**  
Advances in deformation twin characterization using electron backscattered diffraction data. 949-954A  
Deformation twinning in polycrystalline Zr: insights from electron backscattered diffraction characterization. 955-963A
- Zirconium, Microstructure**  
A study of twinning in zirconium using neutron diffraction and polycrystalline modeling. 757-763A  
Bulk and interface boundary diffusion in group IV hexagonal close-packed metals and alloys. 765-775A  
Anisotropy of point defect diffusion in alpha-zirconium. 777-782A  
Mobility of interstitial clusters in alpha-zirconium. 783-789A  
Grain-boundary diffusion by vacancy mechanism in  $\alpha$ -Ti and  $\alpha$ -Zr. 791-796A
- Zirconium, Ternary systems**  
Phase equilibria of the ternary Ni-Cr-Zr system and interfacial reactions in the Ni-Cr/Zr couples. 995-1002A
- Zirconium base alloys, Diffusion**  
Diffusion along grain and interphase boundaries in Alpha Zr and Zr-2.5 Wt Pct Nb alloy. 797-800A
- Zirconium base alloys, Mechanical properties**  
Steady-state creep of  $\alpha$ -zirconium at temperatures up to 850°C. 337-343A  
Anisotropic threshold stress intensity factor, K<sub>IS</sub>, and crack growth rate in delayed hydride cracking of Zr-2.5Nb pressure tubes. 919-925A  
Analysis of steady-state thermal creep of Zr-2.5Nb pressure tube material. 1103-1115A
- Zirconium base alloys, Microstructure**  
Intergranular stresses in ZIRCALOY-2. 749-755A  
Distribution of c- and a-dislocations in tubes of Zr alloys. 867-874A
- Zirconium base alloys, Powder technology**  
Thermally Enhanced and Mechanically Driven Glass Formation Reactions of Multilayered Cu<sub>33</sub>Zr<sub>67</sub> Powders. 2145-2153A
- Zirconium base alloys, X ray analysis**  
Determination of dislocation densities in Hcp metals from X-ray diffraction line-broadening analysis. 859-865A
- Zirconium compounds, Composite materials**  
Intermetallic-reinforced light-metal matrix in-situ composites. 193-201A
- Zirconium compounds, Microstructure**  
Phase Separation Tendency in the As-Solidified Zr3Al-Nb Alloys Studied by Microstructural Observations and Thermodynamic Analysis. 1919-1929A
- Zirconium compounds, Powder technology**  
Solid-state crystalline-glassy cyclic phase transformations of mechanically alloyed Cu<sub>33</sub>Zr<sub>67</sub> powders. 135-143A
- Zirconium dioxide, Joining**  
Phase equilibria of the ternary Ni-Cr-Zr system and interfacial reactions in the Ni-Cr/Zr couples. 995-1002A

